# Strojniški vestnik

# Journal of Mechanical Engineering

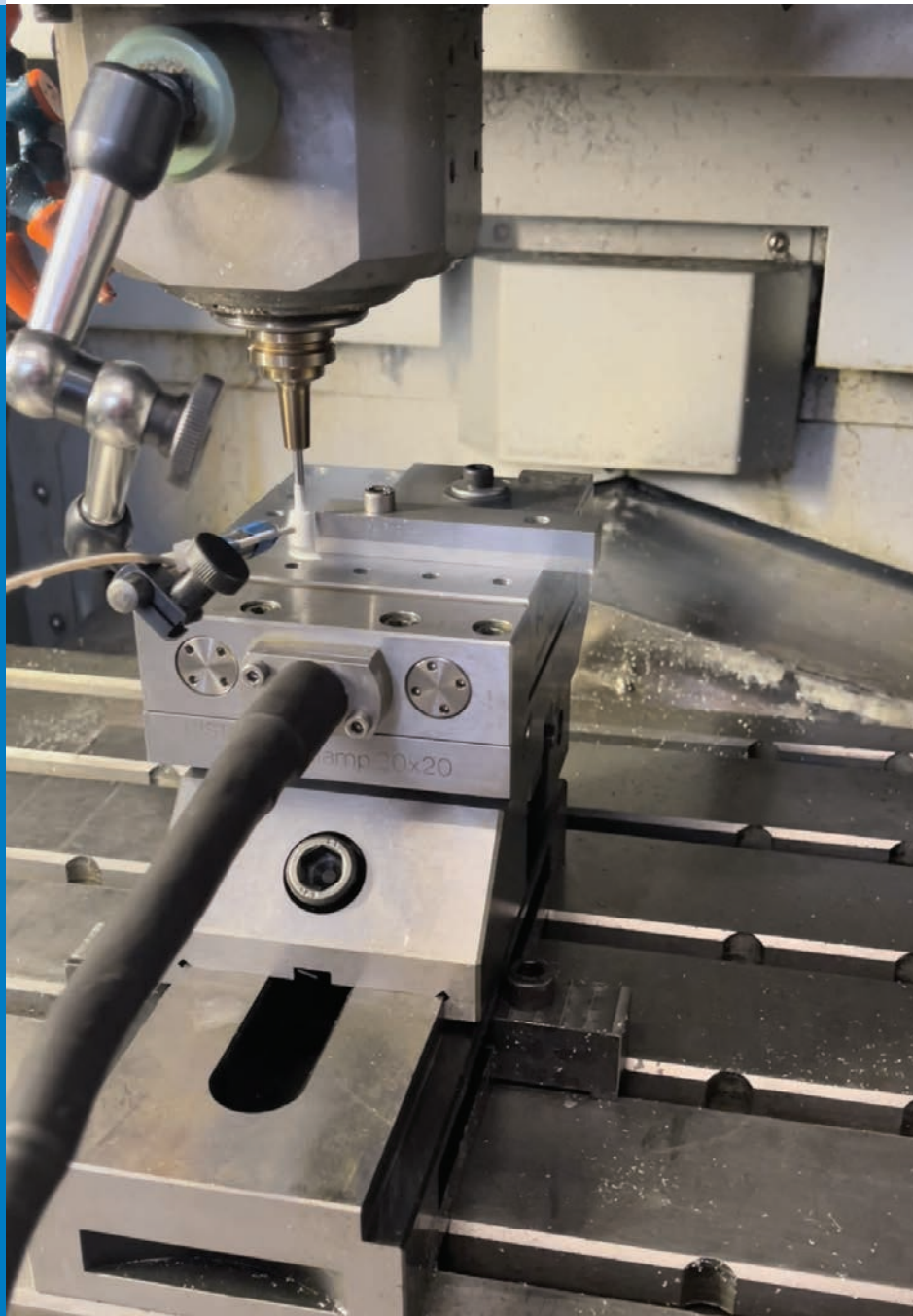

no. 11-12
year 2023
volume 69

# Strojniški vestnik – Journal of Mechanical Engineering (SV-JME)

**Aim and Scope**
The international journal publishes original and (mini)review articles covering the concepts of materials science, mechanics, kinematics, thermodynamics, energy and environment, mechatronics and robotics, fluid mechanics, tribology, cybernetics, industrial engineering and structural analysis.
The journal follows new trends and progress proven practice in the mechanical engineering and also in the closely related sciences as are electrical, civil and process engineering, medicine, microbiology, ecology, agriculture, transport systems, aviation, and others, thus creating a unique forum for interdisciplinary or multidisciplinary dialogue.
The international conferences selected papers are welcome for publishing as a special issue of SV-JME with invited co-editor(s).



**Print:** Demat d.o.o., printed in 240 copies

**Founders and Publishers**
University of Ljubljana, Faculty of Mechanical Engineering, Slovenia
University of Maribor, Faculty of Mechanical Engineering, Slovenia
Association of Mechanical Engineers of Slovenia
Chamber of Commerce and Industry of Slovenia, Metal Processing Industry Association




**Cover:**
Single-channel $LCO_2$+MQL pin grinding using a diamond wheel. The image shows the grinding setup using the $LCO_2$+MQL system. The workpiece is fixed on the dynamometer and the $LCO_2$+MQL nozzle is aimed at the workpiece-wheel interface. The grinding wheel is covered with a frozen layer of $LCO_2$ and MQL.

*Image Courtesy:*
Deepa Kareepadath Santhosh et.al
Laboratory for Machining, Faculty of Mechanical Engineering, University of Ljubljana, Slovenia



**General information**
Strojniški vestnik – Journal of Mechanical Engineering is published in 6 double issues per year.

Institutional prices include print & online access: institutional subscription price and foreign subscription €100,00 (the price of a single issue is €10,00); general public subscription and student subscription €50,00 (the price of a single issue is €5,00). Prices are exclusive of tax. Delivery is included in the price. The recipient is responsible for paying any import duties or taxes. Legal title passes to the customer on dispatch by our distributor. Single issues from current and recent volumes are available at the current single-issue price. To order the journal, please complete the form on our website. For submissions, subscriptions and all other information please visit: *http://www.sv-jme.eu*.

You can advertise on the inner and outer side of the back cover of the journal. The authors of the published papers are invited to send photos or pictures with short explanation for cover content.

We would like to thank the reviewers who have taken part in the peer-review process.

**ISSN 0039-2480, ISSN 2536-2948 (online)**



The journal is subsidized by Slovenian Research and Inovation Agency.

SV-JME is indexed / abstracted in: SCI-Expanded, Compendex, Inspec, ProQuest-CSA, SCOPUS, TEMA. The list of the remaining bases, in which SV-JME is indexed, is available on the website.

Strojniški vestnik - Journal of Mechanical Engineering is available on *https://www.sv-jme.eu*.

# Contents

**Strojniški vestnik - Journal of Mechanical Engineering**
**volume 69, (2023), number 11-12**
**Ljubljana, November-December 2023**
**ISSN 0039-2480**

**Published every two months**

**Papers**

Strojniški vestnik - Journal of Mechanical Engineering 69(2023)11-12, 435-443
DOI:10.5545/sv-jme.2023.658
Original Scientific Paper
Received for review: 2023-05-27
Received revised form: 2023-09-12
Accepted for publication: 2023-10-04


# Grinding of Cemented Carbide Using a Vitrified Diamond Pin and Lubricated Liquid Carbon Dioxide

Deepa Kareepadath Santhosh[1,*] – Franci Pušavec[1] – Peter Krajnik[1,2]
[1] University of Ljubljana, Faculty of Mechanical Engineering, Slovenia
[2] Chalmers University of Technology, Department of Industrial and Materials Science, Sweden

*Despite extensive research on grinding of cemented carbide, few studies have examined abrasive machining of this material using small-diameter super abrasive tools (also known as grinding pins/points), especially with respect to varying cooling-lubrication methods. This study therefore focuses on a comparative experimental investigation of three such methods - dry, emulsion, and lubricated liquid carbon dioxide ($LCO_2$-MQL). The performance of these methods and the resulting grindability are examined in terms of grinding forces, force ratios, specific energy, and through the analysis of wheel loading. The results show that $LCO_2$-MQL grinding has lower grinding forces (normal forces – 8 % to 145 % lower than dry grinding, and 18 % to 33 % lower than emulsion grinding and tangential forces – 4 % to 66 % lower than dry grinding and 28 % to 78 % lower than emulsion grinding) and specific energy 24 % to 51 % lower compared to dry grinding and 64 % to 69 % lower than emulsion grinding, indicating its potential for efficient material removal. However, a challenge with high wheel loading was observed with $LCO_2$-MQL, likely due to the lack of oxygen in the $CO_2$ grinding atmosphere. Despite this issue, the $LCO_2$-MQL method shows potential for efficient operations, especially at higher aggressiveness values where the lowest specific energies were achieved. These results provide new insights into various aspects of cooling-lubrication methods in the pin grinding of cemented carbides.*
**Keywords: diamond, grinding, cemented carbides, cooling-lubrication, carbon dioxide**

**Highlights**
- *Analysis of different cooling-lubrication conditions reveals $LCO_2$-MQL as a potentially superior method.*
- *$LCO_2$-MQL reduces grinding forces and specific energy in pin grinding.*
- *$LCO_2$-MQL achieves the lowest force ratio, indicating superior lubrication capability.*
- *Wheel loading is present in all cooling-lubrication methods but is most severe in $LCO_2$-MQL.*

## 0 INTRODUCTION

Cemented carbides, known for their excellent combination of hardness, wear resistance, and toughness, have become the most common cutting tool materials for machining applications. The combination of the high hardness of tungsten-carbide (WC) grains cemented into a composite by a ductile Co binder yields outstanding mechanical properties [1]. Cemented carbides are considered hard-to-machine materials due to their high strength at elevated temperatures and low modulus of elasticity [2]. This work focuses on the GC1130 grade developed by Sandvik Coromant, which features a high hardness and wear-resistant substrate due to its high chromium content and fine-grained microstructure. The WC grain boundaries are structured to enhance edge toughness, and the grade is designed to resolve tool life and issues associated with chipping, flaking, and thermal cracking in milling operations.

Due to its inherent hardness, the production of cemented carbides almost always includes grinding using diamond grinding wheels at the end of the manufacturing value chain. Diamond wheels typically feature a metal bond, or a hybrid, resinoid-metal, bond. The grinding of cemented carbides is in high demand in the industry, and these processes are accompanied by high grinding forces, specific energy, wheel wear, and low material removal rates [3]. Another concern, common on the shop floor but not extensively researched, is wheel loading, which is especially challenging when grinding with low aggressiveness. In a loaded wheel, the workpiece material becomes embedded within the pores of the diamond wheel, which prevents normal grinding action, i.e., material-removal by chip formation. Badger reported that loading of cemented carbide workpiece material does not appear to be caused by the high ductility of the workpiece material or a chemical reaction, but rather by the short, WC-Co chips [4]. The author proposed the loading be removed via stick-conditioning. In production, grinding machines have conditioning (sticking) done by truing using aluminum oxide wheels, often used in-process while grinding. In some cases, an external truing wheel can be used [5]. In the most challenging applications, diamond-wheel conditioning is done on metal-bonded wheels by spark electric-discharge dressing, which requires a special wheel design and grinding fluid to facilitate electrical conductivity [6].

Grinding fluids reduce the friction in the contact between the tool and the workpiece. This is achieved

*Corr. Author's Address: University of Ljubljana, Faculty of Mechanical Engineering, Aškerčeva 6, 1000 Ljubljana, Slovenia, deepa.kareepadathsanthos@fs.uni-lj.si

through lubrication. Grinding fluids also dissipate heat from the grinding zone, i.e., they provide cooling. While most industrial grinding of cemented carbides is done using (petroleum-based) straight oils, it is also possible to use a solution synthetic fluid, which is considered more environmentally friendly due to the large proportion of water (e.g., 95 %) in the grinding fluid. Both types of grinding fluids typically contain additives, such as chemical substances to inhibit cobalt leaching, i.e., removal of the cobalt binder. To further improve sustainability, it is viable to drastically reduce the amount of grinding fluids used [7]. For example, minimum quantity lubrication (MQL) technology can be used in the grinding of cemented carbides, which employs an oil-mist to lubricate the grinding process at a consumption rate that is on a mL/hour scale [8]. Nevertheless, while MQL can lubricate the process, it has limited cooling capability [9]. Therefore, recent innovative solutions include using subcooled MQL, for example, by using liquid nitrogen to reduce the temperature of the MQL oil mist [10], or by dissolving the oil in liquid carbon dioxide ($LCO_2$), which upon exiting a nozzle drops to a temperature of −78.5 °C and freezes the oil droplets, which measure only 2 micrometers in diameter [11]. Such advanced solutions to cooling and lubrication have not yet been explored in the grinding of cemented carbides. This work focuses on investigating the $LCO_2$ solution, as this technology has proven superior in other machining applications, such as in drilling [12] and milling [13]. Even though the pressure in $LCO_2$ cylinder is nearly 6 MPa (60 bar), it is likely that the air barrier formed around a grinding wheel rotating at high speed would prevent the $LCO_2$ from entering the grinding zone and causing it to be diverted elsewhere. Therefore, the first grinding investigation using $LCO_2$ intentionally involved using a tool with a much smaller diameter that does not create a distinct air barrier and is hence a lower obstacle to gas/oil-mist penetration. In conventional grinding, wheel diameters typically measure 400 mm to 600 mm, whereas the diameter of the grinding pins in focus here was only 6 mm. Grinding with small (generally ≤15 mm) fixed-abrasive tools, such as diamond pins mounted on a high-speed machining center is often referred to as pin or point grinding [14], which has proven to be a capable process for machining of hard and brittle materials with high dimensional accuracy and fine surface finish demands [15], due to a small grit-penetration depth. The available research on pin grinding of cemented carbides is limited. Kadivar et al. [16] studied the process mechanics and surface integrity of micro-grinding of titanium alloys and ceramics. Arrabiyeh et al. [17] studied the importance of process parameters in the micro-grinding of hardened steel. Morgan et al.'s [18] study, specifically focused on cemented carbides, revealed that the specific energy was initially high at the onset of tool-workpiece contact, but rapidly decreased to an almost constant value of 500 J/mm$^3$ after a stable tool engagement. Huang and Kuriyagawa [19] performed grinding of cemented carbide used for mold inserts, achieving better form accuracy and surface roughness even though they found small chipping of the material.

Based on the previous research, it has been observed that critical issues such as high rotational speeds, significant tool deflection, uneven grit protrusion, varying bond layer thickness, rapid tool wear, sensitivity to runout resulting in vibrations, and excessive tool loading are encountered [20]. While challenges such as wear and deflection can be addressed by optimizing grinding parameters, it was recognized that more research is needed, particularly in the areas of cooling and lubrication, and the investigation of vitrified pins, as most studies have focused primarily on electroplated (single layer) tools. In summary, research on pin grinding, particularly for cemented carbide materials, remains limited. Given this knowledge gap, the objective of the present study is to investigate the effects of various cooling-lubrication methods, including dry machining conditions as an extreme reference, on the grinding of cemented carbide using a vitrified diamond grinding pin. A secondary objective is to investigate the wheel-loading phenomena associated with different cooling-lubrication methods. The insights gained from this research could provide valuable information for future efforts to extend these experiments to conventional grinding applications using $LCO_2$.

## 1 EXPERIMENTAL

Pin grinding experiments were conducted using the Sodick MC 430L high-speed milling machine, The employed grinding tool was a vitrified-bonded diamond pin (D32-46-150-V-3195) mounted on a tungsten-carbide shaft, produced by Meister Abrasives. The pin had a diameter of 6 mm. The workpiece material chosen was an uncoated cemented carbide blank (GC1130 grade), designed for a gear-cutting insert and fabricated from the fine-grained, high-chromium by Sandvik Coromant. This workpiece, with dimensions of 85 mm × 15 mm × 13 mm, was subject to hardness testing with a Vickers microhardness tester, yielding a hardness value of

79 HV. Fig. 1 shows images of both the tool and the workpiece utilized in the grinding experiments.

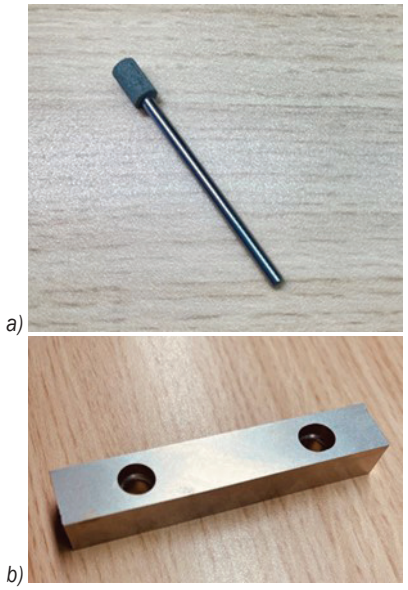

**Fig. 1.** **a**) *Diamond grinding tool, and b) cemented carbide workpiece*

After each test, the grinding wheel underwent a conditioning and cleaning process using a hand-sticking method with a fine-grit mesh silicon-carbide stone. The grinding experiments consisted of five varying grinding wheel speeds, ranging from 4 m/s to 12 m/s, while maintaining a constant workpiece speed (100 mm/min) and depth of cut (10 µm). This range in grinding wheel speeds provided six distinct grinding aggressiveness conditions. Table 1 lists the utilized grinding parameters and the corresponding calculated aggressiveness numbers, *Aggr*.

**Table 1.** *Grinding parameters used in the experiments*

| Experiment no. | Wheel speed [m/s] | Workpiece speed [mm/min] | Depth of cut [$\mu$m] | *Aggr* [-] |
|---|---|---|---|---|
| 1 | 12 | 100 | 10 | 5.68 |
| 2 | 10 | 100 | 10 | 6.82 |
| 3 | 8 | 100 | 10 | 8.52 |
| 4 | 6 | 100 | 10 | 11.36 |
| 5 | 4 | 100 | 10 | 17.04 |

Fig. 2 illustrates the experimental setup used for this study. A Kistler Type 9129AA dynamometer was employed to measure the normal and tangential grinding forces. During the $LCO_2$-MQL trials, the dynamometer was insulated to minimize potential drift and bias in force readings stemming from the low-temperature effects on the piezoelectric dynamometer. To assure the reliability and reproducibility of the results, each experimental test was replicated four times.

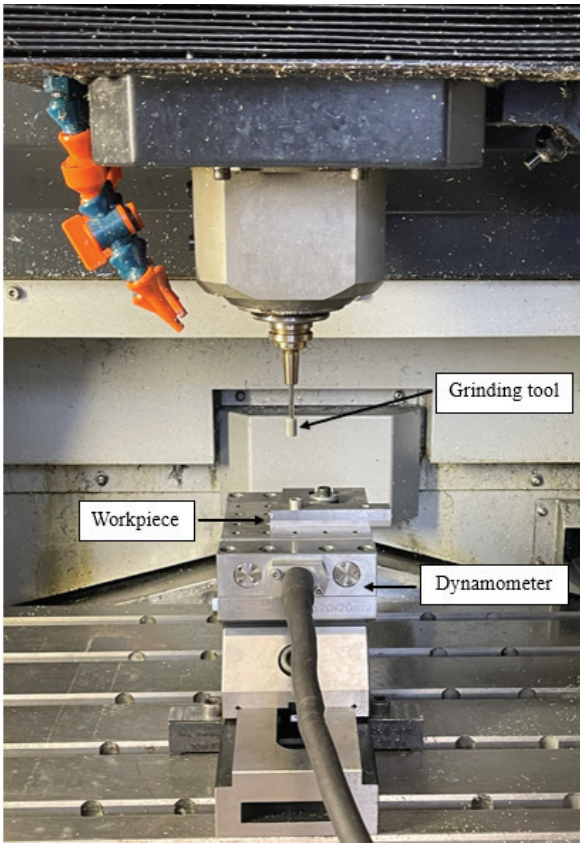


**Fig. 2.** *Experimental setup*

The tool's topography following each experiment was initially assessed utilizing a Keyence VHX 6000 digital microscope. Furthermore, an FEI/Philips XL30 ESEM (Environmental Scanning Electron Microscope) was employed to examine wheel surface and ascertain potential wheel loading or clogging issues.

Three different cooling-lubrication conditions were utilized in the grinding experiments: dry, emulsion, and $LCO_2$-MQL grinding. For "emulsion grinding" a conventional water-based cutting fluid in the form of a soluble oil emulsion with a concentration of 6 % was employed. The $LCO_2$-MQL system deployed, ArcLub One, was developed at the University of Ljubljana, Slovenia. This novel cooling-lubrication approach involves a single-channel supply of a pre-mixed blend of $LCO_2$ and oil, conveyed as MQL. As nonpolar oils, which are completely soluble in $LCO_2$, lead to smaller oil droplet sizes and more uniform distribution in MQL, a low-viscosity,

nonpolar oil was selected as the lubricant [11] and [21]. The chosen lubricant was HAROLBIO 0, a petroleum-free, saturated synthetic ester with a viscosity index of 152 (ASTM D 2270). An external nozzle was used to deliver the cooling lubricant to the grinding zone.

**Fig. 3.** *$LCO_2$-MQL grinding set up*

## 2 RESULTS AND DISCUSSION

In this section, an analysis of the results is presented, focusing on the evaluation of the grinding process through grindability aspects such as grinding forces, grinding force ratios, grinding specific energy, wheel loading, and wheel topography. The significance and novelty of the results are discussed. Limitations associated with the techniques used and the results presented are also highlighted.

### 2.1 Grinding Forces

The normal and tangential grinding forces were measured across four repetitions. Since the measured grinding forces remained relatively constant across these repetitions, average grinding force values were used in Figs. 4 and 5 to show their variation with *Aggr* and cooling-lubrication conditions. Both tangential and normal grinding forces were found to decrease with an increase in cutting speed – an expected result given that higher cutting speeds yield smaller *Aggr* values. In all cases, normal forces exceeded tangential grinding forces, an observation commonly noted in conventional grinding operations as well.

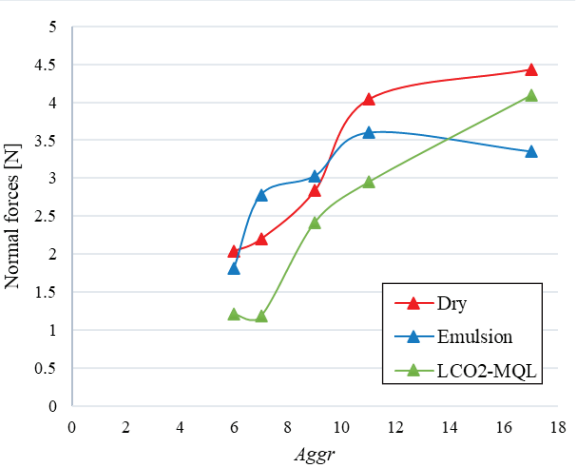


**Fig. 4.** *Normal grinding forces vs. Aggr*

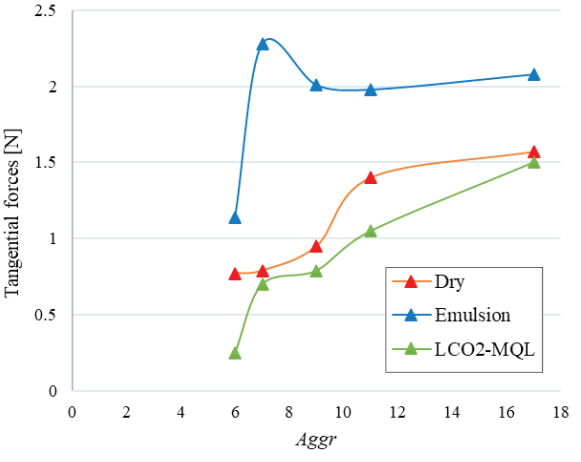


**Fig. 5.** *Tangential grinding forces vs. Aggr*

The normal grinding forces are lower in $LCO_2$-MQL grinding for the first five experiments and range from 1.2 N to 4.09 N, followed by emulsion and dry grinding. The tangential grinding forces are also lower for $LCO_2$-MQL grinding and range from 0.25 N to 1.5 N, followed by dry and emulsion grinding. The grinding force values were found to be exceptionally high in the last experiments of emulsion and $LCO_2$-MQL grinding due to excessive wheel wear and wheel loading. The sixth experiment at the highest *Aggr* is clearly an outlier, and hence not a representative case of normal grinding conditions. The normal and tangential grinding forces are comprised of two components, one due to cutting and one due to sliding on the wear flats [22]. The low tangential grinding forces observed in $LCO_2$-MQL grinding indicate

efficient shear in the grinding zone and lubrication. A boundary-lubricating film was likely formed through polar group adsorption [11]. The lubricating film allows the oil to penetrate the grinding zone, which helps to prevent issues such as evaporation, and adhesion that can occur due to high temperatures, when the lubricant layer is sufficiently thick, it provides an effective lubrication effect, further reducing grinding forces [23]. Hence, the combined effect of $LCO_2$ and MQL can enhance the formation of the lubricating film. This combination facilitates a continuous lubrication effect, which contributes to the reduction of grinding forces and friction [24]. The grinding forces are higher under dry grinding because of the excessive sliding and plowing action [25]. One can also observe very steady levels of normal and tangential forces in $LCO_2$-MQL, which indicate minimal tool wear, until its collapse [26] at excessive (Experiment 6) grinding condition at the highest tested *Aggr*.

The grinding force ratio is further analyzed as it provides indirect information regarding the efficiency of the grinding process. It can characterize the lubrication effect at the wheel/workpiece interface. A high grinding force ratio suggests poor lubrication in the grinding zone, whereas improved lubrication corresponds to a lower force ratio. The force ratio in grinding is synonymous with the coefficient of friction between sliding surfaces. For hard materials, the coefficient of friction is high, indicating worse grindability [27]. The following expression is used to calculate the grinding force ratio:

$$\mu = F_T / F_N, \quad (1)$$

where $F_T$ is the tangential grinding force, and $F_N$ is the normal grinding force.

Fig. 6 shows the grinding force ratios under varying cooling-lubrication conditions. The grinding force ratios for dry grinding range from 0.32 to 0.38. In comparison, grinding with emulsion gives ratios between 0.50 and 0.82, representing an increase of 56 % to 116 % compared to dry grinding. On the other hand, $LCO_2$ shows the lowest force ratios, ranging from 0.21 to 0.37, representing a 3 % to 34 % decrease compared to dry grinding and a 55 % to 58 % decrease compared to emulsion grinding. The grinding force ratio is maximum under emulsion grinding followed by dry grinding. The grinding force ratio in $LCO_2$-MQL grinding is lower compared to that in dry and emulsion grinding, indicating that the grindability, with respect to friction in the grinding zone, is enhanced with $LCO_2$-MQL grinding. The penetration of $LCO_2$-MQL into the grinding zone creating a boundary lubrication layer provides better lubrication, hence reducing friction [23].

## 2.2. Specific Grinding Energy

Specific grinding energy, *u*, is a fundamental parameter for gauging the efficiency of the grinding process. This quantity is defined as the energy expended per unit volume of material removed [28]. Specific energy is dependent on the tangential grinding force, the employed grinding parameters, the workpiece material's grindability, the tool's topography, and the tribological conditions in the grinding zone, which are largely determined by the cooling-lubrication method

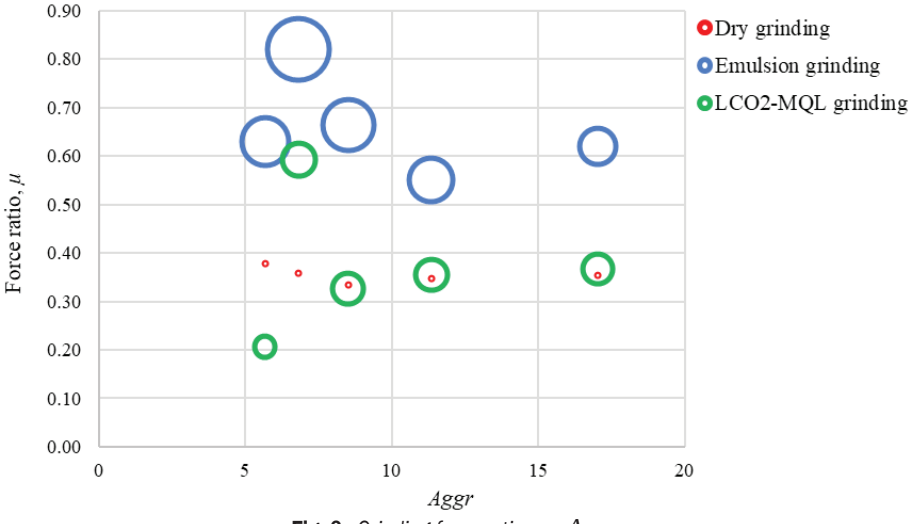


**Fig. 6.** *Grinding force ratios vs. Aggr*

used. The following equation can be used to calculate the specific energy [28]:

$$u = F_T V_s / (V_w a b) \quad (2)$$

where $F_T$ is the tangential grinding force, $V_s$ is the wheel speed, $V_w$ is the workpiece speed, $a$ is the depth of cut, and $b$ is the grinding width of cut.

Badger et al. [29] introduced the dimensionless aggressiveness number, *Aggr*, a fundamental parameter encapsulating the geometry and kinematics of a grinding process. In this study, *Aggr* was therefore used to quantify the intensity of abrasive interaction during the experiments as it is fundamentally linked to the specific grinding energy. As such, the outcomes of the pin-grinding experiments were analyzed and charted across various aggressiveness numbers. The aggressiveness number can be calculated as follows:

$$Aggr = 10^6 (V_w / V_s) (a / d_s)^{1/2}, \quad (3)$$

where $d_s$ is the diameter of the wheel.

The obtained specific grinding energy values for the different cooling-lubrication methods are given in Table 2. The specific energies here were calculated using the measured tangential grinding forces at different *Aggr* values. The specific grinding energy was lower at higher *Aggr*, indicating that increasing the wheel speed improves the efficiency of material removal, since the lower specific energy indicates lower proportions of sliding/friction in the chip formation process [3]. This phenomenon is especially noticeable in pin-grinding or when the depth of cut is very small.

**Table 2.** *Specific grinding energy values for different cooling-lubrication conditions*

| Experiment No. | *Aggr* [-] | Specific energy [J/mm³] | | |
|---|---|---|---|---|
| | | Dry | Emulsion | $LCO_2$-MQL |
| 1 | 5.68 | 55 | 82 | 18 |
| 2 | 6.82 | 47 | 137 | 42 |
| 3 | 8.52 | 45 | 96 | 38 |
| 4 | 11.36 | 50 | 71 | 38 |
| 5 | 17.04 | 37 | 50 | 36 |

In $LCO_2$-MQL grinding, the obtained specific energy values range from 18 J/mm³ to 42 J/mm³, the lowest among the tested cooling-lubrication conditions. By comparison, the values for dry grinding are between 37 J/mm³ and 55 J/mm³, and for emulsion grinding, they span from 50 J/mm³ to 137 J/mm³. These results suggest that $LCO_2$-MQL cooling lubrication enables the most efficient cutting.

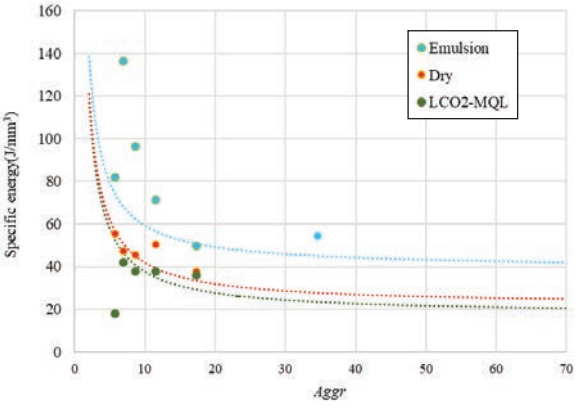


**Fig. 7.** *Specific grinding energy vs. Aggr*

The specific energy curve depicted in Fig. 7 exhibits a typical size effect, indicating that specific energy declines as the aggressiveness number (or undeformed chip thickness) increases. This effect can be attributed to the transitional nature of the grinding process among the sliding, ploughing, and cutting regimes. With larger *Aggr* values, the grinding process is dominated by the cutting regime, where material removal occurs predominantly through shearing. Conversely, at lower *Aggr* values, the grits of the grinding wheel largely slide across the workpiece surface, resulting in limited material removal. The latter behavior necessitates a greater energy expenditure to remove a unit volume of material, thereby contributing to the observed size effect.

### 2.3 Wheel Topography

After each experiment, regardless of the cooling-lubrication method utilized, wheel loading was noted; a phenomenon expected due to the low grinding aggressiveness. The tested *Aggr* values in pin-grinding with a diamond pin are significantly smaller compared to values observed in larger-scale grinding operations. This is mentioned, as the problem of wheel loading is also common in conventional grinding of cemented carbides, particularly when using straight oil as a grinding fluid. This issue was mitigated during the sequence of experiments and their repetitions by conducting a thorough conditioning and cleaning of the grinding wheel surface after each trial using an abrasive stone/stick, as described in Section 1. Figs. 8 to 10 depict images of the wheel topography following grinding under different cooling-lubrication conditions. With dry grinding (Fig 8), the wheel loading is clearly visible after each experiment. This is due to the lack of grinding fluid to flush away the

chips during grinding and to reduce temperatures. In emulsion grinding, the wheel loading is less than in other methods due to the effectiveness of the emulsion in preventing clogging and removing chips. However, $LCO_2$-MQL grinding (Fig. 10) presents a stark contrast. Although $LCO_2$-MQL has the lowest values of grinding forces and specific energy, it has a substantial wheel loading, which is noteworthy. This is likely due to the lack of oxygen in a $CO_2$ atmosphere, which may enhance the adhesion of metal particles (chips) to the grinding wheel.

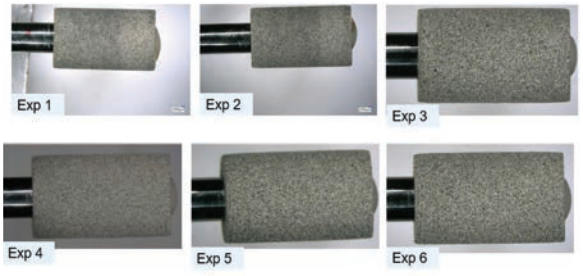


**Fig. 8.** *Wheel loading after dry grinding*

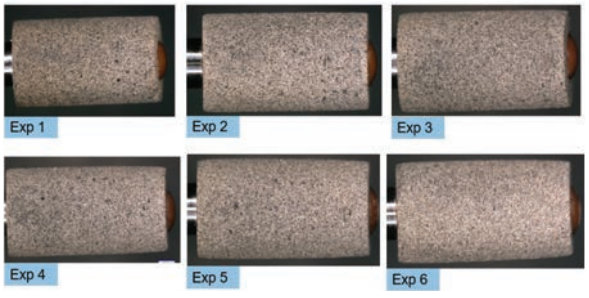


**Fig. 9.** *Wheel loading after grinding with emulsion*

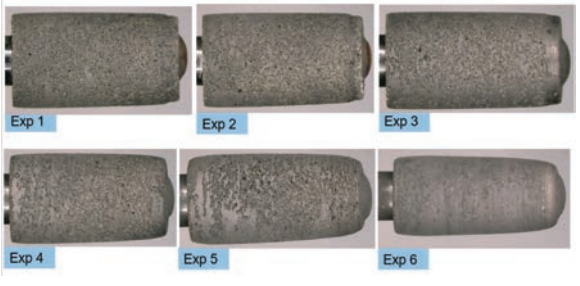


**Fig. 10.** *Wheel loading after $LCO_2$-MQL grinding*

To investigate the loading for the $LCO_2$-MQL case more thoroughly, the pins were gold sputtered before electron back-scatter diffraction pattern analysis was conducted. Fig. 11 displays scanning electron micrographs (Fig. 11a) magnification 350 x, Fig. 11b) magnification 95 x), which reveal the particles loaded onto the wheel. The bright white, shiny areas represent the cemented carbide materials loaded into the wheel, a conclusion further supported by a chemical analysis of the wheel surface. This result could be due to inefficient chip evacuation when using $LCO_2$-MQL, which contradicts previous findings of reduced loading during $LCO_2$-MQL grinding of a titanium alloy with a conventional wheel [30].

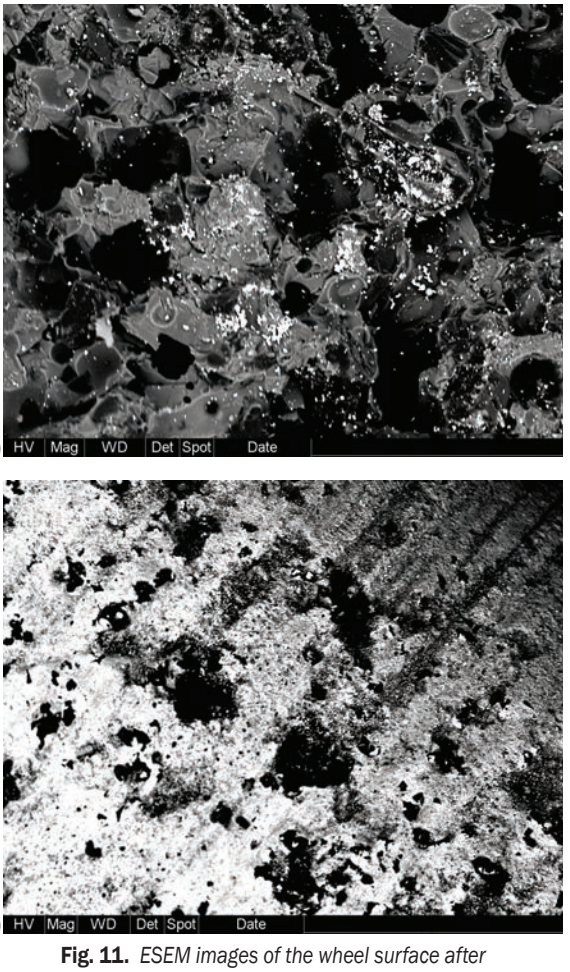


**Fig. 11.** *ESEM images of the wheel surface after $LCO_2$-MQL grinding; a) ESEM (magnification 350×), and b) ESEM (magnification 95×)*

While the presence of oxygen in a typical grinding atmosphere minimizes the sticking, or "adhesion," of metal particles to each other and to the workpiece, enhancing the overall grinding process, its absence in environments like a vacuum or an inert (non-reactive) atmosphere can significantly alter the process. Specifically, the lack of oxygen may increase the likelihood of metal particles sticking to each other and adhering to the workpiece and the grinding wheel [31] and [32]. When oxygen is absent, freshly created metal workpiece particles, or chips, with pristine, uncontaminated surfaces, have a propensity to physically stick to one another and to the wheel

surface. This behavior subsequently leads to the loading and clogging of the wheel [28].

## 3 CONCLUSIONS

In conclusion, this study was conducted to advance the understanding of the effects of varying cooling-lubrication conditions on pin grinding of cemented carbides. Through the detailed investigation of three different conditions: $LCO_2$-MQL, dry, and emulsion grinding – the following results were obtained.

The grinding forces and specific grinding energies were found to be lowest in $LCO_2$-MQL grinding. It was found that grinding under emulsion (flood) conditions resulted in a poorer performance compared to dry grinding.

In addition, the lack of oxygen in a $CO_2$ atmosphere can potentially increase the adhesion of metal particles (chips) to the grinding wheel, leading to challenges in the grinding process, especially severe wheel loading in the case of $LCO_2$-MQL grinding. However, the novel method of cooling-lubrication, using lubricated liquid carbon dioxide, while demonstrating a wheel loading problem, showed potential for improved grinding efficiency.

These findings pave the way for further investigation into optimizing the material removal processes in the pin-grinding of cemented carbides, with a particular focus on addressing wheel loading issues and understanding the role of the grinding atmosphere.

## 4 ACKNOWLEDGEMENTS

The authors would like to express their gratitude to Meister Abrasives and Sandvik Coromant for their invaluable support in this research endeavor. Special appreciation is extended to Mr. Elias Navarro and Mr. Per Norlin for providing the vitrified diamond pins and cemented carbide blanks, respectively. Further, we acknowledge the financial support received from the Slovenian Research Agency (No. 54942. Lastly, partial support from the EIT Manufacturing program, through the project (21193: Transitioning to a Waste-free Production – International Cryogenic + MQL Machining Activity), is gratefully recognized.

## 5 REFERENCES

[1] Hegeman, J.B.J.W., de Hosson, J.Th.M., de With, G. (2001). Grinding of WC-Co hardmetals. *Wear*, vol. 248, no. 1-2, p. 187-196, **DOI:10.1016/s0043-1648(00)00561-5**.

[2] Mahata, S., Mukhopadhyay, M., Kundu, A., Banerjee, A., Mandal, B., Das, S. (2020). Grinding titanium alloys applying small quantity lubrication. *SN Applied Sciences*, vol. 2, no. 2, **DOI:10.1007/s42452-020-2792-2**.

[3] Kadivar, M., Daneshi, A., Azarhoushang, B. (2018). Study of specific energy in grinding of tungsten carbide. XIV$^{th}$ International Conference on High-Speed Machining.

[4] Badger, J. (2015). Grinding of sub-micron-grade carbide: Contact and wear mechanisms, loading, conditioning, scrubbing, and resin-bond degradation. *CIRP Annals*, vol. 64, no. 1, p. 341-344, **DOI:10.1016/j.cirp.2015.04.007**.

[5] Dražumerič, R., Badger, J., Klement, U., Krajnik, P. (2018). Truing of diamond wheels - Geometry, kinematics, and removal mechanisms. *CIRP Annals*, vol. 67, no. 1, p. 345-348, **DOI:10.1016/j.cirp.2018.04.091**.

[6] Koshy, P., Jain, V.K., Lal, G.K. (1997). Grinding of cemented carbide with electrical spark assistance. *Journal of Materials Processing Technology*, vol. 72, no. 1, p. 61-68, **DOI:10.1016/S0924-0136(97)00130-1**.

[7] Krajnik, P., Rashid, A., Pušavec, F., Remškar, M., Yui, A., Nikkam, N., Toprak, M.S. (2016). Transitioning to sustainable production - part III: Developments and possibilities for integration of nanotechnology into material processing technologies. *Journal of Cleaner Production*, vol. 112, p. 1156-1164, **DOI:10.1016/j.jclepro.2015.08.064**.

[8] Hosseini, S.F., Emami, M., Sadeghi, M.H. (2018). An experimental investigation on the effects of minimum quantity nano lubricant application in grinding process of Tungsten carbide. *Journal of Manufacturing Processes*, vol. 35, p. 244-253, **DOI:10.1016/j.jmapro.2018.08.007**.

[9] Pušavec, F., Grguraš, D., Koch, M., Krajnik, P. (2019). Cooling capability of liquid nitrogen and carbon dioxide in cryogenic milling. *CIRP Annals*, vol. 68, no. 1, p. 73-76, **DOI:10.1016/j.cirp.2019.03.016**.

[10] Laakso, V.A.S., Mallipeddi, D., Krajnik, P. (2022). Evaluation of subcooled MQL in CBN hard turning of powder-based Cr-Mo-V tool steel using simulations and experiments. *The International Journal of Advanced Manufacturing Technology*, vol. 118, p. 511-531, **DOI:10.1007/s00170-021-07901-x**.

[11] Grguraš, D., Sterle, L., Krajnik, P., Pušavec, F. (2019). A novel cryogenic machining concept based on lubricated liquid carbon dioxide. *International Journal of Machine Tools and Manufacture*, vol. 145, art. ID 103456, **DOI:10.1016/j.ijmachtools.2019.103456**.

[12] Sterle, L., Krajnik, P., Pušavec, F. (2021). The effects of liquid-$CO_2$ cooling, MQL, and cutting parameters on drilling performance. *CIRP Annals*, vol. 70, no. 1, p. 79-82, **DOI:10.1016/j.cirp.2021.04.007**.

[13] Pušavec, F., Sterle, L., Kalin, M., Mallipeddi, D., Krajnik, P. (2020). Tribology of solid-lubricated liquid carbon dioxide assisted machining. *CIRP Annals*, vol. 69, no. 1, p. 69-72, **DOI:10.1016/j.cirp.2020.04.033**.

[14] Aguirre, F.M., Gonzalez, L.S., Hood, R., Kong, M.C., Novovic, D., Soo, L.S. (2023). Assessment of advanced process configurations for improving workpiece surface finish in point grinding. *CIRP Annals*, vol. 72, no. 1, p. 267-272, **DOI:10.1016/j.cirp.2023.04.078**.

[15] Kadivar, M., Azarhoushang, B., Shamray, S., Krajnik, P. (2018). The effect of dressing parameters on micro-grinding of titanium alloy. *Precision Engineering*, vol. 51, p. 176-185, **DOI:10.1016/j.precisioneng.2017.08.008**.

[16] Kadivar, M., Azarhoushang, B., Klement, U., Krajnik, P. (2021). The role of specific energy in micro-grinding of titanium alloy. *Precision Engineering*, vol. 72, p. 172-183, **DOI:10.1016/j.precisioneng.2021.04.015**.

[17] Arrabiyeh, A.P., Setti, D., Basten, S., Kirsch, B., Aurich, C.J. (2019). Micro grinding 16MnCr5 hardened steel using micro pencil grinding tools with diameters ~ 50 mm. *CIRP Journal of Manufacturing Science and Technology*, vol. 27, p. 1-10, **DOI:10.1016/j.cirpj.2019.10.002**.

[18] Morgan, J.C., Vallance, R.R., Marsh, R.E. (2007). Specific grinding energy while micro grinding tungsten carbide with polycrystalline diamond micro tools. *ICOMM*.

[19] Huang, H., Kuriyagawa, T. (2005). Effect of microstructure on material removal mechanisms in nano/micro grinding of tungsten carbide mould inserts. *International Conference on Leading Edge Manufacturing in 21st Century*, p. 877-882, **DOI:10.1299/jsmelem.2005.2.877**.

[20] Pietrowa, N., Curtis, D., Ghadbeigi, H., Novovic, D., McGourlay, J. (2021). An investigation into the challenges of the point grinding machining process. *Procedia CIRP*, vol. 101. p. 190-193, **DOI:10.1016/j.procir.2020.09.19**5.

[21] Grguraš, D., Sterle, L., Kastelic, L., Courbon, C., Pušavec, F. (2021). Media flow analysis of single-channel pre-mixed liquid CO2 and MQL in sustainable machining. *Strojniški vestnik - Journal of Mechanical Engineering*, vol. 67, no. 1-2, p. 3-10, **DOI:10.5545/sv-jme.2020.7076**.

[22] Macerol, N., Franca, F.P.L., Drazumeric, R., Krajnik, P. (2022). The effects of grit properties and dressing on grinding mechanics and wheel performance: Analytical assessment framework. *International Journal of Machine Tools and Manufacture*, vol. 180, art. ID 103919, **DOI:10.1016/j.ijmachtools.2022.103919**.

[23] Liu, M., Li, C., Yang, M., Gao, T., Wang, X., Cui, X., Zhang, Y., Said, Z., Sharma, S. (2023). Mechanism and enhanced grindability of cryogenic air combined with bio lubricant grinding titanium alloy. *Tribology International*, vol. 187, art. ID 108704, **DOI:10.1016/j.triboint.2023.108704**.

[24] Garcia, E., Pombo, I., Sanchez, A.J., Ortega, N., Izquierdo, B., Plaza, S., Marquinez, I., J., Heinzel, C., Mourek, D. (2013). Reduction of oil and gas consumption in grinding technology using high pour-point lubricants. *Journal of Cleaner Production*, vol. 51, p. 99-108, **DOI:10.1016/j.jclepro.2013.01.037**.

[25] Prashanth, S.G., Sekar, P., Bontha, S., Balan, A.S.S. (2022). Grinding parameters prediction under different cooling environments using machine learning techniques. *Materials and Manufacturing Processes*, vol. 38, no. 2, p. 235-244, **DOI:10.1080/10426914.2022.2116043**.

[26] Badger, J. (2009). Factors affecting wheel collapse in grinding. CIRP Annals, vol. 58, no.1, p. 307-310, **DOI:10.1016/j.cirp.2009.03.048**.

[27] Wu, W., Li, C., Yang, M., Zhang, Y., Jia, D., Hou, Y., Li, R., Cao, H., Han, Z. (2019). Specific energy and G ratio of grinding cemented carbide under different cooling and lubrication conditions. *The International Journal of Advanced Manufacturing Technology*, vol. 105, p. 67-82, **DOI:10.1007/s00170-019-04156-5**.

[28] Malkin, S., Guo, C. (2008). *Grinding Technology: Theory and Applications of Machining with Abrasives: Second Edition*, Industrial Press, Inc., New York.

[29] Badger, J., Dražumerič, R., Krajnik, P. (2021). Application of the dimensionless Aggressiveness number in abrasive processes. *Procedia CIRP*, vol. 102, p. 361-368, **DOI:10.1016/j.procir.2021.09.062**.

[30] Singh, S.K., Jha, A.K., Ray, A., Dewangan, S. (2022). Enhancing grinding parameters of TC4 titanium superalloy by using a hybrid eco-friendly cooling system. *Materials Today*, vol. 62, no. 3, p. 1505-1509, **DOI:10.1016/j.matpr.2022.02.214**.

[31] Duwell, E.J., Hong, I.S., McDonald, W.J. (1969). The effect of oxygen and water on the dynamics of chip formation during grinding. *A S L E Transactions*, vol. 12, no. 1, p. 86-93, **DOI:10.1080/05698196908972250**.

[32] Outwater, J.O., Shaw, M.C. (1952). Surface Temperatures in Grinding. *ASME Journal of Fluids Engineering*, vol. 74, no. 1, p. 73-81, **DOI:10.1115/1.4015689**.

Strojniški vestnik - Journal of Mechanical Engineering 69(2023)11-12, 444-454
DOI:10.5545/sv-jme.2023.601
Original Scientific Paper
Received for review: 2023-04-11
Received revised form: 2023-09-15
Accepted for publication: 2023-09-19


# Aerodynamic Analysis of Mathematically Modelled Propeller for Small UAV Using CFD in Different Temperature Conditions

Tamilselvan Ganesan,* – Niresh Jayarajan
PSG College of Technology, Department of Automobile Engineering, India

*Unmanned aerial vehicle (UAV) usage has witnessed a significant rise owing to its cost-effectiveness and versatile applications. However, the design techniques for UAV propellers, encompassing aerodynamic and structural analysis, have received limited attention from researchers. A well-designed propeller can effectively reduce battery consumption and enhance overall efficiency. This study focuses on mathematically designed propellers and compares them with advanced precision composite (APC) Slow Flyer propeller blades in terms of thrust coefficients, power coefficients, and efficiency. The investigation includes the utilization of tetrahedron meshing in simulations, employing the standard k–ω (k–omega) model. To evaluate the accuracy of the blade element theory (BET) in predicting thrust, the simulation data is compared with BET results. Furthermore, the study encompasses experimental testing to validate the simulation findings. The findings demonstrate that the mathematically modelled propeller outperforms the APC Slow Flyer propeller across all ranges of revolutions per minute (rpm). When comparing the results of both methods, BET exhibits an error difference of 10 % in higher rpm ranges, but this error diminishes as the rpm decreases. This study contributes a novel design technique for modelling propellers using mathematical formulas and provides a comprehensive comparison of their aerodynamic properties with existing propellers, utilizing both BET and computational fluid dynamics (CFD) methods, along with experimental validation.*

**Keywords: unmanned aerial vehicle, propeller, computational fluid dynamics, blade element theory, mathematical design**

**Highlights**

- *Design the propeller based on the mathematical model generated using the Eppler E63-based airfoil due to the amount of lift it generates to increase the UAV thrust and efficiency.*
- *Perform the CFD analysis for these propellers in various temperature conditions and generate the results.*
- *Compare the designed propeller with the APC Slow Flyer, which is among the most commonly used in 10' UAV propellers.*
- *Blade element theory has been used to verify the results generated from the analysis and noted the error difference between these two.*

## 0 INTRODUCTION

Unmanned aerial vehicles (UAVs) play a vital role in defence missions, encompassing remote sensing, surveillance, and data collection in challenging environments with varying temperatures [1]. The lifespan of a drone is crucial in such missions, as numerous operational factors significantly impact its performance and structural integrity [2] to [4]. Rotor blades serve as fundamental components of drones and most UAVs, with operational temperature being a crucial parameter in their design. However, a comprehensive database on UAV performance in harsh environmental conditions is still lacking, which is critical for evaluating battery lifespan and thrust prediction in relation to weather conditions. Our primary objective is to gather data on propeller performance under cold temperatures for preliminary research on the impact of environmental factors on UAV propulsion systems [5] to [9].

In recent years, several experiments have been conducted on small UAVs and their power systems. Brandt and Selig [10] focused on propellers for small unmanned aerial vehicles, creating a reference database that emphasizes thrust generation in windy conditions and propeller behaviour in low Reynolds flow conditions. Scanavino et al. [11] proposed a comparison between blade element theory and experimental results obtained from extreme weather conditions using a 15' × 5' carbon fibre propeller. Another significant contribution was made by Russell et al. [12], who analysed the performance of five commercial UAVs in a wind tunnel under static conditions, providing a comprehensive overview of their overall performance. That article includes information about the experimental analysis, test matrix and results obtained from laser scanner measurements. However, when it comes to UAVs in harsh environments, few papers describe the performance of these vehicles. Precision Hawk [13] conducted environmental experiments on multi-rotor and fixed-wing propellers in partnership with the Automotive Centre of Excellence. Unfortunately, no experimental data from these studies have been made available for investigation. More recently, research on propellers has focused on ice accretion conditions


*Corr. Author's Address: PSG College of Technology, Coimbatore, Tamil Nadu, India, tamilselvanganesan98@gmail.com

[14] to [17], exploring the aerodynamic performance of propellers at various water content and operational temperature levels. The goal of this characterization was to develop a new anti-ice propeller component that would reduce power consumption. A passive solution based on surface wettability and hydrophobic materials has been proposed.

The UAV industry has only recently begun providing end users with information on flying recommendations in extreme circumstances [18] and [19]. For instance, the Alta 8 flying handbook by Freefly Systems includes a table that shows the maximum take-off weight as a function of temperature and altitude. However, beyond conventional flying conditions, data are often based on projections, real-world experiments, and user input.

In our research, we focus on designing propellers using numerical formulas to optimize their efficiency. We specifically employ high lift, low drag airfoils that are well-suited for low Reynolds numbers, such as the Eppler E63 airfoil. By utilizing the airfoil's data coordinates and implementing a spline interpolation technique, we design propellers based on these numerical values using computer aided design (CAD) software. Subsequently, the propellers undergo comprehensive analysis of various aerodynamic properties, including thrust, lift, and drag, through the utilization of computational fluid dynamics (CFD) simulations. To ensure controlled conditions, we employ a specialized climate-controlled facility to collect precise experimental data. The experimental results are then compared with the CFD simulations, as well as benchmarked against industry-leading propellers such as the 10' APC propeller and the classic NACA 4412 propeller. By combining both experimental and computational approaches, our primary objective is to provide a comprehensive analysis of the performance of these mathematically designed propellers.

## 1 ENVIRONMENTAL CONDITIONS

Testing the propeller in harsh environmental conditions is one of this experiment's main objectives. Propeller thrust data will be useful for UAV objectives and will increase reliability while flying in extreme environmental conditions. For this experiment, the pressure is kept constant during propeller testing in various temperature environments. The temperature of the environment influences air density called the isobaric test as shown in Table 1.

**Table 1.** *Isobaric test conditions*

| Temperature [°C] | Pressure [hPa] | Air density [kg/m³] |
|---|---|---|
| 42.5 | 989 | 1.0924 |
| 33.3 | 990 | 1.1256 |
| 29.3 | 990 | 1.1405 |
| 24.8 | 990 | 1.1577 |
| 18.1 | 983 | 1.1760 |
| -13.5 | 978 | 1.3124 |
| -20.3 | 978 | 1.3477 |
| -25.7 | 978 | 1.3771 |
| -28.4 | 977 | 1.3909 |
| -34.5 | 974 | 1.4221 |

## 2 DESIGN OF PROPELLER

### 2.1 Design of Optimal Rotor Blades

The rotation of a propeller blade creates turbulence, which reduces its efficiency. To maintain balance and maximize efficiency, propellers are typically designed with two blades. Adding more blades brings diminishing returns as the blades become

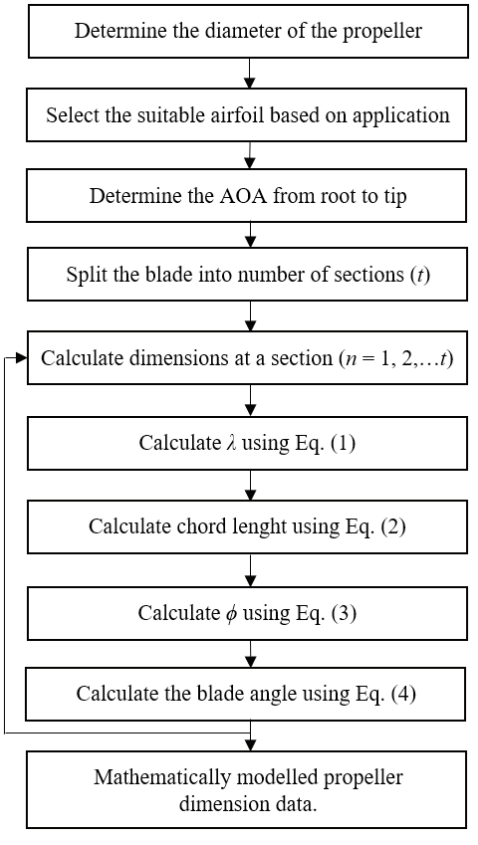


**Fig. 1.** *Methodology*

closer together, further decreasing efficiency. While a tri-blade or quad-blade configuration can provide additional thrust, the benefits are less pronounced. Therefore, most propellers used in small UAVs have two blades. In this research, a 10' propeller is chosen as it is widely used in small UAV applications. To enhance accuracy, each blade of the propeller is divided into 18 sections, resulting in a total of 32 sections for the complete propeller design. This segmentation allows for precise control over chord length and blade angle at each section. The propeller models are created using a set of formulas that define parameters such as chord length, tip speed ratio, air flow angle, and blade angle. The propellers are modelled in methods as shown in Fig. 1. These formulas ensure the propeller is designed with optimal characteristics for efficient performance.

The tip speed ratio (TSR), denoted as $\lambda$, represents the ratio of the tangential speed of the propeller blade tip to the wind velocity. It is a crucial parameter in propeller design as it directly influences various aspects of performance. When the tip speed increases, it can result in increased noise generation and vibrations within the propeller system. The formula for calculating the tip speed ratio is expressed in Eq. (1) as follows:

$$\lambda = \frac{Blade\ tip\ speed}{Wind\ speed} = \frac{\omega \cdot r}{v}, \tag{1}$$

where $\omega$ is rotational speed [rad/s], $r$ radius at the point of computation [m], $R$ radius at the tip [m], and $v$ wind velocity [m/s].

The chord length of a propeller refers to the distance between its leading and trailing edges in the direction of the wind. Increasing the chord length of a propeller can lead to improved efficiency. This is because a propeller with a larger width offers a larger surface area for interaction with the air. According to Newton's Third Law, a propeller can push back a greater number of air particles in a single rotation, resulting in a greater reaction force that propels the vehicle forward. Therefore, increasing the chord length contributes to enhanced propeller performance [20]. The calculation of the chord length is determined by utilizing Eq. (2) as follows:

$$Chord\ length = \frac{5.6 \cdot R^2}{\left(2 \cdot Cl \cdot r \cdot \lambda^2\right)}. \tag{2}$$

The inflow angle is the angle formed between the axis of the propeller and the direction of the airstream. It plays a significant role in the propeller equation [21]. The equation for determining the inflow angle Eq. (3) as follows:

$$\phi = tan^{-1}\frac{2}{3\lambda}. \tag{3}$$

The blade angle is the angle between the chord of the propeller blade and the plane of rotation. It is measured at a specific position along the length of the blade. The blade angle is the sum of the inflow angle and the angle of attack of the propeller, as stated in Eq. (4). To maintain a relatively constant angle of attack (AOA) along the length of the blade, the propeller blade twists along its length. This twist is necessary because the blade speed is significantly higher at the tip compared to the base.

$$Blade\ angle\ =\ Inflow\ angle\ +\ Angle\ of\ attack. \tag{4}$$

### 2.2 Reverse Engineering the APC and NACA Propellers

The APC Slow Flyer 10' propellers are widely used in small UAVs and are manufactured by APC. They are two-bladed propellers that have become popular in the UAV industry. Another commonly used propeller in the past is the NACA 4412 propeller. Both propellers have a diameter of 0.254 m and a fixed pitch.

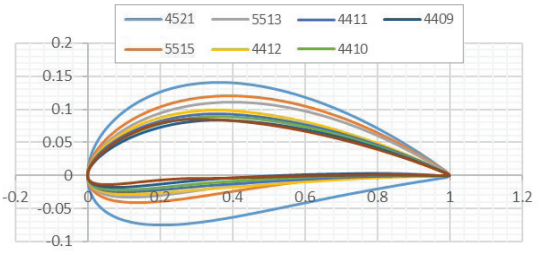


**Fig. 2.** *Sectional airfoil structures of APC*

The APC propeller incorporates a combination of NACA 4 and 5 series airfoils, as depicted in Fig. 2, while the NACA 4412 propeller is based on a single airfoil bearing its name. To obtain detailed information about the propeller profiles, a 3D scanner called ATOS 2M was used. This scanner can capture the product part in the form of images or drawings, a process known as 'reverse engineering'. The scanning process involves mounting the scanner on a tripod for scanning large parts, or it can be operated manually. By obtaining a reference point from the rotating table, the entire propeller is scanned. The scanned blade profiles of the APC and NACA propellers were exported to IGES format, providing valuable data as shown in Fig. 3. The three distinct designs of

**Table 2.** *Propeller design parameters for E63 airfoil*

| S. No | $r / R$ | Tip speed ratio | In flow angle | Chord length [mm] | Angle of attack | Blade angle |
|---|---|---|---|---|---|---|
| 1 | 0.10 | 0.754 | 35.338 | 18.495 | 5.60 | 40.938 |
| 2 | 0.20 | 1.508 | 22.376 | 17.826 | 5.04 | 27.416 |
| 3 | 0.25 | 1.885 | 18.638 | 17.318 | 4.76 | 23.398 |
| 4 | 0.30 | 2.262 | 15.906 | 15.838 | 4.48 | 20.386 |
| 5 | 0.35 | 2.639 | 13.841 | 15.181 | 4.20 | 18.040 |
| 6 | 0.40 | 3.016 | 12.234 | 14.998 | 3.92 | 16.155 |
| 7 | 0.45 | 3.393 | 10.952 | 13.898 | 3.64 | 14.592 |
| 8 | 0.50 | 3.770 | 9.908 | 13.367 | 3.36 | 13.268 |
| 9 | 0.55 | 4.147 | 9.042 | 12.611 | 3.08 | 12.122 |
| 10 | 0.60 | 4.524 | 8.313 | 11.806 | 2.80 | 11.113 |
| 11 | 0.65 | 4.901 | 7.691 | 11.647 | 2.52 | 10.215 |
| 12 | 0.70 | 5.278 | 7.155 | 11.032 | 2.24 | 9.395 |
| 13 | 0.75 | 5.655 | 6.688 | 10.674 | 1.96 | 8.648 |
| 14 | 0.80 | 6.032 | 6.278 | 10.378 | 1.68 | 7.958 |
| 15 | 0.85 | 6.409 | 5.914 | 10.323 | 1.40 | 7.314 |
| 16 | 0.90 | 6.786 | 5.591 | 10.533 | 1.12 | 6.711 |
| 17 | 0.95 | 7.163 | 5.300 | 10.093 | 0.84 | 6.140 |
| 18 | 1.00 | 7.540 | 5.038 | 9.697 | 0.56 | 5.598 |

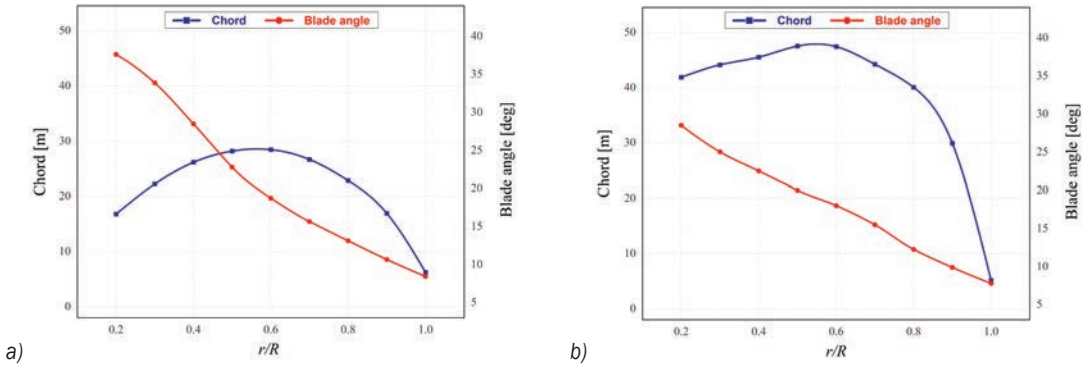


**Fig. 3.** *Data from ATOS 2M: Chord and blade angle of: a) APC propeller, and b) NACA 4412 propeller*


**Fig. 4. a***) Mathematically modelled E63 propeller, b) APC Slow Flyer, and c) NACA 4412 propeller*

propellers as shown in Fig. 4 are made using the CAD design software.

## 3 TURBULENCE SIMULATION MODEL

### 3.1 Selection of Flow Domain

The flow region and numerical predictions were conducted using ANSYS software. The design CAD models were imported into ANSYS Fluent, where the geometry was created. To ensure accurate simulations, a domain was built around the propeller that extended taller than the propeller itself. This was done to prevent the wall boundary, which is closer to the propeller, from heating up quickly due to the airflow generated during propeller rotation. Additionally, the domain was carefully chosen to avoid any recirculation within the domain, as recirculation can introduce variations

in the results. The domain boundary was extended higher than normal and designated as the rotating domain, as illustrated in Fig. 5. A static environment was created around this rotating domain. Before commencing the simulation, the geometry was prepared with the appropriate environment settings, including airflow conditions and Boolean operations for specific regions.

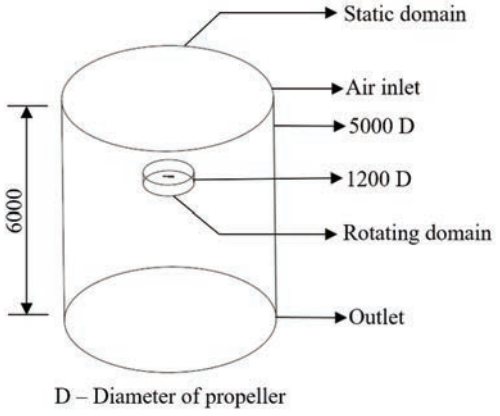


**Fig. 5.** *Flow domain dimensions in [mm]*

### 3.2 Mesh Generation and Dependency Test

Mesh generation must ensure high-quality meshes that balance calculation accuracy and computation time. If the element size of the mesh is too large, the solution's final precision will be compromised. Conversely, if the element size is too small, the computation time will significantly increase. Therefore, an optimal element size must be determined to achieve accurate and efficient simulations. Initially, the computational domain was aligned using a line surface-to-body sequence. Given the large size of the propeller surface and its curvature, efforts were made to reduce curvature effects, particularly through surface splitting and merging techniques.

A mesh dependency study was conducted in the CFD simulation to determine an appropriate mesh size. The study focused on evaluating thrust and drag. Fig. 6 illustrates that consistent results were obtained with a mesh consisting of more than 2.5 million elements. To accurately capture the behaviour of the viscous sub-layer, mesh refinement was applied to all sides of the rotating domain, which was constructed around the propeller blade boundaries. The boundary criterion was determined by selecting the appropriate named selection for the primary part. Table 3 provides details of the node and element sizes for the propeller. Furthermore, Fig. 7 showcases the computational domain and the results of the meshing process. To achieve better simulation results, tetrahedral meshes were employed for both the propeller and its rotating domain. The mesh size of the rotating domain was intentionally kept smaller than that of the static domain, which served as a boundary wall. Proper naming conventions were applied to all faces and domains using named selections to ensure clarity and organization throughout the simulation process.

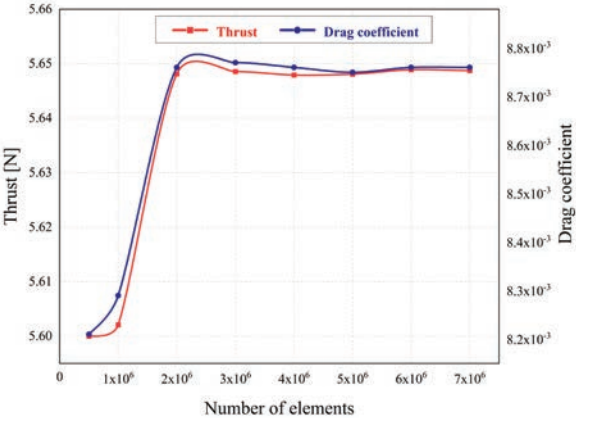


**Fig. 6.** *Results of CFD mesh dependency test*

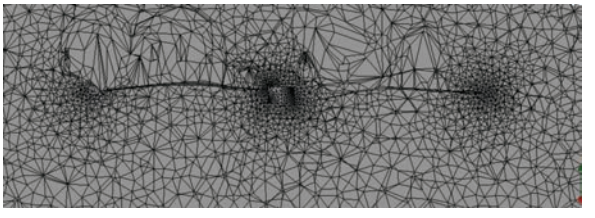

**Fig. 7.** *Tetrahedron mesh generation*

**Table 3.** *Mesh size of each propeller*

| Propeller | Node | Element |
|---|---|---|
| E63 | 451628 | 3215652 |
| NACA | 452587 | 3368426 |
| APC | 458564 | 3224153 |

### 3.3 Turbulence Model Properties

The CFD simulation involved three distinct blade rotation speeds: 4000 rpm, 6000 rpm, and 6500 rpm. The free stream velocity was determined at the intake boundary, while the outflow was set at the outlet boundary. All walls within the domain were assigned as non-slip boundaries. Turbulence modelling played a crucial role in achieving accurate simulation results, and six different turbulence models were considered. The selection of the turbulence model was based on its ability to closely match experimental data. The chosen turbulence model in this investigation was the

k-omega normal model, which exhibited the lowest percentage difference compared to the other models (1.1249 %). The k–omega turbulence model is widely used to capture the effects of turbulent flow conditions and belongs to the Reynolds-averaged Navier-Stokes (RANS) family of turbulence models. It involves solving two transport equations for turbulent kinetic energy ($k$) and turbulent dissipation rate (omega). These equations account for historical effects such as convection and turbulent energy diffusion, providing a comprehensive representation of turbulence.

Kinetic energy equation:

$$\frac{\partial}{\partial t}(\rho k)+\frac{\partial}{\partial x_j}(\rho u_j k)=\rho\tau_{ij}\frac{\partial u_i}{\partial x_j}-\beta\rho k\omega+\frac{\partial}{\partial x_j}\left[\left(\mu+\sigma\frac{\rho k}{\omega}\right)\frac{\partial k}{\partial x_j}\right]. \quad (5)$$

Specific dissipation rate:

$$\frac{\partial}{\partial t}(\rho\omega)+\frac{\partial}{\partial x_j}(\rho u_j\omega)=\alpha\frac{\omega}{k}\rho\tau_{ij}\frac{\partial u_i}{\partial x_j}-\beta\rho\omega^2+\sigma_d\frac{\rho\partial k\partial\omega}{\omega\partial x_j\partial x_j}+\frac{\partial}{\partial x_j}\left[\left(\mu+\sigma\frac{\rho k}{\omega}\right)\frac{\partial\omega}{\partial x_j}\right], \quad (6)$$

**Table 4.** *Simulation parameters*

| Parameters | Values |
|---|---|
| Time | Transient |
| Time step | 0.015 |
| Number of Time Step | 100 |
| Max Iteration per time step | 40 |
| Viscous model | k–omega, Normal |
| Fluid medium | Air |
| Inlet velocity | 15 m/s |
| Type of flow | Transient |
| Air density | 1.225 kg/m³ |
| Pressure-velocity coupling | Simple scheme |
| Gradient | Least squares cell based |
| Interpolating scheme (momentum) | Second-order upwind |
| Interpolating scheme (specific dissipation rate) | Second-order upwind |

The k–omega model is particularly suitable for near-wall treatment and offers improved performance for complex boundary layer flows with adverse pressure gradients and separations, such as in external aerodynamics and turbomachinery applications. The simulation parameters used in the study are summarized in Table 4, ensuring the accuracy and reliability of the simulation results.

The simulation of the propeller employed a second-order upwind interpolation scheme. In computational physics, an upwind scheme is a discretization method used to solve hyperbolic equations and approximate the derivatives in a flow field. To better understand its function, let us consider the one-dimensional (1D) advection equation, Eq. (7). The advection equation is commonly used when analysing the movement of fluid through a passage.

1D advection equation:

$$\frac{\partial u}{\partial t}+a\frac{\partial u}{\partial x}=0. \quad (7)$$

The advection equation represents the propagation of a wave with a specific velocity along the $x$-axis. It is commonly used to analyse one-dimensional linear advection. Let us consider a standard grid point i in a one-dimensional domain. In this domain, point 1 has two directions: towards the negative infinity side (upwind) and towards the positive infinity side (downwind). If the velocity is positive, the wave propagates towards the right side. In this case, the left side of point i is referred to as the upwind side, while the right side is called the downwind side. An upwind scheme is characterized by having a higher number of $\partial u/\partial x$ data points on the upwind side. In the case of the first-order upwind scheme, a 2-point grid data is used in the Taylor series approximation. However, the second-order upwind scheme employs a combination of 3-point backward difference and 3-point forward difference in the data points, as depicted in Eqs. (8) and (9). This method offers improved accuracy due to its reduced diffusivity compared to the first-order upwind scheme.

3-point backward difference:

$$u_x^- = \frac{3u_i^n-4u_{i-1}^n+u_{i-2}^n}{2\Delta x}, \quad (8)$$

3-point forward difference:

$$u_x^+ = \frac{-u_{i+2}^n+4u_{i+1}^n-3u_i^n}{2\Delta x}. \quad (9)$$

## 4 RESULTS

### 4.1 Efficiency

CFD simulations were performed on three different propellers, namely the APC Slow Flyer, NACA 4412, and E63 designed propellers, under normal environmental conditions. The objective was to compare their respective efficiencies. In the CFD analysis, various parameters were calculated, including thrust generated $T$ in [N], torque output $Q$ in

[N·m], fluid density $\rho$ in [kg/m³], propeller speed $n$ in [rpm], propeller diameter $D$ in [m], and power $P$ [W]. To evaluate the performance of the propellers, several coefficients were derived from the CFD data. These include the thrust coefficient $C_T$, torque coefficient $C_Q$, power coefficient $C_P$, advance ratio $J$, and efficiency $\eta$. These coefficients were computed using specific equations. The efficiency values for each propeller are presented in Table 5.

$$J = \frac{V}{nD}, \tag{10}$$

$$C_t = \frac{P}{\rho n^2 D^4}, \tag{11}$$

$$C_p = \frac{P}{\rho n^3 D^5}, \tag{12}$$

$$\eta = \frac{JC_t}{C_p}. \tag{13}$$

**Table 5.** *Efficiency comparison on various advance ratios*

| Advance ratio | Velocity [m/s] | APC $\eta$ | NACA 4412 $\eta$ | E 63 $\eta$ |
|---|---|---|---|---|
| 0.235 | 2.999 | 0.412 | 0.411 | 0.452 |
| 0.336 | 4.234 | 0.527 | 0.498 | 0.534 |
| 0.433 | 5.500 | 0.601 | 0.574 | 0.621 |
| 0.525 | 6.666 | 0.659 | 0.631 | 0.678 |
| 0.580 | 7.250 | 0.670 | 0.643 | 0.694 |
| 0.631 | 7.999 | 0.666 | 0.616 | 0.673 |
| 0.719 | 9.100 | 0.589 | 0.558 | 0.590 |

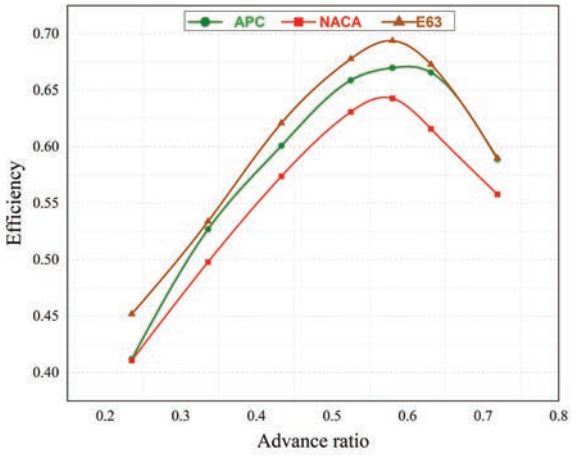


**Fig. 8.** *Propeller efficiency comparison between E63, NACA and APC propellers*

Fig. 8 depicts a comparison graph showcasing the efficiency of the three propellers. Notably, the propeller designed using the E63 airfoil exhibits a remarkable efficiency of nearly 70 % at an advance ratio of 0.58 before experiencing a decline. A common trend among all propellers is that their efficiency gradually decreases beyond the 0.58 advance ratio. In terms of initial efficiency, both the APC and NACA propellers demonstrate similar performance, but as the advance ratio increases, the APC propeller slightly outperforms the NACA propeller. In contrast, the NACA propeller, with its comparatively lower lift structure, exhibits the lowest efficiency among the three propellers. However, the propeller based on the E63 airfoil consistently maintains superior efficiency throughout the entire range. The high lift characteristics of the E63 airfoil contribute to its enhanced efficiency compared to the other two propellers.

### 4.2 Aerodynamic Numerical Solution

The numerical analysis of the three propellers focused on analysing their aerodynamic properties, including thrust, lift force, and drag coefficient. The analysis was conducted at various temperature settings and at three different speeds, resulting in a total of 30 simulations for each aerodynamic property. The analysis revealed that as the propeller speed decreases, both the thrust and lift force decrease as well. While this relationship may seem obvious, it is important to consider that thrust and lift force are directly proportional to the pressure acting on the propeller. The results clearly indicate that the propeller based on the E63 airfoil is less susceptible to pressure compared to the other two propellers, as illustrated in Fig. 9. This suggests that the mathematically modelled propeller exhibits superior efficiency compared to the other propellers. The thrust force generated by the propeller plays a crucial role in propelling a UAV through the air. It is responsible for overcoming the drag and weight of the drone, enabling it to maintain flight.

$$T = \dot{m} \cdot V, \tag{14}$$

where $\dot{m}$ is mass flow rate calculated as:

$$\dot{m} = \rho AV. \tag{15}$$

Substitute the Eq. (14) into Eq. (15), and we get

$$T = \rho AV^2. \tag{16}$$

Fig. 10 demonstrates the thrust generated by different propellers under various environmental conditions and at three rpm ranges. The simulation results clearly show that the mathematically designed E63 propeller outperforms both the NACA and APC propellers in terms of thrust. This superiority is due

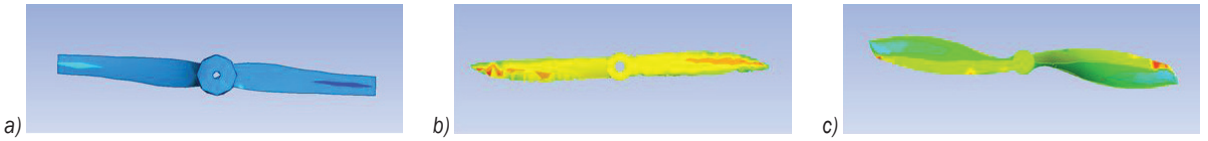


**Fig. 9.** *Pressure acting on the propeller at 6000 rpm*

to the E63 propeller's utilization of the high lift and low drag characteristics of its airfoil structure. Despite the NACA airfoil structure variations along the APC propeller sections, the mathematically designed propeller consistently exhibits better blade angle efficiency along its entire length. This efficiency advantage is particularly evident at 5000 rpm, where the E63 propeller generates nearly twice the thrust force compared to the APC propeller. In contrast, the NACA propeller performs poorly, producing less than 2 N of thrust. The increased efficiency of the E63 propeller results in reduced battery usage, as it generates more lift even at lower rpm ranges.

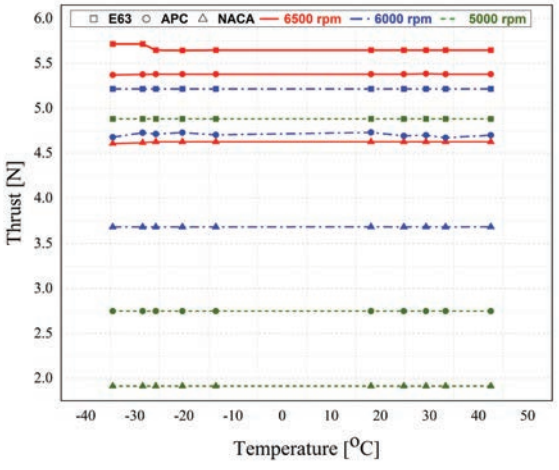


**Fig. 10.** *Thrust vs. temperature in three different rpms*

Drag on the propeller surface is caused by the velocity difference between the top and bottom portions. Aerodynamicists employ the drag coefficient to account for the complex relationships between geometry, angle, and flow conditions, which affect aircraft drag. The drag equation can be rearranged to solve for the drag coefficient in terms of other variables. From Fig. 11, it is evident that the APC propeller exhibits greater drag compared to the other two propellers. The APC propeller experiences high drag across all RPM ranges, primarily due to its utilization of a low lift airfoil structure at the tip. The propeller tip speed ratio being significantly higher than at the root contributes to the NACA series airfoil having higher drag coefficient values when compared to the E63. Consequently, the APC propeller generates more drag than the other two propellers. When comparing these three propellers, the mathematically designed E63-based propeller demonstrates superior performance. The drag force can be calculated as half the product of the drag coefficient, air density, area, and the square of the velocity.

$$Drag\ \ force = \frac{1}{2} C_d \rho A V^2, \tag{17}$$

where $C_d$ is a drag coefficient, and $A$ *is* area of propeller.

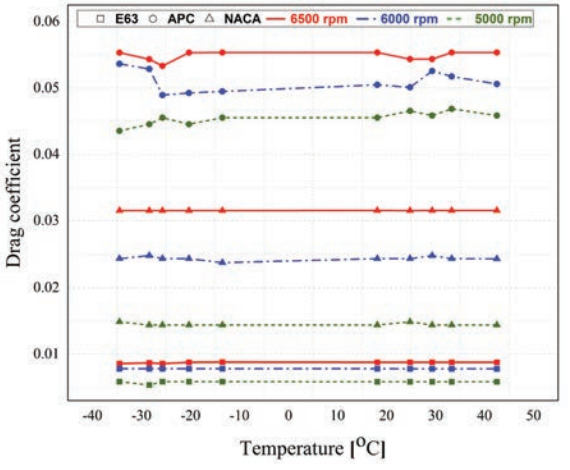


**Fig. 11.** *Drag coefficient vs. temperature in three different rpms*

Lift refers to the total force perpendicular to the incoming flow direction, whereas drag force runs parallel to the flow direction. Lift plays a crucial role in counteracting the force of gravity. From Fig. 12, it is evident that the E63 propeller performs exceptionally well at 6500 rpm. The APC propeller demonstrates a relatively closer lift force to the E63, but its performance diminishes due to the significant drag it generates at lower rpm, resulting in minimal lift production. In contrast, the NACA propeller performs poorly compared to the other two. This is primarily due to the inferior airfoil properties of the NACA 4412 in contrast to the superior characteristics of the E63. Overall, the E63 consistently outperforms both the APC and NACA propellers.

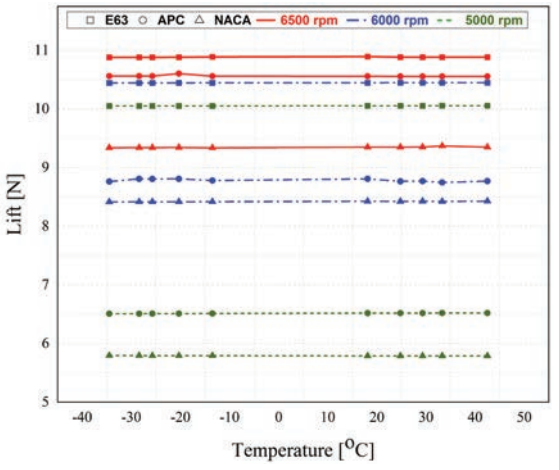


**Fig. 12.** *Lift force vs temperature in three different rpms*

### 4.3 Blade Element Theory

The BET offers the evaluation of propeller performance based on geometrical parameters, aerodynamic coefficients, and operating conditions [4], [22] to [24]. However, this theory overlooks secondary effects like tip vortex and radial flow, which can have a negative impact on total thrust output [25]. The distributions of airfoil profile, chord, and twist are represented as functions of the distance from the propeller hub using Eqs. (18) to (23). As the propeller profile varies, simulations were conducted using a simplified E63 airfoil for the mathematically designed propeller, NACA 4412 airfoil for the NACA propeller, and various NACA airfoils for different sections of the APC propeller. Comparison results between simulation and BET thrust force as shown in Fig. 13.

The angle between the thrust and lift directions is defined as

$$\varphi = \theta - \alpha. \tag{18}$$

The thrust of the blade section can be written as

$$\Delta T = \Delta L \cos\varphi - \Delta D \sin\varphi, \tag{19}$$

where

$$\Delta L = \frac{1}{2} C_L \cdot \rho A V^2 c \cdot dr, \tag{20}$$

$$\Delta D = \frac{1}{2} C_D \cdot \rho A V^2 c \cdot dr. \tag{21}$$

Therefore, the thrust equation becomes

$$\Delta T = \frac{1}{2} \rho A V^2 c (C_L \cos\varphi - C_D \sin\varphi) B \cdot dr. \tag{22}$$

To calculate the total thrust generated by the propeller for a specific rpm

$$T = \Sigma \Delta T. \tag{23}$$

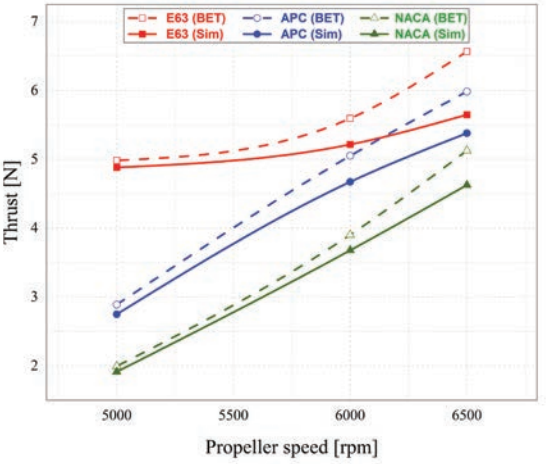


**Fig. 13.** *Thrust comparison between BET and SIM*

Comparisons were made between the experimental data and the results obtained from the blade element theory. The BET technique generally follows similar patterns, but it significantly overestimates the thrust force at higher rpm, with an error margin of approximately 10 % to 15 % compared to the actual results. This indicates that there are interactions between the propellers that are not accounted for in the basic coaxial model. However, both the CFD approach and the BET method yield similar thrust predictions when approaching lower rpm, with differences of less than 13 % between the simulated data and the blade element theory. Notably, the accuracy improves as the rotational speed decreases.

### 4.4 Experimental Ssetup

The experimental setup for propeller thrust calculation involves several components. Firstly, a weighing scale is utilized to measure the lifting force generated by the propeller. The motor responsible for rotating the propeller is securely mounted on a wooden structure. A servo controller is employed to regulate the 2200 kV brushless direct current (BLDC) motor speed and control its rotation. The motor is connected to a 30 A electronic speed controller (ESC) and is powered by a 3S battery. As the propeller rotates, it generates a lifting force that is transferred to the weighing scale. The scale readings are carefully observed and recorded. To convert the readings into Newtons, a

suitable conversion factor or calibration procedure is applied, allowing for accurate measurement of the propeller thrust. The setup image as shown in Fig. 14 and the result compare with the simulation values are tabulated in Table 6.

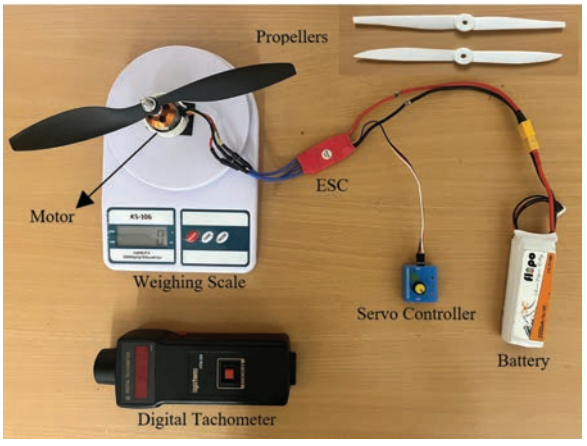


**Fig. 14.** *Experimental setup to test the thrust*

**Table 6.** *Error comparison of simulation thrust to the experimental values*

| Propeller | rpm | Thrust (Sim) | Thrust (Exp) | Error [%] |
|---|---|---|---|---|
| E63 | 6500 | 5.548 | 5.165 | 6.90 |
| | 6000 | 5.216 | 4.868 | 6.67 |
| | 5000 | 4.881 | 4.562 | 6.53 |
| APC | 6500 | 5.380 | 4.963 | 7.75 |
| | 6000 | 4.672 | 4.325 | 7.42 |
| | 5000 | 2.749 | 2.552 | 7.16 |
| NACA | 6500 | 4.627 | 4.289 | 7.30 |
| | 6000 | 3.679 | 3.421 | 7.01 |
| | 5000 | 1.912 | 1.778 | 7.00 |

The E63 propeller, designed based on a mathematical model, was 3D printed using ABS material through the process of fused deposition modelling (FDM). The results of the comparison between the UAV 10' propeller, the novelty developed E63 airfoil structure-based mathematical modelled propeller, the NACA 4412 propeller, and the industry-leading APC Slow Flyer were obtained through both CFD simulation and experimental testing. The analysis revealed an error deviation ranging from 6.5 % to 7.7 % between the predicted and observed values. It was observed that the CFD simulations tended to overestimate the performance values compared to the theoretical predictions. However, it is important to note that the variation was not significantly large, and the results obtained from the CFD simulations were still reasonably comparable to the experimental data.

## 5 CONCLUSION

In conclusion, this research introduced a mathematical model for a UAV propeller, incorporating various airfoil structures. Experimental tests were conducted to evaluate the propeller's performance in terms of thrust, lift, and drag. The designed E63 propeller, utilizing the high lift E63 airfoil structure, exhibited superior characteristics compared to the APC propeller and the NACA 4412. It generated greater thrust, produced higher lift force, and experienced less drag. The APC propeller showed good performance at 6500 rpm but experienced a decline at lower speeds due to increased drag. The NACA propeller performed inadequately when compared to both the E63 and APC. The slight changes in aerodynamic properties observed at different temperatures had minimal impact on propeller performance. Comparisons with calculations from the BET showed satisfactory correlation at lower rpm ranges but increased errors at higher rpms. Nonetheless, the BET remains a valuable tool for preliminary propeller evaluation when the geometry is known. Overall, the mathematically designed propellers incorporating the high lift E63 airfoil structure consistently demonstrated superior performance across various temperature ranges in comparison to the other propellers tested.

## 6 REFERENCES

[1] A.M. Pérez, Lopez, O., Poroseva, S.V., Escobar, J.A. (2019). Computational study of a small rotor at hover using CFD and UVLM. *AIAA Scitech 2019 Forum*, **DOI:10.2514/6.2019-0597**.

[2] Goh, G.D., Agarwala, S., Goh, G.L., Dikshit, V., Sing, S.L., Yeong, W.Y. (2017). Additive manufacturing in unmanned aerial vehicles (UAVs): Challenges and potential. *Aerospace Science and Technology*, vol. 63, p. 140-151, **DOI:10.1016/j.ast.2016.12.019**.

[3] Kontogiannis, S.G., Ekaterinaris, J.A. (2013). Design, performance evaluation and optimization of a UAV. *Aerospace Science and Technology*, vol. 29, no. 1, p. 339-350, **DOI:10.1016/j.ast.2013.04.005**.

[4] Anemaat, W.A., Schuurman, M., Liu, W., Karwas, A.A. (2017). Aerodynamic design, analysis and testing of propellers for small unmanned aerial vehicles. 55$^{th}$ *AIAA Aerospace Sciences Meeting*, **DOI:10.2514/6.2017-0721**.

[5] Kwon, H.I., You, J.Y. & Kwon, O.J. (2012). Enhancement of wind turbine aerodynamic performance by a numerical optimization technique. *Journal of Mechanical Science and Technology*, vol. 26, p. 455-462, **DOI:10.1007/s12206-011-1035-2**.

[6] Yoon, S., Nasa, Diaz, P.V., Boyd, D.D., Chan, W.M., & Theodore, C.R. (2017). Computational Aerodynamic Modeling of Small Quadcopter Vehicles. *'Computational aerodynamic modeling of small quadcopter vehicles,' AHS Forum 73*.

[7] Huang, Y.B., Thomson, S.J., Hoffmann, W.C., Lan, Y.B., Fritz, B.K. (2013). Development and prospect of unmanned aerial vehicle technologies for agricultural production management. *International Journal of Agriculture and Biological Engineering*. vol. 6, no. 3, **DOI:10.3965/j.ijabe.20130603.001**.

[8] Vorotović, G., Burazer, J., Bengin, A., Mitrović, Č., Januzović, M., Petrović, N., Novković, D. (2023). A Case Study of a Methodological Approach to the Verification of UAV Propeller Performance. *Strojniški vestnik - Journal of Mechanical Engineering*, vol. 69, no. 5-6, p. 199-207, **DOI:10.5545/sv-jme.2022.432**.

[9] Gupte, S., Mohandas, P.I.T., Conrad, J.M. (2012). A survey of quadrotor unmanned aerial vehicles. *Proceedings of IEEE Southeast Con*, **DOI:10.1109/SECon.2012.6196930**.

[10] Brandt, J., Selig, M. (2020). Propeller performance data at low reynolds numbers. *AIAA Aerospace Sciences Meeting including the New Horizons Forum and Aerospace Exposition*, **DOI:10.2514/6.2011-1255**.

[11] Scanavino, M., Vilardi, A., Guglieri, G. (2020). An experimental analysis on propeller performance in a climate-controlled facility. *Journal of Intelligent & Robotic Systems*, vol. 100, p. 505-517, **DOI:10.1007/s10846-019-01132-9**.

[12] Russell, C., Jung, J., Willink, G., Glasner, B. (2016). Wind tunnel and hover performance test results for multicopter UAS vehicles. *AHS 72nd Annual Forum*.

[13] Abushahma, R.I.H., Ali, M.A.M., Rahman, N.A.A., Al-Sanjary, O.I. (2019). Comparative features of unmanned aerial vehicle (UAV) for border protection of Libya: A review. *IEEE 15th International Colloquium on Signal Processing & Its Applications*, p. 114-119, **DOI:10.1109/CSPA.2019.8695991**.

[14] Houghton, E.L., Carpenter, P.W. Collicott, S.H., Valentine, D.T. *Aerodynamics for Engineering Students: Seventh Edition*. Butterworth-Heinemann, Oxford.

[15] Liu, Y., Li, L., Ning, Z., Tian, W., Hu, H. (2018). Experimental investigation on the dynamic icing process over a rotating propeller model. *Journal of Propulsion and Power*, vol. 34, no. 4, p. 933-946, **DOI:10.2514/1.B36748**.

[16] Liu, Y., Li, L., Li, H., Hu, H. (2018). An experimental study of surface wettability effects on dynamic ice accretion process over an UAS propeller model. *Aerospace Science and Technology*, vol. 73, p. 164-172, **DOI:10.1016/j.ast.2017.12.003**.

[17] Han, N., Hu, H., Hu, H. (2021). An Experimental investigation on the dynamic ice accretion process over the blade surface of a rotating UAV propeller. *AIAA SCITECH Forum*, **DOI:10.2514/6.2022-1538**.

[18] Patel, Y. Gaurav, A., Srinivas, K., Singh, Y. (2017). A review on design and analysis of the propeller used in UAV. *International Journal of Advanced Production and Industrial Engineering*, vol. 605, p. 20-23.

[19] D. Kim, Y. Lee, S. Oh, Y. Park, J. Choi, D. Park, (2021). Aerodynamic analysis and static stability analysis of Manned/unmanned distributed propulsion aircrafts using actuator methods. *Journal of Wind Engineering and Industrial Aerodynamics*, vol. 214, art. ID 104648, **DOI:10.1016/j.jweia.2021.104648**.

[20] Kutty, H.A. Rajendran, P. (2017). 3D CFD simulation and experimental validation of small APC slow flyer propeller blade. *Aerospace*, vol. 4, no. 1, **DOI:10.3390/aerospace4010010**.

[21] Maalawi, K.Y., Badawy, M.T.S. (2001). A direct method for evaluating performance of horizontal axis wind turbines. *Renewable and Sustainable Energy Reviews*, vol. 5, no. 2, **DOI:10.1016/S1364-0321(00)00017-4**.

[22] Sartori, D. Yu, W. (2019). Experimental characterization of a propulsion system for multi-rotor UAVs. *Journal of Intelligent & Robotic Systems*, vol. 96, p. 529-540, **DOI:10.1007/s10846-019-00995-2**.

[23] Dahal, C., Dura, H.B., Poudel, L. (2021). Design and analysis of propeller for high-altitude search and rescue unmanned aerial vehicle. *International Journal of Aerospace Engineering*, art. ID 6629489, **DOI:10.1155/2021/6629489**.

[24] Ledoux, J., Riffo, S., Salomon, J. (2021). Analysis of the blade element momentum theory. *SIAM Journal of Applied Mathematic*, vol. 81, no. 6, **DOI:10.1137/20m133542x**.

[25] Yaakub, M.F., Wahab, A.A., Abdullah, A., Nik Mohd, N.A.R., Shamsuddin, S.S. (2017). Aerodynamic prediction of helicopter rotor in forward flight using blade element theory. *Journal of Mechanical Engineering and Science*, vol. 11, no. 2, p. 2711-2722, **DOI:10.15282/jmes.11.2.2017.12.0246**.

Strojniški vestnik - Journal of Mechanical Engineering 69(2023)11-12, 455-470
DOI:10.5545/sv-jme.2023.595
Original Scientific Paper
Received for review: 2023-04-05
Received revised form: 2023-09-06
Accepted for publication: 2023-09-15


# Vehicle Technical Inspection Results in Relation to EU Directives and Selected EU Countries

Jernej Klemenc[1,*] – Domen Šeruga[1] – Tomaž Svetina[2] – Jože Tršelič[2]
[1] University of Ljubljana, Faculty of Mechanical Engineering, Slovenia
[2] Slovenian Traffic Safety Agency, Slovenia

*Although road accidents caused by defective vehicles are relatively rare, the roadworthiness of vehicles is important for road safety. In the European Union, the technical conditions that need to be fulfilled by the vehicles using public roads are regulated by EU directives. According to these directives, technical inspections are organized in every EU country. Our study analyzed the vehicle technical inspections in Slovenia over four consecutive years. The statistics for passenger cars and commercial vehicles are compared with two other EU countries: Germany and Finland. From this comparison, it follows that certain differences exist between the countries, although vehicle technical inspections are regulated by the same EU directives. Finally, multivariate regression models were built to predict probabilities of various vehicle defects detected during regular technical supervision as a function of the vehicle's age. It was found that the probability of fault detection can be effectively modelled as a function of vehicle age.*

**Keywords: passenger vehicles, commercial vehicles, technical supervision, fault statistics, statistical modelling**

**Highlights**

- *A statistical analysis on technical supervisions was made for Slovenia.*
- *Linkage between the technical state of vehicles and vehicle participating in road traffic accidents was evaluated for Slovenia.*
- *Technical state of vehicles and typical detected defects were compared for Slovenia, Germany and Finland.*
- *Uniformity of considering the EU directives that regulate the technical safety and roadworthiness was discussed.*

## 0 INTRODUCTION

Every year, many serious traffic accidents occur, causing serious injuries or death to the people involved. There are many reasons for traffic accidents: human factor, inadequate infrastructure, technical defects of vehicles, and various combinations of the previously mentioned factors. Statistics from different countries around the world vary. In more developed countries, more traffic accidents are caused by human factors than by inadequate infrastructure or vehicle defects. In the USA, for example, vehicle defects are the main cause of accidents in 1.3 % to 2.7 % of cases [1], whereas this percentage is between 3 % and 6 % in the EU, according to Thomas et al. [2]. Rolison et al. [3] report that vehicle defects cause up to 12 % of accidents in the UK, but this information may be somewhat unreliable because it was obtained through a survey of police officers. In South Africa, the reported percentage of defect-related accidents varies between values of 2 % for direct causes and 6 % for indirect causes [4]. The most recent report for that country is 14.1 % for direct and indirect causes [5]. According to Van Schoore et al. [4], this percentage in less-developed African countries is higher and reaches 16 %. In India, vehicle defects are responsible for 9 % to 32 % of road traffic accidents, depending on the region [6]. Hudec and Sarkan [7] report that less than 1 % of traffic accidents are caused by vehicle defects in Slovakia. For Slovenia, it was rather difficult to find this data, but Brcar [8] reports that vehicle defects are responsible for only 0.2 % of road traffic accidents. This figure is also questionable because in most non-serious accidents the true cause of the accident is often not determined. Moreover, according to the non-public data available for our study, the causes of traffic accidents are not reported in the police database. In a very recent systematic overview Martin-delosReyes et al. [9] stated that road crashed, which can be attributed to vehicle defects vary between 3 % and 19 % in developed countries and up to 27 % in developing countries.

Others investigated the causes of accidents in a narrower range; for example, Newman and Goode [10] report various influences on road accidents in Australia related to fleet management, maintenance, and use of commercial vehicles. Uchida et al. [11] investigated a relationship between the active safety components of the car and the main types of accidents in Japan. Garnowski and Manner [12] investigated the influence of the parameters of the connecting road to the highway on traffic accidents.

From the above-mentioned studies, it can be concluded that many different parameters, variables, and circumstances cause road accidents. However, when the main cause of accidents is a vehicle defect,

*Corr. Author's Address: University of Ljubljana, Faculty of Mechanical Engineering, Askerceva 6, SI-1000 Ljubljana, Slovenia, jernej.klemenc@fs.uni-lj.si

the following components have been identified as responsible in some selected countries:

- USA: poor condition or inadequate inflation of tyres (35 %), braking system defects (22 %), and steering system defects (3 %) [1], [13] and [14];
- UK: braking system defects, poor condition or inadequate inflation of tyres, steering-system defects, and poor lighting equipment [15];
- South Africa: poor condition or inadequate inflation of tyres (80 %), braking system defects (4 %), and steering system defects (3 %) [5].

Despite the small percentage of road accidents caused by defective vehicles, most of them could be prevented if all technical defects were detected during regular technical inspections. These inspections are required and enforced by the individual member states. In the EU, there are several directives that regulate the technical safety and roadworthiness of road vehicles:

- Council Directive 1999/37/EC on the registration documents for vehicles (document 01999L0037-20180520) [16] and Directive 2014/46/EU amending the Council Directive 1999/37/EC on the registration documents for vehicles (document 32014L0046) [17].
- Directive 2007/46/EC [18], a framework for the approval of motor vehicles and their trailers, and of systems, components, and separate technical units intended for such vehicles (document 02007L0046-20200902).
- Regulation (EC) No 661/2009 [19] concerning type-approval requirements for the general safety of motor vehicles, their trailers and systems, components, and separate technical units intended therefor (document 02009R0661-20190424).
- Directive 2014/45/EU [20] on periodic roadworthiness tests for motor vehicles and their trailers and repealing Directive 2009/40/EC (document 02014L0045-20140429).

Since the national regulations in the EU member states for road vehicle technical inspections are subordinate to the EU directives, it can be assumed that in the various member states with comparable vehicle populations, approximately the same statistics exist on the defects found during roadworthiness testing. Having obtained these statistical data for Slovenia, the data for passenger cars were compared with those of Finland and Germany. In addition, the data for commercial vehicles were compared with Germany. The reason for this is that reliable data sources in publicly available forms were found for these two EU countries.

Then, multivariate regression models were established to predict the probability of defect detection at technical inspections. Different static and dynamic regression models were tested for nine defect groups (lighting and electrical equipment, braking system, steering, vehicle identification, axles, chassis and suspension, visibility, emissions, and other equipment) for the Slovenian fleet of passenger cars, commercial vehicles, and motorcycles and ATVs. Finally, a correlation between the technical condition of vehicles and road accidents in Slovenia was investigated for the same three types of motor vehicles.

The article is organized as follows. After the introductory section, the basic statistical analyses and data models are explained. The third section presents the results and discussion. In this section, first, the process of data preparation is described. Then, the statistical data for Slovenia are presented and discussed, followed by a comparison with Germany and Finland. The section ends with regression models for predicting the probability of fault detection during technical inspections and a discussion of the relationship between the technical condition of vehicles and traffic accidents. The article ends with a concluding section, a list of references, and an acknowledgement.

## 1 METHODS

### 1.1 Data Cleaning and Pre-Processing

The following databases were obtained from the Slovenian Traffic Safety Agency and the Ministry of Internal Affairs:

- Databases of the vehicles' roadworthiness that follow from the technical inspections for the years 2016 to 2022.
- Databases of defects detected during technical inspections for 2016 to 2022.
- Traffic accident databases for the years 2016, 2017, and 2018.

The individual databases were composed of the following data:

- vehicle roadworthiness database (23 factors): vehicle ID, car brand, factory mark, commercial mark, commercial type, VIN number, designation of vehicle category, description of vehicle category, vehicle upgrade (label and description), additional equipment, type of fuel (label and description), date of the first vehicle registration, date of the first registration in Republic of Slovenia (RS), kilometres driven, vehicle owner

code, vehicle user code, technical inspection (TI) date, the outcome of the technical inspection (roadworthiness), the start of TI validity, end of TI validity, implementing contractor;
- vehicle defect database (16 factors): vehicle ID, VIN number, designation of vehicle category, description of vehicle category, vehicle upgrade (label and description), additional equipment, type of fuel (label and description), fault label, detailed fault description, item description (up to four items), vehicle condition assessment;
- traffic accident database (8 factors): vehicle ID, VIN number, licencing plate, car brand, commercial mark, vehicle mass, the maximum technical allowed mass of the vehicle, and date of the traffic accident.

For the statistical analyses, all three bases were linked via the VIN number of the vehicle. This was done using MS Access software by creating various queries that we used to facilitate data review, processing, and cleaning. For data processing and analysis, the vehicles from the databases were divided into five categories:
- passenger cars: categories M1 and M1G;
- buses: categories M2, M2G, M3, and M3G;
- commercial vehicles: categories N1, N1G, N2, N2G, N3, and N3G;
- motorcycles and ATVs: all categories with the designation L*;
- tractors: all categories with the designation T*.

For the most part, the vehicle roadworthiness database and the vehicle defects database clearly recorded the data, although there were some problems related to the letters with a canopy being written with different characters, indicating a mismatch in the text code tables. However, the problem was easily resolved by replacing these letters, as they were the same in all databases.

In addition to this deficiency, the following problems were the most common and troublesome in the individual records:
- Inconsistency of vehicle brand entries for older cars, trucks, and tractors (e.g., the numeral "0" is used instead of the letter "O").
- The same vehicle models have different commercial marks (e.g., a "space" character is used where there should be no space numeral "0" is used instead of the letter "O"). Some commercial marks also contain the manufacturer's name and/or more detailed information about the vehicle (e.g., engine description as 1.9 TDi).
- In some records, there is incorrect information about the commercial mark, or there is no such information at all. The inconsistency of commercial marks is high for motorcycles and tractors. Especially in the case of motorcycles, the number of brands is very large (>300) for two reasons: i.) inconsistent brand names and ii.) brands of which there is only one motorcycle in Slovenia (e.g., various niche manufacturers or local craftsmen). In addition, commercial-mark inconsistency is extremely high for commercial vehicles and tractors. The inconsistency of commercial marks for vehicles extends across all four years.
- The mileage (kilometres driven) is missing or incorrect (e.g., 0, 1, pure multiples of 10). The missing kilometres appear for vehicles that were not registered for the first time in the Republic of Slovenia and only for the first entry in the database. In later years, the kilometre data for these vehicles are entered.
- Duplicate records in the database for the same technical inspection result.

These problems and data inconsistencies were solved as follows:
- Additional data pre-processing with special macros in MS Access. In this way, most of the problems with passenger cars could be solved, but far fewer problems with the other four types of vehicles can.
- Manual correction of vehicle brands and commercial marks for some commercial vehicles, motorcycles, and tractors, which was very time-consuming. Indeed, almost twice as much time was spent correcting the commercial marks of tractors and commercial vehicles for each year than for correcting the names of all passenger cars, even though the databases contained about ten times fewer records for tractors and commercial vehicles than for passenger cars.
- Regression of mileage based on vehicle age and statistical region. The main problem related to this inconsistency was a very large mileage spread. Therefore, this option was applied only to a limited extent so as not to affect the summary statistics too much.
- When processing statistical data on motorcycles, all brands for which only one technical inspection was carried out in the current year were excluded.

Table 1 shows the number of records for the performed technical inspections after the data cleaning was carried out for the individual years and individual types of motor vehicles. It can be concluded from Table 1 that the number of individual technical inspections of vehicles is consistent between

**Table 1.** *Number of considered records for technical inspections of motor vehicles*

| | Year | | | | | | |
|---|---|---|---|---|---|---|---|
| Vehicle type | 2016 | 2017 | 2018 | 2019 | 2020 | 2021 | 2022 |
| Passenger cars | 99821 | 1029319 | 1040114 | 1062620 | 1052913 | 1069943 | 1077562 |
| Commercial vehicles | 118584 | 126839 | 135776 | 143332 | 145706 | 151155 | 153565 |
| Motorcycles and ATVs | 81382 | 103494 | 96187 | 99396 | 99747 | 105387 | 116107 |
| Buses | 5643 | 5876 | 6039 | 6105 | 5454 | 5514 | 5888 |
| Tractors | 103520 | 106124 | 107801 | 110001 | 105892 | 105387 | 111034 |

years, with a slight, but consistant, positive trend for passenger cars and commercial vehicles.

### 1.2 Basic Statistical Analyses

For the five vehicle categories, the following statistical data were calculated:

- vehicle roadworthiness (share of acceptable, conditionally acceptable, or not acceptable vehicles and not acceptable vehicles with critical fault) as a function of the vehicle age summarized at the levels of regions and the whole of Slovenia;
- average mileage as a function of vehicle age summarized at the level of regions and Slovenia as a whole;
- absolute and relative numbers of the nine detected fault groups (according to the nine fault categories: lighting and electrical equipment, braking system, steering, vehicle identification, ak es, chassis and suspension, visibility, emissions, and other equipment) as a function of the vehicle age summarized at the levels of regions and the whole of Slovenia;
- ranking of vehicle commercial marks according to their roadworthiness as a function of the vehicle age for passenger cars, commercial vehicles, and motorcycles;
- statistical distribution of the critical vehicle defects as a function of the vehicle age for commercial marks of passenger cars, commercial vehicles, and motorcycles.

In the last two cases, the statistical data for buses and tractors were not processed because the number of buses is too small, and the data on the roadworthiness of tractors are not reliable. In Slovenia, old tractors make up a significant part of the fleet. In the case of tractors, technical inspections do not have to be carried out at the site of the implementing contractors but can be done at an agreed-upon location in the farm's field. However, the control of such technical inspection points is more difficult and complicated.

### 2.3 Multivariate Regression Models

In various fields, the linear regression method is one of the most widely used methods for modelling the dependence between independent and dependent variables. Let $Y$ represent the dependent variable and $\mathbf{X} = \left( X_1, X_2, ..., X_p \right)$ vector of $p$ independent variables. Then a multivariate linear regression model has the following form [21] and [22]:

$$Y = a_0 + \sum_{i=1}^{p} a_i \cdot X_i, \tag{1}$$

$a_0$ represents the constant term, and $a_i$ represent the $i^{\text{th}}$ regression coefficient. For the application of the multivariate linear regression models, the following conditions must be fulfilled [19]:

- a linear dependence exists between the $Y$ and $X_i$ variables;
- variables $X_i$ are mutually independent;
- prediction errors $\varepsilon_j = \hat{y}_j - y_j$ are mutually independent and normally distributed with a mean value equal to zero and a constant variance.

$\hat{y}_j$ represent a predicted value of the dependent variable for the $j^{\text{th}}$ sample in the set. The constant term and regression coefficients are free parameters of the multivariate linear regression model estimated by the least square method based on pairs of the independent and dependent variables $\left\{ \left( \mathbf{x}_j, y_j \right) \; ; \; j = 1, ..., n \right\}$. If the dependent and independent variables are standardized before building a multivariate linear regression model, then the regression coefficients of the standardized model represent the relative importance of the corresponding independent variables.

By using different transformations of the basic independent variables $X_i$, multivariate regression can also be used to model non-linear dependencies between the independent and dependent variables. In this case, the condition of linear independence between each variable $X_i$ is neglected. In our research, such a transformation was used to square some independent variables, which significantly improved

the quality of the regression models for predicting the probability of defect detection.

Since we had at our disposal databases on vehicle technical inspections for seven consecutive years (2016 to 2022), the dynamic model of the dependence between the dependent ($Y$) and the independent variables ($X_i$) was also built. They were set up either as simple regression models:

$$Y = a_0 + \sum_{i=1}^{p} a_i \cdot X_i + a_{p+1} \cdot t, \quad (2)$$

or as a decoupled time-space models with $b_0$ and $b_1$ being the time-related regression coefficients:

$$Y = \left(a_0 + \sum_{i=1}^{p} a_i \cdot X_i\right) \cdot \left(b_0 + b_1 \cdot t\right). \quad (3)$$

Eq. (3) can be rewritten into the following form:

$$Y = a_0 + \sum_{i=1}^{p} a_i \cdot X_i + a_{p+1} \cdot t + \sum_{i=p+2}^{2 \cdot p+1} a_i \cdot X_i \cdot t. \quad (4)$$

For all regression models, a coefficient of determination $R^2$ was used to assess the quality of the regression model, because it represents a proportion of the data variance that is described by the regression model. The regression model is good if the value of $R^2$ is close to one. IBM SPSS 26 and Microsoft Excel software were used to build the regression models.

Regression models for predicting the probability of defect detection in each of the consecutive four years are presented in Table 2. A total of 135 regression models were built for each year: (3 vehicle categories) × (5 different models) × (9 fault groups). Dynamic regression models for predicting the defect detection probability are presented in Table 3. Altogether, 54 dynamic regression models were built: (3 vehicle categories) × (2 functional models) × (9 fault groups).

## 2 RESULTS AND DISCUSSION

### 2.1 Statistical Data for Slovenia

In Slovenia, different inspection periods are prescribed for different vehicles. For passenger cars, motorcycles,

**Table 2.** *Basic regression models for individual years from 2016 to 2022*

| Model | Independent variables* | | |
|---|---|---|---|
| | Passenger cars | Commercial vehicles | Motorcycles and ATVs |
| Model #1 | $X_1$ = vehicle age | $X_1$ = vehicle age | $X_1$ = vehicle age |
| Model #2 | $X_1$ = vehicle age<br>$X_2$ = fraction of TI per age class | $X_1$ = vehicle age<br>$X_2$ = fraction of TI per age class | $X_1$ = vehicle age<br>$X_2$ = fraction of TI per age class |
| Model #3 | $X_1$ = vehicle age<br>$X_2 = X_1 \cdot X_1$ | $X_1$ = vehicle age<br>$X_2$ = X1 $\cdot X_1$ | $X_1$ = vehicle age<br>$X_2 = X_1 \cdot X_1$ |
| Model #4 | $X_1$ = average mileage per age class | X1 = average mileage per age class<br>$X_2 = X_1 \cdot X_1$ | X1 = average mileage per age class<br>$X_2 = X_1 \cdot X_1$ |
| Model #5 | $X_1$ = average mileage per age class<br>$X_2$ = fraction of TI per age class | $X_1$ = average mileage per age class<br>$X_2$ = fraction of TI per age class | X1 = average mileage per age class<br>$X_2$ = fraction of TI per age class |

* The dependent variable *Y* in each regression model represents the defect detection probability at the technical inspection (TI). Therefore, each regression model has 9 variations for 9 defect groups that are detected at TIs.

**Table 3.** *Dynamic regression models*

| Model | Independent variables*,** | | |
|---|---|---|---|
| | Passenger cars | Commercial vehicles | Motorcycles and ATVs |
| Basic dynamic model | $X_1$ = *vehicle age*<br>$X_2 = X_1 \cdot X_1$<br>$X_3 = t$ = *year* | $X_1$ = *vehicle age*<br>$X_2 = X_1 \cdot X_1$<br>$X_3 = t$ = *year* | $X_1$ = *vehicle age*<br>$X_2 = X_1 \cdot X_1$<br>$X_3 = t$ = *year* |
| Decoupled dynamic model | $X_1$ = *vehicle age*<br>$X_2 = X_1 \cdot X_1$<br>$X_3 = t$ = *year*<br>$X_4$ = *vehicle age* · *year*<br>$X_5 = X_2 \cdot$ *year* | $X_1$ = *vehicle age*<br>$X_2 = X_1 \cdot X_1$<br>$X_3 = t$ = *year*<br>$X_4$ = *vehicle age* · *year*<br>$X_5 = X_2 \cdot$ *year* | $X_1$ = *vehicle age*<br>$X_2 = X_1 \cdot X_1$<br>$X_3 = t$ = *year*<br>$X_4$ = *vehicle age* · *year*<br>$X_5 = X_2 \cdot$ *year* |

* The dependent variable *Y* in each regression model represents the defect detection probability at the technical inspection (TI). Therefore, each regression model has 9 variations for 9 defect groups that are detected at TIs.

** The variable "year" represents the individual database, i.e., 2016 => $X_3 = 1$; 2017 => $X_3 = 2$ etc.

and ATVs, the first technical inspection takes place at the age of four years. After that, technical inspections take place at the ages of six and eight years. After the vehicle is nine years old, technical inspections are performed every year. For commercial vehicles, buses, and tractors, the technical inspections take place every year. In this article, only the results for the entire country of Slovenia are presented to facilitate comparison with Germany and Finland.

For reasons previously explained, this article presents only the statistical data for passenger cars, commercial vehicles, motorcycles, and ATVs. For

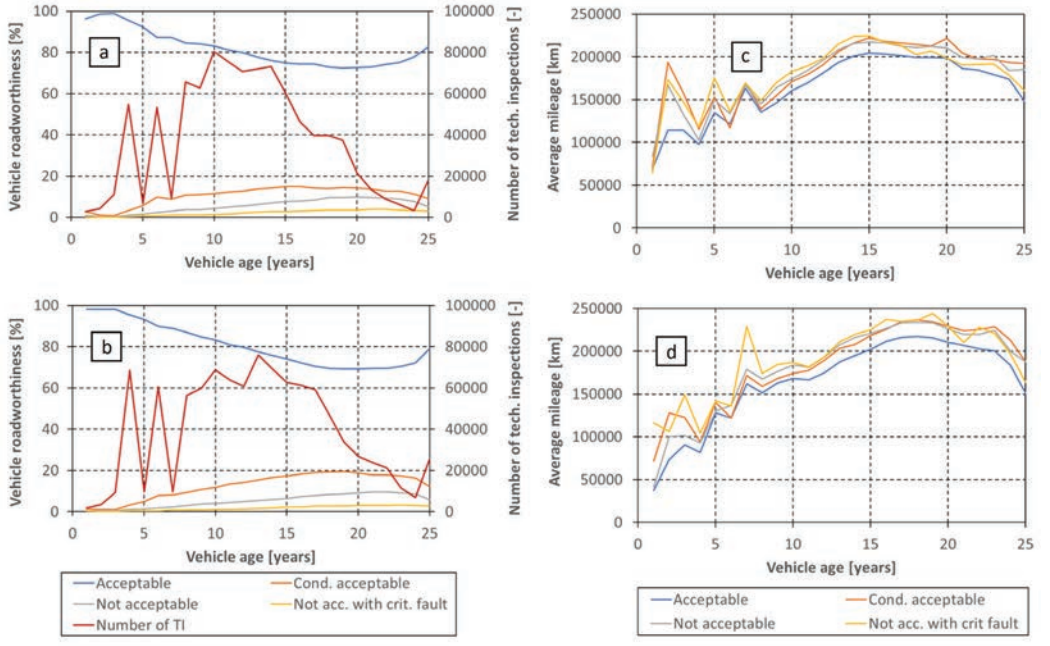


**Fig. 1.** *Results of the technical inspections: a) year 2018, b) year 2021; and average mileage: c) year 2018, d) year 2021; for passenger cars*

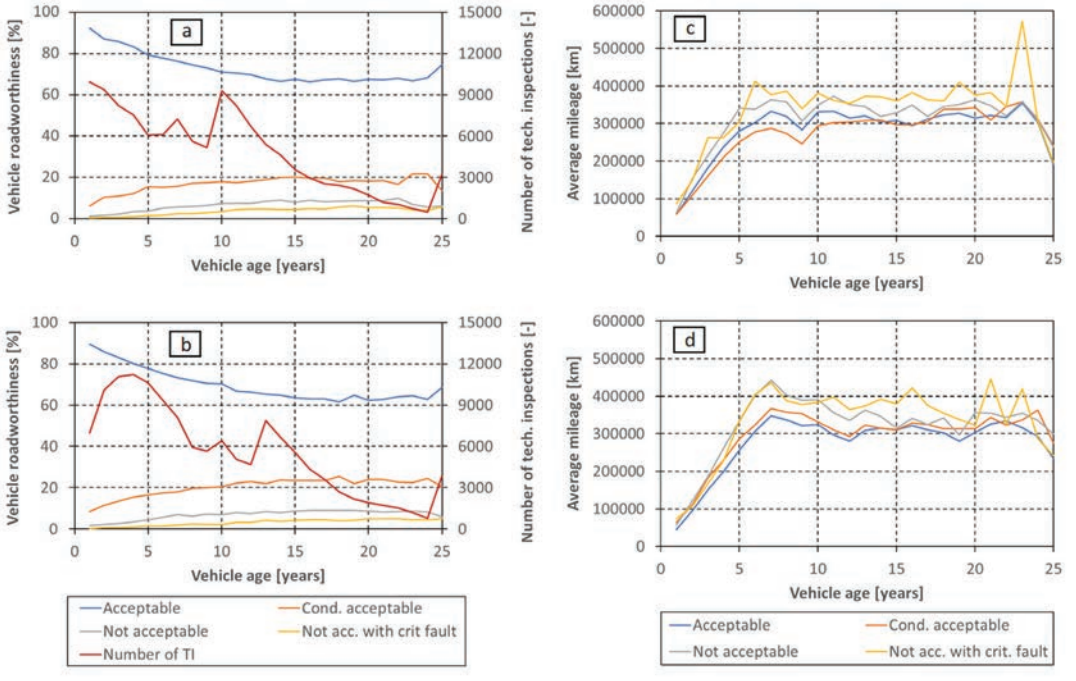


**Fig. 2.** *Results of the technical inspections: a) year 2018, b) year 2021; and average mileage: c) year 2018, d) year 2021; for commercial vehicles*

passenger cars, the average mileage and the results of technical inspections in 2018 and 2021 are presented in Fig. 1. The same statistics are presented in Fig. 2 for commercial vehicles and in Fig. 3 for motorcycles and ATVs. The statistics for the other five years are similar to these figures.

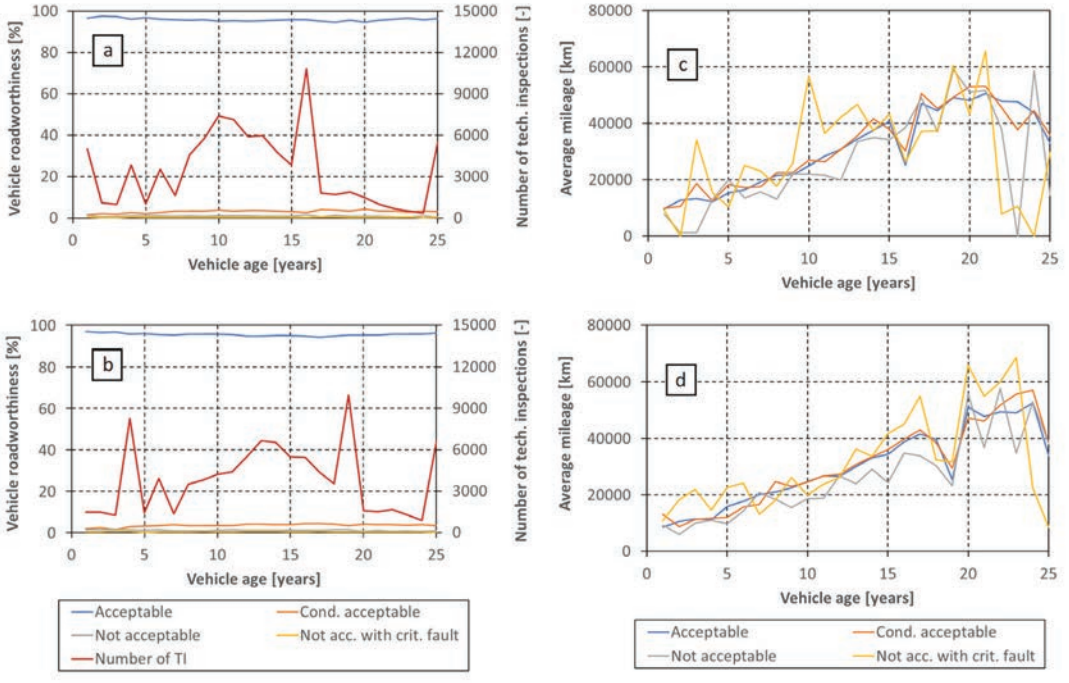


**Fig. 3.** *Results of the technical inspections: a) year 2018, b) year 2021; and average mileage: c) year 2018, d) year 2021; for motorcycles and ATVs*

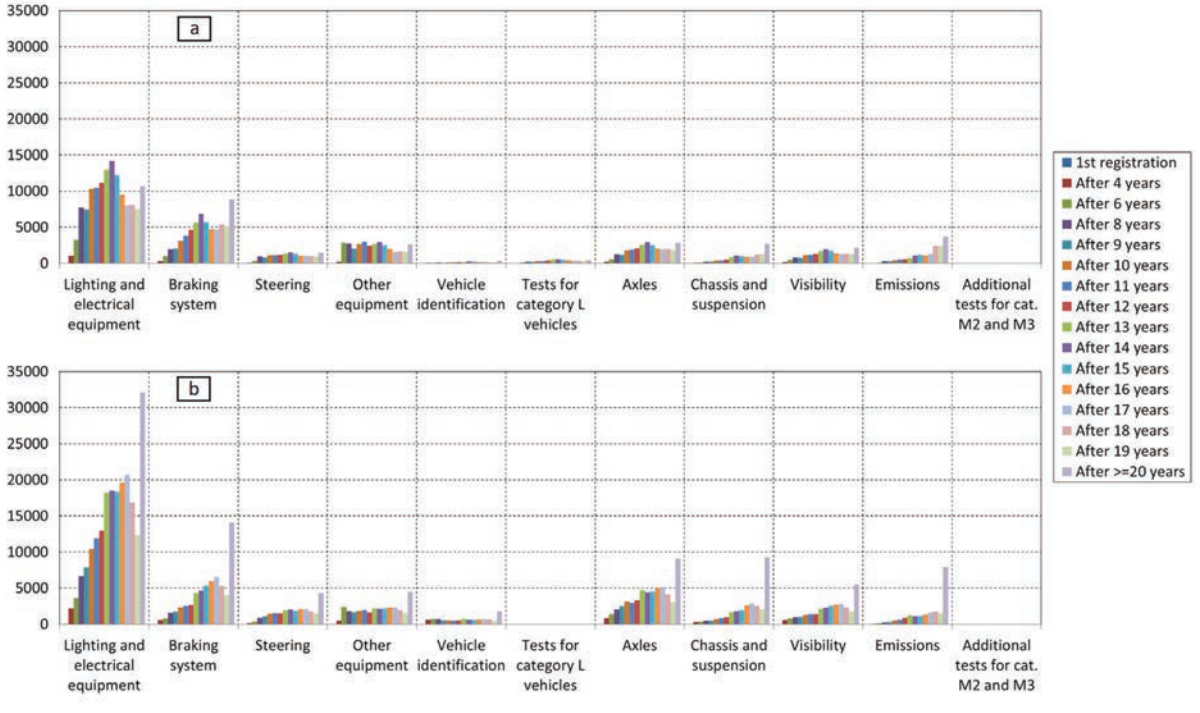


**Fig. 4.** *Detected defects as a function of the vehicle age – passenger cars: a) year 2018, b) year 2021*

Statistical data for 2016 to 2022 are consistent for the three vehicle categories. For passenger cars and commercial vehicles, the average mileage for technical inspections increases slightly but steadily from 2016 to 2022. The older the vehicle, the worse its technical inspection success and the higher its mileage.

After the age of 15 years, the decreasing trend of technical inspection success becomes a fairly constant. The trend in mileage as a function of age is rather proportional for motorcycles and ATVs, but degressive for passenger cars and commercial vehicles. It can also be seen in Figs. 2 and 3 that the peaks of technical inspections are shifted for three years, indicating a rather low volatility of the fleet. Since the number of technical inspections for commercial vehicles is rather small after the vehicle age of twenty years, it can be concluded that owners usually dispose of the worn-out vehicles. Except for passenger cars, the average mileage at technical inspection is not a good indicator of the technical roadworthiness of the vehicle. However, on average, passenger cars with lower mileage have slightly better technical inspection results than cars with higher mileage.

In this part of the study, a comparison was also made between the roadworthiness of vehicles found during technical inspections and the proportion of technically acceptable and unacceptable vehicles involved in traffic accidents. This comparison was made for passenger cars, commercial vehicles, and motorcycles and ATVs for the years 2017, 2018, and 2019. It was found that the relative proportion of acceptable/unacceptable vehicles in technical inspections corresponds very well with the records in the traffic accident database. Specifically, the vehicles that failed the technical inspection for the first time did not cause more accidents than the technically acceptable vehicles, as measured by their relative proportion in the technical inspections. This means that technical faultlessness is really not a major cause of road accidents in Slovenia.

Figs. 4 to 6 show distribution of detected defects according to vehicle age for passenger cars, commercial vehicles, motorcycles and ATVs for 2016 and 2018. For the commercial vehicles, the statistics are shown for every two years.

In Figs. 4 to 6, it can be seen that the detected defects are consistent between the two years, which is also true for the other five years with an exception of the oldest vehicles. After the year 2020 the technical inspections became more strict for this age group, which results in an increased number of detected defects. The same is also true for the first regular technical inspection for motorcycles and ATVs (i.e.

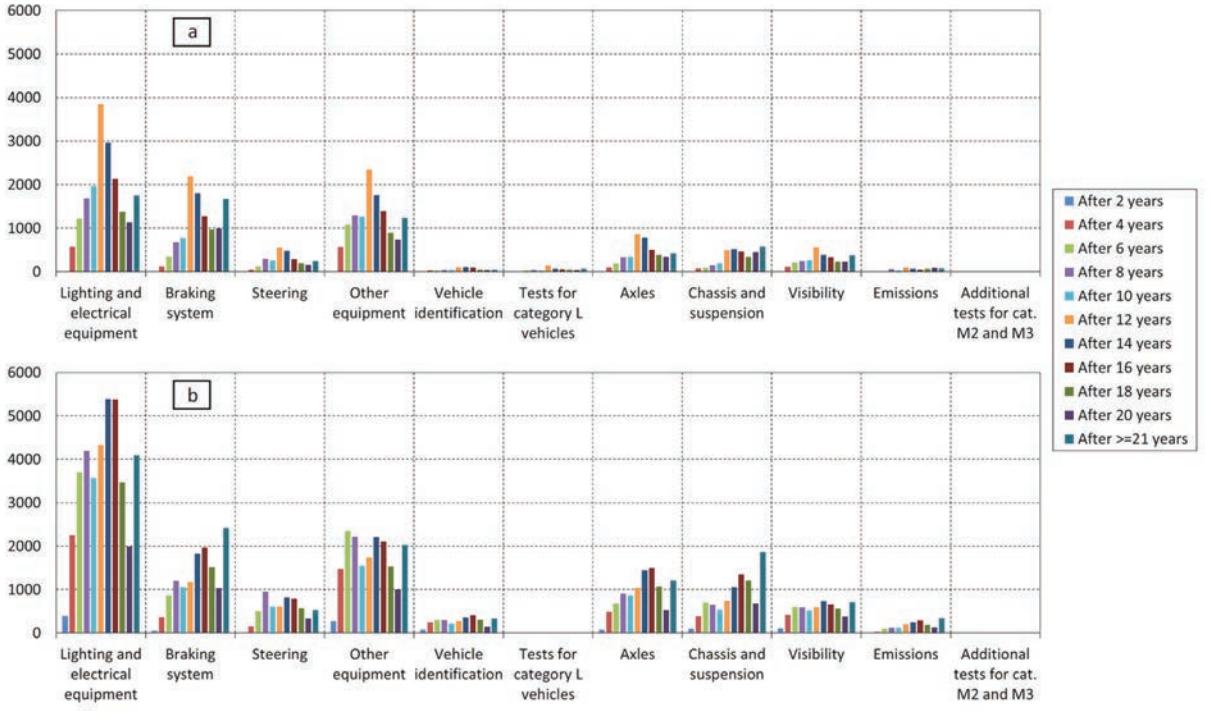


**Fig. 5.** *Detected defects as a function of the vehicle age – commercial vehicles: a) year 2018, b) year 2021*

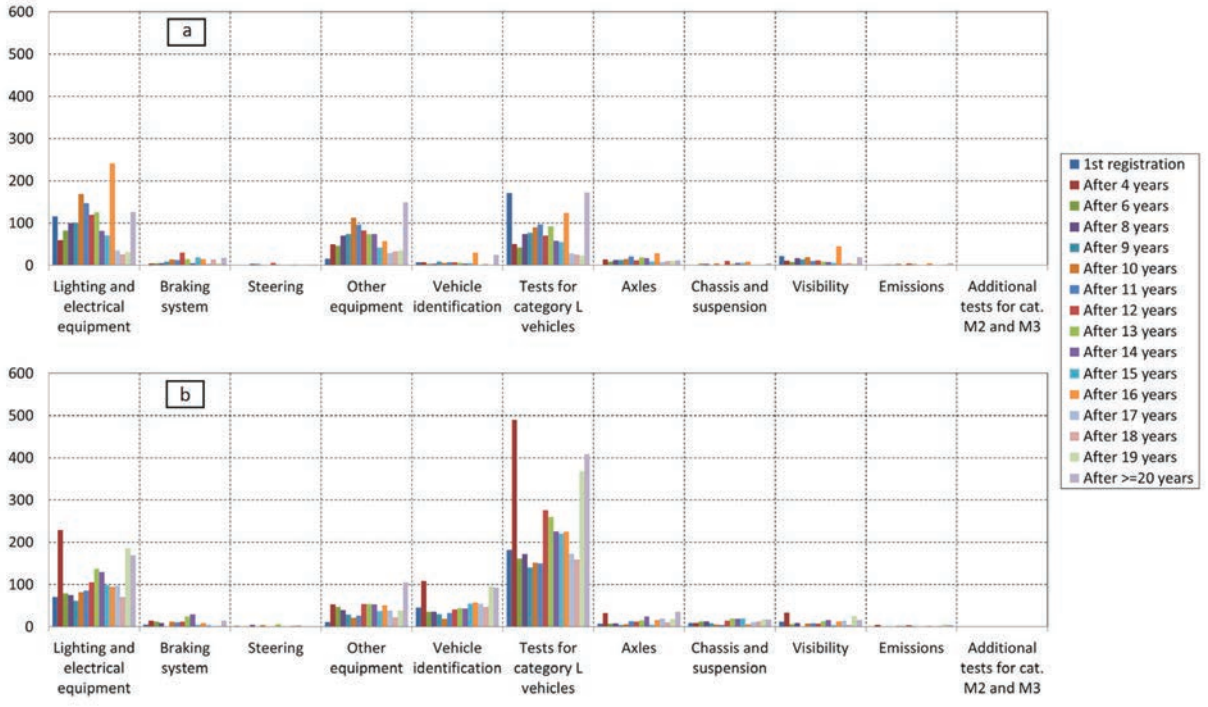


**Fig. 6.** *Detected defects as a function of the vehicle age – motorcycles and ATVs: a) year 2018, b) year 2021*

at the age of four years). For passenger cars and commercial vehicles, the most likely deficiencies are lighting and electrical equipment, braking system, and other equipment (missing first aid kit for passenger cars and fire extinguisher for commercial vehicles). Motorcycles and ATVs are most likely to have deficiencies in lighting, electrical, and other equipment or fail the tests for Class L vehicles.

### 2.2 Comparison with Germany and Finland

For comparison with the other countries, only publicly available data on the Internet were used. Despite the fact that some recently research results on the vehicle technical inspections for different EU countries are published (e.g. see Hudec et al. [23] for all vehicles or Tapak et al. [24] for vehicles with smart technologies) it is difficult to find more detailed statistical data on age-dependent different types of vehicle failures. In most of the published literature a summarized statistical data on the vehicle defects can only be found. For this reason, the statistical data on individual defect types for Slovenia are compared only to the equivalent statistical data for Germany and Finland. For the three countries the available statistical data did not contain detailed information on the generic vehicle's propulsion system (ICE, BEV or PHEV).

For passenger cars, a Traficon database [24] was used for Finland and summarized TUeV reports [26] to [29] were used for Germany. For commercial vehicles, data from Verkehrs Rundschau [30] and [31] journal were used. Although the country-specific regulations for technical vehicle inspections are subordinate to the same EU directives, the main defect groups are subdivided differently into subgroups. For this reason, it was difficult to compare the statistical data between EU countries. To make the comparison possible, the statistical data from the defect subgroups of Finland and Germany were combined so that the data corresponded to the Slovenian defect groups.

Table 4 compares the roadworthiness of passenger cars in Germany and Slovenia. Table 5 compares the probabilities of detecting typical defects in passenger cars in Germany and Slovenia. Fig. 7 compares the probabilities of defect detections for passenger cars in Finland and Slovenia. A comparison between Finland and Slovenia is made only for 2017 to 2019, since data on the technical inspections of passenger cars were not available for Finland for 2016. Fig. 8 shows the roadworthiness of commercial vehicles in Germany. Finally, Fig. 9 compares the probabilities of defect detections for typical commercial vehicle defects between Germany and Slovenia. This comparison for is made only for five years due to data availability for Germany.

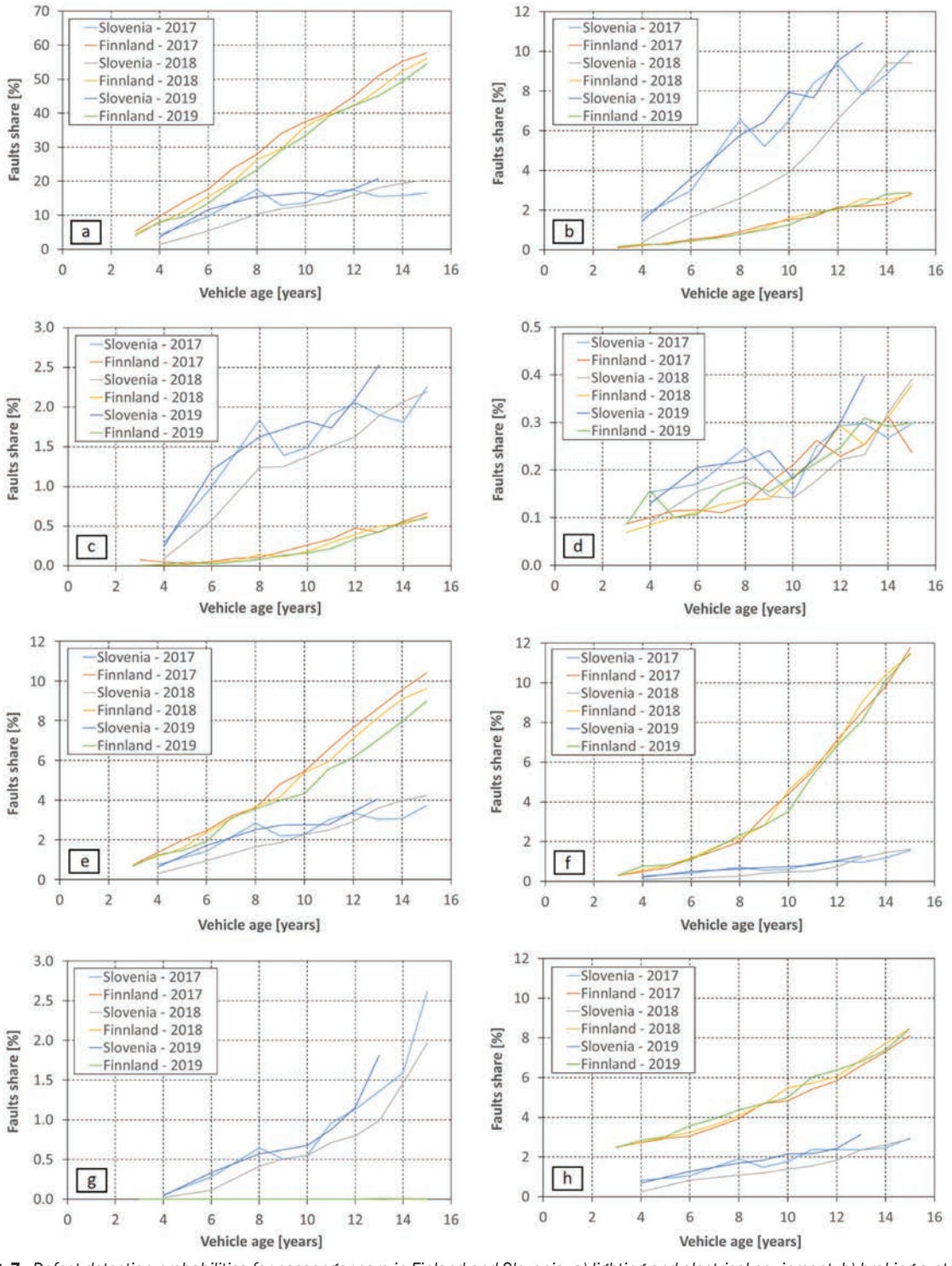


**Fig. 7.** *Defect detection probabilities for passenger cars in Finland and Slovenia: a) lighting and electrical equipment, b) braking system, c) steering equipment, d) vehicle identification, e) axles, wheels and suspension, f) chassis and body, g) emissions, h) visibility*

From Tables 4 and 5, and Fig. 7, the following can be concluded for passenger cars:

- The stringency of technical inspections is higher in Germany for all age classes of passenger cars than in Slovenia, where far fewer vehicles are

considered to be in perfect condition. A direct comparison of the defects detected during technical inspections is only possible to a limited extent due to the different specifications of the defects in Germany and Slovenia. Nevertheless, it can be stated that the proportions of the most common defects (i.e., lighting system and brake system) are similar in Slovenia and Germany.

- In contrast to Germany, it is difficult to claim that technical inspections in Finland are stricter than in Slovenia. For four defect groups (lighting and electrical equipment; axles, wheels and suspension; chassis and body; visibility), more defects are found in Finland than in Slovenia, while for three defect groups (braking system; steering; emissions), more defects are found in Slovenia. No significant differences were found in vehicle identification. In both countries, the most frequent defects are found in the braking system and in lighting and electrical equipment.

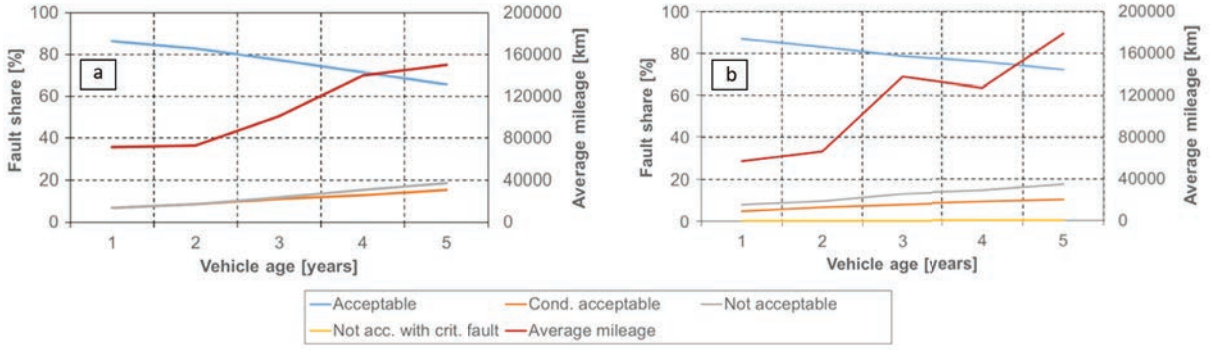


**Fig. 8.** Roadworthiness of commercial vehicles in Germany at technical inspections: a) years 2016/2017, b) years 2019/2020

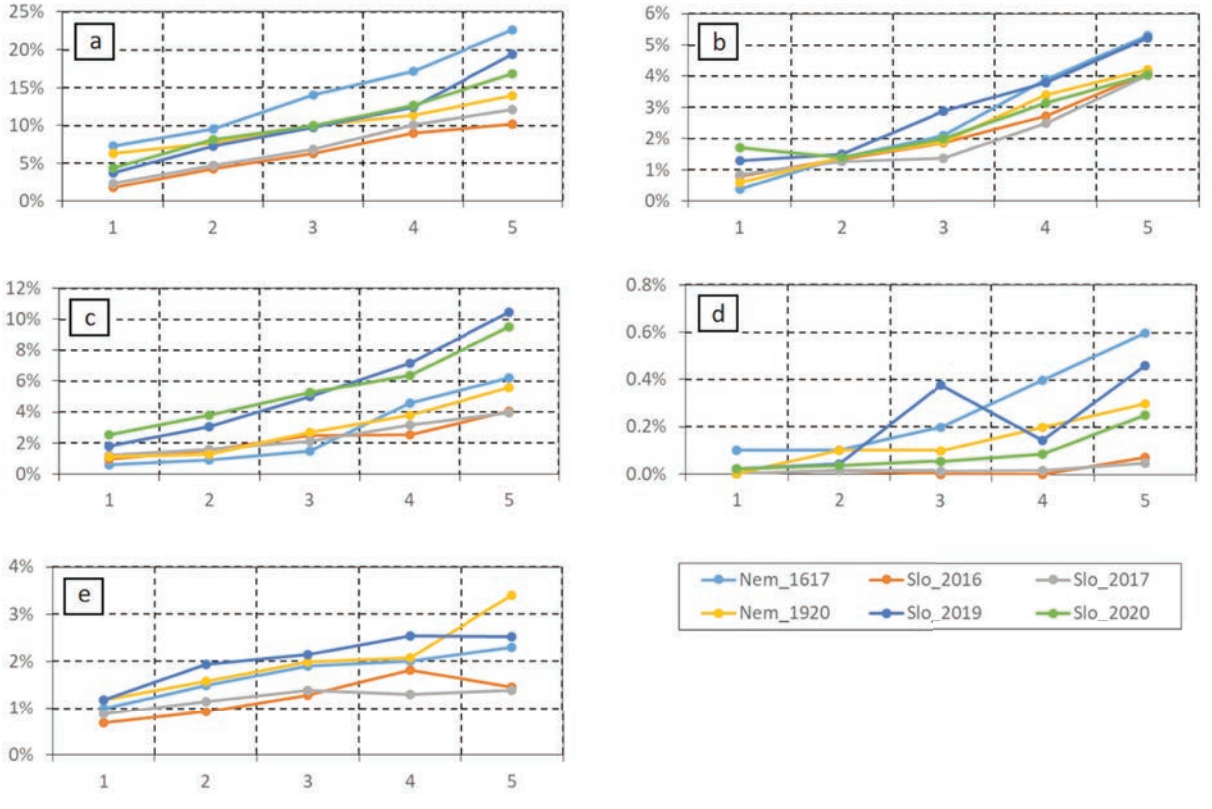


**Fig. 9.** *Defect detection probabilities for 1 to 5 years old commercial vehicles in Germany and Slovenia: a) lighting equipment, b) braking system, c) chassis and suspension, d) emissions, e) visibility*

**Table 4.** *Roadworthiness of passenger cars in Germany and Slovenia at technical inspections*

| Age of the technically unacceptable vehicles | Germany [%] | Slovenia – all technically unacceptable vehicles* [%] | | | |
|---|---|---|---|---|---|
| | | 2016 | 2017 | 2018 | 2019 |
| 4 to 5 | 10.3 | 1.9 | 1.7 | 1.7 | 1.7 |
| 6 to 7 | 16.3 | 3.4 | 3.7 | 3.4 | 3.3 |
| 8 to 9 | 22.2 | 4.6 | 4.8 | 4.8 | 4.6 |
| 10 to 11 | 28.0 | 6.3 | 6.4 | 6.0 | 6.4 |

* The first technical inspection for passenger cars is carried out at the age of four years in Slovenia

**Table 5.** *Probabilities of fault detections for passenger cars in Germany and Slovenia*

| Fault type | Germany | Slovenia | | | |
|---|---|---|---|---|---|
| | | 2016 | 2017 | 2018 | 2019 |
| Lighting equipment | 7.3 % | 10.7 % | 11.9 % | 11.4 % | 10.5 % |
| Suspension elements | 4.5 % | 0.3 % | 0.3 % | 0.3 % | 0.4 % |
| Braking system | 2.8 % | 3.3 % | 3.3 % | 2.9 % | 2.1 % |

From Figs. 2, 8, and 9, the following conclusions can be drawn for commercial vehicles:

- The average mileage of commercial vehicles up to five years old is comparable in Slovenia and Germany, but the percentage of defect-free vehicles (including critical defects) is lower in Slovenia than in Germany for the same vehicle age.
- The relative frequency of detected defects is not the same in Slovenia and Germany, although it is difficult to compare these data because of the different specifications of the defects. Never the less, no significant differences were found for the lighting equipment, brake system, visibility, or chassis and suspension. In both countries, the most common defects are with the lighting system.

From the comparisons presented, it can be concluded that technical inspections in the three countries place a different emphasis on individual defect groups. As a result, the roadworthy condition of vehicles may be assessed differently in these countries. Nevertheless, the most common defects found in these countries are the same, which means that the prescribed technical inspection procedures do not differ to an unacceptable extent.

### 2.3 Regression Models for Predicting the Probability of Fault Detection

Figs. 10 and 11 show the defect detection probabilities at technical inspections in the years 2018 and 2021 for commercial vehicles, motorcycles and ATVs. The statistics for the other five years are similar and will not be presented here. For the passenger cars, these probabilities are shown in Fig. 7 for the years 2017, 2019 and 2021. The statistics for the other years are also similar. When these figures are compared to Fig. 4 to 6 the same trend can be noticed, i.e., that after the year 2020 the technical inspections became more strict. Since more faults were detected at approximately the same number of technical inspections per year the probability of fault detection rose in the years 2020 to 2022.

From Figs. 7, 10, and 11, it can be seen that the probability of defect detection during technical inspections did not increase proportionally with vehicle age. It was also found that vehicle age predicted the probability of defect detection much better than average mileage. Consequently, the basic regression model #3 from Table 2 was consistently found to be the best for the three vehicle categories and defect groups studied. The regression coefficients and the values of the deterministic coefficient $R^2$ for

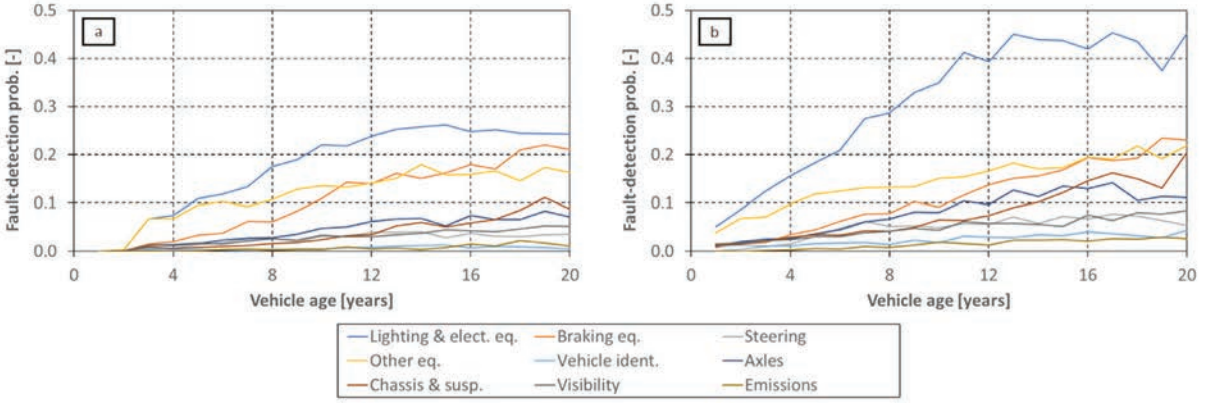


**Fig. 10.** *Defect detection probabilities for commercial vehicles in Slovenia: a) year 2018, b) year 2021*

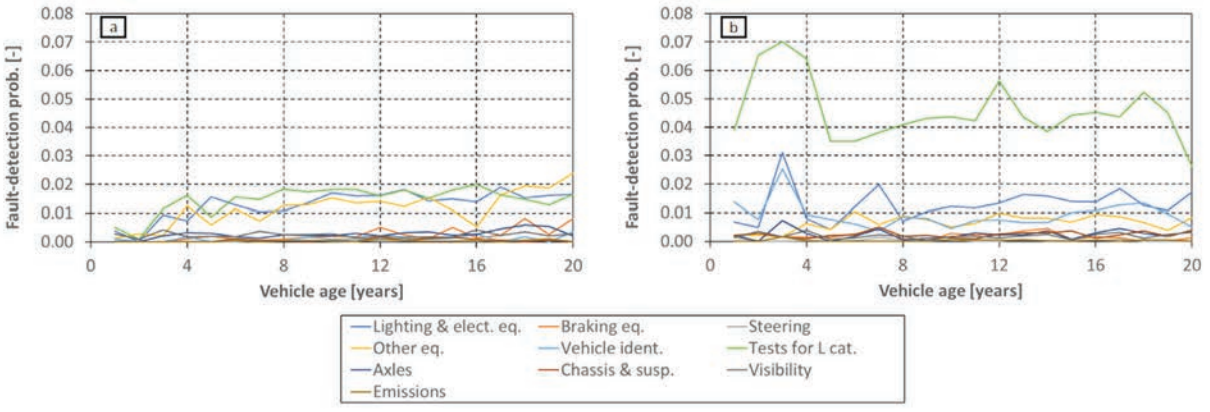


**Fig. 11.** *Defect detection probabilities for motorcycles and ATVs in Slovenia: a) year 2018, b) year 2021*

the basic regression model #3 are shown in Table A1 in Appendix for the relevant fault groups and the year 2018. Since the coefficients for the other six years are very similar, they are not shown here. Both dynamic regression models from Table 3 were also successful in predicting the probability of defect detection, but the decoupled model was consistently better than the basic dynamic model. For this reason, Table A2 in Appendix presents the regression coefficients and the values of the deterministic coefficient $R^2$ for only the decoupled dynamic regression models for the relevant defect groups.

From Table A1, we can conclude that the regression models for passenger cars and commercial vehicles are good, as reflected in high values ($R^2 > 0.7$) of the $R^2$ value for all error groups except emissions and vehicle identification. In contrast, the regression models for motorcycles and ATVs are poor. This results from the following facts: i) the probabilities of fault detection are much lower compared to passenger cars and commercial vehicles, and ii) the probabilities of fault detection vary significantly between different vehicle ages.

Comparing Table A2 with Table A1, we see that the dynamic regression models are comparable the base regression model #3 according to their $R^2$ values remain relatively high ($R^2 > 0.7$) for passenger cars and commercial vehicles. The dynamic regression models for the motorcycles and ATVs are poor for the same reason explained earlier. Never the less, it is advantageous to model the probability of fault detection separately for each year, because it can be concluded from the results, which were presented before, that there are relatively more faults detected at technical inspections after the year 2020.

## 3 CONCLUSIONS

In the EU, several directives regulate the technical safety and roadworthiness of road vehicles. Moreover, national regulations are subordinate to these directives. In our study, the roadworthiness of vehicles found during regular technical inspections was statistically analysed and compared with the road accident database. In this part of the study, it was found that the technically unsound vehicles (i.e., vehicles that did not pass the technical inspection for the first time) do not contribute more to road accidents than the technically roadworthy vehicles, as measured by their relative share determined during the technical inspections.

Then, the statistics for passenger cars and commercial vehicles were compared with those of the other two EU countries (i.e., Germany and Finland). From this comparison, it can be concluded that the individual defect groups are weighted differently in the different countries. This could lead to some differences in roadworthiness ratings across EU countries. Nevertheless, the most frequently identified defects were the same in the countries compared, which means that the prescribed technical inspection procedures do not differ to an unacceptable extent.

To complement this, year-specific and dynamic regression models were also constructed to predict the probability of defect detection for Slovenian passenger cars, commercial vehicles, motorcycles, and ATVs. It was found that the probability of defect identification during technical inspection can be predicted well for almost all defect groups for passenger cars and commercial vehicles. However, due to data variation and inconsistency, this cannot be reliably done for motorcycles and ATVs. Dynamic regression models

were also found to have somewhat lower modelling power than the year-specific base regression models.

## 4 ACKNOWLEDGEMENTS

The authors acknowledge financial support from the Slovenian Research Agency and Slovenian Traffic Safety Agency (CRP project No. V2-1929 entitled "Analiza napak na vozilih ugotovljenih pri postopkih tehničnih pregledov vozil s konvencionalnimi statističnimi metodami in z metodami rudarjenja podatkov" / "Analysis of vehicle defects identified at technical supervisions using conventional statistical methods and data mining").

## 5 NOMENCLATURES

| | |
|---|---|
| $a_0$ | constant term of a linear regression model, [-] |
| $a_i$ | linear regression coefficient of the $i^{th}$ term, [-] |
| $b_0$ | time-related constant term in the dynamic regression model, [-] |
| $b_1$ | time-related linear coefficient in the dynamic regression model, [-] |
| $n$ | number of sample points, [-] |
| $p$ | number of independent random variables, [-] |
| $t$ | time [s] |
| $x_i$ | realization of the $i^{th}$ independent random variable $X_i$, [-] |
| $\mathbf{x}$ | realization of the independent vector $\mathbf{X}$, [-] |
| $X_i$ | $i^{th}$ independent random variable, [-] |
| $\mathbf{X}$ | vector of independent random variables, [-] |
| $y$ | realization of the dependent random variable $Y$, [-] |
| $Y$ | dependent random variable, [-] |
| $\varepsilon$ | prediction error, [-] |
| $j$ | running index, [-] |

## 6 REFERENCES

[1] Singh, S. (2015). Critical Reasons for Crashes Investigated in the National Motor Vehicle Crash Causation Survey. *Traffic Safety Facts Crash-Stats*. Report No. DOT HS 812 115. National Highway Traffic Safety Administration, Washington, DC.

[2] Thomas, P., Morris, A., Talbot, R., Fagerlind, H. (2013). Identifying the causes of road crashes in Europe. *Proceedings of 57th AAAM Annual Conference Annals of Advances in Automotive Medicine*, vol. 57, p. 13-22.

[3] Rolison, J.J., Regev, S., Moutari, S., Feeney, A. (2015). What are the factors that contribute to road accidents? An assessment of law enforcement views, ordinary drivers' opinions, and road accident records. *Accident Analysis and Prevention*, vol. 115, no. 11-24, **DOI:10.1016/j.aap.2018.02.025**.

[4] Van Schoor, O., Van Niekerk, J.L., Grobbelaar, B. (2001) Mechanical failures as a contributing cause to motor vehicle accidents - South Africa. *Accident Analysis and Prevention*, vol. 33, no. 6, p. 713-721, **DOI:10.1016/S0001-4575(00)00083-X**.

[5] Supa Quick. (2019). Top 3 car mechanics most likely to cause road accidents when they fail, from *https://www.supaquick.com/top-3-mechanical-failures-that-cause-road-accidents*, accessed on 2022-08-17.

[6] Kumar, A.K., Selvan, T.R., Siddiqui, N.A., Gautam, A. (2015) Scope for developing accident causation model of road transportation of hazardous materials. *International Advanced Research Journal in Science, Engineering and Technology,* vol. 2, no. 10, p. 57-63, **DOI:10.17148/iarjset.2015.21012**.

[7] Hudec, J., Sarkan, B. (2022) Effect of periodic technical inspections of vehicles on traffic accidents in Slovak Republic. *Operation and Economics in Transport, Communications*, vol. 24, no. 3, p. A142-A159, **DOI:10.26552/com.C.2022.3.A142-A159**.

[8] Brcar, F. (2017) Analysis of traffic accidents in the last 20 years in Slovenia. *Journal of Universal Excellence*, vol. 6, no. 4, p. 323-333. (in Slovenian ).

[9] Martín-delosReyes, L.M., Lardelli-Claret, P., García-Cuerva, L., Rivera-Izquierdo, M., Jiménez-Mejías, E., Martínez-Ruiz, V. (2021). Effect of periodic vehicle inspection on road crashes and injuries: A systematic review. *International Journal of Environmental Research and Public Health*, vol. 18, no. 12, art. ID 6476, **DOI:10.3390/ijerph18126476**.

[10] Newnam, S., Goode, N. (2015). Do not blame the driver: A systems analysis of the causes of road freight crashes. *Accident Analysis and Prevention*, vol. 76, p. 141-151, **DOI:10.1016/j.aap.2015.01.016**.

[11] Uchida, N., Kawakoshi, M., Tagawa, T., Mochida, T. (2010). An investigation of factors contributing to major crash types in Japan based on naturalistic driving data. *IATSS Research*, vol. 34, no. 1, p. 22-30, **DOI:10.1016/j.iatssr.2010.07.002**.

[12] Garnowski, M., Manner, H. (2011). On factors related to car accidents on German Autobahn connectors. *Accident Analysis and Prevention*, vol. 43, p. 1864-1871, **DOI:10.1016/j.aap.2011.04.026**.

[13] Lowman Law Firm. (2022). Top 5 Mechanical Failures that Cause Car Accidents, from *https://www.lowmanlawfirm.com/blog/bid/63142/top-5-mechanical-failures-that-cause-car-accidents*, accessed on 2022-08-16.

[14] Carley, L. (2022). Auto Accidents Caused by Mechanical Failures, from *https://www.aa1car.com/library/auto_accident.htm*, accessed on 2022-07-24.

[15] Statista. (2020). Number of road accidents caused by vehicle defect factors in Great Britain (UK) in 2017, by severity, from *https://www.statista.com/statistics/323086/road-accidents-caused-by-vehicle-defect-factors-severity-in-great-britain-uk/*, accessed on 2022-07-24.

[16] Council Directive 1999/37/EC of 29 April 1999 on the registration documents for vehicles. Document 01999L0037-20180520, from *http://data.europa.eu/eli/dir/1999/37/2018-05-20* accessed on 2022-11-18.

[17] Directive 2014/46/EU of the European Parliament and of the Council of 3 April 2014 amending Council Directive 1999/37/EC on the registration documents for vehicles. Document

32014L0046, from *http://data.europa.eu/eli/dir/2014/46/oj*, accessed on 2022-11-18.

**[18]** Directive 2007/46/EC of the European Parliament and of the Council of 5 September 2007 establishing a framework for the approval of motor vehicles and their trailers, and of systems, components and separate technical units intended for such vehicles. Document 02007L0046-20200902, from *http://data.europa.eu/eli/dir/2007/46/2020-09-02*, accessed on 2022-11-18.

**[19]** Regulation (EC) No 661/2009 of the European Parliament and of the Council of 13 July 2009 concerning type-approval requirements for the general safety of motor vehicles, their trailers and systems, components and separate technical units intended therefor. Document 02009R0661-20190424, from *http://data.europa.eu/eli/reg/2009/661/2019-04-24*, accessed on 2022-11-18.

**[20]** Directive 2014/45/EU of the European Parliament and of the Council of 3 April 2014 on periodic roadworthiness tests for motor vehicles and their trailers and repealing Directive 2009/40/EC. Document 02014L0045-20140429, from *http://data.europa.eu/eli/dir/2014/45/2014-04-29*, accessed on 2022-11-18.

**[21]** Pindyck, R.S., Rubinfeld, D.L. (2000). *Econometric Models and Economic Forecasts*, 4th edition. McGraw-Hill, Singapore.

**[22]** Hayter, A.J. (2012). Probability and Statistics for Engineers and Scientists, 4th edition. Cengage learning, Boston.

**[23]** Hudec, J., Šarkan, B., Cződörová, R. (2021). Examination of the results of the vehicles technical inspections in relation to the average age of vehicles in selected EU states. *Transportation Research Procedia*, vol. 55, p. 2-9, **DOI:10.1016/j.trpro.2021.07.063**.

**[24]** Tapak, P., Kocur, M., Rabek, M., Matej, J. (2023). Periodical vehicle inspections with smart technology. *Applied Sciences*, vol. 13, no. 12, art. ID. 7241, **DOI:10.3390/app13127241**.

**[25]** Toivanen, T., Väisänen, A. (2108). Fault statistics for 2018 car inspections now published, from *https://www.traficom.fi/en/news/fault-statistics-2018-car-inspections-now-published*, accessed on 2022-11-16.

**[26]** Joachim, B., Müller-Gerbes, H. (2019). *TÜVReport 2019 Pressekonferenz*. TÜV e.V. (VdTÜV), Berlin.

**[27]** Mängelzwerge und Mängelriesen. *Auto Bild TÜV Report 2017*.

**[28]** Mängelzwerge und Mängelriesen. *Auto Bild TÜV Report 2018*.

**[29]** Mängelzwerge und Mängelriesen. *Auto Bild TÜV Report 2019*.

**[30]** *Verkehrs Rundschau Extra 40/2017: TÜV Report Nutzfahrzeuge*. Beilage in Kooperation mit dem Verband der TÜV e.V. (VdTÜV) Berlin.

**[31]** *Verkehrs Rundschau Extra 19/2021: TÜV Report Nutzfahrzeuge*. Beilage in Kooperation mit dem Verband der TÜV e.V. (VdTÜV) Berlin.

## 7 APPENDIX

**Table A1.** *Regression coefficients and determination coefficients for the basic regression model #3 for the year 2018*

| Coeffi-cients | Light. & elect. | Brake system | Steering | Other equip. | Vehicle ident. | Cat. L tests | Axles | Chassis & susp. | Visibility | Emissions |
|---|---|---|---|---|---|---|---|---|---|---|
| Passenger cars | | | | | | | | | | |
| $a_0$ | -0.0793 | -0.0336 | -0.0085 | -0.0078 | 0.0000 | n/a | -0.0170 | -0.0040 | -0.0091 | -0.0091 |
| $a_1$ | 0.0319 | 0.0106 | 0.0033 | 0.0062 | 0.0002 | n/a | 0.0061 | 0.0007 | 0.0034 | 0.0017 |
| $a_2$ | -0.0010 | -0.0002 | -0.0001 | -0.0002 | 0.0000 | n/a | -0.0002 | 0.0001 | -0.0001 | 0.0000 |
| $R^2$ | 0.9245 | 0.9079 | 0.9064 | 0.7764 | 0.8657 | n/a | 0.8772 | 0.8520 | 0.8868 | 0.6826 |
| Commercial vehicles | | | | | | | | | | |
| $a_0$ | -0.0487 | -0.0516 | -0.0098 | -0.0059 | -0.0032 | n/a | -0.0225 | -0.0204 | -0.0042 | -0.0039 |
| $a_1$ | 0.0362 | 0.0213 | 0.0059 | 0.0188 | 0.0016 | n/a | 0.0103 | 0.0069 | 0.0043 | 0.0014 |
| $a_2$ | -0.0011 | -0.0005 | -0.0002 | -0.0005 | -0.0001 | n/a | -0.0003 | -0.0001 | -0.0001 | 0.0000 |
| $R^2$ | 0.9662 | 0.9218 | 0.8258 | 0.8854 | 0.6144 | n/a | 0.8879 | 0.7942 | 0.8873 | 0.5675 |
| Motorcycles and ATVs | | | | | | | | | | |
| $a_0$ | 0.0012 | -0.0018 | -0.0002 | 0.0014 | 0.0005 | 0.0174 | -0.0004 | 0.0000 | 0.0022 | -0.0002 |
| $a_1$ | 0.0021 | 0.0007 | 0.0001 | 0.0014 | 0.0000 | -0.0002 | 0.0006 | 0.0001 | 0.0000 | 0.0001 |
| $a_2$ | -0.0001 | 0.0000 | 0.0000 | 0.0000 | 0.0000 | 0.0000 | 0.0000 | 0.0000 | 0.0000 | 0.0000 |
| $R^2$ | 0.5816 | 0.2884 | 0.2038 | 0.5436 | 0.1875 | 0.0048 | 0.3602 | 0.1377 | 0.0787 | 0.1805 |

**Table A2.** *Regression coefficients and determination coefficients for the two dynamic regression models*

| Coeffi-cients | Light. & elect. | Brak. system | Steering | Other equip. | Vehicle ident. | Cat. L tests | Axles | Chassis & susp. | Visibility | Emissions |
|---|---|---|---|---|---|---|---|---|---|---|
| | | | | | Passenger cars | | | | | |
| $a_0$ | -0.0352 | -0.0368 | -0.0071 | 0.0039 | -0.0015 | n/a | -0.0100 | -0.0057 | -0.0073 | -0.0205 |
| $a_1$ | 0.0235 | 0.0123 | 0.0031 | 0.0052 | 0.0002 | n/a | 0.0040 | 0.0011 | 0.0031 | 0.0050 |
| $a_2$ | -0.0008 | -0.0002 | -0.0001 | -0.0002 | 0.0000 | n/a | -0.0001 | 0.0000 | -0.0001 | -0.0001 |
| $a_3$ | -0.0112 | 0.0028 | -0.0006 | -0.0012 | 0.0008 | n/a | -0.0019 | 0.0009 | 0.0003 | 0.0036 |
| $a_4$ | 0.0028 | -0.0008 | 0.0002 | 0.0000 | 0.0000 | n/a | 0.0010 | -0.0002 | 0.0001 | -0.0010 |
| $a_5$ | 0.0000 | 0.0000 | 0.0000 | 0.0000 | 0.0000 | n/a | 0.0000 | 0.0000 | 0.0000 | 0.0000 |
| $R^2$ | 0.9305 | 0.9412 | 0.9214 | 0.8295 | 0.8313 | n/a | 0.9185 | 0.9497 | 0.9194 | 0.8710 |
| | | | | | Commercial vehicles | | | | | |
| $a_0$ | -0.0138 | -0.0191 | -0.0066 | 0.0377 | -0.0027 | n/a | -0.0144 | -0.0133 | -0.0012 | -0.0045 |
| $a_1$ | 0.0227 | 0.0137 | 0.0043 | 0.0150 | 0.0004 | n/a | 0.0070 | 0.0039 | 0.0029 | 0.0013 |
| $a_2$ | -0.0007 | -0.0001 | -0.0001 | -0.0004 | 0.0000 | n/a | -0.0002 | -0.0001 | 0.0000 | 0.0000 |
| $a_3$ | -0.0035 | -0.0022 | -0.0010 | -0.0015 | 0.0005 | n/a | -0.0009 | -0.0002 | 0.0004 | -0.0002 |
| $a_4$ | 0.0053 | 0.0009 | 0.0010 | 0.0006 | 0.0005 | n/a | 0.0014 | 0.0009 | 0.0006 | 0.0002 |
| $a_5$ | -0.0002 | 0.0000 | 0.0000 | 0.0000 | 0.0000 | n/a | 0.0000 | 0.0000 | 0.0000 | 0.0000 |
| $R^2$ | 0.9570 | 0.9149 | 0.8673 | 0.8534 | 0.8447 | n/a | 0.8932 | 0.9213 | 0.9129 | 0.8722 |
| | | | | | Motorcycles and ATVs | | | | | |
| $a_0$ | 0.0076 | -0.0016 | 0.0001 | 0.0060 | 0.0001 | 0.0101 | 0.0015 | 0.0001 | 0.0044 | -0.0003 |
| $a_1$ | 0.0011 | 0.0008 | 0.0000 | 0.0016 | -0.0002 | -0.0007 | 0.0004 | 0.0001 | -0.0002 | 0.0001 |
| $a_2$ | 0.0000 | 0.0000 | 0.0000 | 0.0000 | 0.0000 | 0.0000 | 0.0000 | 0.0000 | 0.0000 | 0.0000 |
| $a_3$ | 0.0002 | 0.0004 | 0.0001 | -0.0004 | 0.0014 | 0.0077 | -0.0001 | 0.0003 | -0.0001 | 0.0001 |
| $a_4$ | 0.0000 | 0.0000 | 0.0000 | 0.0001 | 0.0001 | 0.0000 | 0.0000 | 0.0001 | 0.0001 | 0.0000 |
| $a_5$ | 0.0000 | 0.0000 | 0.0000 | 0.0000 | 0.0000 | 0.0000 | 0.0000 | 0.0000 | 0.0000 | 0.0000 |
| $R^2$ | 0.1514 | 0.1234 | 0.0961 | 0.1299 | 0.1710 | 0.3591 | 0.1128 | 0.1243 | 0.1102 | 0.0916 |

Strojniški vestnik - Journal of Mechanical Engineering 69(2023)11-12, 471-482
DOI:10.5545/sv-jme.2023.604
Original Scientific Paper
Received for review: 2023-04-14
Received revised form: 2023-09-18
Accepted for publication: 2023-09-22


# Impact Behaviour Modelling of Magnetorheological Elastomer Using a Non-Parametric Polynomial Model Optimized with Gravitational Search Algorithm

Amrina Rasyada Zubir – Khisbullah Hudha* – Zulkiffli Abd. Kadir – Noor Hafizah Amer
Department of Mechanical Engineering, National Defence University of Malaysia, Malaysia

*This paper presents an approach to model the impact behaviour of a dual-acting magnetorheological elastomer (MRE) damper using 4th-order polynomial functions optimized with a gravitational search algorithm. MRE is a type of smart material that can change its mechanical properties in response to an injected current, making it well-suited for a wide range of applications such as vibration absorption, noise cancellation, and shock mitigation. The proposed model uses a combination of polynomial functions designed to predict the nonlinearity of MRE during compression and extension stages. The model is tuned and validated using experimental data from impact tests conducted on the MRE damper under various currents. The results indicate that the developed model can accurately track the impact behaviour of MRE with minimum error. Additionally, an interpolation model is proposed to estimate the appropriate forces for median currents. The interpolation model predicts the force between the upper and lower currents, demonstrating the model's ability to predict MRE behaviour accurately. The main contribution of this study is proposing a non-parametric model of MRE that is able to identify the hysteretic behaviour of the MRE based on specific current applied. In addition, an interpolation model is introduced in this study to cover not only the input current starting from 0 A to 2 A but also the intermediate current such as 0.3 A, 0.7 A, 1.3 A and 1.7 A.*

**Keywords: magnetorheological damper, polynomial model, gravitational search algorithm, force-displacement characteristic, interpolated model**

**Highlights**

- *The use of magnetorheological elastomer in the automotive field specific for impact mitigation is one of the precautionary steps to reduce frontal collision towards the vehicle body and passenger.*
- *This study aims to investigate the behaviour of the magnetorheological elastomer damper using a polynomial model optimized with a gravitational search algorithm and compare it with experimental results from the drop impact test.*
- *The polynomic model that can perform at interpolation current has been developed, and the simulation results are well in agreement with the experimental results.*

## 0 INTRODUCTION

The consumption of magnetorheological elastomer (MRE) has grown widely in the automotive field due to its potential to cope with variable stiffness and damping subjected to magnetic fields [1] and [2]. MREs are used in absorbers, isolator devices, and suspension systems to reduce unwanted vibration transmitted to the occupants [3] to [5]. However, during medium and hard collisions in which the vehicle's velocity exceeds 10 mph, MREs cannot protect the vehicle structure and the passenger. To address this problem, researchers have initiated modelling the impact behaviour of the vehicle using non-parametric approaches and have developed a dual-acting MRE damper for the study of impact absorption characteristics.

Previous works on the design of MRE dampers have proposed adaptive variable stiffness absorbers made of two MRE parts attached to both piston and outer cylinder, a multi-layered MRE isolator device, and a semi-active system that incorporates both passive and active elements in the design [6] and [7]. Aside from creating a practical design of MRE-based devices, it is also critical to model and simulate the MRE's dynamic behaviour under various excitation circumstances. In the modelling of MRE-based devices, there are two common approaches: parametric and non-parametric. Non-parametric models are more favourable since they do not need any model parameters and only require input and output to operate [8]. Non-parametric modelling uses intelligent paradigms such as adaptive neuro-fuzzy inference systems (ANFIS), which are capable of modelling MRE damper behaviour under impact loading [9] and [10].

Yu et al. [11] introduced a versatile model capable of predicting dynamic behaviour under diverse excitation conditions, specifically tailored for applications in structural seismic mitigation. This model employs the Kelvin-Voigt element to elucidate the viscoelastic behaviour of the device and leverages the Bouc-Wen hysteresis element to delineate the strain-stiffening phenomenon in its

*Corr. Author's Address: Department of Mechanical Engineering, National Defence University of Malaysia, Malaysia, k.hudha@upnm.edu.my

response. The model's parameters are determined through an improved particle swarm optimization (IPSO) approach aimed at minimizing deviations between observed values and model predictions. Subsequently, the field-dependent properties of the isolator, influenced by varying current levels, are validated using both random and earthquake-induced test data.

A new hybrid model employing a curve-fitting method has also been developed to accurately depict the highly nonlinear and hysteresis relationships between shear force and displacement responses in magnetorheological (MR) elastomer-based isolators [12]. The hybrid content in this model involved the combination of the hyperbolic sine function and Gaussian function to capture the hysteresis loops exhibited by the device responses effectively. Furthermore, an enhanced fruit fly optimization algorithm (FOA) has been introduced for optimizing the model parameters. This improved FOA incorporates a self-adaptive step size mechanism, rather than a fixed step, to strike a balance between the global and local optimum search capabilities of the algorithm. To verify the performance of this innovative hybrid model, both harmonic and random excitations have been employed in comprehensive testing.

This study contributes to the establishment of an effective modelling concept that can analyse the impact behaviour of the MRE damper based on a non-parametric approach using a 4th-order polynomial model. The model is designed to suit various currents ranging from 0 A to 2 A, as well as in-between currents using an interpolation method for the currents of 0.3 A, 0.7 A, 1.3 A and 1.7 A. The effectiveness of the developed model is validated through a model verification procedure by comparing the results between the developed model in Matlab-Simulink software and the experimental results obtained through the drop impact test on the MRE damper. The level of agreement for both responses is observed through the force prediction error, validating the effectiveness of the developed model in predicting the hysteretic behaviour of the MRE [13].

This paper is organized as follows: Section 1 discusses several previous works on the design of an MRE damper; Section 2 describes the design of the dual-acting MRE damper; Section 3 explains the process of fabrication for MRE and the force-displacement characteristics; Section 4 describes the modelling method of MRE behaviour under impact loading using 4th-order polynomial model; Section 5 shows the simulation results and the validation of the model with experimental data. The last section consists of some discussion and conclusion of this study.

## 1 DESIGN OF DUAL-ACTING MAGNETORHEOLOGICAL ELASTOMER DAMPER FOR IMPACT MITIGATION

In this study, a conceptual design for a dual-acting MRE damper is presented. The damper is composed of an upper impactor, a piston, MREs, a coil, and a polyoxymethylene (POM) bobbin, which serves as the isolator of the coil to the housing. To enhance the dual-acting absorption capability of the damper during compression and extension stages, three units of MREs are installed vertically along the housing for both upper and lower sections, as illustrated in Fig. 1. The MREs exhibit variable damping properties and stiffness under changeable applied magnetic fields, allowing the MRE damper to return to its original position after impact [14].

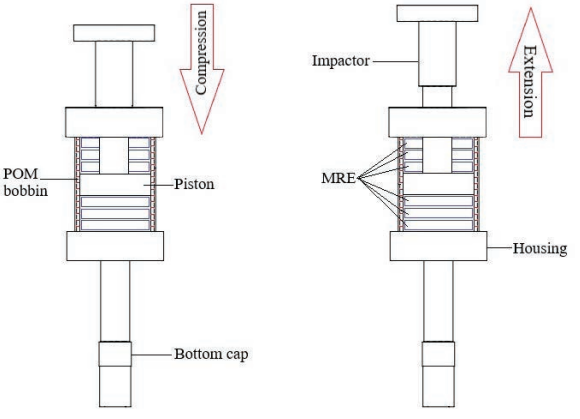


**Fig. 1.** *Design of dual-acting MRE damper*

The damper consists of six main components: the impactor, piston, housing, cap, POM bobbin, and the MRE itself, all made of mild steel, as shown in Fig. 2. This damper is designed to adapt to impacts in both upward and downward directions. To induce current flow to the MRE, a 0.7 mm copper coil is wrapped around the POM bobbin, which acts as an isolator unit between the MRE housing and the coil. This current flow strengthens the bonding between the ferrous particles and the rubber matrix in the MRE [15].

## 2 EXPERIMENTAL SETUP OF DUAL-ACTING MAGNETORHEOLOGICAL ELASTOMER DAMPER

This section outlines the experimental procedure for the fabrication of MRE samples and the subsequent testing using a drop impact machine to obtain force-

**Fig. 2.** *The prototype of a dual-acting MRE damper*

displacement characteristics. The fabrication process was conducted at the Automotive Laboratory of Universiti Pertahanan Nasional Malaysia (UPNM), with the mixing and curing processes carried out manually using an isotropic approach without the presence of a magnetic field [16]. Firstly, the materials needed in the fabrication process of MRE, namely 5 µm of carbonyl iron particles (CIP), room temperature vulcanization (RTV) silicone rubber, carbon black and hardening agent, were measured using a digital scale. The composition of each material was set according to the optimal composition proposed by [17] and shown in Table 1.

**Table 1.** *Share of MRE samples*

| Materials | Share of MRE samples [%] | Weight [g] |
|---|---|---|
| RTV silicone rubber | 30 | 9 |
| Carbonyl iron powder | 60 | 18.9 |
| Additive | 10 of CIP weight used | 1.89 |
| Hardener | 3 of the RTV weight used | 0.27 |

The materials mentioned above were mixed in a container and stirred until a homogeneous combination was obtained. The mixture was then poured into two different types of moulds, solid and ring moulds and left to cure for approximately 24 hours. Before pouring the mixture into the moulds, a releasing agent spray was applied to ease the removal of the samples from the mould [18]. Finally, the MRE samples were ready for the drop impact test. To prepare the specimen for the test, three solid MREs were stacked at the bottom of the damper, and another three ring MREs were placed along the piston. The overall specimen preparation process is illustrated in Fig. 3.

Upon completing the fabrication of MRE samples, the experimental test continues using the Instron Drop Impact Machine to conduct a drop impact test. The primary objective of this test is to assess the impact force of the MRE with the additive material added, which is expected to improve its impact absorption capabilities. To start the test, three

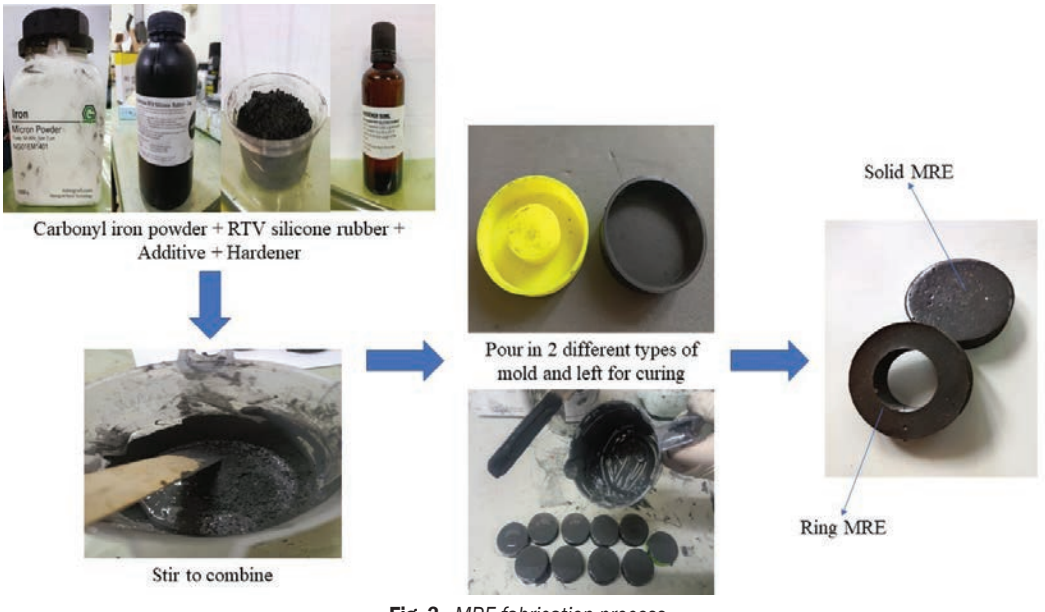


**Fig. 3.** *MRE fabrication process*

units of MRE are loaded into the dual-acting damper in parallel positions for both upper and lower sections. The impactor is then placed at the top of the damper, as shown in Fig. 4. The striker holder is released from a pre-determined position set according to the parameters in the CEAST software, as detailed in Table 2. The impact velocity is set to 2.24 m/s, which represents the impact energy for a light impact.

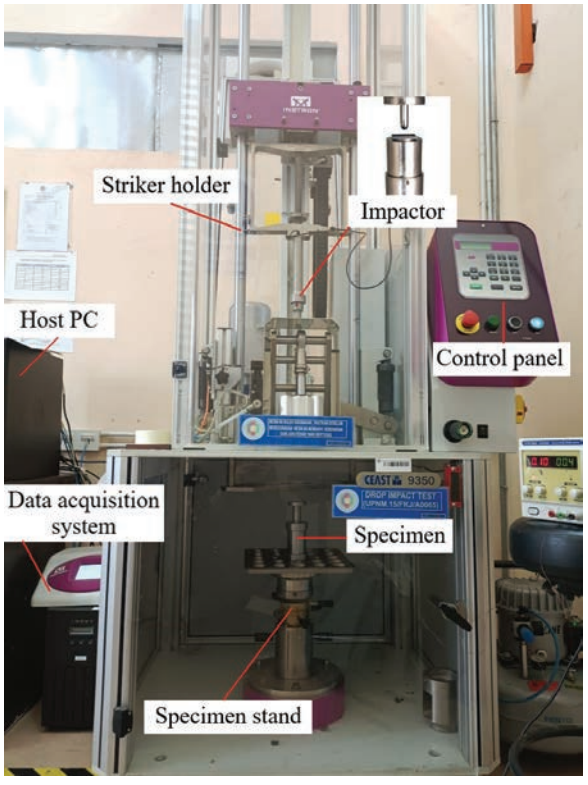


**Fig. 4.** *Experiment setup of MRE drop impact*

**Table 2.** *Experimental parameters set for impact test*

| Parameter | Unit | Value |
|---|---|---|
| Impact energy | [J] | 13.80 |
| Impact velocity | [m/s] | 2.24 |
| Falling height | [mm] | 256.00 |
| Impact point offset | [mm] | 36.00 |
| Tup holder mass | [kg] | 4.30 |
| Tup nominal mass | [kg] | 1.20 |
| Total mass | [kg] | 5.50 |
| Current | [A] | 0 to 2 |

The hydraulic system of the impact machine is equipped with an accelerometer sensor and load cell to record the actual acceleration and impact force during testing. The recorded behaviours of the damper during impact loading by the sensors are then sent to the data acquisition system (DAQ). The impact absorption is analysed by observing the force-displacement characteristics, which will be used as the benchmark for MRE modelling in the next section.

## 3 MODELLING AND OPTIMIZATION OF MAGNETORHEOLOGICAL ELASTOMER UNDER IMPACT LOADING BASED ON POLYNOMIAL MODEL

A non-parametric polynomial model was developed to analyse the dynamic behaviour of the MRE element under impact loading due to varying currents ranging from 0 A to 2 A. Fig. 5 illustrates the typical F-d characteristic of MRE. The blue line indicates the compression state of the MRE, where the force is exerted increasingly until maximum with increasing displacement during impact. Meanwhile, the red line indicates the extension state of the MRE, where the force decreases as the displacement of the MRE decreases to the original state.

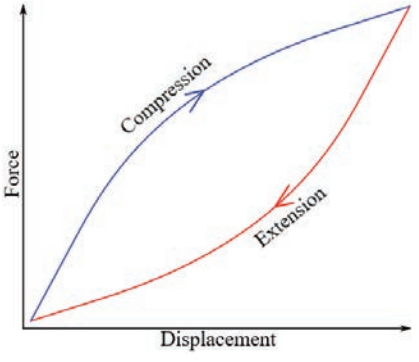


**Fig. 5.** *Force-displacement characteristic*

The polynomial function can be generated by considering a fourth-order polynomial function. In this function, $y_1$ represents the function of the ascending line known as compression force. Meanwhile, $y_2$ represents the function of the descending line known as the extension force, as illustrated in Fig. 5. The functions of both compression and extension stages are shown in Eqs. (1) and (2):

$$y_1 = a_{y1-1}x^4 + a_{y1-2}x^3 + a_{y1-3}x^2 + a_{y1-4}x + a_{y1-5}, \quad (1)$$

$$y_2 = a_{y2-1}x^4 + a_{y2-2}x^3 + a_{y2-3}x^2 + a_{y1-2}x + a_{2-5}. \quad (2)$$

Here, $a_{yij}$ is a real number, and $x$ is the displacement in meters obtained from the experimental data. The values of the constants depend on the curve of the line and can be tuned to obtain better force-displacement characteristics. In this study, the modelling of a non-parametric polynomial model requires the displacement, velocity, impact energy, and current to produce the output force, as explained

in Fig. 6. The unknown values $a_{yij}$ represent the magnitude, following the trend, and connection factor, respectively. The optimized values for the model parameters $a_{yij}$ are required to produce an ideal shape of the hysteresis loops for the yielding element [19].

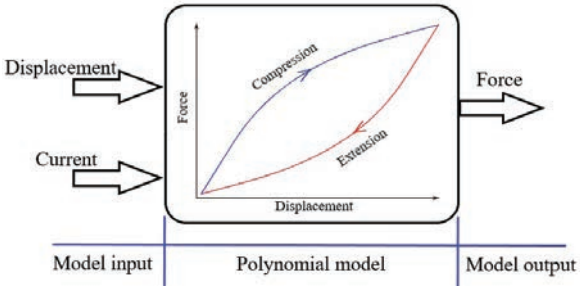


**Fig. 6.** *MRE non-parametric polynomial model*

### 3.1 Optimization of MRE Model with Gravitational Search Algorithm

To obtain the optimized parameters, a gravitational search algorithm (GSA) was implemented in the simulation model as it can identify the parameters that minimize a specific goal or fitness function. The flow chart for the model identification procedure based on GSA is presented in Fig. 7.

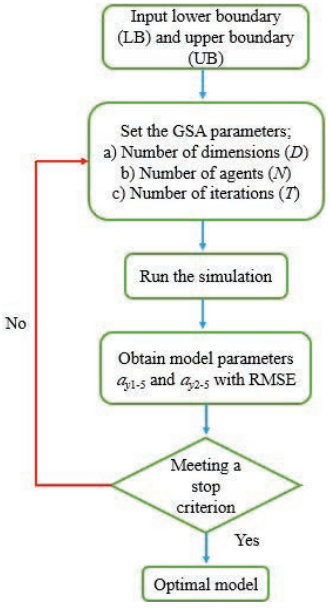


**Fig. 7.** *Model identification procedure based on GSA*

In GSA coding; the system incorporates a set of agents called masses, gravitational law, and Newton's law of motion to achieve the optimal result with a flexible implementation concept. GSA employs a similar approach to PSO, whereby data optimization is achieved through the exploration and exploitation abilities of the agents in the search space [20]. The agents in GSA are analogous to particles in the universe, and their locations can be represented using Eq. (3). The entire system of $N$ agents can be expressed as shown in Eq. (4).

$$X_i = (x_i^1, x_i^2, \ldots, x_i^d, \ldots, x_i^n), \quad (3)$$

$$X = (X_1, X_2, \ldots, X_i, \ldots, X_N). \quad (4)$$

In the preceding equations, $x_i^d$ represents the location of agent $i$ in dimension $d$, $n$ represents the dimension of the search space and $N$ represents the number of individuals (or agents). Eq. (5) is used to calculate the applied force on agent $i$ by agent $j$ at a given time $t$. $M_{aj}$ denotes agent $j$'s active gravitational mass, $M_{pi}$ denotes agent $i$'s passive gravitational mass, $G(t)$ denotes the gravitational constant at time $t$, $\varepsilon$ is a small constant, and $R_{ij}$ denotes the Euclidian distance between the two agents.

$$F_{ij}^d(t) = G(t)\frac{M_{aj}(t) + M_{pi}(t)}{R_{ij}(t) + \varepsilon}(x_j^d(t) - x_i^d(t)). \quad (5)$$

Gravitational fixed $G$ is a time-dependent function that begins with the initial value $G_0$ and decreases over time to control the search accuracy. Eqs. (6) and (7) are used to calculate the value of this function.

$$G(t) = G(G_0, t), \quad (6)$$

$$G(t) = G_0 e^{\frac{-\alpha t}{T}}, \quad (7)$$

where $\alpha$ and $G_0$ are constants and $T$ indicates all iterations. Eqs. (8) to (10) are used to update inertia and gravitational masses in Eq (5).

$$(M_{ai} = M_{pi} = M_{ii} = M_i), \quad i = 1, 2, ..., N, \quad (8)$$

$$m_i(t) = \frac{fit_i(t) - worst(t)}{best(t) - worst(t)}, \quad (9)$$

$$M_i(t) = \frac{m_i(t)}{\sum_{j=1}^{N} m_j(t)}, \quad (10)$$

where $fit_i(t)$ shows the fitness value of agent $i$ at time $t$, and $worst(t)$ and $best(t)$ are calculated using Eq. (11) and (12).

$$best(t) = min_{j\in\{1,2,\ldots,N\}} fit_j(t), \quad (11)$$

$$worst(t) = max_{j\in\{1,2,\ldots,N\}}(t). \quad (12)$$

Here, $best(t)$ is the smallest fitness value among all agents, while $worst(t)$ is the biggest fitness value among all agents. These two important values are used in a minimisation problem where the fitness value,

$fit_j(t)$, influences the mass value of $i^{th}$ agents, which correlates to the particle's position in a search space. The method then examines each agent's fitness, $fit\ (t)$ in relation to the goal function.

### 3.2 Simulation Results of Optimized MRE Model

This study utilizes the GSA method to determine the optimal values for $a_{yi\text{-}j}$ in both the extension and compression stages of a 4th-order polynomial model to create the hysteresis loop. The objective is to optimize the polynomial parameters by comparing the simulation results with experimental responses and adjusting the performance index accordingly. Table 3 displays the initial simulation parameters. The model configuration parameters were set in Matlab-Simulink with a fixed-step size of 0.01 and discrete time (no continuous states). The model was run for 36 s.

**Table 3.** *Initial simulation parameters for GSA*

| Parameters | | Values |
|---|---|---|
| Number of dimensions, $D$ | | 5 |
| Number of agents, $N$ | | 50 |
| Number of iterations, $T$ | | 60 |
| Range of dimension | Compression case: | $-1100 \le a_{y1-1} \le 4000$ |
| | | $-9000 \le a_{y1-2} \le 20000$ |
| | | $-25000 \le a_{y1-3} \le 3000$ |
| | | $4000 \le a_{y1-4} \le 20000$ |
| | | $-300 \le a_{y1-5} \le 400$ |
| | Extension case: | $-9000 \le a_{y2-1} \le 33000$ |
| | | $-62000 \le a_{y2-2} \le 21000$ |
| | | $-8000 \le a_{y2-3} \le 35000$ |
| | | $500 \le a_{y2-4} \le 800$ |
| | | $-70 \le a_{y2-5} \le 3$ |

During the initialization step, the algorithm generates a random number and assigns it to a variable. Next, a random number of agents, $N$, is assigned to each entity in the population. The simulation evaluates the fitness function for each entity and performs random value selection processes [21]. Each agent's fitness is then evaluated for the next iteration, and the constraints are checked. This process is iterated over multiple generations to achieve the best results. Finally, the optimized polynomial model parameters for MRE are tabulated in Table 4.

The optimized parameter values for the simulation model are determined by fitting the model to the experimental data obtained from the drop impact test. The responses of MRE in terms of force-displacement characteristics are observed for both simulation and experiment, from 0 A to 2 A of input currents with 0.5 A increments. As shown in Fig. 8, each impact energy produced by the model can be used to track the energy recorded in the experimental test by forming hysteresis loops for each applied current. To evaluate the accuracy of this model, the differences between the experimental and simulation are examined based on the highest error. The highest errors are marked in the red region in Fig. 8 for all cases. The percentage errors are then calculated based on the difference in force produced as tabulated in Table 5. From the overall results, the percentage error obtained is less than 13 % where within the acceptable range of error [22].

**Table 4.** *Optimized model parameter for each input current*

| Input current [A] | Model parameter | | | |
|---|---|---|---|---|
| | Compression | | Extension | |
| 0 A | $a_{y1-1}$ | –1201.40 | $a_{y2-1}$ | –2198.30 |
| | $a_{y1-2}$ | 4792.40 | $a_{y2-2}$ | 5862.70 |
| | $a_{y1-3}$ | –8317.70 | $a_{y2-3}$ | –1052.60 |
| | $a_{y1-4}$ | 8945.10 | $a_{y2-4}$ | 465.53 |
| | $a_{y1-5}$ | –236.86 | $a_{y2-5}$ | 2.19 |
| 0.5 A | $a_{y1-1}$ | –10630.00 | $a_{y2-1}$ | –8708.80 |
| | $a_{y1-2}$ | 15621.00 | $a_{y2-2}$ | 20027.00 |
| | $a_{y1-3}$ | –3332.90 | $a_{y2-3}$ | –7723.00 |
| | $a_{y1-4}$ | 3968.60 | $a_{y2-4}$ | 1209.50 |
| | $a_{y1-5}$ | 93.28 | $a_{y2-5}$ | –19.39 |
| 1 A | $a_{y1-1}$ | 3422.00 | $a_{y2-1}$ | –2193.60 |
| | $a_{y1-2}$ | –8986.60 | $a_{y2-2}$ | 8677.00 |
| | $a_{y1-3}$ | 2936.20 | $a_{y2-3}$ | –7363.90 |
| | $a_{y1-4}$ | 9330.20 | $a_{y2-4}$ | 7180.70 |
| | $a_{y1-5}$ | 336.52 | $a_{y2-5}$ | –22.37 |
| 1.5 A | $a_{y1-1}$ | –7302.70 | $a_{y2-1}$ | –1962.30 |
| | $a_{y1-2}$ | 8103.30 | $a_{y2-2}$ | 7596.90 |
| | $a_{y1-3}$ | –1859.90 | $a_{y2-3}$ | –2696.10 |
| | $a_{y1-4}$ | 8441.90 | $a_{y2-4}$ | 4795.50 |
| | $a_{y1-5}$ | 37.99 | $a_{y2-5}$ | –65.56 |
| 2 A | $a_{y1-1}$ | –6619.60 | $a_{y2-1}$ | 32293.00 |
| | $a_{y1-2}$ | 19772.00 | $a_{y2-2}$ | –61171.00 |
| | $a_{y1-3}$ | –24021.00 | $a_{y2-3}$ | 35010.00 |
| | $a_{y1-4}$ | 19016.00 | $a_{y2-4}$ | 3166.00 |
| | $a_{y1-5}$ | –105.53 | $a_{y2-5}$ | –58.19 |

**Table 5.** *Force prediction error for input current*

| Current [A] | Experimental data | Simulation data | Percentage error [%] |
|---|---|---|---|
| 0 | 2079.22 | 1821.72 | 12.38 |
| 0.5 | 5458.78 | 5810.15 | 6.44 |
| 1.0 | 6603.41 | 6097.63 | 7.66 |
| 1.5 | 7231.52 | 6501.59 | 10.09 |
| 2 | 6421.51 | 6035.60 | 6.01 |

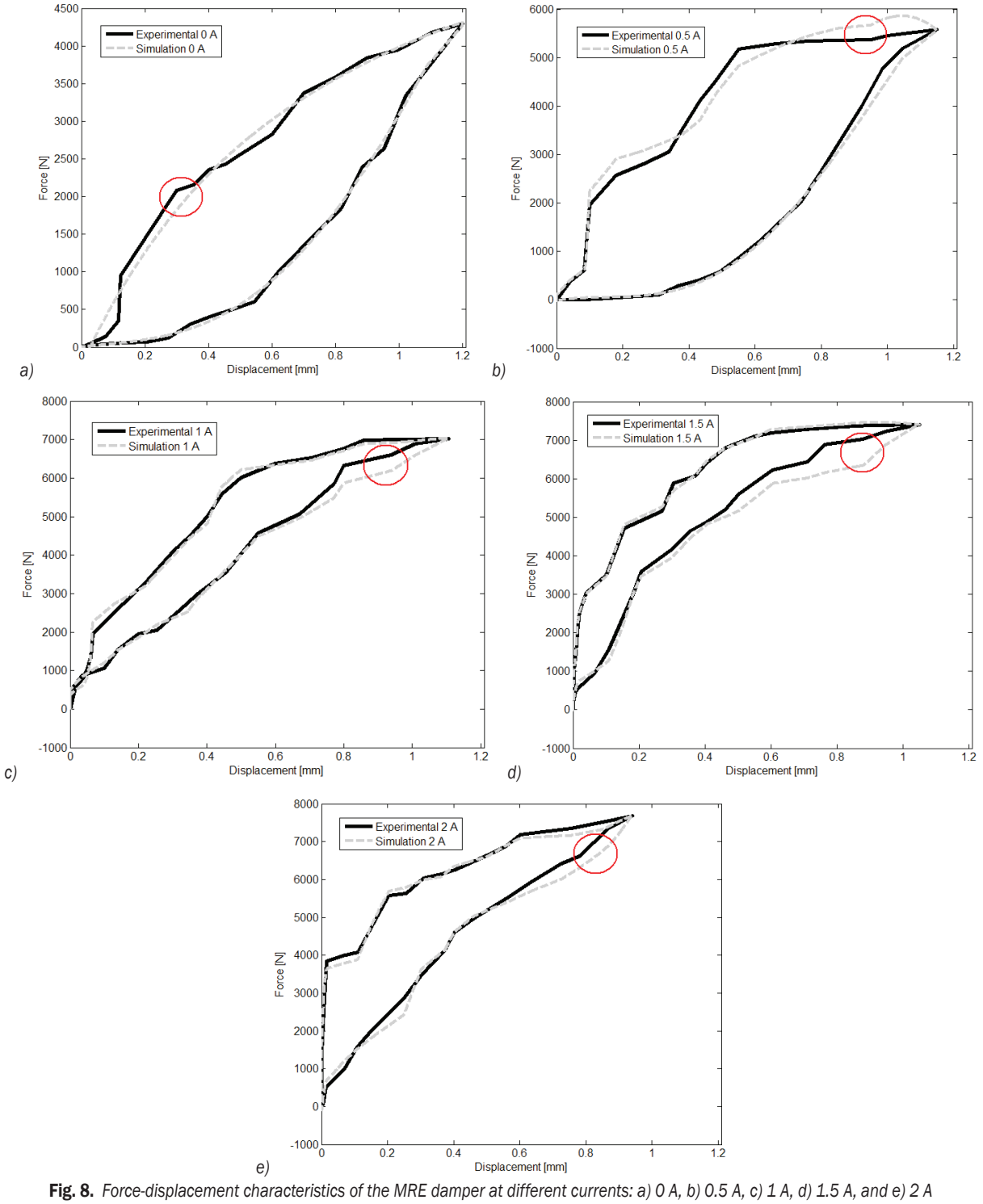


**Fig. 8.** *Force-displacement characteristics of the MRE damper at different currents: a) 0 A, b) 0.5 A, c) 1 A, d) 1.5 A, and e) 2 A*

Fig. 9 shows the superimposed force-displacement model responses for all currents. The trend indicates that the MRE force increases proportionally with the input current while the MRE displacement decreases proportionally with the input current. These simulation results demonstrate that the MRE model can provide variable stiffness for an active impact device. The hysteresis loop results also show a consistent increment of impact force, with a maximum value of 7600 N for both 1.5 A and 2 A.

The insignificant difference in impact force for 2 A compared to 1.5 A might be due to the limitations of the MRE design in terms of its stroke, resulting in an almost similar magnitude of impact force. However, the reduced displacement characteristic of 2 A compared to 1.5 A is still within the acceptable range of impact force that can be used as an active impact device.

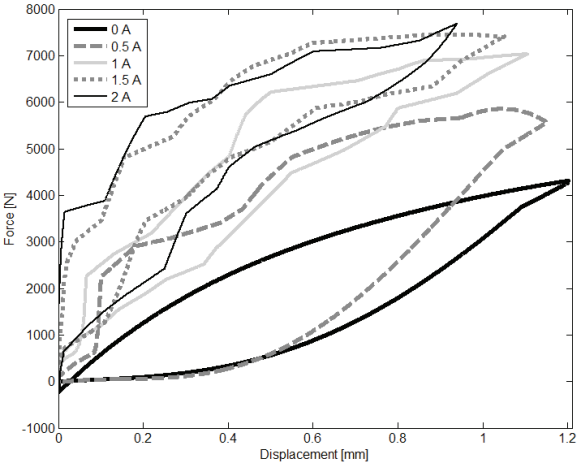


**Fig. 9.** *Comparison of force-displacement curve for simulation at varying current*

## 4 INTERPOLATION MODEL FOR MEDIAN FORCES OF MRE DAMPER

The next contribution of this study is proposing a method for predicting median forces based on median applied currents using an interpolation approach. Interpolation is a curve-fitting method that uses linear polynomials to create new data points within a given range. For instance, if the range of the current set is from 0.5 A to 1 A, with known forces of $f_{0.5}$ and $f_1$ obtained in the previous section, the interpolation approach can predict the force produced by the MRE for a median current of 0.7 A. The predicted force for $f_{0.7}$ can be calculated using the following equation:

$$\frac{C_{0.7}-C_{0.5}}{C_1-C_{0.5}}=\frac{f_{0.7}-f_{0.5}}{f_1-f_{0.5}}. \qquad \text{X}$$

By inserting the values of $C_{0.5}$ and $C_1$ as well as data for both $f_{0.5}$ and $f_1$, the final equation to predict the hysteresis loop for $f_{0.7}$ is written as follows:

$$f_{0.7}=\frac{(0.7-0.5)(f_1-f_{0.5})+f_{0.5}}{(1-0.5)}. \qquad \text{X}$$

The interpolation model for MRE was executed in the Matlab-Simulink environment using input currents of 0.3 A, 0.7 A, 1.3 A, and 1.7 A, as shown in Fig. 10. The output force of the subsystems for each current was combined to generate a force-displacement curve for the developed interpolation model.

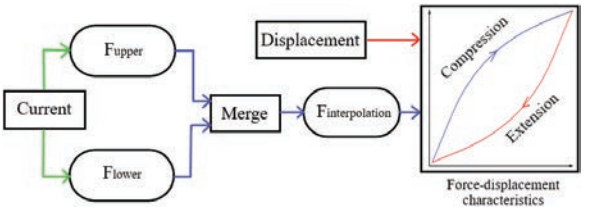


**Fig. 10.** *The structure of the interpolation current prediction model*

### 4.1 Validation of the Dual-Acting MRE Behaviours for The Middle Current

The behaviours of a dual-acting magnetorheological (MRE) damper for middle currents have been tested by comparing simulation results obtained from Matlab with experimental results obtained from a drop impact machine. To begin, drop impact tests were carried out on the MRE damper by applying a set of input currents of 0.3 A, 0.7 A, 1.3 A, and 1.7 A. The force-displacement characteristic responses obtained in simulation for each input current were then compared with the experimental data for validation purposes. Based on the results shown in Fig. 11, the model's behaviours showed an increase in force with increasing input current despite a decrease in displacement. The trend of the input current at 0.3 A and 0.7 A demonstrated the hysteresis behaviour of the MRE, which experienced compression and tension when an external force was applied. Similarly, for input currents of 1.3 A and 1.7 A, the model managed to follow the trend for the compression part, but the tension part for both currents diverged, and the trends were not as well-defined as those for the 0.3 A and 0.7 A currents.

**Table 6.** *Force prediction error for the interpolation current*

| Current [A] | Experimental data | Simulation data | Percentage error [%] |
|---|---|---|---|
| 0.3 | 5025.37 | 5187.61 | 3.23 |
| 0.7 | 6376.98 | 6253.14 | 1.94 |
| 1.3 | 6884.49 | 6270.71 | 8.92 |
| 1.7 | 7423.21 | 6240.26 | 15.94 |

To check the similarity between the developed model and the experimental results of the MRE, the percentage error is evaluated by undergoing a similar procedure as the input currents of 0 A to 2 A. The

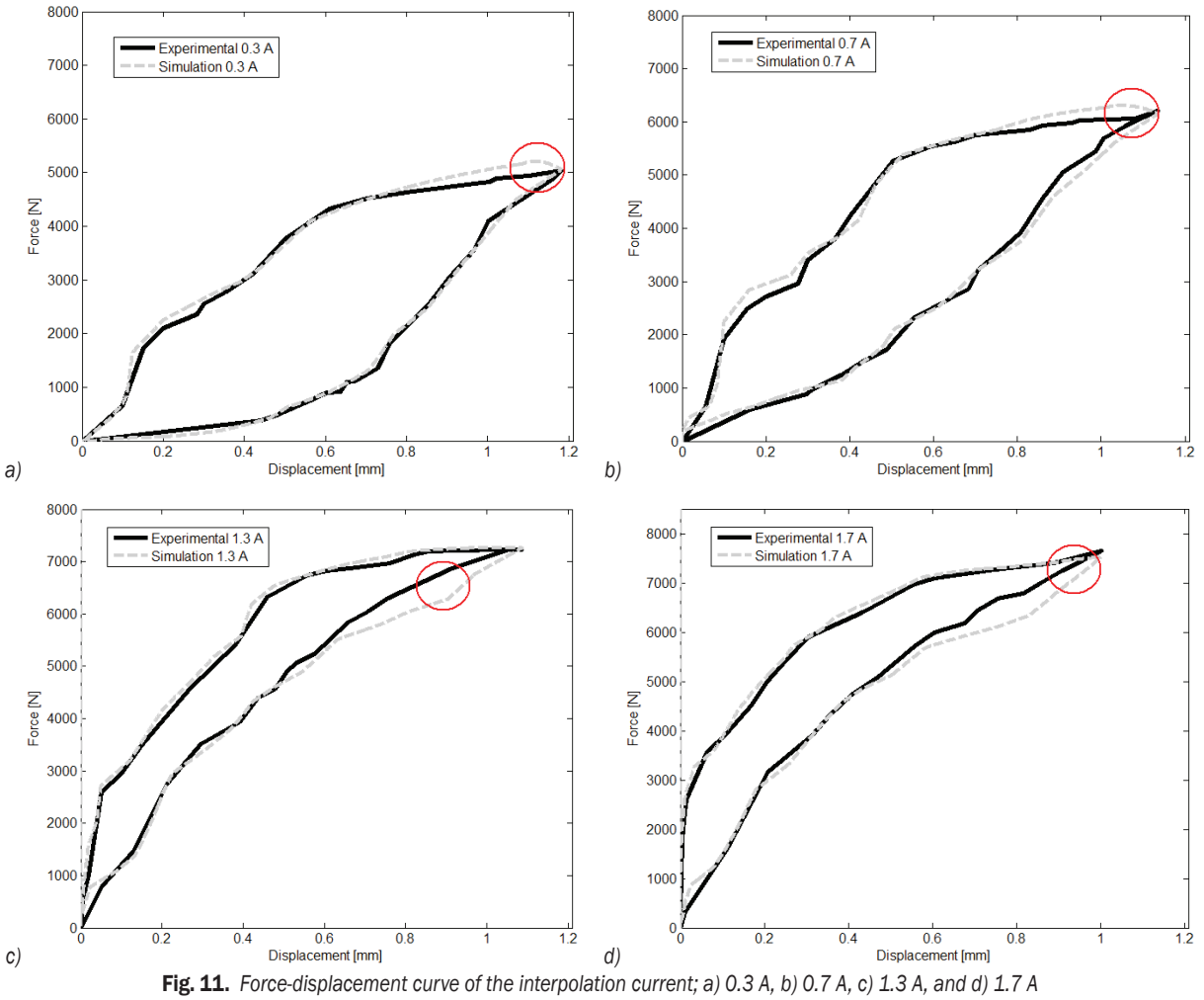


**Fig. 11.** *Force-displacement curve of the interpolation current; a) 0.3 A, b) 0.7 A, c) 1.3 A, and d) 1.7 A*

difference between the simulation and experimental forces are marked as presented in Fig. 11, and their values are tabulated in Table 6. From the percentage of error, it can be seen that the error is less than 20 %, which is within an acceptable range of error [22].

### 4.2 Verification of the MRE Middle Current with Upper and Lower Responses

To check the acceptable range of interpolation models, the force-displacement characteristics were compared with upper and lower currents for each case. For instance, the interpolation model with a 0.3 A current it is compared with 0 A and 0.5 A. Based on the comparison results, it can be observed that the force for the compression stage is within the range of forces produced for 0 A to 0.5 A, which indicates that it falls within an acceptable range. Similarly, for the extension stage, the force produces a similar range between 0 A to 0.5 A currents, which is also within the acceptable range. Fig. 12 illustrates all the interpolation models for 0.7 A, 1.3 A, and 1.7 A currents, and the model successfully generates the in-between currents and validates the proposed interpolation model.

### 4.3 Effects of Varying GSA Size and the Number of Iterations

The number of iterations plays a crucial role in GSA, as it sets the duration for which particles can search for the optimal solution. Generally, increasing the number of iterations can enhance the algorithm's capacity to discover the global optimum, as it provides the agents with more time to explore the search space and converge on the best solution. Nevertheless, after a certain point, additional iterations may not contribute to any further enhancement in the solution, as the agents may have already converged to a local

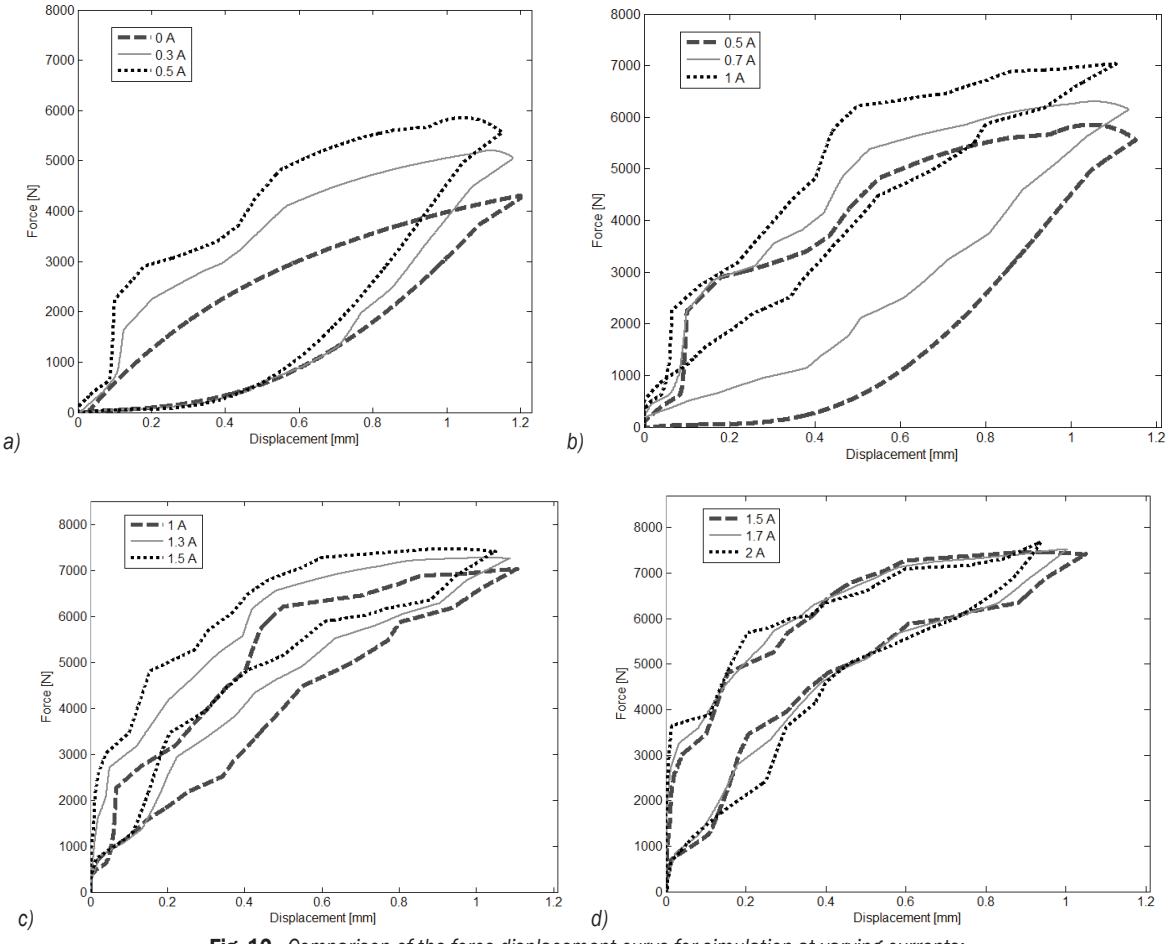


**Fig. 12.** *Comparison of the force-displacement curve for simulation at varying currents; a) 0 A to 0.5 A, b) 0.5 A to 1 A, c) 1 A to 1.5 A, and d) 1.5 A to 2 A*

optimum. Conversely, decreasing the number of iterations can lead to faster execution times but at the risk of potentially missing out on better solutions. Thus, it is vital to strike a balance between the number of iterations and the desired level of performance index and execution time. Based on Fig. 13, 100 iterations were chosen as they have a quick convergence rate and can achieve a superior performance index.

Enlarging the agent size can enhance the exploration of the solution space on a global level since a greater number of agents are involved in the search. Nonetheless, it may escalate the computational expenses and impede the convergence rate because of an increased need for communication and updates among the agents. Based on the results depicted in Fig. 14, this study opted for a size of 100, which exhibited a swift convergence rate.

In order to check the validity of the proposed model, the simulation results for currents 0 A, 1 A and 2 A are compared with the Multi-Layers Exponential based Preisach Model, the MRE modelling carried out by **[23]** as presented in Fig. 15.

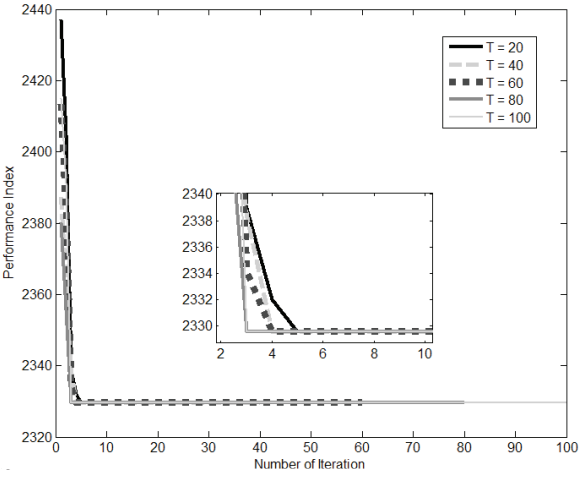


**Fig. 13.** *Effect of varying the number of iterations on the performance of GSA*

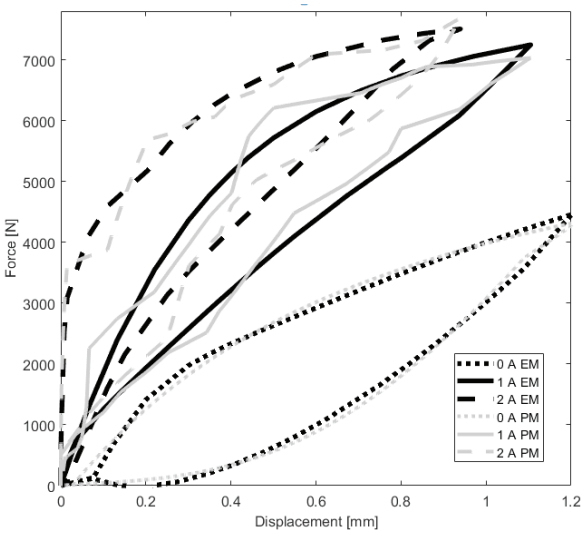


**Fig. 14.** *Effect of varying the number of particles on the performance of GSA*

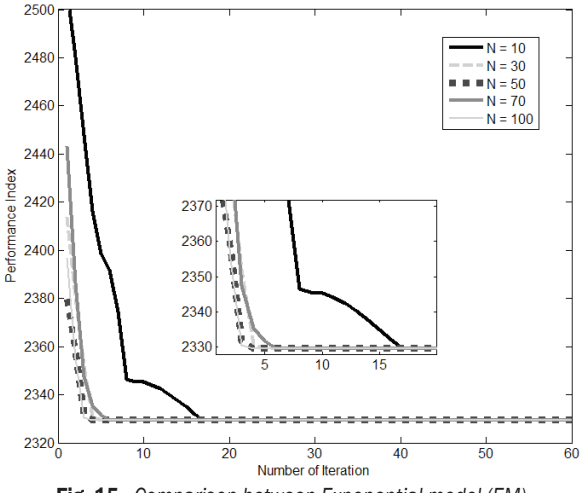


**Fig. 15.** *Comparison between Exponential model (EM) and Polynomial model (PM)*

## 5 CONCLUSIONS

This paper presents a comprehensive study on the hysteresis behaviour modelling of magnetorheological elastomers under impact loadings. The study introduces a 4th-order polynomial model that is optimized with the gravitational search algorithm, resulting in a reliable and accurate framework that can capture the complex hysteresis behaviour of the material. The developed model is shown to perform exceptionally well in capturing the dynamic response of magnetorheological elastomers under various impact-loading scenarios. The model's response closely matches the experimental data, with a maximum prediction error of less than 13 %. Additionally, the interpolated model's response agrees well with the experimental data, with a maximum percentage error of less than 15.94 %. The study also investigates the impact of changing the number of iterations and the number of agents on the performance of the gravitational search algorithm. Overall, the results suggest that the proposed model is a promising approach for accurately predicting the hysteresis behaviour of magnetorheological elastomers under impact loads. For future study of this research, the developed MRE model will be used as an actuator for the active bumper system to absorb impact force during frontal collision. It is expected that the MRE actuator can reduce the impact force and thus reduce vehicle acceleration and jerks.

## 6 ACKNOWLEDGEMENTS

The research has been carried out under the Fundamental Research Grant Scheme project FRGS/1/2021/TK02/UPNM/02/1 provided by the Ministry of Education of Malaysia.

## 7 REFERENCES

[1] Fu, J., Liu, J., Lai, J., Zhong, C., Dai, Z., Yu, M. (2023). Robustness analysis of magnetorheological elastomer-based vibration isolation system with optimal fuzzy controller. *Smart Materials and Structures*, vol. 32, no. 3, **DOI:10.1088/1361-665X/acb577**.

[2] Ahamed, R., Rashid, M.M., Ferdaus, M. M., Yusof, H.M. (2016). Advancement in energy harvesting magneto-rheological fluid damper. *Korea Australia Rheology Journal*, vol. 28, p. 67-74, **DOI:10.1007/s13367-016-0007-6**.

[3] Masa'id, A., Lenggana, B.W., Ubaidillah, U., Susilo, D.D., Choi, S.-B. (2023). A review on vibration control strategies using magnetorheological materials actuators: Application perspective. *Actuators*, vol. 12, no. 3, art.ID. 113, **DOI:10.3390/act12030113**.

[4] Yu, Y., Li, J., Li, Y., Li, S., Li, H., Wang, W. (2019). Comparative investigation of phenomenological modeling for hysteresis responses of magnetorheological elastomer devices. *International Journal of Molecular Sciences*, vol. 20, no. 13, art. ID 3216, **DOI:10.3390/ijms20133216**.

[5] Choi, Y.T., Wereley, N.M. (2022). Adaptively tunable magnetorheological elastomer-based vibration absorber for a propeller aircraft seat. *AIP Advances*, vol. 12, no. 3, art. ID 035332, **DOI:10.1063/9.0000323**.

[6] Zhao, L., Yu, M., Fu, J., Zhu, M., Li, B (2017). A miniature MRE isolator for lateral vibration suppression of bridge monitoring equipment: design and verification. *Smart Materials and Structures*, vol. 26, no. 4, art. ID 047001, **DOI:10.1088/1361-665X/aa5d97**.

[7] Gu, X., Li, J., Li, Y., Askari, M. (2015). Frequency control of smart base isolation system employing a novel adaptive magneto-rheological elastomer base isolator. *Journal of*

*Intelligent Material Systems and Structures*, vol. 27, no. 7, p. 849-858, **DOI:10.1177/1045389X15595291**.

**[8]** Rahmat, M.S., Hudha, K., Kadir, Z.A., Amer, N.H., Nor, N.M., Choi, S.B. (2021). A hybrid skyhook active force control for impact mitigation using magneto-rheological elastomer isolator. *Smart Materials and Structures*, vol. 30, no. 2, art. ID 25043, **DOI:10.1088/1361-665X/abd911**.

**[9]** Yang, J., Sun, S., Tian, T.F., Li, W., Du, H., Alici, G., Nakano, M. (2016). Development of a novel multi-layer MRE isolator for suppression of building vibrations under seismic events. *Mechanical Systems and Signal Processing*, vol. 70-71, p. 811-820, **DOI:10.1016/j.ymssp.2015.08.022**.

**[10]** Norouzi, M., Sajjadi Alehashem, S.M., Vatandoost, H., Ni, Y.Q., Shahmardan, M.M. (2016). A new approach for modeling of magnetorheological elastomers. *Journal of Intelligent Material Systems and Structures*, vol. 27, no. 8, p. 1121-1135, **DOI:10.1177/1045389X15615966**.

**[11]** Yu, Y., Hoshyar, A.N., Li, H., Zhang, G., Wang, W. (2021). Nonlinear characterization of magnetorheological elastomer-based smart device for structural seismic mitigation. *International Journal of Smart and Nano Materials*, vol. 12, no. 4, p. 390-428, **DOI:10.1080/19475411.2021.1981477**.

**[12]** Yu, Yang, Yousefi, A.M., Yi, K., Li, J., Wang, W., Zhou, X. (2021). A new hybrid model for MR elastomer device and parameter identification based on improved FOA. *Smart Structures and Systems*, vol. 28, no. 5, p. 617-629, **DOI:10.12989/sss.2021.28.5.617**.

**[13]** Rossi, A., Orsini, F., Scorza, A., Botta, F., Belfiore, N.P., Sciuto, S.A. (2018). A review on parametric dynamic models of magnetorheological dampers and their characterization methods. *Actuators*, vol. 7, no. 2, art. ID 16, **DOI:10.3390/act7020016**.

**[14]** Kwon, S.H., Lee, J.H., Choi, H.J. (2018). Magnetic particle filled elastomeric hybrid composites and their magnetorheological response. *Materials*, vol. 11, no. 6, art. ID 1040, **DOI:10.3390/ma11061040**.

**[15]** Alias, N.F., Muthalif, A.G.A., Arpan, K.A.M., Nordin, N.H.D. (2018). Experimental investigation of static properties of magnetorheological elastomer. *Iranian Journal of Science and Technology - Transactions of Mechanical Engineering*, vol. 42, p. 185-197, **DOI:10.1007/s40997-017-0081-5**.

**[16]** Kang, S.S., Choi, K., Nam, J.-D., Choi, H.J. (2020). Magnetorheological elastomers: Fabrication, characteristics, and applications. *Materials*, vol. 13, no. 20, art. ID 4597, **DOI:10.3390/ma13204597**.

**[17]** Sobri, N.S., Lin, P.G., Haniffah, N.A., Kadir, Z.A., Hudha, K., Rahmat, M.S. (2021). Impact testing of magnetorheological elastomer based matrix material and magnetic particle. *IEEE 9th Conference on System, Process and Control*, p. 70-74, **DOI:10.1109/ICSPC53359.2021.9689137**.

**[18]** Brancati, R., Di Massa, G., Di Vaio, M., Pagano, S., Santini, S. (2019). Experimental investigation on magneto-rheological elastomers. *Mechanisms and Machine Science*. Springer, Cham, vol. 68, p. 441-448, **DOI:10.1007/978-3-030-03320-0_48**.

**[19]** Siddique, N., Adeli, H. (2016). Gravitational search algorithm and its variants. *International Journal of Pattern Recognition and Artificial Intelligence*, vol. 30, no. 8, art. ID 1639001, **DOI:10.1142/S0218001416390018**.

**[20]** Rashedi, E., Rashedi, E., Nezamabadi-pour, H. (2018). A comprehensive survey on gravitational search algorithm. *Swarm and Evolutionary Computation*, vol. 41, p. 141-158. **DOI:10.1016/j.swevo.2018.02.018**.

**[21]** Wang, Y., Gao, S., Zhou, M., Yu, Y. (2020). A multi-layered gravitational search algorithm for function optimization and real-world problems. *IEEE/CAA Journal of Automatica Sinica*, vol. 8, no. 1, p. 94-109, **DOI:10.1109/JAS.2020.1003462**.

**[22]** Subari, M.A., Hudha, K., Kadir, Z.A., DArdin, S.M.F.S.M., Amer, H.H. (2022). Path following control of tracked vehicle using modified sup controller optimized with particle swarm optimization (PSO). *International Journal of Dynamics and Control*, vol. 10, p. 1461-1470, **DOI:10.1007/s40435-021-00900-6**.

**[23]** Mohd. Alawi, A.H., Hudha, K., Kadir, Z.A., Amer, N.H. (2023). Hysteresis behavior modeling of magnetorheological elastomers under impact loading using a multilayer exponential-based preisach model enhanced with particle swarm optimization. *Polymers*, vol. 15, no. 9, art. ID 2145, **DOI:10.3390/polym15092145**.

Strojniški vestnik - Journal of Mechanical Engineering 69(2023)11-12, 483-496
DOI:10.5545/sv-jme.2023.627
Original Scientific Paper
Received for review: 2023-05-02
Received revised form: 2023-07-24
Accepted for publication: 2023-09-13


# Optimization Method of Multi-parameter Coupling for a Hydraulic Rolling Reshaper Based on Factorial Design

Hongfei Li – Min Luo – Tingting Xu – Qiaozhen Li – Yanming Hou
Northeast Petroleum University, School of Mechanical Science and Engineering, China

*A hydraulic rolling reshaper is an advanced shaping technology with superior protection for casings, and the structural parameters of the reshaper affect its shaping effect on deformed casing directly. To improve the shaping capacity of the reshaper, a multi-parameter coupling optimization method of hydraulic rolling reshaper is proposed to optimize the design of the factors with significant influence under the premise of screening multi-structural parameters. In this paper, according to the working principle of the reshaper, considering the contact nonlinearity between the hydraulic rolling reshaper and deformed casing, as well as the material nonlinearity of the casing, a parametric finite element model of the hydraulic rolling reshaper repairing the shrinkage deformation of casings was developed. The remarkable factors were screened by factorial design, the sample points were generated by optimal Latin hyper-cube design (OLHD), and the response surface models were established by stepwise regression. Therefore, with the maximum plastic deformation of casings as the objective function, the maximum equivalent stress, residual stress, and the plastic deformation of casings as the constrained conditions, an optimized mathematical model for a reshaper was constructed, and the genetic algorithm (GA) is performed to obtain the optimal combination of parameters. The results showed that the optimal reshaper made the shaping process safe and effective, the plastic deformation of casings after single shaping was increased by 11.38 %, and the shaping effect was better (96.48 %), which can effectively improve the safety performance and shaping ability of the reshaper.*

**Keywords: hydraulic rolling reshaper, structural optimization, factorial design, orthogonal test**

**Highlights**

- *Optimization of a hydraulic rolling reshaper used to repair deformed casings in oilfields has been performed by numerical simulation.*
- *Considering both the material and contact nonlinearities, a parametric finite element model of a hydraulic rolling reshaper repairing shrinkage deformation of casings was developed.*
- *An orthogonal test was performed to analyse the multi-geometric parameters and find five significant parameters of the reshaper on the shaping effect.*
- *Nonlinear interactive regression models of response variables were established using stepwise regression based on the sampling and calculation of OLHD.*

## 0 INTRODUCTION

In recent years, with the development of downhole casing shaping technology, higher requirements have been put forward for the safety and efficiency of the shaping tools. As one of the advanced shaping tools to repair deformed casings, the hydraulic rolling reshaper has been widely used because of its advantages in protecting the damaged casing, fewer multiple trips to the well, and low construction cost. Fig. 1 shows the working principle of the hydraulic rolling reshaper when repairing horizontal wells. According to its working principle, the work section directly contacts the inner wall of the deformed casing to transmit the repairing load provided by the ground devices, and its structural dimensions directly impact the shaping effect of the casing.

For the structural optimization of shaping tools, the current research focuses on traditional shaping tools, such as the pear-shaped tube expander and the eccentric tube expander. Jiang [1] discussed the influence of the angle of the shaping tool on the shaping effect by establishing the mechanical and finite element model of the deformed casing of the pear-shaped tube expander, and the reasonable taper angle of the expander is 30° to 40°. Chen et al. [2] used an ANSYS / LS-DYNA explicit structural dynamic analysis module to calculate the stress of different cone angles under different diameters and

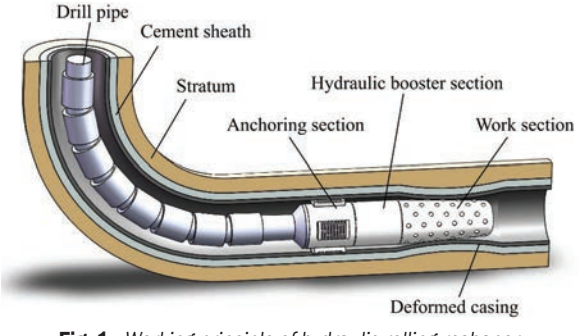


**Fig. 1.** *Working principle of hydraulic rolling reshaper*

*Corr. Author's Address: Northeast Petroleum University, Xuefu Road 99#, Daqing, China, 1538937270@qq.com

determined the reasonable cone angle of the eccentric expander under different diameters. Bai [3] used the numerical simulation method to conduct finite element analysis on the shaping process of four types (spherical, curved, stepped and conical), and obtained the conclusion that the shaping effect of a conical shaping cone is the best and the best cone angle is 15° to 20°. In addition, most of the studies on hydraulic rolling reshapers are focused on analysing its shaping process and shaping law by using numerical simulation combined with laboratory tests. Lin et al. [4] obtained the relationship between load and torque required for shaping casing based on the established mechanical model of repairing elliptic deformation casing combined with laboratory tests. Deng et al. [5] established the calculation method of shaping force required by rolling reshaper to repair the deformed casing, and verified the reliability of the calculation method through tests. Luo et al. [6] took a single ball on the hydraulic rolling reshaper to perform a radial extrusion test on the casing, obtained the relationship between the shaping force and the radial displacement of the inner wall of the casing, and established a corresponding finite element model for verification. Xu et al. [7] gave a research method for the single shaping limit of casing and established the finite element model of roll-shaping shrinkage deformation casing to obtain the single shaping limit of casing with different axial deformation lengths.

In summary, regarding the optimization of shaping tools, most researchers used the method of fixing other variables and changing a geometric parameter to explore the influence of this parameter on the shaping effect. The research process is equivalent to the "selection" rather than "optimization" of parameters. Moreover, there are few reports on the optimization of hydraulic rolling reshaper, and the present research [8] only optimizes the structural parameters of a part of the reshaper, and the influence of other parameters on the shaping effect has not been analysed or screened.

Therefore, to improve the shaping ability of the hydraulic rolling reshaper in the premise of ensuring the safety bearing capacity of the casing, it is necessary to perform structural optimization with full consideration of the key structural parameters of the reshaper. However, the structural complexity of the reshaper and the high nonlinearity of its contact with the inner wall of the casing make it difficult to calculate and evaluate the shaping effect using the traditional analytical method, which needs to be simulated by numerical simulation. Based on this, taking the shrinkage deformation casing as an example, the process of repairing the deformed casing by hydraulic rolling reshaper is simulated and analysed, and the deformed state and stress distribution of the casing during the shaping process are explored. Subsequently, a multi-parameter coupling optimization method of a hydraulic rolling reshaper based on the factorial design is proposed. The response surface model is constructed by stepwise regression, and the optimal structural parameters of the reshaper are obtained by genetic algorithm (GA).

## 1 RELATED OPTIMIZATION THEORY

### 1.1 Optimized Mathematical Model

Generally, an optimization problem with $M$ optimization objectives and $N$ design variables can be simplified into an optimized mathematical model:

$$\begin{aligned} \min \quad & f(x)=\left[f_1(x), f_2(x), \cdots, f_m(x)\right], m=1,2,\cdots,M \\ \text{s.t.} \quad & g_i(x)=0, i=1,2,\cdots,s \\ & h_j(x)\geq 0,\ j=1,2,\cdots,k \\ & x=\left[x_1,x_2,\cdots,x_r,\cdots,x_N\right] \\ & x_{n\min}\leq x_n\leq x_{n\max}, n=1,2,\cdots,N \end{aligned} \quad , \tag{1}$$

where $M$ is the total number of optimization objectives, $f_m(x)$ is the $m^{\text{th}}$ objective function, $g_i(x)=0$ is the $i^{\text{th}}$ equality constraint, $h_j(x)\geq 0$ is the $j^{\text{th}}$ inequality constraint, $x$ is the $N$-dimensional design variable, $x_{n\max}$ and $x_{n\min}$ are the upper and lower limits of the feasible region of the $n^{\text{th}}$ design variable.

### 1.2 Design of Experiment

The Design of Experiment involved in this paper includes a factorial design and an Optimal Latin hyper-cube design (OLHD).

1. Factorial design

   A factorial design is a screening experimental design method that aims to find the design variables involved in optimization by screening out remarkable factors from multi-factors [9] to [11]. To judge the influence of different factors on the response and reduce the number and cost of experiments, an orthogonal test is chosen to analyse and screen the related influencing factors. The different values of influencing factors are called levels. According to the orthogonality, a representative combination of levels is selected from a full-scale test to form an orthogonal table for experimental design, and multi-factors are screened to simplify the subsequent optimization.

2. Optimal Latin hyper-cube design
   An optimal Latin hyper-cube design (OLHD) is a sampling experimental design method that improves the uniformity of the traditional Latin hyper-cube design. It can reflect the relationship between factors and responses more realistically and accurately, with better space-filling and equilibrium. Fig. 2 is quoted from [12], Fig. 2a shows the test points randomly generated by the Latin hyper-cube design, and Fig. 2b shows the more uniformly distributed test points generated by OLHD.

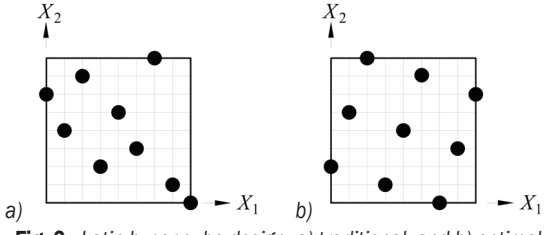


**Fig. 2.** *Latin hyper-cube design; a) traditional; and b) optimal*

### 1.3 Polynomial Fitting Based on Response Surface Methodology

Response surface methodology is a statistical method to obtain the relationship between multiple influencing factors and responses in complex systems so as to establish polynomial regression models [13]. The basic idea is to select suitable sample points in the design space and calculate the responses, use polynomial fitting to obtain explicit formulas between variables and responses in complex systems, and finally, the structural parameters are optimized based on the optimization algorithms.

Due to the complex structure of the hydraulic rolling reshaper and the large number of related variables, the stepwise regression is chosen for fitting. Stepwise regression is a multiple linear regression method [14]. However, considering only the linear relationship between variables and responses will reduce the fitting effect of the model, so in order to consider the nonlinear relationship between variables, interactions, and responses, it is necessary to generalize linearity to nonlinearity by making a power series of single-factor variables and considering interactions to form a new set of variables before stepwise regression. In the process of regression, statistical tests should be carried out on each variable in each step, remarkable variables are automatically screened and added; the variables are introduced into the regression model in turn according to the influence degree of each variable on the response. There are two reference values for judging the significance, which are the values of inclusion ($\alpha_c$) and deletion ($\alpha_d$). If the $p$-value of the variable is less than or equal to $\alpha_c$, the variable is automatically identified and added to the regression model; if the $p$-value is greater than $\alpha_d$, the variable is eliminated. The final regression model is obtained when the $p$-values of all variables not in the model are greater than $\alpha_c$ and less than or equal to $\alpha_d$.

There are two coefficients to determine the fitting effect of the model: the coefficient of determination ($R^2$) and the degree-of-freedom adjusted coefficient of determination ($R^2_{adj}$), and the calculation methods are shown in Eqs. (2) and (3). $R^2$ is used to represent the goodness of fit for the regression models, and the higher the value, the higher the goodness of fit of the models. $R^2_{adj}$ includes the number of design variables in the model, which can better reflect the pros and cons of the regression model [15]. Moreover, the closer $R^2$ and $R^2_{adj}$ are to 1, the better the fitting effect of the model is.

$$R^2 = 1 - \frac{SS_E}{SS_T}, \tag{2}$$

$$R^2_{adj} = 1 - \frac{SS_E/(t-w)}{SS_T/(t-1)}, \tag{3}$$

where $t$ is the total number of samples, and $w$ is the total number of terms in the regression model.

## 2 OVERALL RESEARCH IDEA

The optimization flow of the hydraulic rolling reshaper is shown in Fig. 3. Firstly, a preliminary analysis of the reshaper is required to determine the geometric parameters of the structure and the response variables of the optimization problem. Then, enter the experimental design stage, the orthogonal test is used to sample and obtain the different combinations of multi-geometric parameters, and the corresponding responses are solved by invoking the parametric finite element model repeatedly. Therefore, the factorial design of multi-geometric parameters is performed to screen out the remarkable factors and determine the design variables involved in the subsequent optimization. On this basis, OLHD is used for scientific sampling in the feasible region, and the responses of the sample points are calculated by invoking the finite element model, and the response surface model is established based on responses. Thus, with the maximum plastic deformation of the casing as the objective function, the maximum equivalent stress, residual stress, and the plastic deformation of the casing as the constrained conditions, an optimized

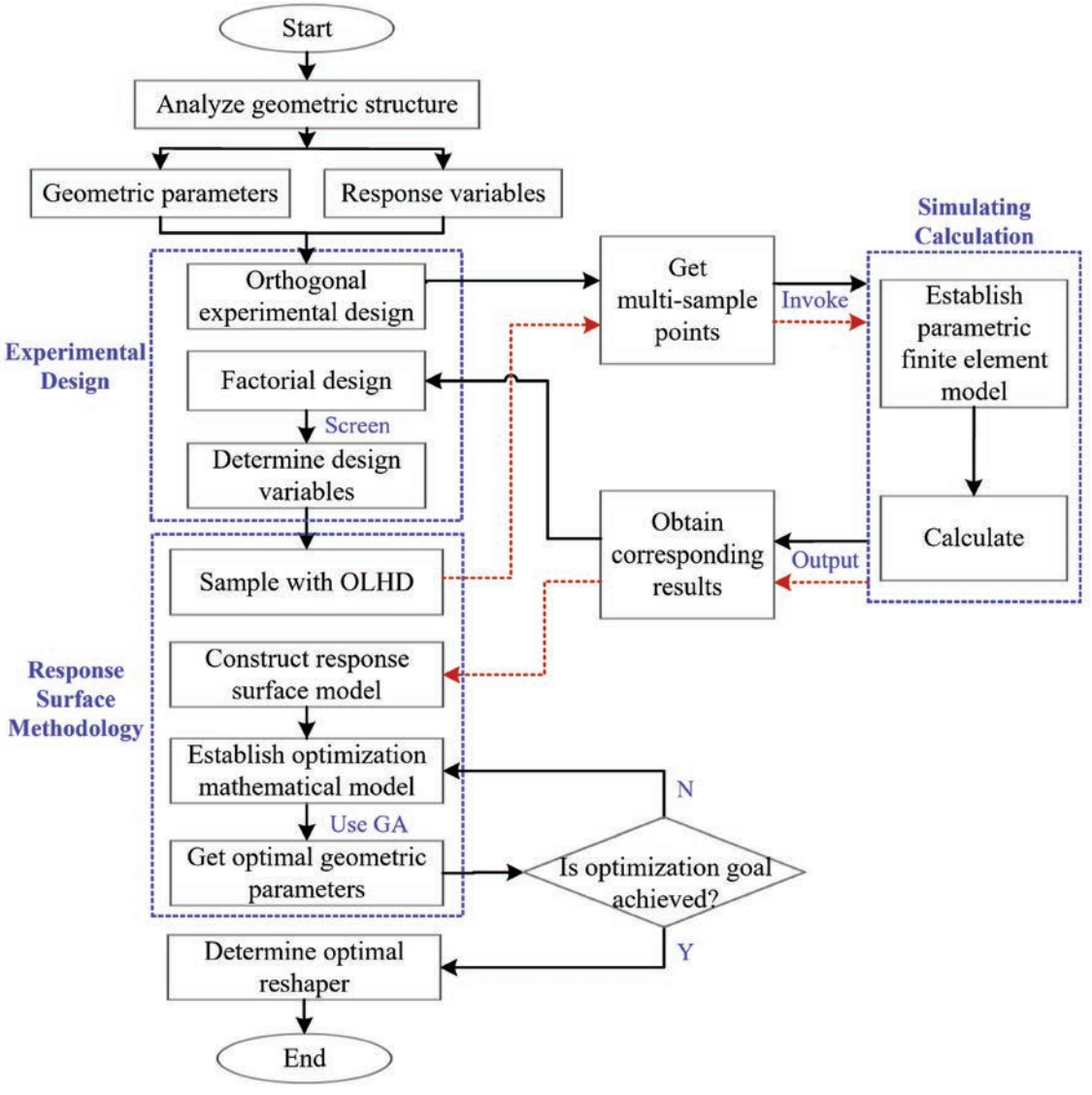


**Fig. 3.** *Optimization flow chart*

mathematical model for reshaper is constructed. Thereafter, GA is used to optimize and evaluate the shaping effect of the reshaper before and after optimization, and finally the optimal structure of the reshaper is obtained.

## 3 MECHANICAL ANALYSIS OF SHAPING PROCESS

### 3.1 Parametric Finite Element Model

Fig. 4 is the basic structure of the hydraulic rolling reshaper. It is mainly composed of a work section, a charging section, and a connective section. The rolling balls in the work section are the key component in direct contact with the inner wall of the casing, and they are also the main working body to transmit the shaping load and achieve the repair goal, so the reshaper is simplified into the multi-stage tapered structure shown in Fig. 4. There are 7-stage balls in the reshaper, and the first 6 stages are called "shaping stage", which are used to roll the inner wall of the casing to achieve the repairing goal and diameters of each stage increase in steps with the conical degree of 1.145°. Moreover, the 7$^{th}$ stage is called "reinforced stage", which is used to strengthen the shaping effect. Furthermore, the total length of the reshaper is 300 mm, and the axial distance of each stage is 50 mm. The rolling balls (the outer diameter is 20.64 mm) are

embedded in the grooves located at the work section, and the exposed size of the ball relative to the surface of the reshaper is 5 mm. The main body diameter of the 1st stage is 100 mm (the maximum equivalent diameter is 110 mm), and the diameters of the 6th and 7th stages are 110 mm (the maximum equivalent diameter is 120 mm).

The shrinkage deformation casing is the object of this research, and the ideal casing with material P110 and specification of $5_{1/2}$ in (Φ 139.7 mm × 9.17 mm) is selected. The axial deformation length of the casing is 300 mm, and the minimum diameter (110 mm) is located in the middle of the casing. To avoid the influence of the boundary effect, both ends of the deformed section are connected with intact casing (length is 100 mm), as shown in Fig. 5. Before the shaping process begins, the section of the 1st stage on reshaper coincides with the A-A section shown in Fig. 5.

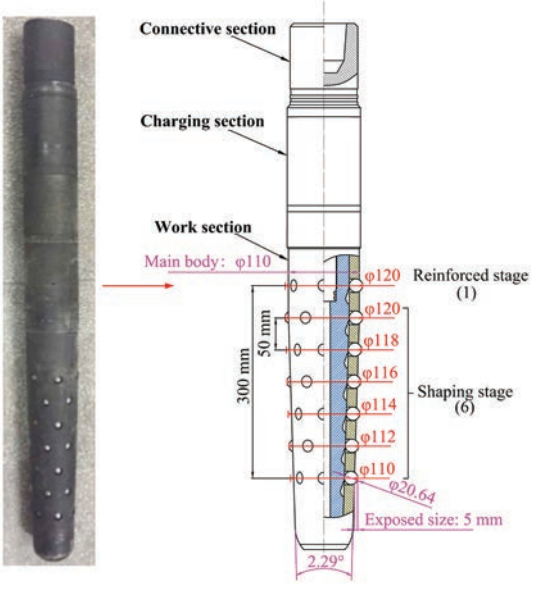


**Fig. 4.** *Structural parameters of hydraulic rolling reshaper*

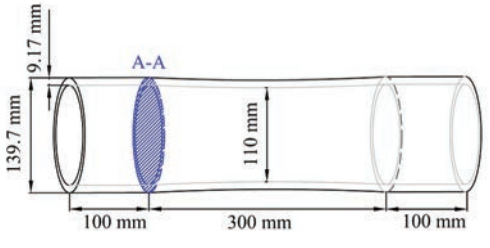


**Fig. 5.** *Structural parameters of shrinkage deformation casing*

According to the API 5CT standard for casing material properties, the P110 casing with an elastic modulus of 210 GPa, Poisson's ratio of 0.3, yield limit $\sigma_s$ of 851 MPa, and strength limit $\sigma_b$ of 933 MPa is taken as an example for calculation. In addition, the multilinear isotropic hardening model is used to characterize the stress-strain relationship of casing [16], as shown in Fig. 6.

To simplify the calculation, the assumptions have been given for the simulation as follows. (1) Simplify the reshaper into a rigid body. (2) Ignore the influence of temperature on the mechanical properties of the material during the shaping process. (3) The central axis of the reshaper always coincides with the axis of the casing during the shaping process. (4) Ignore the wall thickness variation of the deformed casing. (5) Ignore the influence of the initial residual stress of deformed casing on the shaping effect.

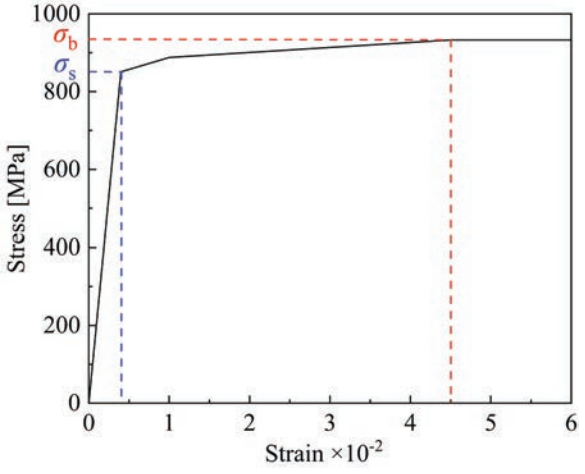


**Fig. 6.** *Stress-strain curve of casing*

According to the structural characteristics of the reshaper, parametric modelling is carried out on the basis of clarifying the geometric relationship between the structural parameters, and the casing is discretized into solid elements by the finite element method. Moreover, target elements and contact elements are created on the outer surface of the reshaper and the inner surface of the casing, respectively. Considering the computational cost and accuracy comprehensively, the global grid density is determined, and the key geometric features (such as the contact interface between the reshaper and the inner wall of the casing) are refined with the local grid refinement. According to the loading features of the integral structure, the end faces on both sides of the casing are set as fully fixed constraints. The axial translational velocity of the reshaper is $v$ = 1 mm/s, the rotating angular velocity is $\omega$ = 0.48 rad/s, and the friction coefficient between the outer surface of the reshaper and the inner wall of

the casing is 0.1. Therefore, the mechanical model and finite element model of the hydraulic rolling reshaper shaping deformed casing are shown in Fig. 7.

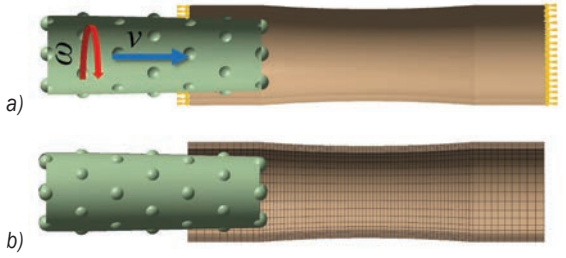


**Fig. 7.** *Models of the shaping process; a) mechanical model; and b) finite element model*

### 3.2 Solving Algorithm

To reflect the material nonlinearity of the casing and the contact nonlinearity of the contact interface involved in the shaping process, the overall mechanical equilibrium equation of the shaping process is determined as

$$\left[\mathbf{K}\left(\delta\right)+\mathbf{K}_{\mathrm{c}}\left(\delta\right)\right]\delta=\mathbf{F}+\mathbf{F}_{\mathrm{c}}, \tag{4}$$

where $\boldsymbol{\delta}$ is the node displacement array, $\mathbf{K}(\boldsymbol{\delta})$ is the elastic-plastic stiffness matrix of casing material, $\mathbf{K}_{\mathbf{C}}(\boldsymbol{\delta})$ is the contact stiffness matrix, $\mathbf{F}$ is nodal force array, $\mathbf{F}_{\mathbf{C}}$ is the contact force array.

Since the elastic-plastic analysis is involved, and the nonlinearity of the contact area and contact pressure on the contact interface, the solution uses intermediate sub-steps, and the convergence of each sub-step is achieved by stepwise iterative solution, so as to track the load path correctly and complete the overall calculation. Therefore, the modified Newton-Raphson method is chosen to solve the nonlinear problems involved in this paper. The reliability of the algorithm in solving the double nonlinear problems involved in the shaping process has been verified by Xu et al. [7] in our research group through the combination of numerical simulation and experiment.

### 3.3 Results and Discussion

The shaping process is calculated for 700 s, and the maximum equivalent stress and radial displacement of the deformed casing under different times are shown in Fig. 8.

The figures show that when the reshaper moves to 136.56 s, the 1st stage ball of the reshaper starts to contact with the inner wall of the casing, and the casing begins to deform elastically. At 166.55 s, the equivalent stress of the casing exceeds the yield limit, and the casing produces plastic deformation. As the reshaper keeps moving forward, the stress and strain of the casing increase, and the plastic deformation area gradually expands. The maximum equivalent stress of the casing is 933 MPa at 315.08 s, and the maximum radial displacement of the casing is 5.133 mm at 427.37 s. When the reshaper moves to 587.56 s, the rolling balls are completely separated from the inner wall of the casing, the repairing load is unloaded, and the shaping process is completed. At this time, the residual stress of the casing is 809.38 MPa, and the radial displacement is rebounded by 0.213 mm due to elastic strain, so the plastic deformation of the casing after single shaping is 4.920 mm. Hence, the equivalent stress and radial displacement nephogram of the casing at important times are shown in Fig. 9. However, it should be noted that the maximum equivalent stress of the casing reaches the strength

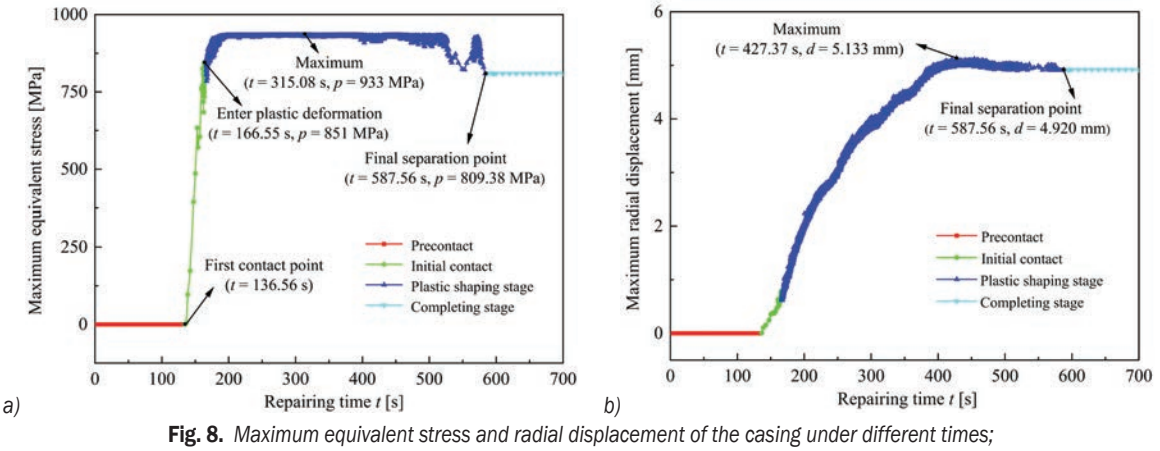


**Fig. 8.** *Maximum equivalent stress and radial displacement of the casing under different times; a) maximum equivalent stress; and b) maximum radial displacement*

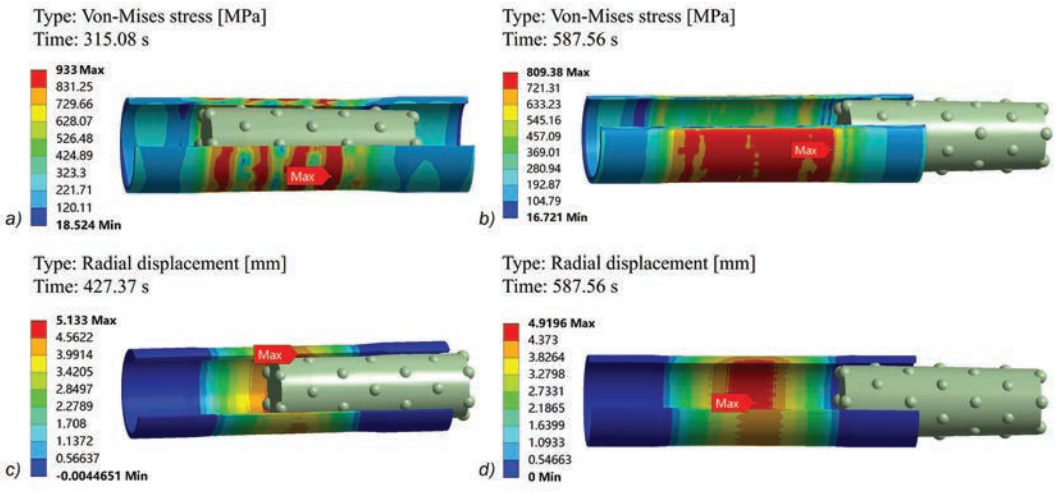


**Fig. 9.** *Von-Mises stress and radial displacement nephogram at important times in repairing process; a) Von-Mises stress nephogram at 315.08 s; b) Von-Mises stress nephogram at 587.56 s; c) radial displacement nephogram at 427.37 s; and d) radial displacement nephogram at 587.56* s

limit during the shaping process at 315.08 s, and the casing will be destroyed in the actual construction, so this reshaper cannot repair this deformed casing.

## 4 FACTORIAL DESIGN

By analysing the mutually restrictive relationship between the geometric parameters of the reshaper, the following eight geometric parameters are selected as influencings to participate in the factorial design, as shown in Fig. 10: main body diameter of the 1st stage ($D_1$), reshaper's taper ($\alpha$), length of the shaping stage ($L$), helix angle ($\beta$, replaced by the pitch $H$ while modelling, $\beta$=arctan($H/\pi D_1$)), diameter of the ball ($D_b$), number of balls each stage ($s$), total number of stages of reshaper ($k$), exposed size of the ball ($h$).

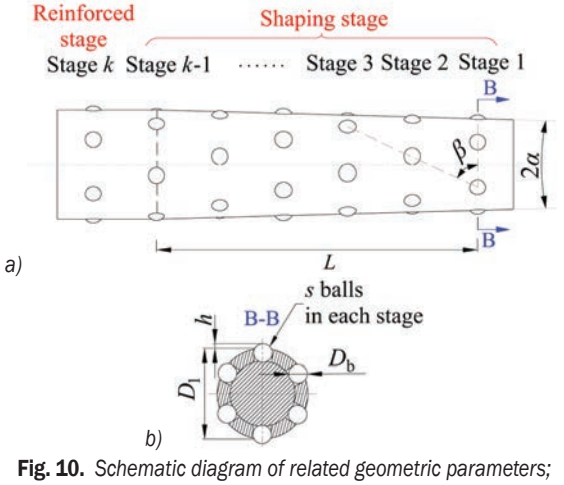


**Fig. 10.** *Schematic diagram of related geometric parameters; a) front view of the reshaper; and b) B-B section*

Considering the trafficability of the reshaper and the rationality of the structure, combined with the requirements of GB/T 308.1-2013, the range of eight influencing factors is obtained by preliminary analysis. According to the central composite design method [17] and [18], three levels of eight influencing factors are selected for the 8-factor 3-level orthogonal test, and the values are shown in Table 1.

**Table 1.** *Factor values for the orthogonal test*

| No. | Factors | Unit | Level | | |
|---|---|---|---|---|---|
| | | | 1 | 2 | 3 |
| 1 | $L$ | mm | 220 | 230 | 240 |
| 2 | $D_1$ | mm | 97.5 | 98.5 | 99.5 |
| 3 | $\alpha$ | ° | 1.15 | 1.2 | 1.25 |
| 4 | $h$ | mm | 3.5 | 4 | 4.5 |
| 5 | $H$ | mm | 400 | 600 | 800 |
| 6 | $D_b$ | mm | 20.64 | 21.43 | 22.22 |
| 7 | $k$ | stage | 6 | 7 | 8 |
| 8 | $s$ | piece | 4 | 5 | 6 |

To reduce the downhole frequency of the reshaper and shorten the construction period of workover, it is necessary to ensure that the plastic deformation of the casing after single shaping is the largest under the safety of the casing when evaluating the shaping effect of the reshaper. At the same time, the residual stress of the shaped casing will also weaken its own load-bearing capacity, so it is necessary to minimize the residual stresses of the shaped casing. Therefore, the maximum equivalent stress ($p_{max}$), residual stress ($p_r$), and plastic deformation of the casing after

**Table 2.** *Schemes and responses of orthogonal test*

| Sample No. | Geometric parameters | | | | | | | | Responses | | |
|---|---|---|---|---|---|---|---|---|---|---|---|
| | $L$ [mm] | $D_1$ [mm] | $\alpha$ [°] | $h$ [mm] | $H$ [mm] | $D_b$ [mm] | $k$ [stage] | $s$ [piece] | $p_{max}$ [MPa] | $p_r$ [MPa] | $d$ [mm] |
| 1 | 220 | 99.5 | 1.2 | 4 | 800 | 21.43 | 7 | 5 | 880.05 | 692.54 | 0.84 |
| 2 | 230 | 97.5 | 1.15 | 4.5 | 800 | 20.64 | 8 | 6 | 797.49 | 328.73 | 0.38 |
| 3 | 240 | 97.5 | 1.15 | 4 | 600 | 20.64 | 7 | 5 | 585.84 | 215.39 | 0.17 |
| 4 | 220 | 97.5 | 1.25 | 3.5 | 600 | 21.43 | 8 | 5 | 18.177 | 2.9887 | 0.01 |
| 5 | 240 | 99.5 | 1.15 | 4.5 | 600 | 22.22 | 7 | 4 | 930.36 | 752.92 | 1.68 |
| 6 | 220 | 99.5 | 1.25 | 4 | 600 | 20.64 | 8 | 4 | 905.80 | 670.05 | 0.95 |
| 7 | 230 | 97.5 | 1.25 | 4.5 | 400 | 21.43 | 7 | 4 | 889.39 | 677.74 | 0.58 |
| 8 | 220 | 99.5 | 1.15 | 4 | 400 | 22.22 | 6 | 6 | 856.19 | 656.66 | 0.58 |
| 9 | 230 | 99.5 | 1.2 | 3.5 | 600 | 21.43 | 6 | 4 | 847.77 | 650.73 | 0.41 |
| 10 | 240 | 98.5 | 1.25 | 3.5 | 800 | 22.22 | 6 | 4 | 836.07 | 520.20 | 0.34 |
| 11 | 220 | 98.5 | 1.2 | 4.5 | 800 | 20.64 | 7 | 4 | 895.91 | 692.24 | 0.63 |
| 12 | 230 | 99.5 | 1.25 | 3.5 | 400 | 20.64 | 7 | 6 | 870.60 | 705.28 | 0.72 |
| 13 | 240 | 99.5 | 1.25 | 4.5 | 800 | 20.64 | 6 | 5 | 931.53 | 806.39 | 1.91 |
| 14 | 230 | 98.5 | 1.25 | 4 | 400 | 22.22 | 7 | 5 | 875.67 | 667.63 | 0.75 |
| 15 | 230 | 97.5 | 1.2 | 4.5 | 600 | 22.22 | 6 | 5 | 849.1 | 606.62 | 0.54 |
| 16 | 240 | 97.5 | 1.2 | 4 | 400 | 22.22 | 8 | 4 | 760.19 | 322.70 | 0.21 |
| 17 | 230 | 98.5 | 1.15 | 4 | 800 | 21.43 | 8 | 4 | 793.61 | 418.97 | 0.30 |
| 18 | 230 | 98.5 | 1.2 | 4 | 600 | 20.64 | 6 | 6 | 847.55 | 577.83 | 0.47 |
| 19 | 220 | 98.5 | 1.15 | 4.5 | 400 | 21.43 | 6 | 5 | 870.77 | 708.42 | 0.55 |
| 20 | 240 | 98.5 | 1.2 | 3.5 | 400 | 20.64 | 8 | 5 | 738.45 | 300.02 | 0.25 |
| 21 | 220 | 97.5 | 1.2 | 3.5 | 800 | 22.22 | 7 | 6 | 0 | 0 | 0 |
| 22 | 240 | 97.5 | 1.25 | 4 | 800 | 21.43 | 6 | 6 | 847.05 | 536.95 | 0.47 |
| 23 | 240 | 98.5 | 1.15 | 3.5 | 600 | 21.43 | 7 | 6 | 636.87 | 230.57 | 0.64 |
| 24 | 230 | 99.5 | 1.15 | 3.5 | 800 | 22.22 | 8 | 5 | 782.71 | 403.77 | 0.37 |
| 25 | 220 | 98.5 | 1.25 | 4.5 | 600 | 22.22 | 8 | 6 | 892.80 | 679.19 | 1.13 |
| 26 | 220 | 97.5 | 1.15 | 3.5 | 400 | 20.64 | 6 | 4 | 0 | 0 | 0 |
| 27 | 240 | 99.5 | 1.2 | 4.5 | 400 | 21.43 | 8 | 6 | 927.77 | 809.90 | 1.93 |

single shaping ($d$) are selected as response variables. The table of the 8-factor 3-level orthogonal test is generated by SPSS, and 27 combined schemes are obtained. By invoking the parametric finite element model, the responses corresponding to each combined scheme are obtained, as shown in Table 2.

The $p$-value and $t$-value of each factor for the three response variables are shown in Table 3, and the Pareto diagrams are shown in Fig. 11. The abscissa "standardized effect" in Fig. 11 represents the absolute value of the $t$-value obtained by the $t$-test, and the ordinates are arranged in descending order of the value of the standardized effect. Based on the significance level α of 0.05, the statistical significance threshold of 2.101 is obtained, which corresponds to the critical value of the $t$-value of the red reference line in Fig. 11. The variable is statistically significant when $p \leq 0.05$ or the bar in the Pareto diagram exceeds the reference line [19]. Hence, it can be seen from the chart that the geometric parameters that have a great

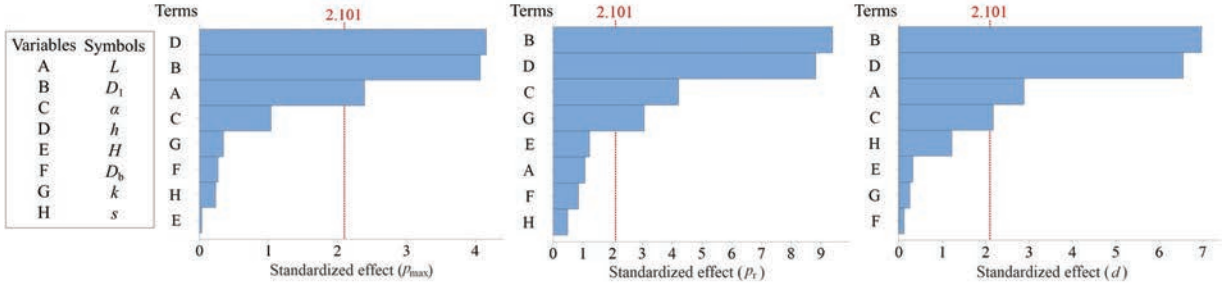


**Fig. 11.** *Pareto charts of response variables*

influence on the response variables are $D_1$, $h$, $L$, $\alpha$, and $k$, so these five parameters are selected as the design variables for optimization.

**Table 3.** *The p-value and t-value of the response variables*

| Variables | $p_{max}$ | | $p_r$ | | $d$ | |
|---|---|---|---|---|---|---|
| | *p*-value | *t*-value | *p*-value | *t*-value | *p*-value | *t*-value |
| $L$ | 0.028 | 2.39 | 0.3 | 1.07 | 0.01 | 2.88 |
| $D_1$ | 0.001 | 4.07 | 0 | 9.39 | 0 | 6.97 |
| $\alpha$ | 0.313 | 1.04 | 0.001 | 4.21 | 0.044 | 2.17 |
| $h$ | 0.001 | 4.16 | 0 | 8.82 | 0 | 6.54 |
| $H$ | 0.975 | -0.03 | 0.239 | -1.22 | 0.749 | -0.32 |
| $D_b$ | 0.792 | 0.27 | 0.405 | 0.85 | 0.908 | 0.12 |
| $k$ | 0.735 | -0.34 | 0.007 | -3.06 | 0.802 | 0.25 |
| $s$ | 0.818 | -0.23 | 0.63 | -0.49 | 0.238 | 1.22 |

## 5 OPTIMIZATION DESIGN

### 5.1 Elements of the Mathematical Model

The optimized mathematical model includes three elements: objective function, design variable and constraint.

1. Objective function

The key to the hydraulic rolling reshaper is to ensure that the casing has a large plastic deformation after single shaping ($d$) under safe conditions to ensure a rapid and effective workover. Therefore, $d$ is selected as the objective function.

2. Design variable

Based on the requirements for performance and dimensions of the reshaper and its trafficability of deformed casing, the value ranges of the 5 design variables will be determined separately.

(1) Main body diameter of the 1st stage ($D_1$)

At present, the maximum equivalent diameter of the reshaper is 120 mm, and it determines the diameter of the casing through which the reshaper can pass and the shaping effect on the casing. After analysis, the maximum equivalent diameter is affected by three geometric parameters: main body diameter of the 1st stage ($D_1$), exposed size of the ball ($h$), and reshaper's taper ($\alpha$), so the main body diameter of the 1st stage is determined first. According to the working principle of the reshaper, the balls will retract into the grooves after the centre shaft is lifted up, and Fig. 12 shows the minimum limit state for the main body diameter of the 1st stage when the balls are not exposed.

As can be seen from the figure, the contact point at the bottom corner of the groove is point B, point O is the centre of the centre shaft, point A is the contact point between the ball and the bottom surface of the groove, and the diameter of the ball is $D_b$. According to the geometric relationship in the figure, $D_1 > \left(\frac{1}{\tan\alpha} + 2\right) D_b$, and the diameter of the ball is 20.64 mm, $\alpha$ = 30°. After calculation, the minimum $D_1$ is 77.03 mm, and the safety factor is taken as 1.1, the minimum value of $D_1$ is 84.73 mm which is rounded up to 85 mm.

Based on past experience, the smaller the diameter of the work section, the easier to wedge into the minimum diameter of the casing for repair. Therefore, the main body diameter of the 1st stage is 100 mm as the upper limit of this design variable, so the range of $D_1$ is determined to be 85 mm $\leq D_1 \leq$ 100 mm.

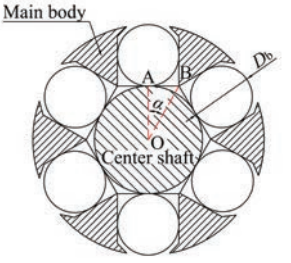


**Fig. 12.** *Minimum limit state for the main body diameter of the 1st stage*

(2) Exposed size of the ball ($h$)

The balls will be extruded from the grooves when the charging section pushes the centre shaft forward, so the exposed size of the ball has a certain impact on the shaping effect of the casing, if it is too small, the shaping ability of the reshaper will be reduced, and the desired effect will not be achieved. Simultaneously, in order to ensure that the balls cannot fall out of the grooves, the exposed size of the ball should not be greater than 1/4 of its diameter, the range of $h$ is determined to be 3 mm $\leq h \leq$ 5.16 mm.

(3) Length of the shaping stage ($L$)

The balls on the work section are spirally distributed and build the helical line by controlling the pitch and cycle number in parametric modelling. Therefore, the number of turns of the spiral is set to one, and the helix angle is replaced by the pitch for representation. To facilitate the subsequent analysis, the shaping stage of the reshaper is expanded along the ring direction of the 1st stage, and the side unfolded drawing of spirally arranged balls on the shaping stage is obtained, as shown in Fig. 13.

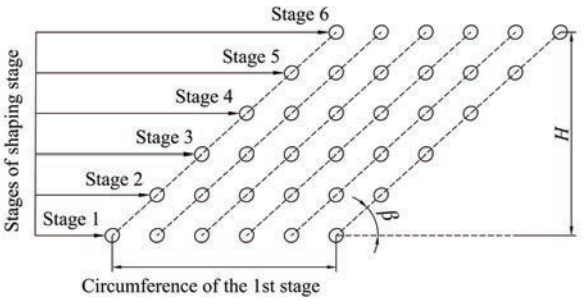


**Fig. 13.** *Side unfolded drawing of spirally arranged balls on the shaping stage*

The reference circle is established by the circumference of the 1st stage, and the circumference of the reference circle is $\pi D_1$ after expansion, so the conversion relationship between pitch ($H$) and helix angle ($\beta$) is $\beta = \arctan(H/\pi D_1)$. For structural parameters of the reshaper, $D_1 = 100$ mm, $H = 600$ mm, so the helix angle is equal to 62.36°. Take the geometric relationship between the 1st and 2nd balls as an example (Fig. 14). Combined with the practical processing technology, at least 1/2 diameter processing allowance should be left between each stage, MN = 30.96 mm, so the minimum interval between each stage is MN·sin$\beta$. After calculation, the minimum interval between each stage is 27.43 mm.

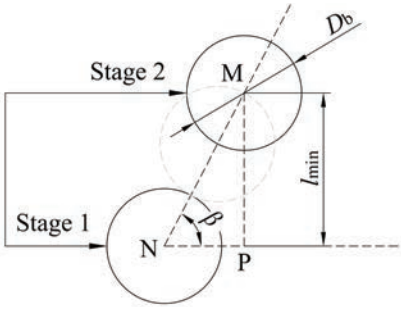


**Fig. 14.** *Schematic diagram of the geometric relationship between the 1st and 2nd balls*

The hydraulic rolling reshaper is one of the main shaping tools for repairing deformed casing in horizontal wells. To improve the applicability of the reshaper so that it can pass through a horizontal well with a smaller radius, the length of the reshaper should be reduced on the current basis. The total number of shaping stages should be less than 9 (250 mm/27.43 mm = 9.11) with 8 intervals, so the length of the shaping stage should be greater than $27.43 \times 8 = 219.44$ mm and rounded upward to 220 mm. Hence, the range of $L$ is determined to be 220 mm $\leq L \leq$ 250 mm.

(4) Reshaper's taper ($\alpha$)

The inner diameter of the intact casing is 121.36 mm, and if the expanded size of the ball reaches the maximum (5.16 mm), the maximum diameter of the main body is 111.04 mm. According to the expression of the reshaper's taper: $\alpha = \arctan\left(\frac{D_k - D_1}{L}\right)$. ($D_k$ indicates the main body diameter of the $k^{\text{th}}$ stage), the main body diameter of the 1st stage ranges from 85 mm to 100 mm through the analysis of point (1). After calculation, when $D_1 = 85$ mm, $\alpha \leq 3.387°$, when $D_1 = 100$ mm, $\alpha \leq 1.437°$. The current reshaper's taper is 1.145°, in order to obtain the remarkable result of shaping, the range of $\alpha$ is determined to be $1.145° \leq \alpha \leq 1.437°$.

(5) Total number of stages of reshaper ($k$)

The balls in the reinforced stage play a role in consolidating the shaping effect, so it is necessary to set up 1 stage to strengthen. For the shaping stage, in addition to the first and final stages of the shaping stage, at least two stages of balls should be set between these two stages to ensure that the reshaper has a more uniform shaping effect during the spinning process, so the total number of stages of reshaper should be at least 5 stages, as shown in Fig. 15.

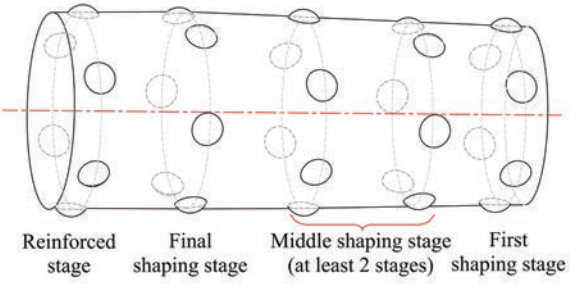


**Fig. 15.** *Structure diagram of 5-stage reshaper*

According to the analysis of point (3), the minimum interval between each stage is 27.43 mm, and the number of shaping stages is not higher than 9. In addition, it is necessary to add another stage for reinforcement; then, the total number of stages of reshaper should not be higher than 10, so the range of $k$ is determined to be $k = 5, \ldots, 10$.

3. Constraint condition

According to the simulation results in Section 2.2, the non-optimized shaper cannot repair the deformed casing with the axial deformation length of 300 mm and the minimum diameter of 110 mm. To ensure the integrity of the casing, the maximum equivalent stress of the casing is required to be lower than the strength limit, and the residual stress of the casing after

shaping is lower than the yield limit. Considering a certain safety margin (1 %), the maximum equivalent stress of the casing is lower than 923.67 MPa, and the residual stress is lower than 842.49 MPa. Therefore, the maximum plastic deformation of casing that can be shaped is 5.68 mm ((121.36−110)/2=5.68 mm), and $d$ should be less than 5.68 mm.

### 5.2 Response Surface Model

OLHD is used to conduct scientific sampling in the feasible region of the design variables, and 50 sample points are obtained, which are brought into the finite element calculation module to calculate the corresponding responses, and the nonlinear interactive regression model of three response variables is established by stepwise regression, as shown in Eqs. (5) to (7). $R^2$ and $R^2_{adj}$ of the three regression models are shown in Table 4, and it is considered that the regression models have high accuracy.

$$\begin{aligned} p_{max} = {} & 1639917 - 7983L - 16495D_1 - 1436683\alpha + \\ & 29129h - 3837\alpha^2 - 574.2h^2 + 79.5LD_1 + \\ & 6467L\alpha + 21.6Lh + 7975\alpha h + 14220D_1\alpha - \\ & 288.22D_1h + 7975\alpha h - 63.51LD_1\alpha - 37.4Lh\alpha, \end{aligned} \quad (5)$$

$$\begin{aligned} p_r = {} & -2668966 + 72108D_1 + 32808\alpha + 197139h - \\ & 14.37k - 640D_1^2 - 314.4D_1\alpha - 4054D_1h - \\ & 507\alpha h + 1.861D_1^3 + 20.91D_1^2h, \end{aligned} \quad (6)$$

$$\begin{aligned} d = {} & -58.12 + 0.0221L + 0.50495D_1 + 4.476\alpha - \\ & 0.57h + 0.1845h^2. \end{aligned} \quad (7)$$

**Table 4.** $R^2$ and $R^2_{adj}$ of the regression model

| Responses | $R^2$ [%] | $R^2_{adj}$ [%] |
|---|---|---|
| $p_{max}$ | 99.92 | 99.83 |
| $p_r$ | 97.39 | 95.76 |
| $D$ | 99.55 | 99.44 |

To summarize, combined with Eqs. (5) to (7), the multi-parameter coupling optimization of the hydraulic rolling reshaper is transformed into an optimized mathematical model with constraints as

$$\begin{aligned} \max \quad & d(L, D_1, \alpha, h, k) \\ \text{s.t.} \quad & p_{max} < 923.67 \text{ MPa} \\ & p_r < 842.49 \text{ MPa} \\ & d \le 5.68 \text{ mm} \\ & 220 \text{ mm} \le L \le 250 \text{ mm} \\ & 85 \text{ mm} \le D_1 \le 100 \text{ mm} \\ & 1.145^\circ \le \alpha \le 1.437^\circ \\ & 3 \text{ mm} \le h \le 5.16 \text{ mm} \\ & k = 5, ..., 10 \end{aligned} \quad . \quad (8)$$

### 5.3 Comparison of Optimization Results

For the optimization problem of hydraulic rolling reshaper, the geometric parameters have both continuous and discrete variables, which will lead to a higher degree of nonlinearity in the optimization process. For such highly nonlinear optimization problems, a genetic algorithm is more advantageous [20]. The number of the initial population is 5000, the samples' number for one iteration is 1000, the maximum allowable Pareto percentage is 70 %, the stable convergence percentage is 2 %, and the maximum number of iterations is 20 [21] and [22]. The iteration converges when the number of iterative evaluations is 13556, and the optimal solution of this optimization problem is obtained. The comparison with the structural parameters before the reshaper optimization is shown in Table 5.

**Table 5.** *Comparison of structural parameters of reshaper before and after optimization*

| Geometrical parameters | | Non-optimization | Optimization |
|---|---|---|---|
| Design variables | $L$ [mm] | 250.00 | 238.68 |
| | $D_1$ [mm] | 100 | 100 |
| | $\alpha$ [°] | 1.145 | 1.345 |
| | $h$ [mm] | 5.000 | 5.131 |
| | $k$ [stage] | 7 | 7 |
| Other variables | Axial distance of each stage [mm] | 50.00 | 47.74 |
| | Length of reshaper [mm] | 300.00 | 286.42 |
| | Equivalent diameter of stage 1 [mm] | 110.00 | 110.26 |
| | Maximum equivalent diameter [mm] | 120.00 | 121.41 |

The parametric finite element model is called again to simulate the shaping process of the deformed casing with an axial deformation length of 300 mm and a minimum diameter of 110 mm. The minimum

diameter in the middle of the casing is a dangerous position in the shaping process; its shaping effect is also worthy of attention. Fig. 16 shows the distribution of plastic deformation at the minimum diameter of the casing before and after optimization. It can be seen that the shaping effect of the casing is more uniform while the plastic deformation of the casing is expanded. The maximum equivalent stress and radial displacement of the casing before and after optimization under different times are shown in Fig. 17, and the comparison of the evaluation parameters is shown in Table 6.

**Table 6.** *Comparison of the results of evaluation parameters before and after optimization*

| Results comparison | Is the casing reshaped safely? | Effect of reshaping [%] | $p_{max}$ [MPa] | $p_r$ [MPa] | $d$ [mm] |
|---|---|---|---|---|---|
| Optimization | Yes | 96.48 | 922.97 | 799.25 | 5.480 |
| Non-optimization | No | / | 933.00 | 809.38 | 4.920 |
| Degree of optimization [%] | / | / | -1.08 | -1.25 | 11.38 |

Depending on the above chart, it can be seen that the optimal reshaper can safely repair the shrinkage deformation casing with a minimum deformation diameter of 110 mm and an axial deformation length of 300 mm. The shaping effect of the casing is the ratio of $d$ to the maẋ mum plastic deformation of the casing that can be shaped, so the shaping effect reaches 96.48 %. In addition, compared with the non-optimized reshaper, $p_{max}$ is reduced by 1.08 %, $p_r$ is reduced by 1.25 %, and the area of high-stress distribution on the deformed casing is reduced. Also, $d$ is increased by 11.38 %, which can effectively improve the efficiency of workover.

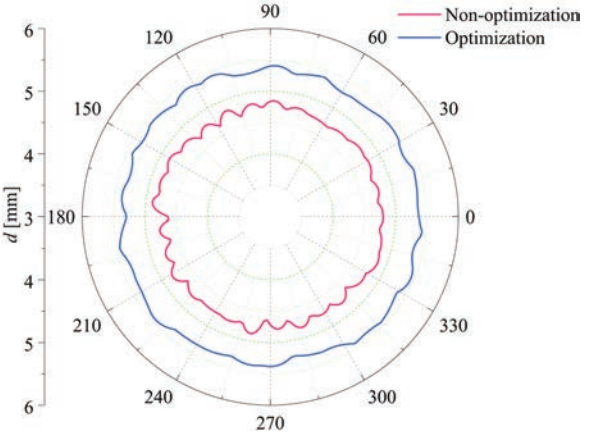


**Fig. 16.** *Distribution of plastic deformation at the minimum diameter of the casing before and after optimization*

Furthermore, the reshaping effect of the casings with different deformation diameters before and after optimization is calculated, and the results and comparisons of the evaluation parameters are shown in Table 7. It can be seen from the table that the optimized reshaper can safely repair the deformed casing, and the reshaping effect of the casing and the single shaping ability of the reshaper are improved.

## 6 CONCLUSIONS

The present work presents a multi-parameter coupling optimization method for the complex structure of a

**Table 7.** *Comparison of evaluation parameters for repairing deformed casings before and after optimization*

| Minimum diameter [mm] | Evaluation parameters | Non-optimization | Optimization | Degree of optimization [%] | Effect of reshaping [%] |
|---|---|---|---|---|---|
| 112 | $p_{max}$ [MPa] | 933.00 | 920.58 | -1.33 | 96.30 |
| | $p_r$ [MPa] | 793.38 | 804.97 | 1.46 | |
| | $d$ [mm] | 3.725 | 4.507 | 20.99 | |
| 114 | $p_{max}$ [MPa] | 932.19 | 920.1 | -1.30 | 93.75 |
| | $p_r$ [MPa] | 805.72 | 805.63 | -0.01 | |
| | $d$ [mm] | 2.758 | 3.450 | 25.09 | |
| 116 | $p_{max}$ [MPa] | 930.45 | 917.76 | -1.36 | 91.49 |
| | $p_r$ [MPa] | 805.27 | 779.03 | -3.26 | |
| | $d$ [mm] | 1.676 | 2.452 | 46.30 | |
| 118 | $p_{max}$ [MPa] | 852.77 | 908.2 | 6.50 | 93.21 |
| | $p_r$ [MPa] | 564.26 | 739.6 | 31.07 | |
| | $d$ [mm] | 0.542 | 1.566 | 188.93 | |

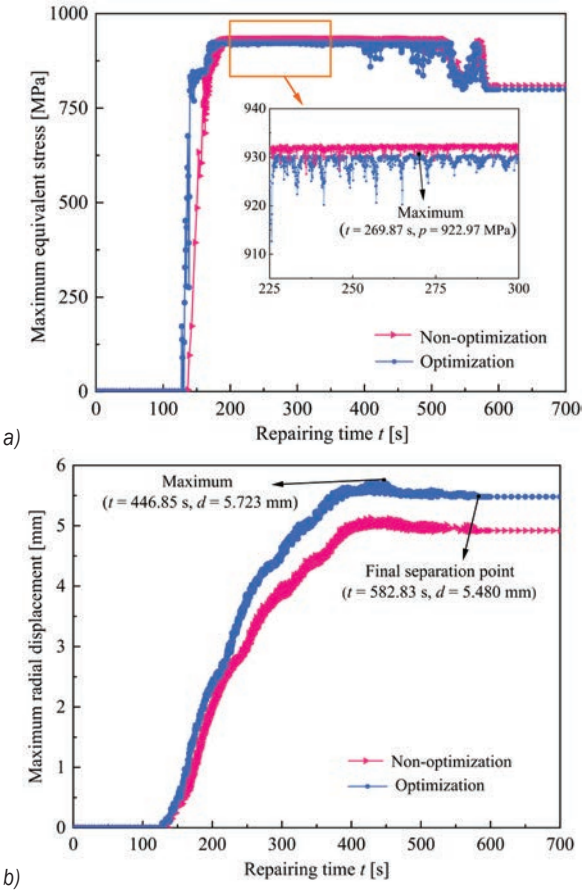


**Fig. 17.** *Correlation parameters of the casing before and after optimization under different times; a) maximum equivalent stress; and b) maximum radial displacement*

hydraulic rolling reshaper. The deformed state and stress distribution of the casing during the shaping process are discussed in detail, and an optimization method for screening multi-factors is given. Some interesting conclusions can be drawn from the results:

1. Based on the structural characteristics and working principle of the hydraulic rolling reshaper, considering the dual nonlinear characteristics of the contact and material, a parametric finite element model of hydraulic rolling reshaper repairing shrinkage deformation casing is developed.
2. The orthogonal test is performed to analyse and screen the eight geometric parameters of the reshaper, and the following five structural parameters are determined which have a significant effect on the shaping effect: the main body diameter of the 1st stage, exposed size of the ball, the reshaper's taper, length of the shaping stage, and the total number of stages of the reshaper.
3. By analysing the coupling relationship between structural parameters and combining it with the processing requirements, the value range of the five significant factors is reasonably determined, the regression model of the responses is obtained by stepwise regression method, and the multi-parameter coupling optimization mathematical model of a hydraulic rolling reshaper is obtained.
4. The optimal structure of the reshaper is obtained after optimization: the main body diameter of the 1st stage is 100 mm, the exposed size of the ball is 5.131 mm, the reshaper's taper is 1.345°, the length of the shaping stage is 238.68 mm, and the total stages of reshaper is 7. Moreover, the optimized reshaper can protect the casing better and improve the shaping effect of the casing with different deformation diameters, which can effectively improve the efficiency of the workover.

In addition, to facilitate the calculation, the numerical simulation in this paper has been simplified to a certain extent. To better reflect the stress change and distribution law in the shaping process, more factors that may affect the shaping effect can be considered, such as: considering the rolling contact of the ball with the casing and the body of the reshaper, considering the change of high-temperature material properties in the shaping process and the influence of the initial residual stress of the casing on the shaping effect, etc., so as to further improve the level of simulation and improve the optimization results.

## 7 ACKNOWLEDGEMENTS

The authors are thankful for the financial support of the National Natural Science Foundation of China [51674088] and the Natural Science Foundation of Heilongjiang [LH2021E011].

## 8 REFERENCES

[1] Jiang, D.M. (2004). *The optimized research of the structure of plastic tool for repairing the destroyed casing well*. Daqing Petroleum Institute, Daqing, p. 46. (in Chinese)

[2] Chen, X.J., Wang, Z.C., Liu, H. (2005). Mechanical behavior of eccentric tube expander in shaping process. *Oil-gas Field Surface Engineering*, vol. 24, no. 1, p. 20, **DOI:10.3969/j.issn.1006-6896.2005.01.011**. (in Chinese)

[3] Bai, H.L. (2016). *Mechanics analysis of casing repair and optimum design for cone angle of shaper*. China University of Petroleum (East China), Qingdao, p. 57-63. (in Chinese)

[4] Lin, Y.H., Deng, K.H., Zeng, D.Z., Liu, W.Y., Zhu, H.J., Xie J., Zhou, Y., Wang, W.J. (2013). Numerical and experimental study on working mechanics of pear-shaped casing swage. *Advances in Mechanical Engineering*, vol. 5, art. ID 893723, **DOI:10.1155/2013/893723**.

[5] Deng, K.H., Liu, W.Y., Liu, B., Lin, Y.H., Singh, A. (2019). Repairing force for deformed casing shaping with spinning casing swage and damage behavior of cement sheath. *Applied Mathematical Modelling*, vol. 70, p. 425-438, **DOI:10.1016/j.apm.2019.01.042**.

[6] Luo, M., Jia, L., Gu, H.W., Leng, D.C., Shi, J.B., Li, Q. (2018). Experimental research and mechanical analysis of radial compression casing for hydraulic ball shaper. *Chemical Engineering & Machinery*, vol. 45, no. 5, p. 538-542, **DOI:10.3969/j.issn.0254-6094.2018.05.003**. (in Chinese)

[7] Xu, T.T., Luo, M., Chi, X., Leng, D.C., Yin, W.J., Zhang, J.H. (2020). Mechanical analysis and single shaping limit research of casing rolling shaping. *Machine Tool & Hydraulics*, vol. 48, no. 5, p. 88-92, **DOI:10.3969/j.issn.1001-3881.2020.05.019**. (in Chinese)

[8] Jin, C.J. (2022). Mechanical analysis and structural optimization of the shaping necking sleeve of the hydraulic ball shaper. *Northeast Petroleum University*, Daqing, p. 24-29, DOI:10.26995/d.cnki.gdqsc.2022.000 467. (in Chinese)

[9] De Oliveira Araújo M.S., Dantas Grassi, E.N., Carlos de Araújo, J. (2021). Fatigue tests of superelastic NiTi wires: an analysis using factorial design in single cantilever bending. *Smart Materials & Structures*, vol. 30, no. 12, art. ID 125017, **DOI:10.1088/1361-665X/ac2f82**.

[10] Zhang, F.B., Zhang, J.Q., Ni, H.J., Zhu, Y., Wang, X.X., Wan, X.F., Chen, K. (2021). Optimization of AlSi10MgMn alloy heat treatment process based on orthogonal test and grey relational analysis. *Crystals*, vol. 11, no. 4, art. ID 385, **DOI:10.3390/cryst11040385**.

[11] Pohya, A.A., Kai, W., Kilian, T. (2022). Introducing variance-based global sensitivity analysis for uncertainty enabled operational and economic aircraft technology assessment. *Aerospace Science and Technology*, vol. 122, art. ID 107441, **DOI:10.1016/j.ast.2022.107441**.

[12] Wang, D.F., Lu, F. (2015). Body-in-white lightweight based on multidisciplinary design optimization. *Journal of Jilin University (Engineering and Technology Edition)*, vol. 45, no. 1, p. 29-37, **DOI:10.13229/j.cnki.jdxbgxb201501005**. (in Chinese)

[13] Swain, G., Singh, S., Sonwani, R.K., Singh, R.S., Jaiswal, R.P., Rai, B. N. (2021). Removal of Acid Orange 7 dye in a packed bed bioreactor: Process optimization using response surface methodology and kinetic study. *Bioresource Technology Reports*, vol. 13, art. ID 100620, **DOI:10.1016/j.biteb.2020.100620**.

[14] Salehnia, N., Ahn, J. (2022). Modelling and reconstructing tree ring growth index with climate variables through artificial intelligence and statistical methods. *Ecological Indicators*, vol. 134, art. ID 108496, **DOI:10.1016/j.ecolind.2021.108496**.

[15] Ribeiro, R., Gama, J., Melo, L. (2014). Sectional analysis for volume determination and selection of volume equations for the Tapajos National Forest. *Cerne*, vol. 20, no. 4, p. 605-612, **DOI:10.1590/010477 60201420041400**. (in Potuguese)

[16] Liu, B., Zhou, L. (2007). The design of material compositions of P110 resist collapse casing. *Metal Materials and Metallurgy Engineering*, vol. 185, no. 3, p. 14-18, **DOI:10.3969/j.issn.1005-6084.2007.03.004**. (in Chinese)

[17] Medan, N., Banica, M. (2016). Taguchi versus full factorial design to determine the influence of process parameters on the impact forces produced by water jets used in sewer cleaning. *IOP Conference Series: Materials Science and Engineering*, vol. 161, no. 1, art. ID 012016, **DOI:10.1088/1757-899X/161/1/012016**.

[18] Montgomery, D.C. (2013). *Design and Analysis of Experiments*. 8th Edition. John Wiley & Sons Inc., New York.

[19] Wang, Y., Wang, X.L., Zhang Z.L., Li, Y., Liu, H.L., Zhang, X., Hočevar, M. (2021). Optimization of a self-excited pulsed air-water jet nozzle based on the response surface methodology. *Strojniški vestnik - Journal of Mechanical Engineering*, vol. 67, no. 3, art. ID 75-87, **DOI:10.5545/sv-jme.2020.6995**.

[20] Raji, M.F., Zhao, H., Monday, H.N. (2019). Fast optimization of sparse antenna array using numerical Green's function and genetic algorithm. *International Journal of Numerical Modelling Electronic Networks Devices and Fields*, vol. 33, no. 4, art. ID e2554, **DOI:10.1002/jnm.2544**.

[21] Yang, C.M., Ma, Y.Q., Liu, T.B., Ding, Y.C., Song, W.L. (2023). Lightweight optimization design of beam and column tool rest based on topology and MOGA algorithm. *Mechanical Science and Technology for Aerospace Engineering*, vol. 43, p. 1-9, **DOI:10.13433/j.cnki.1003-8728.20230056**. (in Chinese)

[22] Van, A.L., Nguyen, T.T. (2022). Optimization of friction stir welding operation using optimal taguchi-based ANFIS and genetic algorithm. *Strojniški vestnik - Journal of Mechanical Engineering*, vol. 68, no.6, art. ID 424-438, **DOI:10.5545/sv-jme.2022.111**.

Strojniški vestnik - Journal of Mechanical Engineering 69(2023)11-12, 497-508
DOI:10.5545/sv-jme.2023.651
Original Scientific Paper
Received for review: 2023-05-20
Received revised form: 2023-08-23
Accepted for publication: 2023-09-13


# Surface Quality of AZ91D Magnesium Alloy After Precision Milling with Coated Tools

Jarosław Korpysa* – Józef Kuczmaszewski – Ireneusz Zagórski
Lublin University of Technology, Faculty of Mechanical Engineering, Poland

*This study investigates the surface quality of AZ91D magnesium alloy specimens after precision milling. The milling was conducted with the use of $TiB_2$- and TiAlN-coated carbide end mills. The following variables were used in the milling process: cutting speed $v_c$, feed per tooth $f_z$ and axial depth of cut $a_p$. The surface quality was analysed based on surface roughness parameters and Abbott-Firestone curves. The results showed that the surface quality after machining depended on the tool coating type and applied machining parameters; the only exception was the axial depth of cut because changes in its value did not have any significant effect on the obtained surface quality. After precision milling, AZ91D specimens were characterized by very low surface roughness parameters. The impact of machining conditions was also evaluated with ANOVA analysis, which confirmed the significant effect of cutting speed and feed per tooth. It also indicated the dependence of the roughness parameters on the tool coating type. The tool coating type and machining conditions did not have any significant effect on the Abbott-Firestone curves. Despite the changes applied, the shape of the curves remained similar. The obtained results provide both theoretical and practical knowledge about the achievable surface roughness of AZ91D magnesium alloy specimens after precision milling.*
**Keywords: precision milling, surface quality, Abbott-Firestone curve, ANOVA, coated tools**

**Highlights**

- *Precision milling of AZ91D magnesium alloy enables the formation of high-quality surfaces with low roughness parameter values.*
- *The effect of a change in process parameters on surface roughness depends on the tool coating type.*
- *The changes in the cutting speed and feed per tooth have a significant influence on the surface roughness parameters, validated by ANOVA analysis.*
- *Abbott-Firestone curves have a degressive-progressive shape, favourable in functional terms.*

## 0 INTRODUCTION

Surface roughness is the main factor determining the quality of a machined surface. This is particularly important in precision machining, which is oriented at manufacturing high-accuracy parts; thus, any surface unevenness is an important factor of allowable dimensional and geometrical deviations. The achievement of a surface with the required quality is a very complex problem because it depends on many factors, such as machining strategy and conditions, cutting tool type or cooling conditions. Therefore, conducting research on the effects of individual factors on surface roughness to determine optimum machining conditions is of vital importance regardless of the machined material [1] to [5].

Among the most commonly applied surface roughness parameters is the arithmetic mean height *Ra*, belonging to the group of amplitude parameters. These parameters serve as a basis for evaluating surface texture and describing the roughness of machined surfaces quite well. It should, however, be stressed that the *Ra* parameter has no specific information about the shape of a surface roughness profile. Single peaks have an insignificant effect on this parameter. In effect, this parameter is an absolute measure, which means that it does not take into account whether a given profile has valleys or peaks. Despite its shortcomings, this parameter is very useful for evaluating the stability and control of a technological process [6] to [7]. Another commonly studied surface roughness parameter is the total height of the roughness profile *Rt*, which is determined between the largest profile peak height and the largest profile valley depth. *Rt* is another amplitude-related parameter. *Rt* and *Rz* parameters also provide much more information on fatigue strength [8]. In addition, the *Rt* parameter can affect the functional properties of a surface, including fatigue strength, reflexivity, friction and wear, lubrication, mechanical strength, as well as assembly tolerances [9]. Still, for a comprehensive analysis of surface quality, it is necessary to examine the widest possible range of parameters, because an analysis of a single parameter will only provide basic information about surface texture. Surface topography is examined based on two-dimensional (2D) and three-dimensional (3D) parameters, surface topography maps or isotropy [10] to [12].

As previously mentioned, studies investigating surface roughness after machining usually focus on the *Ra* parameter. For example, a study [13]

*Corr. Author's Address: Lublin University of Technology, Faculty of Mechanical Engineering, Poland, j.korpysa@pollub.pl

investigated changes in the *Ra* parameter after the AM60 magnesium alloy milling process with the use of a carbide end mill with TiN coatings. The *Ra* parameter value for optimal machining parameters was estimated to be approximately 0.3 μm. In a study **[14]** devoted to face milling of AZ61 alloy with the use of a milling cutter with carbide inserts, the obtained *Ra* parameter ranged from 0.1 μm to 0.4 μm. A study **[15]** investigated the machinability of AZ61 alloy. The machining process was conducted with the use of a face milling cutter with carbide inserts, and the obtained *Ra* parameter values ranged approx. 0.14 μm to 0.8 μm (direct feed) and 0.2 μm to 0.7 μm (reversed feed). In a study **[16]**, the authors performed high-speed machining using a face milling cutter, which made it possible to archive very low surface roughness of AZ91D alloy, with the *Ra* parameter ranging from 0.06 μm to 0.13 μm. A study on milling AZ31B alloy specimens **[17]** reported that the surface has deteriorated with increasing the feed per tooth and amount of cutting edges. Similar findings were obtained in a study **[18]**, where the surface roughness parameter *Ra* increased due to an increase in the cutting speed as well as the feed per tooth. A study conducted on milling AZ31B alloy **[19]** demonstrated that a cutting zone cooling method was also of significant importance. The results of a milling process conducted with an AlTiN-coated carbide end mill with four cutting edges showed that the use of cryogenic cooling led to approximately 20 % lower *Ra* when compared to oil cooling. In another study **[20]**, the milling of ZE41 alloy was performed using a face milling cutter with carbide inserts. It was found that the *Ra* parameter value primarily depended on the feed per tooth and the cutting speed (*Ra* ranged from approx. 1.4 μm to 4.1 μm) and that an increase in their values led to increased surface roughness. Research on this magnesium alloy was also described in **[21]**, in which the effect of different cutting parameters on surface roughness was analysed, although using a high-speed steel (HSS) tool. It was shown that increasing the feed per tooth and the depth of cut resulted in a linear increase in the *Ra* parameter, which varied from 0.306 μm to 0.679 μm.

Interesting results were also obtained in a study on Mg-SiC/$B_4C$-reinforced magnesium matrix composite **[22]**. The lowest values of the *Ra* parameter range from approx. 0.4 μm to 0.5 μm were archived when machining was performed with a TiN-coated tool. A study **[23]** examined the influence of variable milling parameters on surface roughness. The milling process of AZ91 alloy was conducted with variable cutting speed, feed per tooth and depth of cut, using a 50 mm diameter face mill with carbide inserts. Obtained values of *Ra* parameter ranged from 0.067 μm to 0.208 μm, and the results showed that surface roughness primarily depended on the feed per tooth, which was also confirmed by ANOVA analysis. That line of research was continued in a study **[24]**, which focused on the determination of optimum milling conditions by TOPSIS analysis based on vibration signals. The results also confirmed that reduced surface roughness primarily resulted from decreased feed per tooth. A more comprehensive analysis of AZ91D alloy surface roughness was conducted in **[25]**, in which profile and areal roughness parameters and surface topography maps were taken into consideration. The results showed that the surface quality of AZ91D alloy specimens milled using a TiAlN-coated carbide tool could considerably be improved by changing values of the cutting speed and feed per tooth.

Improved surface quality can also be obtained by using top-quality carbide milling end mills, as well as tools with cutting edges made of polycrystalline diamond (PCD). To give an example, for the face milling process of Mg-Ca0.8 alloy elements, the obtainable *Ra* values can range from 0.2 μm to 0.8 μm if PCD face mills are used **[26]**. *Ra* parameter values of approx. 0.4 μm were also obtained by combined dry milling and burnishing **[27]** and **[28]**. In a study **[29]**, which was conducted on milling Mg-Ca0.8 alloy specimens using a face mill with uncoated carbide inserts, the obtained *Ra* values were from 0.9 μm to 1.4 μm during normal milling and from 0.09 μm to 0.8 μm during inverse milling. In a study **[30]** investigating the Mg-Ca1.0 alloy in a milling process conducted using a face mill with diamond-like carbon (DLC)-coated inserts, the obtained surface roughness parameter *Ra* values ranged from 0.10 μm to 0.16 μm. The cooling method used may also have a significant impact on the machining effect. Jouini et al. **[31]** proved in their paper that the use of cryogenic cooling for AZ91D magnesium alloy machining can result in a significant improvement in surface quality. However, the improvement only occurred under specific conditions. Minimum quantity lubrication (MQL) can also be an effective cooling method. Research presented in **[32]** indicated that surface roughness could also be reduced using this method, but it was less effective than changing the cutting speed.

In addition to using basic surface roughness parameters, which are well-known and widely used, surface quality can also be evaluated based on the Abbott-Firestone curve and parameters describing this curve. The use of these parameters is a different approach to surface texture evaluation, one that can

effectively be employed to evaluate the quality of surfaces obtained by different machining methods [33] to [35]. Material ratio curves were used, for instance, in the paper [36]. The curves obtained on the surfaces of the AZ91D alloy had mostly a degressive-progressive shape, while changes in machining conditions mainly caused a change in their inclination. The course of the curves also looked similar after trochoidal milling of AZ91D and AZ31 alloys [37]. The curves flattened when the cutting speed was increased, and the trochoidal step was reduced. Trochoidal milling was also performed in the paper [38], analysing Incoloy 800 surfaces. Increasing the feed rate resulted in an increase in the values of the *Spk* and *Sk* parameters, while the trochoidal stepover mainly increased the *Spk* parameter. Based on the curve shape, one can infer the tribological wear resistance of a given surface. A progressive shape of the curve means that the analysed surface has rounded peaks and is more wear-resistant than surfaces described by degressive shape curves. The curve shape is described by parameters, which are determined based on that curve. These parameters include reduced peak height *Rpk*, reduced valley depth *Rvk* and core roughness depth *Rk*. Based on these parameters, one can predict the influence of surface texture on the operational aspects of machine components [39] and [40]. The effect of reduced friction can also occur when the reduced valley depth *Rvk* is higher than the reduced peak height *Rpk* [8] and [41]. The material contribution curves in the case of AZ61 alloy were also used to analyse dry sliding wear behaviour [42].

According to the presented review of recent publications in the field of magnesium alloy milling, a considerable number of papers are limited to the analysis of only one surface roughness parameter. Such an approach is highly inadequate, and this does not allow an appropriate description of the surface quality. A more comprehensive representation of the surface is only possible after analysis of more parameters, including functional parameters. Furthermore, all these papers concern conventional machining, whereas the research described in the present paper involves precision milling, which is the main novelty of this study. The application of precision milling for magnesium alloy machining has hardly been used thus far, which is confirmed by the very small number of available publications on this subject. Due to the different machining process mechanics under these machining conditions, the results obtained in conventional machining cannot be directly transferred to precision machining, so that requires separate research. The main objective of the research is, therefore, to obtain a knowledge base on the impact of cutting factors such as technological conditions or tool coating type on surface roughness. An important element of the paper is also the analysis of functional parameters and Abbott-Firestone curves to evaluate the surface in terms of possible component interaction. The effect of the various cutting parameters and tool coating type on surface roughness was also assessed using ANOVA.

## 1 EXPERIMENTAL

This study involved conducting the milling process under precision machining conditions and evaluating the obtained surface quality. Test specimens were made of the AZ91D magnesium alloy. This is one of the most widely applied magnesium alloys in many industrial branches. The machining process was performed on the AVIA VMC 800HS milling centre (Fig. 1). The machine has a maximum rotational speed of 24,000 rpm, which allows for conducting milling processes at a very high cutting speed.

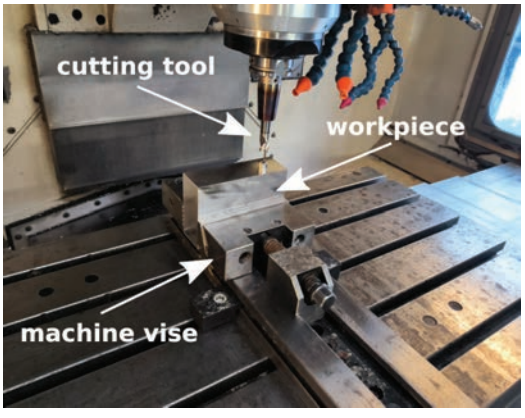


**Fig. 1.** *Experimental setup*

Milling tests were performed with the use of two cutting tools with two different types of coating: $TiB_2$ and TiAlN. These coatings are dedicated to the machining of magnesium alloys. The tools were AM3SSD1600A100 Mitsubishi end mills, each having a diameter of 16 mm and three cutting edges. The end mills were mounted in Celsio heat-shrinking tool holders from Schunk. To ensure increased stability of the machining process, the holder-tool system was balanced at G2.5 to a speed of 25,000 rpm in compliance with the ISO 21940-1 standard [43].

Apart from the cutting tools, the basic technological parameters of the milling process, i.e., cutting speed $v_c$, feed per tooth $f_z$ and axial depth of cut $a_p$, were made variable too. The study was conducted

for 3 levels of variability. In contrast, the radial depth of cut $a_e$ was constant. A plan of the experiment and values of the milling parameters applied therein are stated in Table 1.

**Table 1.** *Plan of the experiment and milling parameters*

| Cutting tool | $v_c$ [m/min] | $f_z$ [μm/tooth] | $a_p$ [μm] | $a_e$ [mm] |
|---|---|---|---|---|
| TiB2-coated, TiAlN-coated | 400 | 5 | 80 | 14 |
| | 800 | | | |
| | 1200 | | | |
| | 800 | 1 | 80 | |
| | | 5 | | |
| | | 9 | | |
| | 800 | 5 | 60 | |
| | | | 80 | |
| | | | 100 | |

Surface quality after the machining tests was examined based on obtained surface roughness profile parameters and Abbott-Firestone curves. Surface roughness was measured using the Hommel Etamic T8000 RC120-400 in compliance with PN-EN ISO 4287 [44] and PN-EN ISO 13565 [45] standards, with a measuring length $ln$ = 4 mm, a sampling length $lr$ = 0.8 mm and a traverse speed $v_t$ = 0.5 mm/s. Each measurement was repeated ten times per every machined surface in order to determine mean values and standard deviations. The necessary number of repetitions was previously estimated.

## 3 RESULTS AND DISCUSSION

### 3.1 Surface Roughness Analysis

The surface quality of the test specimens after precision milling was examined in terms of surface roughness amplitude parameters *Ra*, *Rv*, *Rp*, *Rt* and the functional parameters *Rvk*, *Rk*, *Rpk* describing the Abbott-Firestone curve. To illustrate the discussed surfaces, Fig. 2 presents examples of surface topography maps obtained during the milling process with intermediate values of technological parameters and with both cutting tools.

From the isometric images shown, it can be seen that both surfaces have a fairly homogeneous structure, as there are no high peaks or deep valleys, and the tool marks are also small. The surfaces machined with the use of both tools do not differ noticeably from each other. However, a greater share of valleys can be observed on the surface obtained with an end mill with TiAlN coating.

In the following part of the study, an analysis of the effect of changing technological parameters on the surface structure was carried out based on the surface roughness parameters. The influence of cutting speed and type of coating on the mean values of the roughness parameters is presented in Figs. 3 to 5.

The mean values of the *Ra* parameter obtained for both end mills were similar, and their range is relatively narrow. During the milling process with the $TiB_2$-coated tool, an increase in the cutting speed led to a decrease in the *Ra* parameter value first and then to its increase. In contrast, the use of the TiAlN-coated tool led to a decrease in the *Ra* parameter over the entire range of tested cutting speed. The results obtained with the TiAlN-coated tool are also characterized by a greater scatter of values.

The results demonstrate that the *Rv*, *Rp*, and *Rt* parameters depend on cutting speed. In the milling process conducted with the $TiB_2$-coated tool, the values of these parameters decreased initially and subsequently increased again with the highest tested cutting speed value. When the milling process was

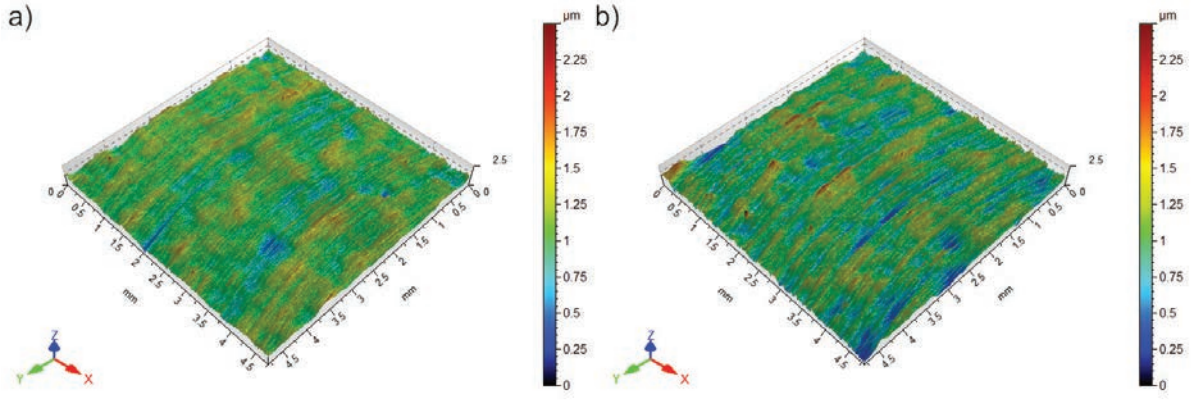


**Fig. 2.** *Surface topography maps obtained using; a) TiB2-coated, and b) TiAlN-coated tool*

performed with the use of the TiAlN-coated tool, these parameters decreased in a roughly linear manner. The peak heights are insignificantly higher than the valley depth, which indicates a relatively symmetric surface roughness profile distribution. As a result of using the $TiB_2$-coated tool, the above surface roughness parameters are lower, and the scatter of their values is smaller.

Similar dependencies were also observed for the *Rvk*, *Rk*, and *Rpk* parameters. In the milling process conducted with the $TiB_2$-coated tool, an increase in the cutting speed leads to a decrease in these parameters first and then in their increase. When the milling was conducted with the TiAlN-coated tool, values of these parameters decreased throughout the tested cutting speed range. Also, one can again observe a close correlation between the parameters *Rvk* and *Rpk* and the parameters *Rv* and *Rp*. Higher valley depth and peak heights result in higher values of *Rvk* and *Rpk*.

Figs. 6 to 8 show the influence of feed per tooth and tool coating type on the analysed surface roughness parameters.

The effect of feed per tooth on surface roughness is similar, albeit less powerful, to that observed in relation to cutting speed. An analysis of the results also demonstrates that there are greater differences between values of the surface roughness parameters depending on the tool used. The highest values of *Ra* are obtained with the lowest tested feed per tooth value. This suggests that the ploughing phenomenon may occur in this range. For the $TiB_2$-coated tool, an increase in the feed per tooth causes a clear decrease in these parameters first and then a slight increase in their values again. The use of the TiAlN-coated tool leads to a steady reduction in their values with increasing the feed per tooth. The decrease in value is associated with a reduction in the ploughing phenomenon and an increasing contribution of the material-cutting process. This phenomenon is typical for precision machining, which is a significant difference from conventional machining.

Similar dependencies can be observed for the *Rv*, *Rp* and *Rt* parameters. Depending on the tool used, their mean values differ more significantly

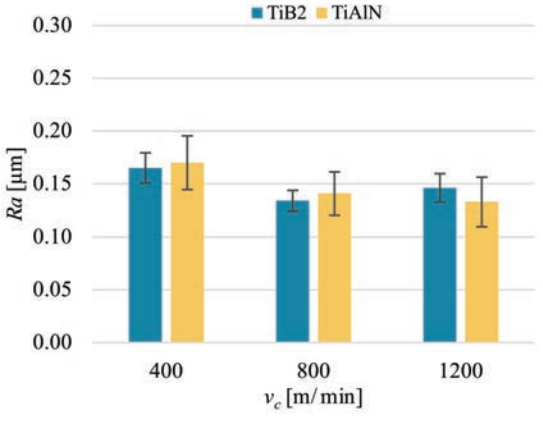


**Fig. 3.** *Ra* parameter vs. cutting speed $v_c$

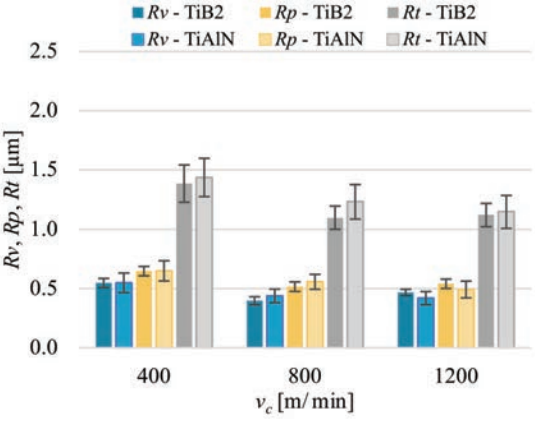


**Fig. 4.** *Rv*, *Rp* and *Rt* parameters vs. cutting speed $v_c$

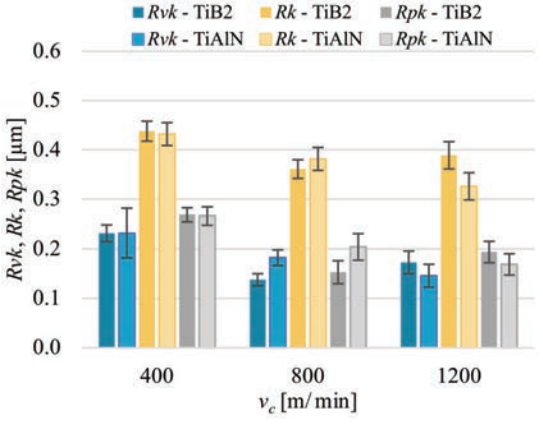


**Fig. 5.** *Rvk, Rk, and Rpk parameters* vs. *cutting speed* $v_c$

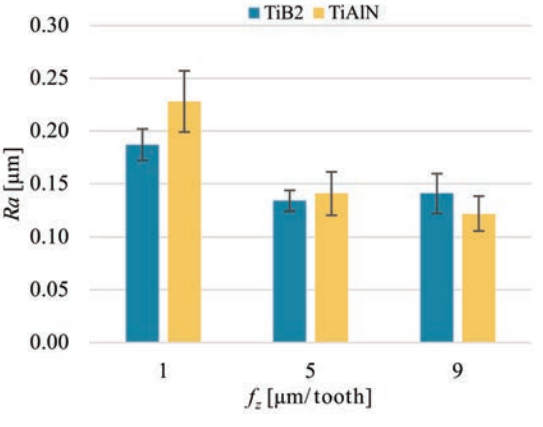


**Fig. 6.** *Ra* parameter vs. feed per tooth $f_z$

than those obtained for the variable cutting speed. The highest values are again obtained for the milling process conducted with the lowest tested feed per tooth value. A further increase in the feed per tooth leads to a relatively high decrease in the values of these parameters, followed by their moderate increase. When the TiAlN-coated tool is used, the surface roughness parameters gradually decrease. Although the peak heights are higher, the difference between them and the valley depth is not great, which indicates that the roughness profile distribution was relatively uniform.

The effect of feed per tooth on the *Rvk*, *Rk* and *Rpk* parameters is similar to that observed for other surface roughness parameters. In the milling process conducted with the $TiB_2$-coated tool, the values of these parameters decrease first and then slightly increase. When the milling process is conducted with the TiAlN-coated tool, the surface roughness parameters decrease as the feed per tooth value increases. Again, one can observe a correlation between *Rvk* and *Rpk* as well as *Rv* and *Rp*.

The surface roughness results obtained during machining with a variable axial depth of cut are given in Figs. 9 to 11.

In contrast to the variable cutting speed and feed per tooth, the variable depth of cut has no significant impact on the analysed surface roughness parameters. The mean value of the *Ra* parameter remains comparable, irrespective of the applied depth of cut and tool type. Nonetheless, the results obtained for the milling tests carried out with the use of the TiAlN-coated tool are characterized by a greater scatter of values.

A similar trend can be observed for the parameters *Rv*, *Rp*, and *Rt*. Irrespective of the axial depth of the cut value, the mean values of these parameters are similar. Here again, the peak height is higher than the valley depth. For the milling process conducted with the $TiB_2$-coated end mill, the mean values of these

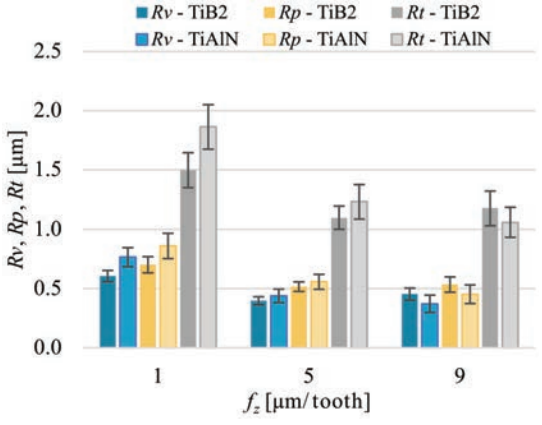


**Fig. 7.** *Rv*, *Rp* and *Rt* parameters vs. feed per tooth $f_z$

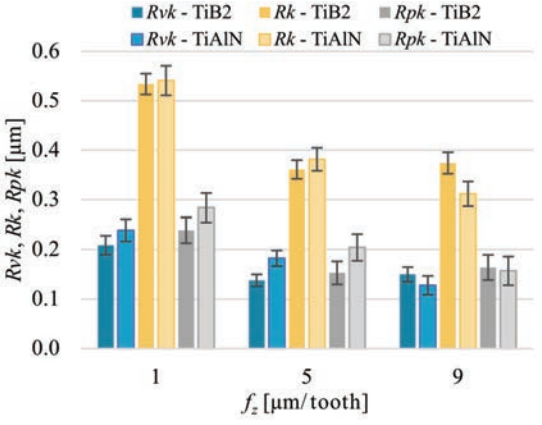


**Fig. 8.** *Rvk, Rk, and Rpk* parameters vs. feed per tooth $f_z$

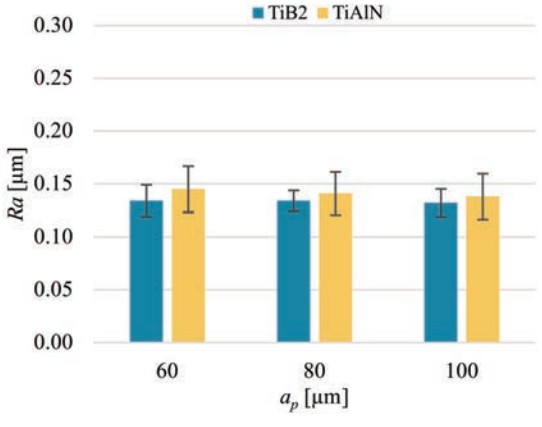


**Fig. 9.** *Ra parameter* vs. *axial depth of cut* $a_p$

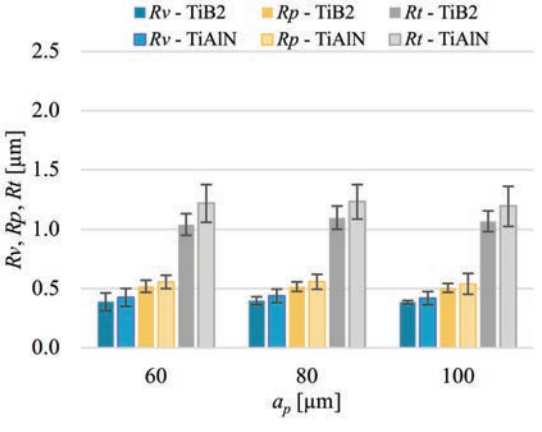


**Fig. 10.** *Rv*, *Rp* and *Rt* parameters vs. axial depth of cut $a_p$

parameters are lower, and the result scatter is smaller, which can best be observed for the *Rt* parameter.

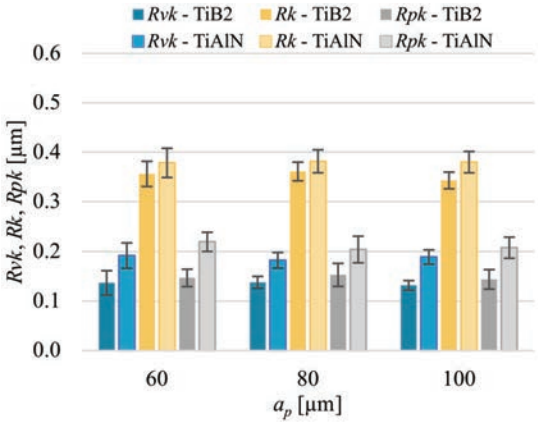


**Fig. 11.** *Rvk, Rk, and Rpk* parameters vs. axial depth of cut $a_p$

The variable axial depth of cut has no significant effect on the parameters *Rvk*, *Rk*, and *Rpk*. The mean values of these parameters are generally similar, and their lower values are received for the surfaces machined with the $TiB_2$-coated tool. Here again, one can observe a relationship between *Rvk* and *Rpk*, as well as *Rv* and *Rp*. Due to the non-significant effect of the axial depth of the cut, it appears to be possible to increase the process efficiency without a noticeable deterioration in surface quality.

### 3.2 Abbott-Firestone Curves Analysis

During measurements of surface quality, the Abbott-Firestone curves were also obtained. The curves were used to determine the values of the previously analysed parameters *Rvk*, *Rk*, and *Rpk*. The curves make it possible to determine specifically the functional properties of the surfaces after machining. Examples of the curves obtained for variable milling parameters and both tool coating types are shown in Figs. 12 to 14.

Irrespective of the change in technological parameters and cutting tool, the obtained Abbott-Firestone curves have a similar degressive-progressive pattern. Although all curves have similar inclination angles, the curves obtained from milling with the TiAlN-coated tool are slightly more inclined. This indicates the presence of sharper peaks, which entails reduced abrasive resistance of the surface. The obtained Abbott-Firestone curves have a roughly symmetric distribution, which is confirmed by the fact that the parameters *Rvk* and *Rpk* have similar values. The surfaces generated during milling are devoid of high peaks and deep valleys, and the core roughness depth predominates.

An analysis of the Abbott-Firestone curves obtained from milling with the $TiB_2$-coated tool also reveals a greater concentration of the material in the core area. This implies that the abrasion period will

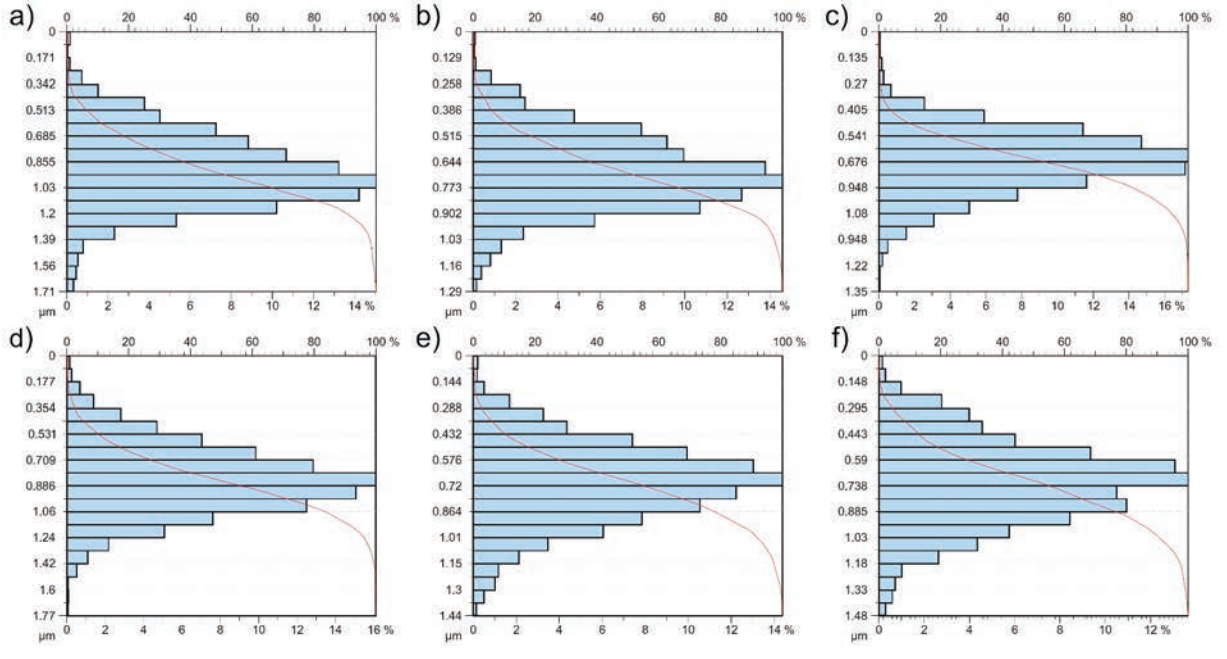


**Fig. 12.** *Abbott-Firestone curves obtained from milling with a $TiB_2$-coated tool: a) $v_c$ = 400 m/min, b) $v_c$ = 800 m/min, c) $v_c$ = 1200 m/min; and with a TiAlN-coated tool: d) $v_c$ = 400 m/min, e) $v_c$ = 800 m/min, f) $v_c$ = 1200 m/min*

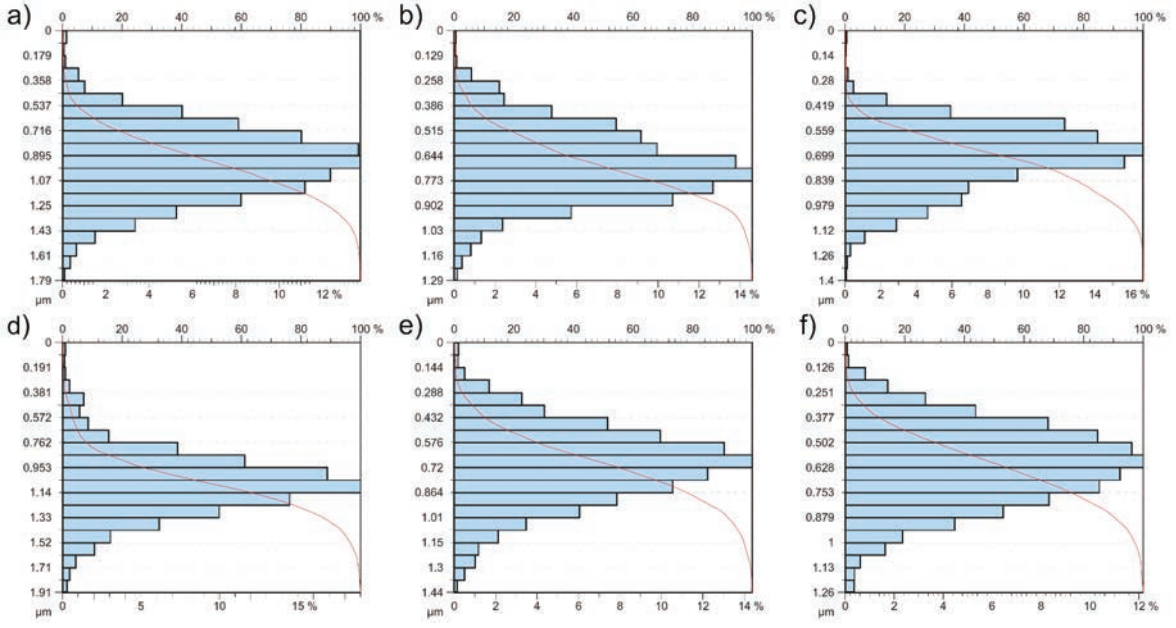


**Fig. 13.** *Abbott-Firestone curves obtained from milling with a $TiB_2$-coated tool: a) $f_z$ = 1 µm/tooth, b) $f_z$ = 5 µm/tooth, c) $f_z$ = 9 µm/tooth; and with a TiAlN-coated tool: d) $f_z$ = 1 µm/tooth, e) $f_z$ = 5 µm/tooth, f) $f_z$ = 9 µm/tooth*

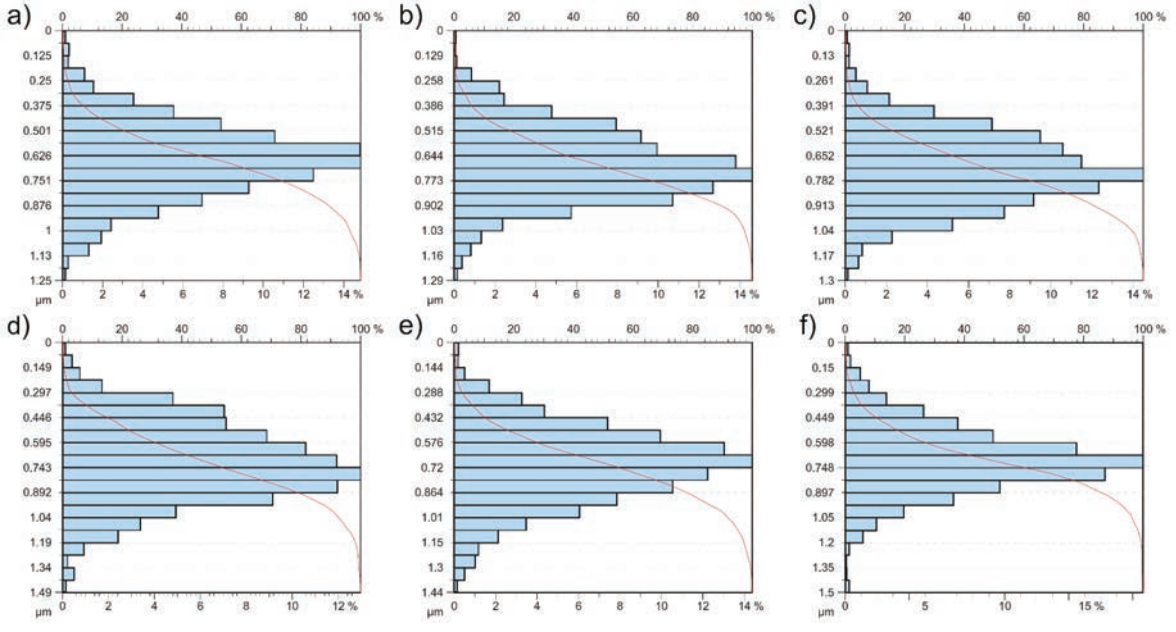


**Fig. 14.** *Abbott-Firestone curves obtained from milling with a $TiB_2$-coated tool: a) $a_p$ = 60 µm, b) $a_p$ = 80 µm, c) $a_p$ = 100 µm; and with a TiAlN-coated tool: d) $a_p$ = 60 µm, e) $a_p$ = 80 µm, f) $a_p$ = 100 µm*

be shorter due to the lack of high peaks. As for the TiAlN-coated tool, the material is more spread over the entire roughness profile height. Consequently, the values of *Rvk* and *Rpk* parameters are higher than those obtained with the $TiB_2$-coated tool. High peaks will result in faster abrasion. In contrast, deep valleys encourage the accumulation of lubricant, which reduces friction and facilitates the movement of cooperating surfaces. In terms of the variable milling parameters, the Abbott-Firestone curves only reveal the presence of small changes in the area size of valley depths, core roughness and peak heights. No significant changes can, however, be observed in the patterns of these curves, which means that the surface

quality and, thus, its functional properties have not undergone any profound changes. Therefore, by modifying the machining conditions, it is feasible to attempt to reduce the values of the preferred surface roughness parameters without compromising the functional properties of the surfaces.

### 3.3 ANOVA Analysis

The obtained results were also analysed statistically using ANOVA with an assumed level of confidence $\alpha = 0.05$. The analysis was performed using Statistica 13 software. The analysis determined the significance of the effect of changing individual technological parameters and the tool coating type on surface roughness parameters. The results of the analysis are presented in Tables 2 to 4.

**Table 2.** *ANOVA results for variable cutting speed*

| | Factor | *S* | *df* | *MS* | *F* | *p* |
|---|---|---|---|---|---|---|
| *Ra* | $v_c$ | 0.011 | 2 | 0.006 | 15.879 | 0.000 |
| | Coating | 0.000 | 1 | 0.000 | 0.005 | 0.946 |
| | Total | 0.011 | 3 | 0.006 | | |
| *Rv* | $v_c$ | 0.190 | 2 | 0.095 | 31.471 | 0.000 |
| | Coating | 0.000 | 1 | 0.000 | 0.017 | 0.898 |
| | Total | 0.190 | 3 | 0.095 | | |
| *Rp* | $v_c$ | 0.204 | 2 | 0.102 | 27.219 | 0.000 |
| | Coating | 0.000 | 1 | 0.000 | 0.013 | 0.908 |
| | Total | 0.204 | 3 | 0.102 | | |
| *Rt* | $v_c$ | 0.912 | 2 | 0.456 | 25.336 | 0.000 |
| | Coating | 0.075 | 1 | 0.075 | 4.153 | 0.046 |
| | Total | 0.986 | 3 | 0.531 | | |
| *Rvk* | $v_c$ | 0.069 | 2 | 0.035 | 37.914 | 0.000 |
| | Coating | 0.001 | 1 | 0.001 | 0.565 | 0.456 |
| | Total | 0.070 | 3 | 0.035 | | |
| *Rk* | $v_c$ | 0.068 | 2 | 0.034 | 39.460 | 0.000 |
| | Coating | 0.004 | 1 | 0.004 | 4.510 | 0.038 |
| | Total | 0.072 | 3 | 0.038 | | |
| *Rpk* | $v_c$ | 0.102 | 2 | 0.051 | 71.800 | 0.000 |
| | Coating | 0.001 | 1 | 0.001 | 1.324 | 0.255 |
| | Total | 0.103 | 3 | 0.052 | | |

Sum-of-squares (SS), Degrees of freedom (df), Mean squares (MS), F ratio (F), and p-value (p).

The performed statistical analysis confirmed that the change in cutting speed had a statistically significant effect on the mean values of all analysed surface roughness parameters ($p < 0.05$). By changing them, it is, therefore, possible to impact the surface roughness. It was also shown that the tool coating type had no statistically significant effect on roughness parameters. The results obtained were, therefore, similar for both cutting tools. The exceptions were the *Rt* and *Rk* parameters, where the type of coating had a significant effect on their mean values measured on the machined surfaces.

**Table 3.** *ANOVA results for variable feed per tooth*

| | Factor | *S* | *df* | *MS* | *F* | *p* |
|---|---|---|---|---|---|---|
| *Ra* | $f_z$ | 0.071 | 2 | 0.036 | 69.907 | 0.000 |
| | Coating | 0.001 | 1 | 0.001 | 2.744 | 0.103 |
| | Total | 0.073 | 3 | 0.037 | | |
| *Rv* | $f_z$ | 0.980 | 2 | 0.490 | 81.671 | 0.000 |
| | Coating | 0.023 | 1 | 0.023 | 3.866 | 0.054 |
| | Total | 1.004 | 3 | 0.513 | | |
| *Rp* | $f_z$ | 0.963 | 2 | 0.482 | 61.847 | 0.000 |
| | Coating | 0.023 | 1 | 0.023 | 2.979 | 0.090 |
| | Total | 0.987 | 3 | 0.505 | | |
| *Rt* | $f_z$ | 3.885 | 2 | 1.943 | 64.165 | 0.000 |
| | Coating | 0.243 | 1 | 0.243 | 8.021 | 0.006 |
| | Total | 4.128 | 3 | 2.186 | | |
| *Rvk* | $f_z$ | 0.078 | 2 | 0.039 | 75.703 | 0.000 |
| | Coating | 0.005 | 1 | 0.005 | 8.839 | 0.004 |
| | Total | 0.083 | 3 | 0.044 | | |
| *Rk* | $f_z$ | 0.428 | 2 | 0.214 | 265.190 | 0.000 |
| | Coating | 0.001 | 1 | 0.001 | 1.280 | 0.263 |
| | Total | 0.429 | 3 | 0.215 | | |
| *Rpk* | $f_z$ | 0.116 | 2 | 0.058 | 66.380 | 0.000 |
| | Coating | 0.013 | 1 | 0.013 | 15.345 | 0.000 |
| | Total | 0.129 | 3 | 0.071 | | |

**Table 4.** *ANOVA results for variable axial depth of cut*

| | Factor | *S* | *df* | *MS* | *F* | *p* |
|---|---|---|---|---|---|---|
| *Ra* | $a_p$ | 0.000 | 2 | 0.000 | 0.343 | 0.711 |
| | Coating | 0.001 | 1 | 0.001 | 3.237 | 0.077 |
| | Total | 0.001 | 3 | 0.001 | | |
| *Rv* | $a_p$ | 0.003 | 2 | 0.001 | 0.436 | 0.649 |
| | Coating | 0.020 | 1 | 0.020 | 6.674 | 0.012 |
| | Total | 0.023 | 3 | 0.022 | | |
| *Rp* | $a_p$ | 0.003 | 2 | 0.001 | 0.446 | 0.642 |
| | Coating | 0.020 | 1 | 0.020 | 6.170 | 0.016 |
| | Total | 0.023 | 3 | 0.022 | | |
| *Rt* | $a_p$ | 0.017 | 2 | 0.008 | 0.527 | 0.593 |
| | Coating | 0.318 | 1 | 0.318 | 20.191 | 0.000 |
| | Total | 0.334 | 3 | 0.326 | | |
| *Rvk* | $a_p$ | 0.000 | 2 | 0.000 | 0.347 | 0.708 |
| | Coating | 0.041 | 1 | 0.041 | 126.588 | 0.000 |
| | Total | 0.041 | 3 | 0.041 | | |
| *Rk* | $a_p$ | 0.001 | 2 | 0.000 | 0.920 | 0.404 |
| | Coating | 0.011 | 1 | 0.011 | 20.310 | 0.000 |
| | Total | 0.012 | 3 | 0.011 | | |
| *Rpk* | $a_p$ | 0.001 | 2 | 0.000 | 0.599 | 0.553 |
| | Coating | 0.059 | 1 | 0.059 | 125.954 | 0.000 |
| | Total | 0.060 | 3 | 0.060 | | |

The analysis also confirmed a significant effect of the change in feed per tooth for all the analysed surface roughness parameters. In this case, the tool coating type was also more important, proving to be significant for the *Rt, Rvk* and *Rpk* parameters. However, for the other parameters, the tool coating type had no significant effect on the mean values of surface roughness parameters.

A completely opposite relationship occurred for the results obtained when the precision milling process was performed with a variable axial depth of cut. ANOVA results indicated that the change in the depth of cut had no significant effect on any of the analysed surface roughness parameters. However, the type of coating proved to be significant in this case, and it influenced the mean values of measured roughness parameters. The only exception was the *Ra* parameter, for which the tool coating type was not significant.

From the performed statistical analysis, it can be concluded that the change in cutting speed and feed per tooth had the greatest influence on the roughness parameters measured on the machined surfaces. However, the change in axial depth was not significant, which makes it possible to increase machining efficiency without any deterioration in surface quality. The significance of the tool coating type depends on the changed cutting parameter.

## 4 CONCLUSIONS

This experimental study and its findings made it possible to evaluate the surface quality of AZ91D magnesium alloy specimens after precision milling. The results demonstrated that the effect of the applied machining conditions on the analysed surface roughness parameters depended on the tool coating type. The only exception was the variable axial depth of cut because changes in its value did not have any significant effect on the obtained surface quality, irrespective of the tool coating type. Cutting speed and feed per tooth were the most significant factors, which resulted in a reduction in roughness parameters by up to 52 %. Whereas in milling conducted with the TiAlN-coated tool, the use of variable cutting speed and feed always led to a gradual decrease in the surface roughness parameters. In contrast, when the machining was performed with the $TiB_2$-coated tool, the surface roughness parameters decreased first and then increased again. For this reason, it appears to be preferable to use intermediate machining conditions for the $TiB_2$ tool, whereas the highest parameters for the TiAlN tool. Still, the mean values of the surface roughness parameters in the most optimal conditions were mostly similar for both tool coating types, and their differences did not exceed 16 %. This is also confirmed by the ANOVA analysis. A definite indication of a tool coating type providing better results is, therefore, not possible. Similar surface roughness can be achieved with both coatings. The results obtained for the surface machined with the $TiB_2$-coated tool were, however, characterised by a smaller scatter of values. An analysis of the Abbott-Firestone curves demonstrated that the cutting parameters and the type of tool coating had no significant effect on the surface roughness profile shape. Small changes were only observed for the curves describing the parameters *Rvk*, *Rk*, and *Rpk*. Nonetheless, those changes were too small to have any profound impact on the functional properties of the surface. The relatively small inclination angle of the Abbott-Firestone curves indicates that the surfaces after precision machining have reasonably high abrasion resistance. The obtained surface structure and low roughness parameters values confirm that the precision milling process can be successfully used to manufacture magnesium alloy components characterised by a high surface quality.

In future studies, the number of analysed values of technological parameters for which machining will be carried out should be increased. This will enable a more accurate determination of the effect of varying machining conditions on surface roughness. The extension of the research will also enable optimisation of the machining conditions in order to achieve the highest possible surface quality. Collecting more information will also enable the process to be optimised by simulating test results.

## 5 ACKNOWLEDGEMENTS

This research was financed by the Mechanical Engineering Discipline Fund of Lublin University of Technology (Grant No. FD-20/IM-5/060).

## 6 REFERENCES

[1] Gobivel, K., Vijay Sekar, K.S. (2022). Influence of cutting parameters on end milling of magnesium alloy AZ31B. *Materials Today: Proceedings*, vol. 62, p. 933-937, **DOI:10.1016/j.matpr.2022.04.075**.

[2] Karkalos, N.E., Karmiris-Obratański, P., Kurpiel, S., Zagórski, K., Markopoulos, A.P. (2021). Investigation on the surface quality obtained during trochoidal milling of 6082 aluminum alloy. *Machines*, vol. 9, no. 4, art. ID 75, **DOI:10.3390/machines9040075**.

[3] Kuczmaszewski, J., Pieśko, P., Zawada-Michałowska, M. (2016.) Surface roughness of thin-walled components made of aluminium alloy EN AW-2024 following different milling strategies. *Advances in Science and Technology Research Journal*, vol. 10, no. 30, p. 150-158, **DOI:10.12913/22998624/62515**.

[4] Natarajan, M., Chinnasamy, B., Bejaxhin Alphonse, B. (2022). Investigation of machining parameters in thin-walled plate milling using a fixture with cylindrical support heads. *Strojniški vestnik - Journal of Mechanical Engineering*, vol. 68, no. 12, p. 746-756, **DOI:10.5545/sv-jme.2022.273**.

[5] Dung, H., Nguyen, N., Quy, T., Thien, N. (2019). Cutting forces and surface roughness in face-milling of SKD61 hard steel. *Strojniški vestnik - Journal of Mechanical Engineering*, vol. 65, no. 6, p. 375-385, **DOI:10.5545/sv-jme.2019.6057**.

[6] Pradeep Kumar, M., Venkatesan, R., Manimurugan, M. (2022). Optimization of process parameters in turning of magnesium AZ91D alloy for better surface finish using genetic algorithm. *Acta Innovations*, vol. 43, p. 54-62, **DOI:10.32933/ActaInnovations.43.5**.

[7] Zagórski, I., Szczepaniak, A., Kulisz, M., Korpysa, J. (2022). Influence of the tool cutting edge helix angle on the surface roughness after finishing milling of magnesium alloys. *Materials*, vol. 15, no. 9, art. ID 3184, **DOI:10.3390/ma15093184**.

[8] Grzesik, W. (2015). Effect of the machine parts surface topography features on the machine service. *Mechanik*, vol. 8-9, p. 587-593, **DOI:10.17814/mechanik.2015.8-9.493**. (in Polish)

[9] Sedlaček, M., Vilhena, L.M.S., Podgornik, B., Vižintin, J. (2011). Surface topography modelling for reduced friction. *Strojniški vestnik - Journal of Mechanical Engineering*, vol. 57, no. 9, p. 674-680, **DOI:10.5545/sv-jme.2010.140**.

[10] Grobelny, P., Legutko, S., Habrat, W., Furmański, L. (2018). Investigations of surface topography of titanium alloy manufactured with the use of 3D print. *IOP Conference Series: Materials Science and Engineering*, vol. 393, art. ID 012108, **DOI:10.1088/1757-899X/393/1/012108**.

[11] Pawlus, P., Reizer, R., Wieczorowski, M. (2021). Functional importance of surface texture parameters. *Materials*, vol. 14, no. 18, art. ID 5326, **DOI:10.3390/ma14185326**.

[12] Skoczylas, A., Zaleski, K., Matuszak, J., Ciecieląg, K., Zaleski, R., Gorgol, M. (2022). Influence of slide burnishing parameters on the surface layer properties of stainless steel and mean positron lifetime. *Materials*, vol. 15, no. 22, art. ID 8131, **DOI:10.3390/ma15228131**.

[13] Sathyamoorthy, V., Deepan, S., Sathya Prasanth, S.P., Prabhu, L. (2017). Optimization of machining parameters for surface roughness in end milling of magnesium AM60 alloy. *Indian Journal of Science and Technology*, vol. 10, no. 32, p. 1-7, **DOI:10.17485/ijst/2017/v10i32/104651**.

[14] Alharti, N.H., Bingol, S., Abbas, A.T., Ragab, A.E., El-Danaf, E.A., Alharbi, H.F. (2017). Optimizing cutting conditions and prediction of surface roughness in face milling of AZ61 using regression analysis and artificial neural network. *Advances in Materials Science and Engineering*, vol. 2017, art. ID 7560468, **DOI:10.1155/2017/7560468**.

[15] Chirita, B., Grigoras, C., Tampu, C., Herghelegiu, E. (2019). Analysis of cutting forces and surface quality during face milling of a magnesium alloy. *IOP Conference Series: Materials Science and Engineering*, vol. 591, art. ID 012006, **DOI:10.1088/1757-899X/591/1/012006**.

[16] Ruslan, M.S., Othman, K., Ghani, J.A., Kassim, M.S., Haron, C.H. (2016). Surface roughness of magnesium alloy AZ91D in high speed milling. *Jurnal Teknologi*, vol., 78, no. 6-9, p. 115-119, **DOI:10.11113/jt.v78.9158**.

[17] Kim, J.D., Lee, K.B. (2010). Surface roughness evaluation in dry-cutting of magnesium alloy by air pressure coolant. *Engineering*, vol. 2, no. 10, p. 788-792, **DOI:10.4236/eng.2010.210101**.

[18] Shi, K., Zhang, D., Ren, J., Yao, C., Huang, X. (2016). Effect of cutting parameters on machinability characteristics in milling of magnesium alloy with carbide tool. *Advances in Mechanical Engineering*, vol. 8, no. 1, p. 1-9, **DOI:10.1177/1687814016628392**.

[19] Chhetir, S., Tariq, M., Mohapatra, S., Sumi, V., Zhimomi, A., Davis, R., Singh, A. (2020). Surface characteristics enhancement of biocompatible Mg alloy AZ31B by cryogenic milling. *IOP Conference Series: Materials Science and Engineering*, vol. 1004, art. ID 012011, **DOI:10.1088/1757-899X/1004/1/012011**.

[20] Sivam, S.P., Bhat, M.D., Natarajan, S., Chauhan, N. (2018). Analysis of residual stresses, thermal stresses, cutting forces and other output responses of face milling operation on ZE41 magnesium alloy. *International Journal of Modern Manufacturing Technologies*, vol. 10, no. 1, p. 92-101.

[21] Kumar, R., Katyal, P., Kumar, K. (2023). Effect of end milling process parameters and corrosion behaviour of ZE41A magnesium alloy using Taguchi based GRA. *Biointerface Research in Applied Chemistry*, vol. 13, no. 3, art. ID 214, **DOI:10.33263/briac133.214**.

[22] Muralidharan, S., Karthikeyan, N., Kumar, A.B., Aatthisugan, I.A. (2017). A study on machinability characteristic in end milling of magnesium composite. *International Journal of Mechanical Engineering and Technology*, vol. 8, no. 6, p. 455-462.

[23] Marakini, V., Pai, S., Bhat, U., Singh, D., Achar, B. (2022). High speed machining for enhancing the AZ91 magnesium alloy surface characteristics: Influence and optimisation of machining parameters. *Defence Science Journal*, vol. 72, no. 1, p. 105-113, **DOI:10.14429/dsj.72.17049**.

[24] Marakini, V., Pai, S., Bhat, A., Bangera, S. (2022). Surface integrity optimization in high speed milling of AZ91 magnesium alloy using TOPSIS considering vibration signals. *Materials Today: Proceedings*, vol. 52, p. 802-809, **DOI:10.1016/j.matpr.2021.10.154**.

[25] Zagórski, I., Korpysa, J. (2019). Surface quality in milling of AZ91D magnesium alloy. *Advances in Science and Technology Research Journal*, vol. 13, no. 2, p. 119-129, **DOI:10.12913/22998624/108547**.

[26] Guo, Y.B., Salahshoor, M. (2010). Process mechanics and surface integrity by high-speed dry milling of biodegradable magnesium-calcium implant alloys. *CIRP Annals*, vol. 59, no. 1, p. 151-154, **DOI:10.1016/j.cirp.2010.03.051**.

[27] Salahshoor, M., Guo, Y.B. (2011). Surface integrity of magnesium-calcium implants processed by synergistic dry cutting-finish burnishing. *Procedia Engineering*, vol. 19, p. 288-293, **DOI:10.1016/j.proeng.2011.11.114**.

[28] Salahshoor, M., Guo, Y.B. (2011). Cutting mechanics in high speed dry machining of biomedical magnesium-calcium alloy using internal state variable plasticity model. *International Journal of Machine Tools and Manufacture*, vol. 51, no. 7-8, p. 579-590, **DOI:10.1016/j.ijmachtools.2011.04.004**.

[29] Qiao, Y., Wang, S., Guo, P., Yang, X., Wang, Y. (2018). Experimental research on surface roughness of milling medical magnesium alloy. *IOP Conference Series: Materials Science and Engineering*, vol., 397, art. ID 012114, **DOI:10.1088/1757-899X/397/1/012114**.

[30] Desai, S., Malvade, N., Pawade, R., Warhatkar, H. (2017). Effect of high speed dry machining on surface integrity and biodegradability of Mg-Ca1.0 biodegradable alloy. *Materials Today: Proceedings*, vol. 4, no. 6, p. 6817-6727, **DOI:10.1016/j.matpr.2017.06.447**.

[31] Jouini, N., Ruslan, M.S.M., Ghani, J.A., Haron, C.H.C. (2023). Sustainable high-speed milling of magnesium alloy AZ91D in dry and cryogenic conditions. *Sustainability*, vol. 15, no. 4, art. ID 3760, **DOI:10.3390/su15043760**.

[32] Kanan, M., Zahoor, S., Habib, M.S., Ehsan, S., Rehman, M., Shahzaib, M., Khan, S.A., Ali, H., Abusaq, Z., Hamdan, A. (2023). Analysis of carbon footprints and surface quality in green cutting environments for the milling of AZ31 magnesium alloy. *Sustainability*, vol. 15, no. 7, art. ID 6301, **DOI:10.3390/su15076301**.

[33] Buk, J. (2022). Surface Topography of Inconel 718 alloy in finishing WEDM. *Advances in Science and Technology Research Journal*, vol. 16, no. 1, p. 47-61, **DOI:10.12913/22998624/142962**.

[34] Skoczylas, A., Zaleski, K. (2019). Effect of centrifugal shot peening on the surface properties of laser-cut C45 steel parts. *Materials*, vol. 12, no. 21, art. ID 3635, **DOI:10.3390/ma12213635**.

[35] Pisula, J., Budzik, G., Przeszłowski, Ł. (2019). An analysis of the surface geometric structure and geometric accuracy of cylindrical gear teeth manufactured with the direct metal laser sintering (DMLS) method. *Strojniški vestnik - Journal of Mechanical Engineering*, vol. 65, no. 2, p. 78-86, **DOI:10.5545/sv-jme.2018.5614**.

[36] Zagórski I., Korpysa, J. (2020). Surface quality assessment after milling AZ91D magnesium alloy using PCD tool. *Materials*, vol. 13, no. 3, art. ID 617, **DOI:10.3390/ma13030617**.

[37] Kulisz, M., Zagórski, I., Matuszak, J., Kłonica, M. (2019). Properties of the surface layer after trochoidal milling and brushing: experimental study and artificial neural network simulation. *Applied Sciences*, vol. 10, no. 1, art. ID 75, **DOI:10.3390/app10010075**.

[38] Karmiris-Obratański, P., Karkalos, N.E., Kudelski, R., Markopoulos, A.P. (2022). Experimental study on the effect of the cooling method on surface topography and workpiece integrity during trochoidal end milling of Incoloy 800. *Tribology International*, vol. 176, art. ID 107899, **DOI:10.1016/j.triboint.2022.107899**.

[39] Zaleski, K., Matuszak, J., Zaleski, R. (2018). *Surface Layer Metrology*, Lublin University of Technology Publishing House, Lublin.

[40] Wieczorowski, M. (2009). *Use of Topographic Analysis in the Measurement of Surface Irregularities*. Publishing House of Poznan University of Technology, Poznan.

[41] Sedlaček, M., Gregorčič, P., Podgornik, B. (2017). Use of the roughness parameters Ssk and Sku to control friction - a method for designing surface texturing. *Tribology Transactions*, vol. 60, no. 2, p. 260-266, **DOI:10.1080/10402004.2016.1159358**.

[42] El-Shenawy, E.H., Farahat, A.I.Z. (2023). Surface quality and dry sliding wear behavior of AZ61Mg alloy using Abbott firestone technique. *Scientific Reports*, vol. 13, art. ID 12437, **DOI:10.1038/s41598-023-39413-x**.

[43] ISO 21940-1:2019. *Mechanical vibration - Rotor balancing - Part 1: Introduction*, International Organization for Standardization, Geneva.

[44] ISO 4287:1999. *Geometrical Product Specifications (GPS) - Surface texture: Profile method - Terms, definitions and surface texture parameters*. International Organization for Standardization, Geneva.

[45] ISO 13565-2:1996. *Geometrical Product Specifications (GPS) - Surface texture: Profile method; Surfaces having stratified functional properties*. International Organization for Standardization, Geneva.

Strojniški vestnik - Journal of Mechanical Engineering 69(2023)11-12, 509-521
DOI:10.5545/sv-jme.2023.680
Original Scientific Paper
Received for review: 2023-06-08
Received revised form: 2023-08-16
Accepted for publication: 2023-09-19


# Active Disturbance Rejection Control Algorithm for the Driven Branch Chain of a Polishing Robot

Kaifeng Dong[1] – Jun Li[1] – Mengyao Lv[1] – Xin Li[1] – Wei Gu[2] – Gang Cheng[1,2,*]

[1] China University of Mining and Technology, School of Mechatronic Engineering, China
[2] Shangdong Zhongheng Optoelectronic Technology Co., China

*To overcome poor error suppression performance and low control accuracy in the polishing robot-driven branch chain control system, this paper proposes an improved active disturbance rejection control (ADRC) from the design of the derived nonlinear function. Subsequently, the tracking differentiator (TD), extended state observer (ESO) and nonlinear state error feedback (SEF) are designed in the ADRC, and the driven branch's ADRC servo-control system is established based on the permanent magnet synchronous motor (PMSM) with each driven branch. Meantime, by establishing first-order and second-order ADRC, current-loop control, and speed-and-position-loop control are realized, respectively. Finally, this study analysed differences in the speed and motor rotor error performance between the proportional-integral-derivative (PID)control and ADRC control strategy by using Simulink. Furthermore, an experiment platform, including hardware and software, is built to validate some inclusions. The results show that the ADRC not only realises high-precision trajectory tracking control but also ensures the rapid response performance of the system.*

**Keywords: active disturbance rejection control, trajectory tracking, parallel mechanism, driven branch chain**

**Highlights**

- *An ADRC algorithm-based derivable nonlinear function was established.*
- *The established first-order and second-order ADRC controller can effectively control the current loop, and speed-and-position loop, respectively.*
- *The experimental results showed that the introduction of the ADRC algorithm could achieve better performance of trajectory-tracking control during motor operation.*
- *The innovation of this paper is applying the proposed ADRC algorithm to the driven branch chain of a polishing robot.*

## 0 INTRODUCTION

An important element of a country's manufacturing level is the precision of optical components and ultra-precision processing technology, which is the key and foundation of advanced manufacturing technology [1]. Continued developments in the requirements of optical components' application have placed high demands on the workspace, rigidity and accuracy performance of optical polishing process equipment. The above factors mean that current ultra-precision polishing machine tools can no longer meet the relevant requirements.

The parallel mechanisms have the advantages of high rigidity, low inertia, and no accumulated machining mistakes; they have become taken over as the main structure of processing machine tools. Meanwhile, parallel robotics have grown the research of relevant scholars [2] and [3]. However, the significant nonlinearity, strong coupling, and vulnerability to ek ernal interference characteristics of the parallel robot-driven branch chain pose challenges to the controller design.

The robot trajectory was initially tracked using proportional-integral-derivative (PID) control. The PID control algorithm based on the negative feedback principle is not required to take into consideration the robot dynamics model. However, in external load disturbances, highly nonlinear and tightly coupled situations, the stability of the PID controller cannot be guaranteed, making it challenging to achieve perfect dynamic response tracking. The stability analysis of the control systems is a sensitive topic, and the Lyapunov function and the LaSalle-Youshizawa theorem were applied as commonly used methods in the book [4]. In order to deal with the above challenges, some scholars have proposed other control strategies.

The performance of the control system is enhanced by the introduction of extended state observer (ESO), which assesses all uncertain perturbations as a whole and eliminates the perturbations through feedback on the output error. In fact, many scholars have applied the ESO to a control system. As a way to transform linear results into fuzzy design processes, Precup et al. [5] proposed iterative feedback tuning (IFT) and ESO, which control servo-controllers that can be defined as integral second-order systems. Roman et al. [6] used ESO to tune proportional-integral (PI) controllers and utilized the image foresting transform (IFT) algorithm,

*Corr. Author's Address: China University of Mining and Technology, School of Mechatronic Engineering, China, chg@cumt.edu.cn

which is ultimately evaluated experimentally on a tower crane (TCS). Researchers have also studied control systems in unstable conditions. Safaei et al. [7] proposed a solution to the nonlinear subject network formation tracking problem with completely unknown dynamics and unknown perturbations. In contrast, Jin et al. [8] have enhanced the traditional controller based on PID. In order to reduce the drawbacks of bilateral control algorithms that depend on model parameters, Asad et al. [9] proposed a three-channel state convergence architecture supported by a disturbance observer.

Han and Yuan [10] summarized the idea of the cybernetics design method and formally proposed active disturbance rejection control (ADRC) including tracking differentiator (TD) [11], state error feedback (SEF) [12] and ESO [13]. Due to its features of a simple algorithm, a minimal overshoot, and great control accuracy, the ADRC is widely used in motor control [14], robot control [15], aircraft control [16], ship track control [17] and similar.

The application of ADRC in engineering practice has increased as a result of advancements in its theoretical foundation. Gao [18] used the ADRC design idea of the normalized parameter, which provided the design concept for the engineering application of ADRC. A backstep sliding mode-based attitude control law was created by Dou et al. [19], using linear ESO to estimate each system state. Roman et al. [20] proposed a virtual reference feedback tuning (VRFT) that integrates two control methods which are active immunity control and fuzzy control. The relative scholars have made plenty of theoretical progress, which lays the theoretical foundation for ADRC to be widely used. Also, the ADRC's various performances are better than PID's in some engineering applications, such as robustness, accuracy, and rapidity.

The ADRC control is a superior option to other control methods for enhancing the quality of parallel robots. Xu et al. [21] built the ESO to estimate the total disturbance, which is composed of the shipborne stable platform dynamic uncertainty, the unknown time-varying external disturbance and the coupling between the motion state variables. The Stewart platform was made by Zhang et al. [22], which is a time-varying nonlinear system for big radio telescopes. The system is fine-tuned using a disturbance rejection controller built for a single servo-branch and a control approach based on joint space. A novel 6-degree-of-freedom (6-DOF) parallel robot is driven by six novel linear motors, and Shi et al. [23] designed a fractional-order active disturbance rejection controller (FOADRC) to track their own desired trajectories for six linear motors. Based on the reduced dynamic model, Zhang et al. [24] used ADRC to track the trajectory of the Delta mechanism. A self-stable domain approach and the Lyapunov function ex amined the stability of the ESO and the closed-loop controller, respectively.

The above literature indicates that relevant scholars have combined ADRC control strategy with various application situations. However, the ADRC method for the driven chain of the optical mirror-polishing robot has hardly been researched. Meanwhile, the cycle of obtaining a finished mirror is usually one to two years, which is a long time for data-driven control approaches to acquire the relative data. Therefore, in order to make up for the above research gap, based on the driven chain of the optical mirror-polishing robot, the first-order and second-order ADRC controllers are established to control the current loop, and the speed-and-position loop, respectively.

The paper is organized as follows: Section 1 introduces the parallel mechanism component and control object of the optical mirror-polishing robot. Section 2 presents a servo-driven branch chain control system based on the improved ADRC algorithm. Section 3 demonstrates that the method significantly elevates the motion accuracy of the entire branch chain to reach the target position. The servo-system's motion control accuracy is guaranteed by reducing the disturbance error based on the improved ADRC controller. Section 4 concludes the paper.

## 1 DRIVEN CHARACTERISTIC ANALYSIS

### 1.1 Structure Analysis of Optical Mirror-Polishing Robot

The optical mirror-polishing robot is the study object in this paper. Its main structure consists of a rotor with 2-DOF and a parallel mechanism with 3-DOF, which is made up of a series of connections. The parallel mechanism includes UP constrained branch chain, UPS driven unconstrained branch chain, a moving platform, and a base platform distributed symmetrically. Here, U stands for Hooke joint, P stands for prismatic pair, and the constraint branch chain is connected by Hooke joint and prismatic pair. A ball hinge is used to join the moving platform to the UPS branch chain above, while a hooker hinge is used to join the opposite end of the latter to the base platform. One end of the UP-constrained branch has a fixed connection to the moving platform, while the other end is attached to the base platform by a hooker hinge that is orthogonal to the plane of the ball hinge centre point in the branch direction. The Figs. 1 and

2 display the configuration and the structure of the polishing robot.

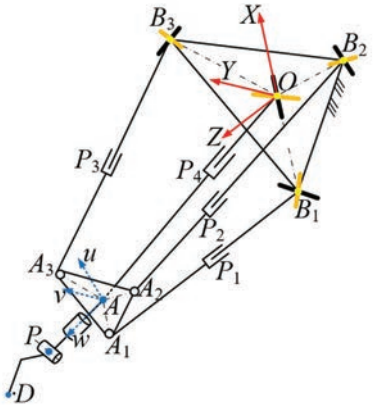


**Fig. 1.** *Configuration of the polishing robot*

In $B_1B_2B_3$ plane of the base platform, fixed coordinate system $O-XZY$ is established with point $O$ as the origin. For $A_1A_2A_3$ plane of the moving platform, point $A$ is used as origin for the construction of dynamic coordinate system $A-uvw$. In fixed coordinate system $O-XZY$, the UP branch chain axis and $X$ axis coincide, while $Z$ axis is perpendicular to base platform $B_1B_2B_3$ and axis can be determined by the right-hand rule. In coordinate system $A-uvw$, the $u$ axis coincides with the UP axis, while the $w$ axis is perpendicular to the moving platform. The $v$ axis direction can be determined by the right-hand rule.

### 1.2 Driven Branch Chain Control Objects

The motor and ball-screw-based transmission system serves as the primary control object of the driven branch chain servo-system. A servo-motor from the Panasonic A6 series is fully utilized, which can create a control model based on specific parameters. The permanent magnet synchronous motor (PMSM) is a parameter and nonlinear time-varying system whose windings have an obvious saturation effect and nonlinear magnetization characteristics. To simplify the analysis, the PMSM is assumed to be an ideal motor and following assumptions are considered: the saturation of the motor core is ignored; eddy current and hysteresis loss in the motor are not accounted; the conductivity of the permanent magnet in the motor is regarded as zero; the motor rotor and permanent magnet damping have no impact; with a constant magnetic field in the air gap; the current excitation component is $i_d$ during the directional control of pole position.

In the $d$-$p$ coordinate system, the specific flux link equation is expressed as follows:

$$\begin{cases} \psi_d = L_d i_d + \psi_f \\ \psi_q = L_q i_q \end{cases}, \tag{1}$$

where $\psi_d$ denotes the $d$-axis flux linkage, $L_d$ denotes the $d$-axis inductance, $\psi_q$ denotes the $q$-axis flux linkage, denotes the $q$-axis inductance, $i_d$ denotes the straight-axis current, $i_q$ denotes the cross-axis current.

In the $d$-$p$ coordinate system, the voltage balance equation corresponding to the motor stator can be expressed as follows:

$$\begin{cases} u_d = Ri_d + \dot{\psi}_d - w_m\psi_q \\ u_q = Ri_q + \dot{\psi}_q + w_m\psi_d \end{cases}, \tag{2}$$

where $u_d$ and $u_q$ represent the straight-axis and cross-axis component of the stator voltage, respectively. $R$ represents the resistance value of the stator, $w_m$ represents the true angular velocity.

As $\psi_f = 0$, voltage equation corresponding to the motor stator and electromagnetic torque are as follows:

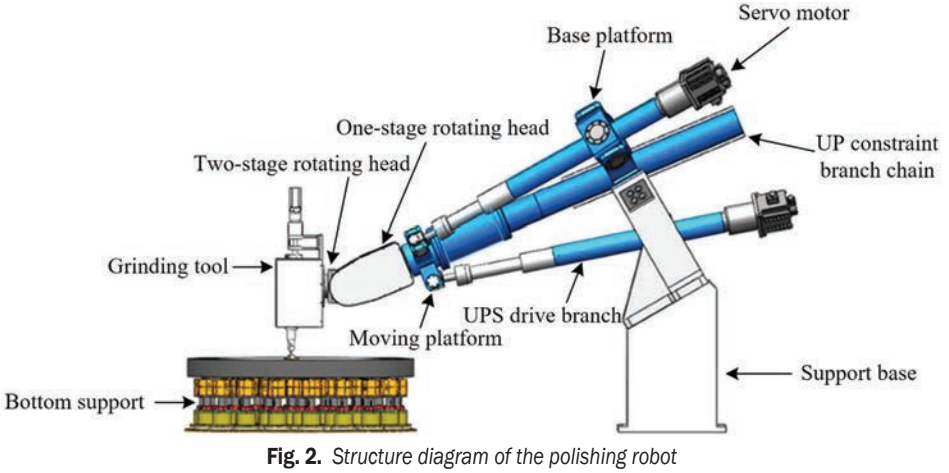


**Fig. 2.** *Structure diagram of the polishing robot*

$$\begin{bmatrix} u_d \\ u_q \end{bmatrix} = \begin{bmatrix} R & 0 \\ 0 & R \end{bmatrix} \begin{bmatrix} i_d \\ i_q \end{bmatrix} + \begin{bmatrix} L_d & 0 \\ 0 & L_q \end{bmatrix} \frac{d}{dt} \begin{bmatrix} i_d \\ i_q \end{bmatrix} + w_m \begin{bmatrix} -L_q i_q \\ L_d i_d + \psi_f \end{bmatrix}, \quad (3)$$

$$T_e = \frac{3}{2} p(\psi_d i_q - \psi_q i_d) = \frac{3}{2} p(\psi_f i_q + (L_d - L_q) i_d i_q). \quad (4)$$

The mechanical equation of motion is expressed as follows:

$$T = J\dot{w} + Bw + T_L, \quad (5)$$

where $J$ represents the value of the inertia moment, $T_L$ expresses the value of the load torque, $B$ represents the size of the viscous damping coefficient, $w$ states the mechanical angular velocity value corresponding to the rotor.

The control mode $i_d$=0 is used, so that it can achieve linear decoupling control of the electromagnetic torque, high performance of the speed regulation, and simple control scheme implementation. In terms of the direct axis current having little impact on the torque, the given value of the straight axis current is set to 0. As a result, the equation of state for the PMSM on the $d$-$q$ axis can be determined through Eq. (6):

$$\begin{bmatrix} \dot{w} \\ \dot{i}_d \\ \dot{i}_q \end{bmatrix} = \begin{bmatrix} 0 & 1.5p\psi_f / J & -B/J \\ -R/L_d & pw & 0 \\ -pw & -R/L_q & -p\psi_f / L_q \end{bmatrix} \begin{bmatrix} i_d \\ i_q \\ w \end{bmatrix} + \begin{bmatrix} -T_L / J \\ u_d / L_d \\ u_q / L_q \end{bmatrix}. \quad (6)$$

With the performing the Laplace transform on Eq. (6), the transfer function of a PMSM is given as:

$$\frac{W(s)}{U_q(s)} = \frac{K_t}{LJs^2 + (LB + RJ)s + RB + K_t\psi_f}, \quad (7)$$

where $K_t = 3p\psi_f / 2$ represents the motor torque constant.

The specific model diagram can be constructed as shown in Fig. 3.

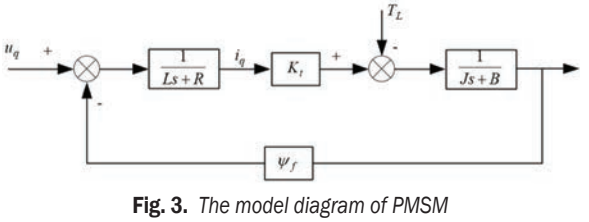


**Fig. 3.** *The model diagram of PMSM*

The ball screw in each driven branch converts the rotational motion of the servo-motor (see Table 1) into linear motion. Then the displacement state of each driven branch chain can be expressed as:

$$\dot{x} = \frac{r}{2\pi} w, \quad (8)$$

where $r$ represents the ball screw lead.

**Table 1.** *Servo-motor parameters*

| Parameter | Value |
|---|---|
| Inductance $L$ [mH] | 3.45 |
| Resistance $R$ [Ω] | 2.6 |
| Inertia $J$ [kg·m²] | 0.0035 |
| Torque coefficient $Kt$ [N·m/A] | 3.58 |
| Viscous damping coefficient $B$ [N·s/m] | 0.2 |
| Lead screw lead $r$ [mm] | 60 |

## 2 DRIVEN BRANCH CHAIN ACTIVE DISTURBANCE REJECTION SERVO-CONTROL

### 2.1 The Based Derivable Nonlinear Function ADRC Controller

The TD, SEF, and ESO are three core components of ADRC, which is a control method for nonlinear and uncertain systems. About the traditional PID controller' speed and overshoot paradox the TD tracking transition mechanism resolves the contradiction and adds the system robustness. ESO as the primary component of ADRC, which can withstand both internal and external interference while estimating the state variables of the system. The SEF control law is formed by the sum of the errors in the TD output and the ESO observation output. The controlled object input is comprised of the SEF control rule output and the ESO system interference estimator. As shown in Fig. 4, the ESO has the characteristic of real-time estimation of various disturbances in the system, so as to realize timely feedback and compensation of signal input errors, so that the whole control system has good dynamic characteristics.

The original nonlinear function is given as:

$$fal(e,\alpha,\delta) = \begin{cases} \dfrac{e}{\delta^{1-\alpha}}, |e| \le \delta \\ |e|^{\alpha} \, sign(e), |e| > \delta \end{cases}. \quad (9)$$

The derivation of Eq. (9) is:

$$fal'(e,\alpha,\delta) = \begin{cases} \dfrac{1}{\delta^{1-\alpha}}, 0 < e \le \delta \\ \alpha e^{\alpha-1}, e > \delta \end{cases}. \quad (10)$$

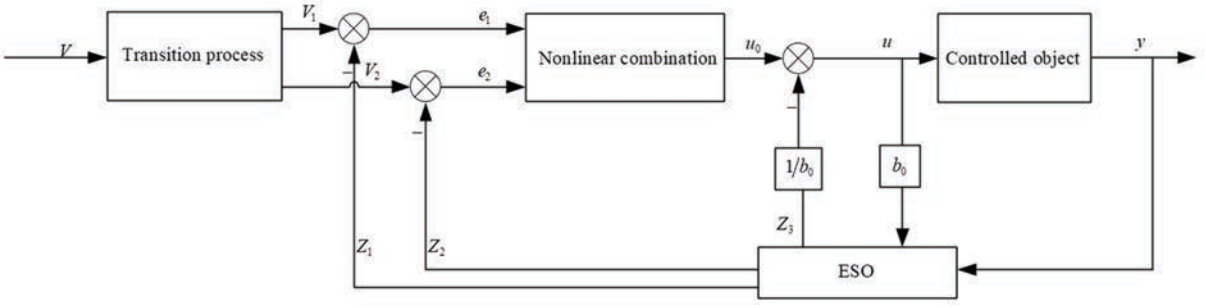


**Fig. 4.** *ADRC control block diagram*

From the mathematic perspective, the function *fal* can be observed to be continuous. For a kind of piecewise function, its switching point cannot be derived. Also, the slope of the function *fal* in the linear segment has an inverse relationship with the size of the function *fal*'s linear interval 2$\delta$. Under this premise, the driven branch chain's performance under the ADRC will eventually become unstable when the linear interval 2$\delta$ is minimal. This is because the dynamic gain of the function *fal* will abruptly change, leading to a high-frequency chattering phenomenon. To lessen system tremor and increase stability, the function *fal* needs to be enhanced when the linear interval is minimal.

According to the characteristics of the function *fal*, its expression is optimized accordingly. Based on ensuring the continuity of the function image, it is required to be derivable at the switching point of the segmented function, and the optimized expression of the function ***a*** *wfal* is as follows:

$$newfal = \begin{cases} k_1 \sin(e) + k_2 \tan(e), |e| \le \delta \\ |e|^{\alpha}\ sign(e), |e| > \delta \end{cases}, \quad (11)$$

where $k_1$ and $k_2$ can be determined by the following equation:

$$\begin{cases} k_1 = \dfrac{\delta^{\alpha} - \alpha\delta^{\alpha-1}\sin(\delta)\cos(\delta)}{\sin^3(\delta)} \\ k_2 = \dfrac{\alpha\delta^{\alpha-1}\sin(\delta) - \delta^{\alpha}\cos(\delta)}{\sin(\delta)\tan^2(\delta)} \end{cases}. \quad (12)$$

From the design concept of the function ***a*** *wfal*, it can be known that it is conductible at the switching point, and the derivative value does not change abruptly at the $e = \pm\delta$ , which ensures the stability of the driven chain motion under the active disturbance rejection controller. Therefore, by optimizing the *fal* in the active disturbance rejection controller to the function ***a*** *wfal*, the stability of the system will be guaranteed.

### 2.2 Current Loop Control Based on First-order Active Disturbance Rejection Controller

To achieve motor speed, position, and torque control, electromagnetic torque control, which essentially controls the three-phase alternating current (AC) and direct current (DC) in the model, is especially important. In an AC PMSM servo-control system, the control of the inner ring current loop is a prerequisite for achieving high-performance servo-control. Therefore, the current loop control should make its steady-state characteristics have relatively high quality, and the transient response ought to be fairly quick. PI regulators are now commonly used. However, if the controller current loop has parameter changes, a dead zone effect, or back electromagnetic fields (EMF), controller disturbance suppression and command tracking capabilities will not meet the relevant requirements. In order to cope with the above-mentioned undesirable factors, the paper proposes an improved first-order ADRC.

The current loop dynamic equation for the *q*-axis is:

$$i_q = \frac{u_q^*}{L_q} - \left(\frac{R}{L_q} i_q + \frac{w_m}{L_q}\psi_f\right) - \frac{u_q^* - u_q + w_m L_d i_d}{L_d}. \quad (13)$$

The control amount is set as $u = u_q$. Due to the influence of temperature, magnetic field, vibration, and external working conditions on the inductor, the known disturbance is $f(x) = -Ri_q / L_q - w_m\psi_f / L_q$, and $f(x)$ can be calculated by the motor parameters and the shaft feedback current. Also, the unknown disturbance is set as , and the total disturbance of the system is $w(t) = -\bar{u}_q^* - u_q + w_m L_d i_d / L_q$.

Thus, the equation of the *q*-axis current state is as follows:

$$\begin{cases} y = x_1 = i_q \\ \dot{x}_1 = x_2 + bu. \\ x_2 = a(t) \end{cases} \tag{14}$$

To ensure the steady of inner current loop, the equation of state is a first-order link, and the ADRC controller can be ensured as follows:

(1) The TD is:

$$\begin{cases} e_{11} = v_{11} - i_q^* \\ \dot{v}_{11} = v_{12} \\ \dot{v}_{12} = fhan(e_{11}, v_{12}, r_0, h) \end{cases}, \tag{15}$$

where $i_q^*$ is a given current signal, $v_{12}$ is the differential signal of $q$-axis current reference value.

(2) The ESO is:

$$\begin{cases} e_{12} = z_{11} - x_1 \\ \dot{z}_{11} = z_{12} - \beta_{11} fal(e_{12}, \alpha_{11}, \delta_1) + bu, \\ \dot{z}_{12} = -\beta_{12} fal(e_{12}, \alpha_{12}, \delta_1) \end{cases} \tag{16}$$

where $x_1 = i_q$ is the system output, $z_{11}$ is the $x_1$ tracking value, $z_{12}$ is the observation of the current loop system total disturbance.

(3) The NLSEF control law is:

$$\begin{cases} e_{13} = v_{12} - z_{11} \\ u_0 = -\beta_{13} e_{13} \\ u = u_0 - z_{12} / b \end{cases}, \tag{17}$$

where $b = 1/L_q$ states current loop compensation coefficient; $u = u_q^*$ represents the reference value for $q$-axis voltage.

The reference current $i_q^*$ on $q$-axis passes through first-order tracking differentiator, then the corresponding differential signal will be obtained. Also, $i_q$ goes through expanding state observer to obtain total perturbation of the system and the corresponding tracking signal. Meanwhile, the proportional adjustment is implemented, and the appropriate feed-forward compensation is given leading to the reference input $u_q$ being obtained.

### 2.3 Position Speed Control Based on Second-order Active Disturbance Rejection Controller

To reduce the adverse effects of coupling between torque current and exciting current, various external disturbances and internal parameter perturbations on the servo-control system. The position-based output equation second-order ADRC is proposed in the paper. One controller handles both rotational speed and position. The revolution speed of PMSM is:

$$\frac{d^2\theta}{dt^2} = \frac{d\omega}{dt} = \frac{3p\psi_f}{2J} i_q - \frac{T_L}{J} - \frac{B\omega}{J}, \tag{18}$$

$$\ddot{\omega} = -B\dot{\omega} - \frac{p\psi_f^2}{JL}\omega - \frac{3p\psi_f R}{2JL} i_q - \frac{3p^2\psi_f^2}{2JL}\omega - \frac{p}{J}\dot{T}_L + \frac{3p\psi_f u_q}{2JL}. \tag{19}$$

The control variable is $u_0 = i_q$, a comprehensive disturbance is $f(x_1, x_2) = -Bw/J$, load torque disturbance and external uncertain disturbance are $w(t) = -rT_L/2\pi J$ and $b = 3rp\psi_f/4\pi J$, respectively.

Therefore, there is $\ddot{\theta} = a(t) + bu_0$, where $a(t) = f(x_1, x_2) + w(t)$.

Then the equation of state can be rewritten as:

$$\begin{cases} y = x_1 = \theta \\ \dot{x}_1 = x_2 = \omega = \dfrac{d\theta}{dt} \\ \dot{x}_2 = \dot{\omega} = \hat{a}(t) + b_0 u_0 \end{cases}, \tag{20}$$

where $\hat{a}(t)$ represents an estimation of the total perturbation, $b_0$ represents an estimation of the $b$.

Based the principle of ADRC, the corresponding TD, ESO, and NLSEF are designed, as follows:

(1) The TD is:

$$\begin{cases} e_{21} = v_{21} - \theta^* \\ \dot{v}_{21} = v_{22} \\ \dot{v}_{22} = fhan(e_{21}, v_{22}, r_0, h) \end{cases}, \tag{21}$$

where $\theta^*$ states specific position of the given rotor, $v_{21}$ represents the tracking signal corresponding to $\theta^*$, $v_{22}$ is the $\theta^*$ corresponding differential signal.

(2) The ESO is:

$$\begin{cases} e_{22} = z_{21} - \theta \\ \dot{z}_{21} = z_{22} - \beta_{21} e_{22} \\ \dot{z}_{22} = z_{23} - \beta_{22} fal(e_{22}, \alpha_{21}, \delta_2) + b_0 i_q^*, \\ \dot{z}_{23} = -\beta_{23} fal(e_{22}, \alpha_{22}, \delta_2) \end{cases} \tag{22}$$

where $\theta$ represents specific feedback signal corresponding to the rotor position, $z_1$ expresses estimated tracking value corresponding to the actual position $\theta$, $z_2$ represents differential signal corresponding to $z_1$, $z_3$ is total perturbation observation, $e_{02}$ represents error value of the $z_1$ tracking output value $\theta$, $i_q^*$ expresses given value of the $q$-axis current command.

(3) The NLSEF control law is:

$$\begin{cases} e_{23} = v_{21} - z_{21} \\ e_{24} = v_{22} - z_{22} \\ u_0 = \beta_1 fal\left(e_{23}, \alpha_{23}, \delta_2\right) + \beta_2 fal\left(e_{24}, \alpha_{24}, \delta_2\right). \\ i_q^* = u_0 - \dfrac{z_3}{b_0} \end{cases} \quad (23)$$

After $\theta^*$ passing the TD, the tracking signal and the corresponding differential signal will be obtained. And after $\theta$ going through the ESO, total disturbance estimation and system state estimation will be obtained. After the error nonlinear adjustment, the corresponding reference signal $i_q^*$ is gained in feedforward compensation process. Thus, high-precision position control is achieved in the ADRC controller.

The currently under-study servo-control system encompasses three close-loop, which is the position-loop, current-loop and velocity-loop. The velocity-loop controller in the central loop is used to realize the stable adjustment of velocity. The position-loop controller in the outer loop is used to compare actual feedback position and rotor position-related instructions under the given command, and makes the error signal perform certain calculations by position-loop controller.

Subsequently, the speed reference signal could be obtained by the position-loop. Comparing the speed reference signal with rotor feedback signal to obtain the corresponding error, then control the error to get the relative current control volume of current loop. The current-loop controller in the inner loop is used to obtain the corresponding reference voltage as well as signalled the inverter circuit. The servo-system will produce a three-phase sinusoidal current which is fed into the motor, and destination of motor servo-control is accomplished.

## 3 SIMULATION RESULTS AND EXPERIMENT

### 3.1 Experimental Verification

In this paper, an experimental platform of the optical mirror-polishing robot is established to test the performance of the ADRC algorithm in motion trajectory tracking. When the robot is polishing optical mirrors, once the entire optical mirror polishing process and polishing paths are determined, the fast, stable and high-precision point-to-point motion of the polishing robot executing mechanism can be achieved. The hardware component of the experimental control system mainly includes one industrial personal computer (IPC), one programmable multi-axes controller (PMAC), some ball screws, one servo-system and various sensors. A detection module and a data processing component are part of the software system, and they are both electrically coupled to the power module. The data processing module's input electrical connection human-machine interaction module and detection module, as well as its output electrical connection motion control module. The detection module can measure the electrical signal in the power module, and the power module can accept and carry out the power cut-off command given by

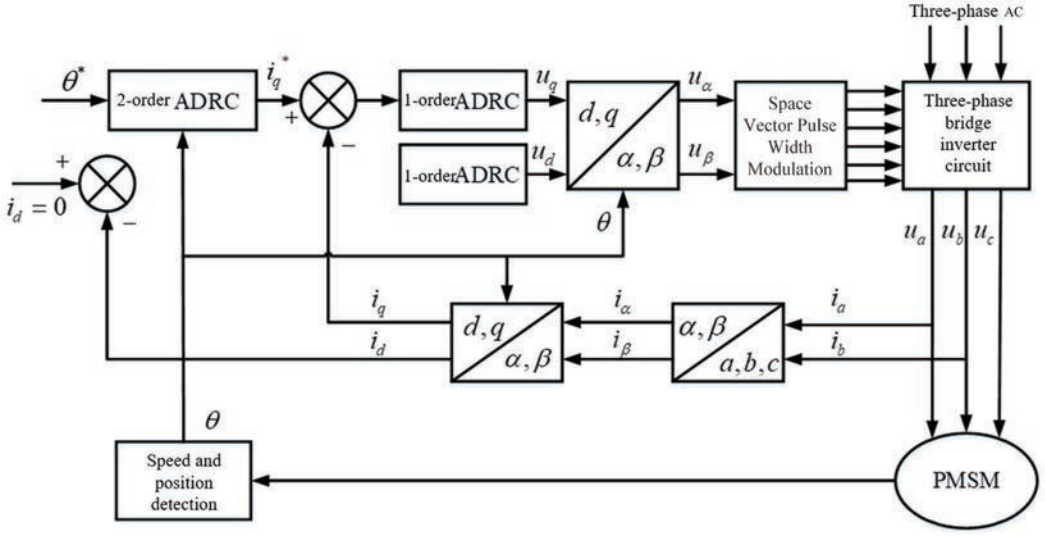


**Fig. 5.** *Permanent magnet synchronous motor active disturbance rejection servo-control diagram*

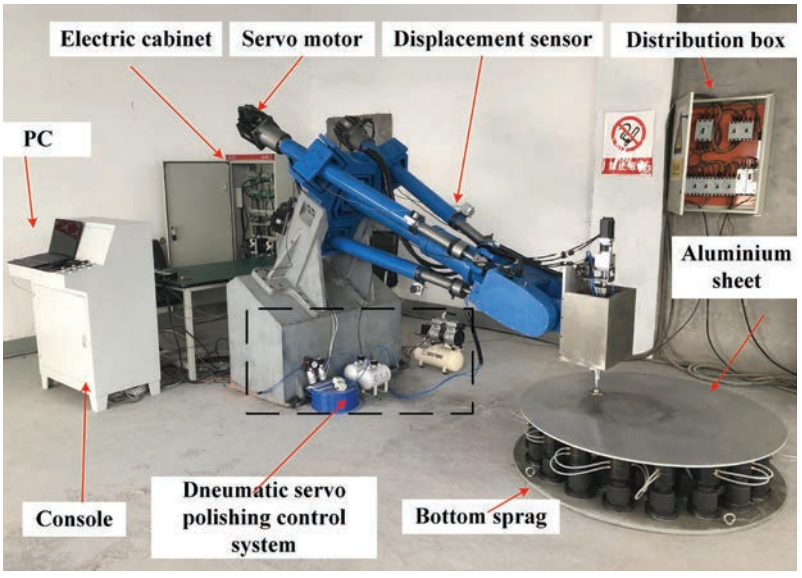


**Fig. 6.** *Experimental body and experimental environment*

the data processing module. The processing device is electrically coupled to both the input and output ends of the motion control and detection modules.

In order to verify that the input motion instructions can achieve the predetermined motion of the robot, this paper conducts real-time measurements of the displacement of each branch chain and the trajectory tracking of the centre point of the moving platform. Only a simple trajectory motion curve is given here. Fig. 6 show experimental body and experimental environment.

The motion trajectory of the centre point of the moving platform is input into the designed software platform, which solves through the inverse kinematics and controls each driven branch chain to follow the given trajectory. The trajectory of the centre point of the given moving platform is an arc curve as the trajectory tracking accuracy experiment test path. In order to reflect the control performance of the designed controller better, the manipulator is controlled by writing in the multi-axis motion controller written in the PID and ADRC control algorithms. And the encoder and displacement sensor inside the motor has been used to collect relevant data. The individual-driven chain displacement tracking error is the result of the data fitting diagrams at Figs. 7 to 9.

According to the displacement change data information of the three driven branch chains, the paper performs kinematics calculations to obtain the trajectory tracking situation of the moving platform centre point under the application of the PID and ADRC control algorithms. Also, the tracking error of

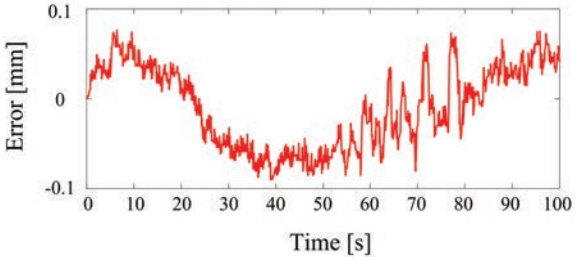


**Fig. 7.** *Displacement tracking error of the first driven branch*

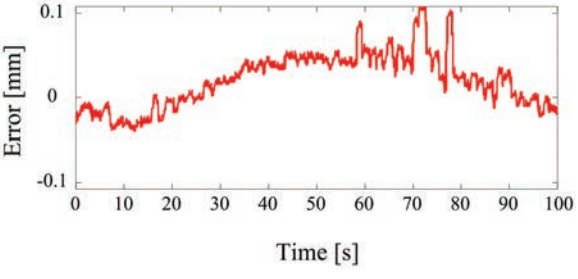


**Fig. 8.** *Displacement tracking error of the second driven branch*

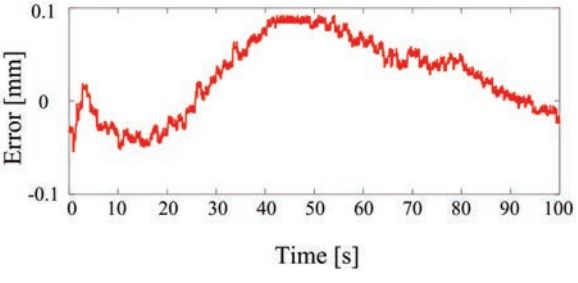


**Fig. 9.** *Displacement tracking error of the third driven branch*

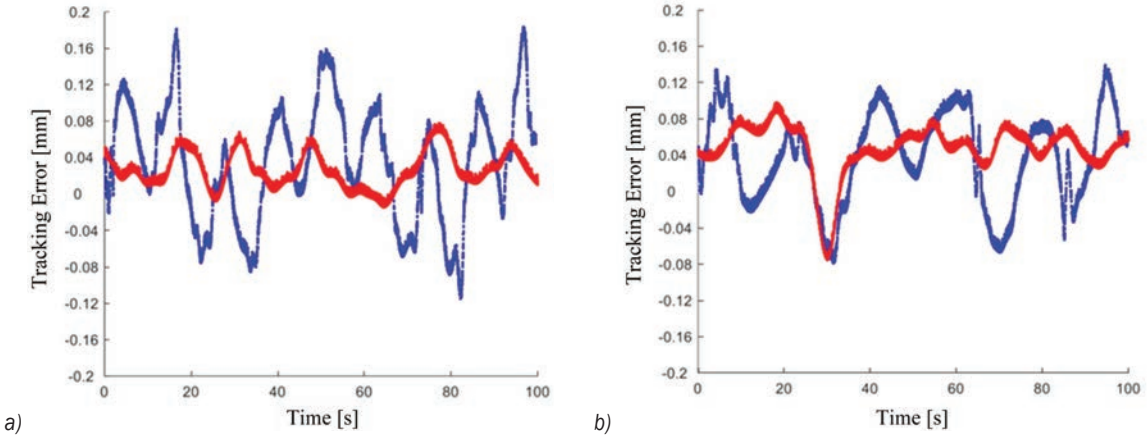


**Fig. 10.** *Trajectory tracking error at the centre point of the moving platform; a) X-direction; b) Y-direction*

the mobile platform is listed in Table 2 to analyse the operating accuracy of the moving platform based on PID and ADRC.

In Fig. 10, the red data curve is the control effect curve created in this article based on ADRC, whereas the blue data curve represents the PID control effect curve. Only the data results in the *X* and *Y* directions of the centre point of the moving platform are assessed. As shown in Table 2, the PID control algorithm has an error range of around 0.3 mm, but the algorithm under study in the research has an error range of approximately 0.1 mm. The ADRC overall control effect outperforms the PID algorithm by a wide margin.

**Table 2.** *Trajectory tracking error of the mobile platform*

| | Max. in X | Amplify in X | Max. in Y | Amplify in Y |
|---|---|---|---|---|
| ADRC | 0.08 | 0.1 | 0.09 | 0.14 |
| PID | 0.18 | 0.3 | 0.17 | 0.22 |

### 3.2 Driven Branch Chain Response Verification Experiment

The control object of the driven branch servo-system primarily focused on the transmission system what is composed of the motor and ball screw to verify the stability and control accuracy of the established ADRC control algorithm. In this paper, first-order active disturbance rejection controller of the current

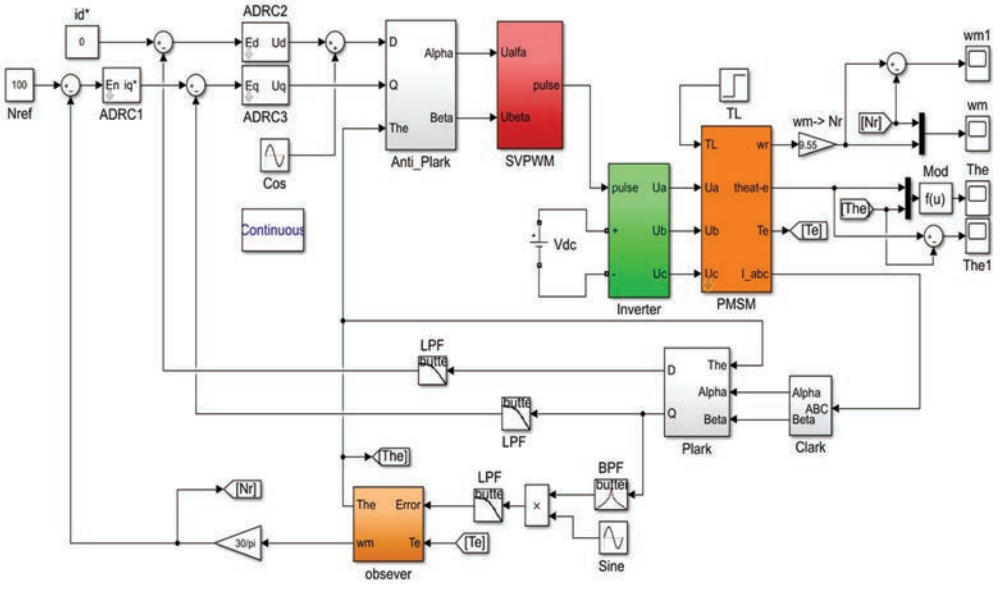


**Fig. 11.** *Simulink model diagram of permanent magnet synchronous motor*

loop and second-order active disturbance rejection controller of position speed loop are established. The Simulink model diagram of the PMSM is constructed as shown in Fig. 11. Subsequently, the motor rotation estimation error of the ADRC system and the speed response under the two control strategies are measured, respectively. At the same time, relevant characteristics are analysed, and corresponding conclusions are drawn.

In this paper, the variability of parameters such as electromagnetic torque, *d*-axis current, and *q*-axis current of the motor is gained by inputting varying external load torque to the system. As shown in Figs. 12 and 13, in addition to the peak phenomenon of the motor performance indicators during the start-up phase, the electromagnetic torque fluctuates at $t$ = 0.05 s, which is from –4 N·m is changed to 0 N·m, and it can be assumed that a sudden change in the load torque occurs. The *d*-axis current and *q*-axis current fluctuate when the load torque varies abruptly, but they quickly return to a stable value since the ADRC can swiftly suppress the perturbations when the load torque fluctuates.

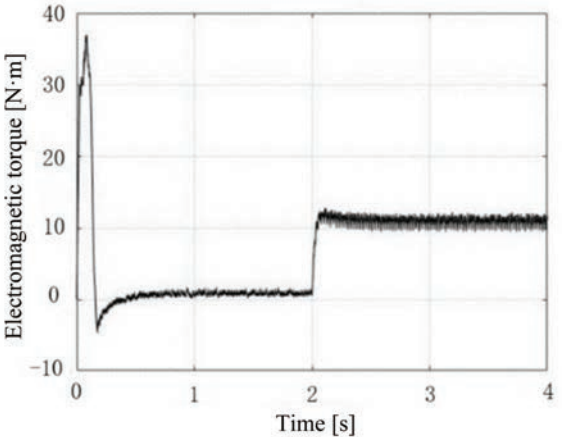


**Fig. 12.** *Electromagnetic torque response diagram*

In order to test the capacity of the ADRC control system to resistant to load disturbances, the system is

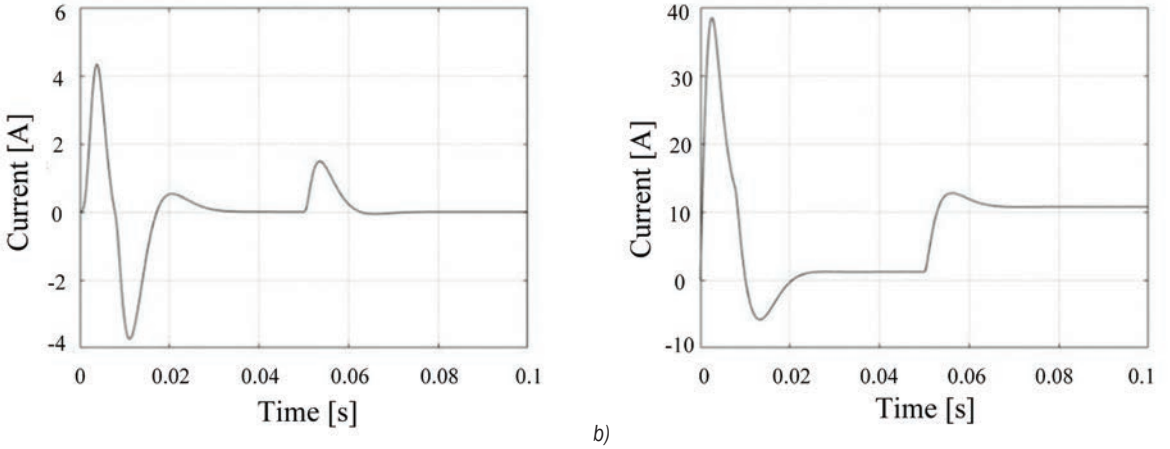


a) b)

**Fig. 13.** *Current response diagram a) d-axis; b) q-axis*

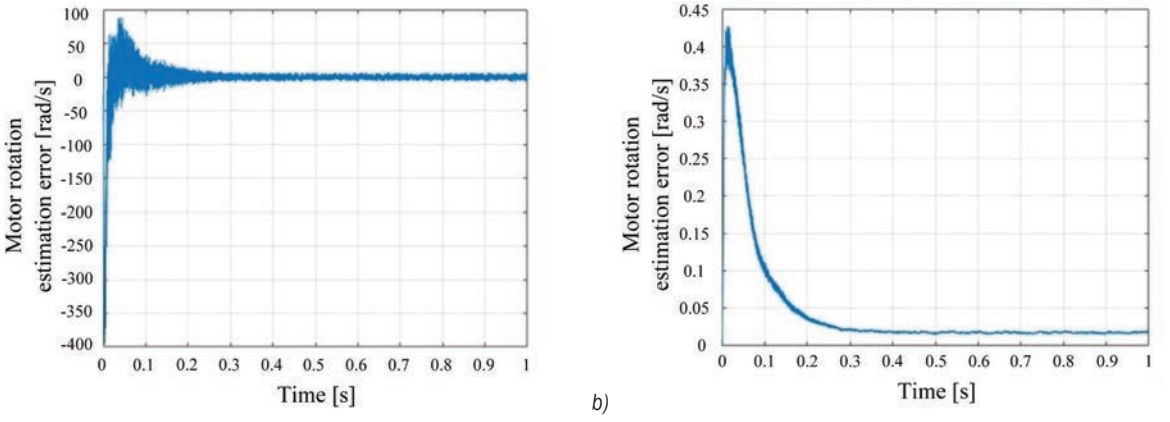


a) b)

**Fig. 14.** *Motor rotation estimation error; a) motor speed; b) motor position*

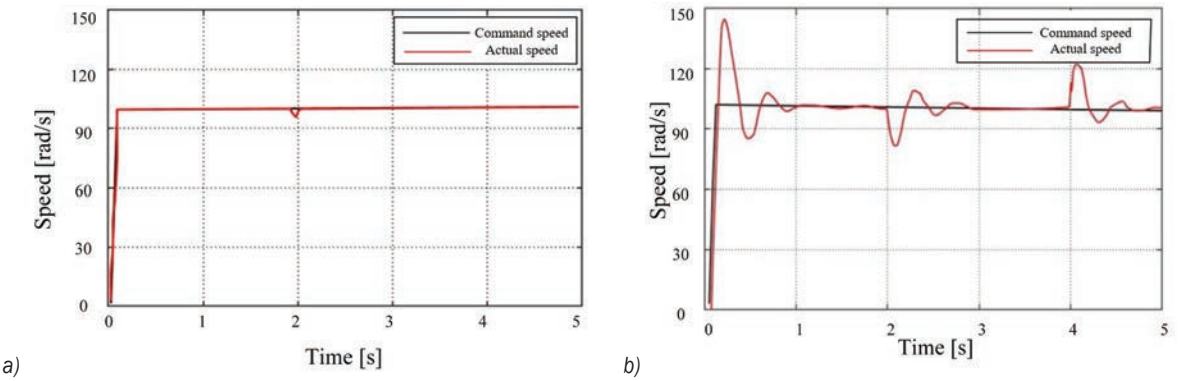


**Fig. 15.** *Speed response and load disturbance curve; a) ADRC regulation, b) PID regulation*

configured to a stated speed of 100 r/min and an initial load torque of 30 N·m. Fig. 14 shows the variation curves of the servo-motor speed estimation error and rotor position estimation error of the system under the ADRC. As seen in Fig. 14, the motor's rotor position error and rotational speed error are initially not very stable, especially the rotational speed error, which exhibits some fluctuation phenomena. However, with the aid of the ADRC's adjustment, the information for errors gradually tends to zero in a short time, and the fluctuation range is narrowing from 0 s to 0.3 s.

To test the speed response of the system with ADRC and PID controllers when a load is applied, in this study, Simulink experiments are performed to obtain the trajectory tracking of the speed response under the two control methods. The system is provided a step signal with output final value of 100 r/min. The simulation time is 5 s, in order to test the ability of ADRC and PID controllers to resist disturbances, a load torque of 10 N·m is applied at $t$ = 2 s in this experiment, and the simulation results are shown in Fig. 15.

As shown in Table 3, after the motor starts to run, the speed reaches the set value of about 1 s. At the same time, overshooting of the speed occurs, the maximum speed is about 145 r/min, and the overshooting amount is 45 %. At $t$ = 2 s, the motor speed fluctuation at a pace of around 1 s to temporarily restore stability, but the motor speed fluctuation oscillates again in 4 s to 5 s. In Fig. 15a, the motor starts to run and reaches the set value almost at the same time as the commanded speed, which is about 1s earlier than the traditional PID control. This improves the tracking performance of the system and eliminates overshooting amounts. Also, when the 10 N·m load is applied to the system at $t$ = 2 s, the system undergoes a slight fluctuation, but the rotational speed returns to stability within about 0.1 s, which is 0.9 s less than that of the conventional PID.

**Table 3.** *Speed response and load perturbation*

| | Given rate [rad/s] | Load [N·m] | Overshoot [%] | Disturbance value [rad/s] | Rise time [s] | Max. speed [rad/s] |
|---|---|---|---|---|---|---|
| ADRC | 100 | 10 | 0 | 2.5 | 0.1 | 100 |
| PID | 100 | 10 | 45 | 17 | 1 | 145 |

From the comparison of the aforementioned simulation results, it is clear that the ADRC-based synchronous control of the motor is less affected by the extrinsic load torque. Meanwhile. the motor can track up to the target speed quickly, and the robustness is also improved when compared to the traditional PID control strategy.

## 4 CONCLUSIONS

To meet the demand for parallel robot control in the process of processing optical mirrors, a new type of ADRC is established based on derivable function, and the improved ADRC algorithm is embedded in the driven branch chain servo-system of the polishing robot. A first-order active disturbance rejection controller for the current loop control and second-order active disturbance rejection controller for speed-and-position loop control are designed. The control model is created by using Simulink; a specific experimental platform and corresponding experimental environment are built to verify the performance of the ADRC algorithm on the trajectory tracking of robot motion. It is validated that the introduction of active disturbance rejection algorithm can effectively suppress error information, improve accuracy and efficiency in the motor operation process. When facing load disturbance, the speed

response shows that the ADRC can more effectively ensure the operation state of the servo-system than PID control, and stability of the position and attitude adjustment process of each driven branch chain are guaranteed. To some extent, it can explain the high accuracy control of the established ADRC algorithm. Moreover, idealized elements like swirl and hysteresis loss, the conductivity of a permanent magnet and permanent magnet damping have little impact on the outcomes of the experiment.

## 5 ACKNOWLEDGEMENTS

This work was supported by the Priority Academic Program Development of Jiangsu Higher Education Institutions (PAPD) and the National Natural Science Foundation of China (Grant No. 52275039) and is gratefully acknowledged. The authors also would like to thank the Shandong Zhongheng Optoelectronic Technology Co., Ltd. for providing experimental devices and physical prototype of the hybrid robot for verifying effectiveness of the proposed approach.

## 6 REFERENCES

[1] Wang, D.S., Da, S., Liu, W.G. (2010). Ultra-precision optical component manufacturing technology. *Defense Manufacturing Technology*, no. 5, p. 5-10.

[2] Rasheed, T., Long, P., Caro, S. (2020). Wrench-feasible workspace of mobile cable-driven parallel robots. *ASME Journal of Mechanisms and Robotics*, vol. 12, no. 3, art. ID 031009, **DOI:10.1115/1.4045423**.

[3] Cheng, G., Gu, W, Yu, J.L., Tang, P. (2010). Overall structure calibration of 3-UCR parallel manipulator based on quaternion method. *Strojniški vestnik - Journal of Mechanical Engineering*, vol. 57, no. 10, p. 719-729, **DOI:10.5545/sv-jme.2010.167**.

[4] Precup, R.E., Roman, R.C., Safaei, A. (2022). Introduction. *Data-Driven Model-Free Controllers*. CRC Press, Boca Raton, p. 1-22, **DOI:10.1201/9781003143444-1**.

[5] Precup, R.E., Preitl, S., Rudas, I.J., Tomescu, M.L., Tar, J.K. (2008). Design and experiments for a class of fuzzy controlled servo systems. *IEEE/ASME Transactions on Mechatronics*, vol. 13, no, 1, p. 0-35, **DOI:10.1109/tmech.2008.915816**.

[6] Roman, R.C., Precup, R.E., Hedrea, E.L., Preitl, S., Zamfirache, I.A., Bojan-Dragos, C.A., Petriu, E.M. (2022). Iterative feedback tuning algorithm for tower crane systems. *Procedia Computer Science*, vol. 199, p. 157-165, **DOI:10.1016/j.procs.2022.01.020**.

[7] Safaei, A., Mahyuddin, M.N. (2018). A solution for the cooperative formation-tracking problem in a network of completely unknown nonlinear dynamic systems without relative position information. *International Journal of Systems Science*, vol. 49, no, 16, p. 3459-3475, **DOI:1080/00207721.20198.15442755**.

[8] Jin, Z.J., Cheng, G., Xu, S.C., Yuan, D.P. (2022). Error prediction for a large optical mirror processing robot based on deep learning. *Strojniški vestnik - Journal of Mechanical Engineering*, vol. 68, no. 3, p. 175-184, **DOI:10.5545/sv-jme.2021.7455**.

[9] Asad, M.U., Farooq, U., Gu, J., Liu, R., Abbas, G., Balas, V. (2021). Disturbance-observer-supported three-channel state convergence architecture for bilateral teleoperation systems. *ACTA Press*, vol. 36, no. 5, p. 316-324, **DOI:10.2316/J.2021.206-0411**.

[10] Han, J.Q., Yuan, L.L. (1999). The discrete form of tracking - differentiator. *Journal of Systems Science and Mathematical Sciences*, vol. 19, no. 3, p. 268-273.

[11] Wang, C.W., Ji, X.H., Zhang, Z.Y., Zhao, B., Quan, L., Plummer, A.R. (2022). Tracking differentiator-based back-stepping control for valve-controlled hydraulic actuator system. *ISA Transactions*, vol. 199, p. 208-220, **DOI:10.1016/j.isatra.2021.02.028**.

[12] Chen, Q., Shi, H.H., Sun, M.X. (2020). Echo state network-based backstepping adaptive iterative learning control for strict-feedback systems: An error-tracking approach. *IEEE Transactions on Cybernetics*, vol. 50, no. 7, p. 3009-3022, **DOI:10.1109/TCYB.2019.2931877**.

[13] Sancak, K.V., Bayraktaroglu, Z.Y. (2021). Bayraktaroglu Observer-based friction compensation in heavy-duty parallel robot control. *Journal of Mechanical Science and Technology*, vol. 35, p. 3693-3704, **DOI:10.1007/s12206-021-0738-2**.

[14] Tang, X.G., Yang, G.Y., Xun, H. (2022). Permanent magnet synchronous motor RBF network magnetic field vector control system for robotic arms. *Journal of Beijing Institute of Technology*, vol. 42, no. 10, p. 1089-1096, **DOI:10.15918/j.tbit1001-0645.2021.267**. (in Chinese)

[15] Yang, L.B., Zhang, W.G., Huang, D.G. (2015). Robust trajectory tracking of quadcopter based on attitude decoupling of ADRC. *Transactions of Beijing University of Aeronautics & Astronautics*, vol. 41, no. 6, p. 1026-1033, **DOI:10.13700/j.bh.1001-5965. 2014.0392**. (in Chinese)

[16] Meng, Z.P., Yang, L.Q., Wang, B., Liu, Y.B. (2022). ADRC controller design for folding wing vehicle based on improved equilibrium optimization. *Journal of Beijing University of Aeronautics & Astronautics*, **DOI:10.13700/j.bh.1001-5965.2022.0698**. (in Chinese)

[17] Li, R.H., Li, T.S., Piao, R.X. (2013). Under-driven surface vessel track tracking self-disturbance rejection control. *Journal of Dalian Maritime University*, vol. 39, no. 2, p. 5-8, **DOI:10.16411/j.cnki.issn1006-7736.2013.02.005**. (in Chinese)

[18] Gao, Z.Q. (2013). On the foundation of active disturbance rejection control. *Control Theory and Technology*, vol. 30, no. 12, p. 1498-1510, **DOI:10.7641/CTA.2013.31087**.

[19] Dou, J.X., Kong, X.X., Wen, B.C. (2016). Reverse sliding mode self-disturbance rejection control and stability of quadcopter attitude. *Journal of Northeastern University (Natural Science Edition)*, vol. 37, no. 10, p. 1415-1420, **DOI:10.3969/j.issn.1005.3026.2016.10.011**. (in Chinese)

[20] Roman, R.C., Precup, R.E., Petriu, E.M. (2021). Hybrid data-driven fuzzy active disturbance rejection control for tower crane systems. *European Journal of Control*, vol. 58, p. 373-387, **DOI:10.1016/j.ejcon.2020.08.001**.

[21] Xu, M., Du, J.L., He, G.J. (2020). Mailah stability control law design of parallel three-degree-of-freedom shipborne

stable platform based on ADRC. *Journal of Dalian Maritime University*, vol. 46, no. 1, p. 20-28, **DOI:10.16411/j.cnki.issn1006-7736.2020.01.003**. (in Chinese)

**[22]** Zhang, Y.F., Zhang, A., Duan, B.Y. (2005). Disturbance rejection control and experimental study of fine-tuning system of large radio telescope. *Mechanical Strength*, no. 6, p. 748-751, **DOI:10.16579/j.issn.1001.9669.2005.06.007**. (in Chinese)

**[23]** Shi, X.X., Huang, J.C., Gao, F.Z. (2020). Fractional-order active disturbance rejection controller for motion control of a novel 6-DOF parallel robot. *Mathematical Problems in Engineering*, vol. 2020, art. ID 3657848, **DOI:10.1155/2020/3657848**.

**[24]** Zhang, Y., Chen, Z.Q., Zhang, X.H., Sun, Q.L., Sun, M.W. (2018). A novel control scheme for quadrotor UAV based upon active disturbance rejection control. *Aerospace Science & Technology*, vol. 79, p. 601-609, **DOI:10.1016/j.ast.2018.06017**.

# Vsebina

**Strojniški vestnik - Journal of Mechanical Engineering**
**letnik 69, (2023), številka 11 12**
**Ljubljana, november-december 2023**
**ISSN 0039-2480**

**Izhaja dvomesečno**

**Razširjeni povzetki** (extended abstracts)

Strojniški vestnik - Journal of Mechanical Engineering 69(2023)11-12, SI 49

Prejeto v recenzijo: 2023-05-27
Prejeto popravljeno: 2023-09-12
Odobreno za objavo: 2023-10-04

# Brušenje cementnega karbida z uporabo vitrificiranega diamantnega zatiča in mazanega tekočega ogljikovega dioksida

Deepa Kareepadath Santhosh[1,*] – Franci Pušavec[1] – Peter Krajnik[1,2]

[1] Univerza v Ljubljani, Fakulteta za strojništvo, Slovenija

[2] Tehnološka univerza Chalmers, Oddelek za industrijsko znanost in znanost o materialih, Göteborg, Švedska

Karbidne trdine zaradi svoje trdote, obrabne odpornosti in žilavosti spadajo med težko obdelovalne materiale. V izdelovalnih procesih rezalnih orodij se tako soočamo s težavami pri brušenju le teh, saj so procesi povezani z velikimi rezalnimi silami, specifično energijo brušenja, obrabo brusa in nizko stopnjo odvzema materiala. Za mazanje in hlajenje se v pri industrijskem brušenju karbidnih trdin običajno uporabljajo mineralna olja, ki niso okolju prijazna. Zmanjšanje količin uporabljenih hladilno-mazalnih tekočin pa lahko prispeva k večji trajnosti proizvodnih procesov. Vse bolj atraktivno alternativo predstavljajo kriogeno-MQL sistemi, kjer sta v rezalno cono dovedena ogljikov dioksid in oljna megla. Enega od takih sistemov predstavlja ArcLub One, ki je obravnavan v tem delu. Ta inovativna tehnologija hlajenja in mazanja, ki se je izkazala za učinkovito pri odrezovalnih procesih, kot sta vrtanje in frezanje, uporablja enokanalni dovodni sistem za dovod kapljevite faze kriogenega medija v rezalno cono. Na podlagi pregleda literature je ugotovljeno, da so raziskave brušenja karbidnih trdin z majnimi orodji omejene. Zato je cilj tega dala preučiti obdelovalnost pri brušenju, vključno s topografijo brusa in fenomenom zaprtja por, povezanih z različnimi tehnikami hlajenja/mazanja.

Eksperimentalno delo obsega spreminjanje hitrosti brusa v območju od 2 do 12 m/s pri konstantni hitrosti obdelovanca (100 mm/min) in globini rezanja (10 μm), kar je omogočilo testiranje šestih različnih pogojev agresivnosti brušenja. Pri eksperimentih so bili uporabljeni trije pogoji hlajenja in mazanja: suho, z emulzijo in z $LCO_2$-MQL opcijo. Vrednotenje obdelovalnosti je vključevalo analizo sil brušenja, specifične energije brušenja, topografijo brusa in mašenje por brusa z materialom obdelovanca. Ugotovitve so pokazale, da so pri brušenju z $LCO_2$-MQL sile brušenja najmanjše. V primeru normalnih sil, so te za 8 % do 145 % manjše od brušenja na suho, in za 18 % do 33 % manjše od brušenja z emulzijo. Na drugi strani so tangencialne sile za 4 % do 66 % manjše od suhega brušenja in za 28 % do 78 % manjše od brušenja z emulzijo. Poleg tega je specifična energija za 24 % do 51 % nižja v primerjavi s suho obdelavo in za 64 % do 69 % nižja v primerjavi z emulzijo, kar kaže na sposobnost učinkovitega odrezavanja. Na tem mestu je potrebno omeniti, da se pri suhem brušenju razmerja med silami brušenja gibljejo med 0,32 in 0,38. Za primerjavo, uporaba emulzije pri brušenju daje razmerja od 0,50 do 0,82, kar pomeni povečanje za 56 % do 116 % v primerjavi s suhim brušenjem. Najnižje razmerje sil pa ima $LCO_2$-MQL, in sicer med 0,21 in 0,37, kar pomeni zmanjšanje za 3 % do 34 % v primerjavi s suhim brušenjem in za 55 % do 58 % v primerjavi z brušenjem z emulzijo. Opozoriti pa je potrebno, da je bilo kljub najnižjim vrednostim sil in specifične energije, pri brušenju z $LCO_2$-MQL ugotovljeno občutno mašenje por na površini brusa. Verjeten vzrok za to je pomanjkanje kisika v $CO_2$ atmosferi, kar lahko poveča adhezijo kovinskih delcev (odrezkov) na brus. Kljub temu uporaba $LCO_2$-MQL hladilno-mazalne tehnike kaže potencial za učinkovito brušenje, zlasti pri višjih stopnjah agresivnosti procesa, katerega opredeljujejo najnižje specifične energije.

Ugotovitve dela tako predstavljajo priložnosti za nadaljnje raziskave izboljšanja odrezavanja pri brušenju karbidnih trdin, zlasti z vidika obremenitve/mašenja brusa in razumevanja vloge atmosfere pri procesu brušenja. Ugotovitve pridobljene s to raziskavo, bodo vsekakor lahko koristne pri razširitvi poskusov na konvencionalno brušenje z uporabo $LCO_2$-MQL.

**Ključne besede: brušenje, karbidne trdine, hlajenje in mazanje, diamantni brus, kapljeviti ogljikov dioksid ($LCO_2$), enokanalni dovod, minimalna količina mazanja (MQL)**

*Naslov avtorja za dopisovanje: Univerza v Ljubljani, Fakulteta za strojništvo, Aškerčeva 6, 1000 Ljubljana, Slovenija, deepa.kareepadathsanthos@fs.uni-lj.si

Strojniški vestnik - Journal of Mechanical Engineering 69(2023)11-12, SI 50

Prejeto v recenzijo: 2023-04-11
Prejeto popravljeno: 2023-09-15
Odobreno za objavo:2023-09-19

# Aerodinamična analiza matematično modeliranega propelerja za majhna brezpilotna zračna plovila z uporabo CFD v različnih temperaturnih pogojih

Tamilselvan Ganesan,* – Niresh Jayarajan
Tehniški kolidž PSG, Oddelek za avtomobilsko strojništvo, Indija

Uporaba brezpilotnih zračni plovil (UAV) je v zadnjem času doživela velik porast zaradi njihove stroškovne učinkovitosti in vsestranskosti. Kljub temu je razvoj propelerjev UAV, ki zahteva celovito analizo tako aerodinamičnih kot strukturnih vidikov, pritegnil malo pozornosti raziskovalne skupnosti.

Dobro zasnovan propeler lahko bistveno zmanjša porabo baterije in izboljša splošno učinkovitost delovanja. Ta študija se osredotoča na zasnovo propelerjev, ki temeljijo na matematičnih modelih, in jih primerja s široko uporabljenimi naprednimi preciznimi kompozitnimi (APC) lopaticami propelerjev Slow Flyer glede koeficientov potiska, koeficientov moči in splošne učinkovitosti.

Da bi olajšali to preiskavo, numerične simulacije uporabljajo tetraedrično mrežo, ki vključuje standardni $k–\omega$ (k-omega) model za natančno zajemanje aerodinamičnega obnašanja. Drug pomemben vidik te študije je matematično modeliranje propelerjev na podlagi profila Eppler E63, ki je bil izbran zaradi njegovega vrhunskega vzgona za izboljšanje potiska in splošne učinkovitosti UAV. Za te propelerje so bile izvedene obsežne analize računalniške dinamike tekočin (CFD) pod različnimi temperaturnimi pogoji, ki zagotavljajo dragocen vpogled v njihovo aerodinamično zmogljivost. Ti rezultati se ne uporabljajo le za izboljšanje zasnove propelerjev UAV, ampak tudi za zagotavljanje celovite primerjave aerodinamičnih značilnosti matematično modeliranih propelerjev z merilnimi propelerji APC Slow Flyer. Poleg tega bo uporaba metod teorije elementov rezila (BET) in CFD skupaj z eksperimentalno validacijo zagotovila zanesljivo oceno teh zasnov propelerjev. Študija obravnava tudi vprašanje natančnosti BET pri napovedovanju potiska s primerjavo simulacijskih podatkov z rezultati, izpeljanimi iz BET. Poleg tega so bili izvedeni eksperimentalni testi za potrditev ugotovitev, pridobljenih z numeričnimi simulacijami. Rezultati te preiskave kažejo, da matematično zasnovani propelerji dosledno delujejo bolje kot propelerji za počasno letenje APC v vseh območjih hitrosti.

Primerjava med obema metodama, in sicer BET in CFD, kaže, da ima metoda BET približno 10-odstotno razliko v napaki v višjih območjih hitrosti. Vendar se to odstopanje zmanjšuje, ko se hitrost zmanjšuje, kar kaže na primernost uporabe metode BET za določene scenarije delovanja.

Če povzamemo, ta študija ponuja nov in matematično temelječ pristop k načrtovanju propelerjev, ki prikazuje prednosti potiska in učinkovitosti takšnih modelov za UAV. Vključuje natančno CFD analizo v različnih okoljskih pogojih in temeljito primerjavo z APC Slow Flyerjem in široko uporabljenim propelerjem UAV. Navsezadnje raziskava ponuja dragocen vpogled v tehnike načrtovanja propelerjev, kar koristi industriji UAV in povečuje učinkovitost brezpilotnih zračnih plovil.

**Ključne besede: brezpilotna zračna plovila, propeler, računalniška dinamika tekočin, teorija lopatic, matematično načrtovanje**



*Naslov avtorja za dopisovanje: Tehniški kolidž PSG, Oddelek za avtomobilsko strojništvo, Indija, tamilselvanganesan98@gmail.com

Strojniški vestnik - Journal of Mechanical Engineering 69(2023)11-12, SI 51

Prejeto v recenzijo: 2023-04-05
Prejeto popravljeno: 2023-09-06
Odobreno za objavo: 2023-09-15

# Analiza uspešnosti tehničnih pregledov vozil glede na directive EU in izbrane države EU

Jernej Klemenc[1,*] – Domen Šeruga[1] – Tomaž Svetina[2] – Jože Tršelič[2]
[1] Univerza v Ljubljani, Fakulteta za strojništvo, Slovenija
[2] Javna agencija RS za varnost prometa, Slovenija

Čeprav so prometne nesreče, ki jih povzročijo okvarjena vozila, relativno redke, je tehnična brezhibnost vozil pomembna za varnost v cestnem prometu. V Evropski uniji so tehnični pogoji, ki jih morajo izpolnjevati vozila na javnih cestah, urejeni z direktivami EU. V skladu s temi direktivami so v vsaki državi EU organizirani tehnični pregledi. Ker so nacionalni predpisi v državah članicah EU za tehnične preglede vozil v cestnem prometu podrejeni direktivam EU, lahko domnevamo, da je v različnih državah članicah EU s primerljivo populacijo vozil približno enaka statistika ugotovljenih napak na tehničnem pregledu.

Najprej smo statistične podatke o tehničnih pregledih vozil analizirali za Slovenijo za sedem zaporednih let. Iz statističnih podatkov lahko sklepamo, da so odkrite napake konsistentne med obravnavanimi leti z izjemo najstarejših vozil. Po letu 2020 so se namreč tehnični pregledi za to starostno skupino vozil poostrili, kar ima za posledico povečano število odkritih napak. Enako velja tudi za prvi redni tehnični pregled motornih koles in štirikolesnikov. Pri osebnih in gospodarskih vozilih so najverjetnejše napake na svetlobni in električni opremi, zavornem sistemu in drugi opremi (npr. manjkajoči komplet prve pomoči za osebna vozila oz. gasilni aparat za gospodarska vozila). Motocikli in štirikolesniki imajo najverjetnejše napake na svetlobni, električni in drugi opremi ali pa bodo ne naredijo na preskusov za vozila kategorije L.

Statistične podatke za osebna vozila v Sloveniji smo primerjali s Finsko in Nemčijo. Poleg tega smo podatke za slovenska gospodarska vozila primerjali z nemškimi. Ugotovili smo, da je v Nemčiji strogost tehničnih pregledov višja za vse starostne razrede osebnih avtomobilov kot v Sloveniji. Neposredna primerjava napak, ugotovljenih na tehničnih pregledih, je zaradi različnih specifikacij napak v Nemčiji in Sloveniji možna le v omejenem obsegu. Kljub temu lahko trdimo, da sta deleža najpogostejših okvar (tj. svetlobne opreme in zavornega sistema) v Sloveniji in Nemčiji podobna. V nasprotju z Nemčijo ne moremo sklepati, da so tehnični pregledi na Finskem strožji kot v Sloveniji. Pri štirih skupinah napak (svetlobna in električna oprema; osi, kolesa in vzmetenje; podvozje in karoserija; vidljivost) je na Finskem ugotovljenih več napak kot v Sloveniji, medtem ko je bilo pri treh skupinah napak (zavorni sistem; krmiljenje; emisije) več napak. najdenih v Sloveniji. Pri identifikaciji vozil ni bilo ugotovljenih bistvenih razlik. V obeh državah so najpogostejše okvare na zavornem sistemu ter na svetlobni in električni opremi.

Na koncu so bili izdelani še multivariatni regresijski modeli za napovedovanje verjetnosti odkrivanja napak pri tehničnih pregledih. Različne variante statičnih in dinamičnih regresijskih modelov so bile testirani za devet skupin napak (svetlobna in električna oprema, zavorni sistem, krmiljenje, identifikacija vozila, osi, podvozje in vzmetenje, vidljivost, emisije in druga oprema) za slovenski vozni park osebnih vozil, gospodarskih vozil ter motornih kolesa in štirikolesnikov. Ugotovljeno je bilo, da je verjetnost odkrivanja napak mogoče učinkovito modelirati kot funkcijo starosti vozila.

**Ključne besede: osebna vozila, gospodarska vozila, tehnični pregledi, statistika napak, statistično modeliranje**

*Naslov avtorja za dopisovanje: Univerza v Ljubljani, Fakulteta za strojništvo, Aškerčeva 6, 1000 Ljubljana, Slovenija, jernej.klemenc@fs.uni-lj.si

Strojniški vestnik - Journal of Mechanical Engineering 69(2023)11-12, SI 52

Prejeto v recenzijo: 2023-04-14
Prejeto popravljeno: 2023-09-18
Odobreno za objavo: 2023-09-22

# Modeliranje vedenja magnetoreološkega elastomera ob trku z brezparametričnim polinomskim modelom, optimiziranim z gravitacijskim iskalnim algoritmom

Amrina Rasyada Zubir – Khisbullah Hudha* – Zulkiffli Abd. Kadir – Noor Hafizah Amer
Malezijska obrambna univerza, Oddelek za strojništvo, Malezija

Uporaba magnetoreoloških elastomerov (MRE) v avtomobilski industriji je v porastu, saj ti materiali omogočajo spreminjanje togosti in blaženja v prisotnosti magnetnega polja. MRE so bili v tej študiji uporabljeni v blažilniku z dvosmernim delovanjem, ki deluje kot aktuator v sistemu aktivnega sprednjega odbijača za preprečevanje nezaželenega prenosa vibracij na vozilo in potnike. Zgolj uporaba MRE pa ne zadostuje za zaščito vozila in potnikov v primeru srednjih in močnih trkov, kjer pri hitrostih vožnje nad 15 km/h nastopijo kritične poškodbe.

Raziskovalci so se zato lotili modeliranja vedenja vozil ob trku na podlagi brezparametričnega polinomskega modela 4. reda. Model je zasnovan za različne tokove od 0 A do 2 A, z interpolacijo pa tudi za vmesne tokove v višini 0,3 A, 0,7 A, 1,3 A in 1,7 A. Uspešnost postavljenega modela je bila validirana po postopku verifikacije s primerjavo rezultatov modela v paketu Matlab-Simulink in eksperimentalnih rezultatov, pridobljenih v padnem udarnem preizkusu blažilnika MRE. Stopnja ujemanja obeh odgovorov je bila analizirana z napako napovedovanja sile, validacijo uspešnosti razvitega modela in napovedjo histereznih lastnosti MRE.

Razvit je bil brezparametrični polinomski model za analizo dinamičnega vedenja elementov MRE pod udarno obremenitvijo pri različnih tokovih v območju od 0 A do 2 A. Uporabljena je bila polinomska funkcija četrtega reda.

Brezparametrični polinomski model je bil postavljen ob upoštevanju odmika, hitrosti, energije udarca in toka za doseganje izhodne sile. Neznanke so velikost, trend sledenja in faktor povezave. Optimizirane vrednosti modelnih parametrov so potrebne za določitev idealne oblike histereznih zank podajnega elementa.

V ta namen je bila uporabljena metoda GSA za določitev optimalnih vrednosti v fazi iztegovanja in stiskanja pri polinomskem modelu 4. reda. Cilj je optimizacija parametrov polinoma s primerjavo rezultatov simulacije in eksperimentov ter ustrezna prilagoditev indeksa zmogljivosti. Algoritem v fazi inicializacije ustvari naključno število in ga dodeli spremenljivki. Nato je vsaki entiteti v populaciji dodeljeno naključno število agentov N. Simulacija izračuna funkcijo prileganja za vsako entiteto in opravi proces izbire naključnih vrednosti. Nato se izračuna prileganje vsakega agenta v naslednji iteraciji in preverijo se omejitve. Rezultat po iteraciji tega procesa v več generacijah so optimizirani modelni parametri za vsak tokovni vhod.

Oblikovan je bil tudi interpolacijski model, ki pokriva vmesne vrednosti tokov 0,3 A, 0,7 A, 1,3 A in 1,7 A. Interpolacija je metoda iskanja prilega krivulje, ki uporablja linearne polinome za ustvarjanje novih podatkovnih točk v danem območju.

Interpolacijski model MRE je bil postavljen v okolju Matlab-Simulink z vhodnimi tokovi 0,3 A, 0,7 A, 1,3 A in 1,7 A, kot prikazuje slika 3. Izhodne sile podsistemov za vsak tok so bile kombinirane v krivuljo sila-odmik za oblikovani interpolacijski model.

Odgovor tega modela se dobro ujema z eksperimentalnimi podatki, največja napaka napovedi je manjša od 13 %. Odgovor interpolacijskega modela se dobro ujema z eksperimentalnimi podatki, največja napaka pa je manjša od 15,94 %.

Karakterizacija MRE je bila testirana z udarno hitrostjo 2,24 m/s v padnem udarnem preizkusu s polovično vrednostjo dejanskih parametrov vozila zaradi omejitev zasnove.

Glavni prispevek študije je predlog brezparametričnega modela MRE, ki lahko identificira histerezne lastnosti MRE pri danem električnem toku. Predstavljena je tudi metoda interpolacije, ki ne pokriva le vhodnega toka 2 A, temveč tudi vmesne vrednosti 0,3 A, 0,7 A, 1,3 A in 1,7 A.

**Ključne besede: magnetoreološki elastomer, MR blažilnik, polinomski model, gravitacijski iskalni algoritem, karakteristika sila-odmik, interpolacijski model**



*Naslov avtorja za dopisovanje: Malezijska obrambna univerza, Oddelek za strojništvo, Malezija, k.hudha@upnm.edu.my

Strojniški vestnik - Journal of Mechanical Engineering 69(2023)11-12, SI 53

Prejeto v recenzijo: 2023-05-02
Prejeto popravljeno: 2023-07-24
Odobreno za objavo: 2023-09-13

# Metoda za optimizacijo večparametrske sklopitve pri hidravlični valjalni oblikovalni napravi na podlagi faktorske zasnove

Hongfei Li – Min Luo – Tingting Xu – Qiaozhen Li – Yanming Hou
Severovzhodna univerza za naftno industrijo, Šola za tehniške vede in strojništvo, Kitajska

Hidravlična valjalna oblikovalna naprava je napredno orodje za popravila deformiranih vrtin, konstrukcijski parametri naprave pa neposredno vplivajo na učinek oblikovanja vrtine. Predstavljen je predlog optimizacijske metode za preučitev stanja deformacij in porazdelitve napetosti v cevi vrtine med popravilom ter analizo stopnje vpliva konstrukcijskih parametrov oblikovalne naprave na učinek oblikovanja. Metoda je primerna za kompleksne večparametrske konstrukcije kot je dana naprava ter lahko izboljša njeno varnost in zmogljivost oblikovanja.

V članku je predstavljena optimizacija konstrukcije hidravlične valjalne oblikovalne naprave ob upoštevanju glavnih konstrukcijskih parametrov. Zaradi visoke stopnje nelinearnosti stika med oblikovalno napravo in notranjo steno vrtine je težko izračunati učinek oblikovanja po tradicionalnih metodah. Ob upoštevanju nelinearnosti materiala vrtine ter kontakta med oblikovalno napravo in vrtino je bil postavljen parametrični model po metodi končnih elementov za deformacije cevi vrtine med popravilom z oblikovalno napravo. Proces oblikovanja vrtine med popravilom je podrobno analiziran. Nato je bila pripravljena faktorska zasnova z več geometrijskimi parametri za določitev signifikantnih faktorjev, razpon konstrukcijskih spremenljivk pa je bil določen glede na točnost in prileganje pri montaži. Za vzorčenje je bila uporabljena optimalna zasnova latinske hiperkocke, modeli odzivne površine pa so bili razviti s koračno regresijo. Nato je bil postavljen optimiziran matematični model in uporabljen je bil genetski algoritem za določitev optimalne kombinacije parametrov.

Iz rezultatov sledijo naslednji zaključki:

1) Ob upoštevanju dvojno nelinearnih karakteristik kontakta in materiala je bil razvit parametrični model po metodi končnih elementov za popravila deformacij na cevi vrtine s hidravlično valjalno oblikovalno napravo.
2) Opravljen je bil ortogonalni test za analizo in vrednotenje osmih geometrijskih parametrov oblikovalne naprave. Določenih je bilo pet parametrov, ki signifikantno vplivajo na oblikovanje.
3) Določeno je bilo območje vrednosti signifikantnih dejavnikov in opredeljena sta bila regresijski model odgovorov po metodi koračne regresije ter matematični model za optimizacijo oblikovalne naprave.
4) Po optimizaciji je bila opredeljena optimizirana konstrukcija oblikovalne naprave, ki bolje ščiti vrtino in izboljša učinkovitost popravil.

Numerične simulacije v študiji so bile nekoliko poenostavljene za lažje računanje. Upoštevati je mogoče več dejavnikov vpliva na oblikovanje, kot so: kotalni stik krogle s cevjo in telesom oblikovalne naprave, visokotemperaturne lastnosti materiala, vpliv začetnih preostalih napetosti v vrtini na oblikovanje itd.

Upoštevane so nelinearnosti v materialu in kontaktu. Razvit je bil parametrični model deformacij vrtine pri popravilih s hidravlično valjalno oblikovalno napravo, preučena pa sta bila tudi deformirano stanje in porazdelitev napetosti v cevi vrtine. Z ortogonalnim testom so bili prvič analizirani konstrukcijski parametri oblikovalne naprave. Za konstrukcijske spremenljivke je bilo izbranih pet parametrov s signifikantnim vplivom, s čimer je bila v veliki meri poenostavljena optimizirana delovna obremenitev večparametrske konstrukcije. Določen je bil razpon konstrukcijskih spremenljivk z obravnavo sklopitve med več geometrijskimi parametri. Model odzivne površine je bil razvit s koračno regresijo in postavljen je bil ustrezen optimiziran matematični model. Za rešitev je bil uporabljen genetski algoritem. Rezultati raziskave izboljšujejo varnost in zmogljivost oblikovalne naprave ter omogočajo učinkovito optimizacijo hidravlične valjalne oblikovalne naprave oz. kompleksnih konstrukcij.

**Ključne besede: hidravlična valjalna oblikovalna naprava, optimizacija konstrukcije, faktorska zasnova, ortogonalni test, metoda odzivnih površin, obnova vrtin**

*Naslov avtorja za dopisovanje: Severovzhodna univerza za naftno industrijo, Šola za tehniške vede in strojništvo, Kitajska, 1538937270@qq.com

Strojniški vestnik - Journal of Mechanical Engineering 69(2023)11-12, SI 54

Prejeto v recenzijo: 2023-05-20
Prejeto popravljeno: 2023-08-23
Odobreno za objavo: 2023-09-13

# Kakovost površin magnezijeve zlitine AZ9Đ po natančnem rezkanju z oslojenimi orodji

Jarosław Korpysa* – Józef Kuczmaszewski – Ireneusz Zagórski
Tehniška univerza v Lublinu, Fakulteta za strojništvo, Poljska

Strojna obdelava magnezijevih zlitin je težavna zaradi nevarnosti vžiga, zato se je treba izogibati njihovi abrazivni obdelavi. Za visoko kakovost obdelanih površin so potrebni alternativni obdelovalni postopki, kot rešitev pa se ponuja natančno rezkanje. Kakovost površin je še posebej pomembna pri magnezijevih zlitinah, ki se uporabljajo za komponente v avtomobilski, letalski in vesoljski industriji, izdelki pa morajo izpolnjevati najstrožje kakovostne standarde. Za obdelavo magnezijevih zlitin so se do sedaj uporabljali samo konvencionalni postopki obdelave z odrezavanjem, toda teh rešitev ni mogoče prenesti na natančno obdelavo z odrezavanjem zaradi drugačne mehanike procesa. Za omenjeno skupino materialov so torej potrebne ločene raziskave natančnega odrezavanja.

Študija preučuje kakovost površine preizkušancev iz magnezijeve zlitine AZ91D po natančnem rezkanju. Le-to je bilo opravljeno s trdokovinskimi steblastimi rezkarji s prevleko $TiB_2$ oz. TiAlN. Pri rezkanju so bile upoštevane te spremenljivke: rezalna hitrost $v_c$, podajanje na zob $f_z$ in aksialna globina reza $a_p$. Kakovost površine je bila analizirana na podlagi parametrov površinske hrapavosti in krivulj Abbott-Firestone. Vpliv različnih rezalnih parametrov in vrste orodne prevleke na površinsko hrapavost je bil analiziran tudi po metodi ANOVA.

Rezultati razkrivajo, da je kakovost površine po obdelavi odvisna od vrste prevleke na orodju in od uporabljenih parametrov obdelave. Edina izjema je bila aksialna globina reza, saj njene spremembe niso signifikantno vplivale na kakovost površin. Za preizkušance iz materiala AZ91D so bili značilni zelo nizki parametri površinske hrapavosti po natančnem rezkanju. Pri rezkanju z orodjem s prevleko TiAlN je uporaba variabilne rezalne hitrosti in podajanja na zob vedno povzročila postopno zmanjšanje parametrov površinske hrapavosti. Pri obdelavi z orodjem s prevleko $TiB_2$ so se parametri površinske hrapavosti sprva zmanjšali, nato pa so spet zrasli. Za rezultate pri obdelavi površin z orodjem s prevleko $TiB_2$ je značilen manjši raztros vrednosti. Vpliv pogojev pri obdelavi je potrdila tudi analiza ANOVA. Vrsta orodne prevleke in pogoji pri obdelavi niso signifikantno vplivali na krivulje Abbott-Firestone. Razmeroma majhen naklon krivulj Abbott-Firestone kaže na to, da imajo površine po natančni obdelavi razmeroma visoko obstojnost proti abraziji.

V prihodnjih raziskavah bo mogoče povečati število zajetih tehnoloških parametrov obdelave za točnejšo določitev vpliva spreminjajočih se pogojev obdelave na površinsko hrapavost. Razširitev raziskave bo omogočila tudi optimizacijo pogojev obdelave za najvišjo kakovost površin.

Pomembna novost, obravnavana v pričujočem članku, je natančna obdelava magnezijevih zlitin. Ta še ni razširjena v praksi in je bila do sedaj opisana v le nekaj člankih. Opravljena raziskava tako prinaša osnovno znanje o natančni obdelavi magnezijeve zlitine AZ91D in dosegljivi površinski hrapavosti. Predstavljena študija je pomemben prispevek na področju obdelave zlitin lahkih kovin z odrezavanjem. Izbor primernih orodij in obdelovalnih pogojev lahko v vsakem primeru vpliva na kakovost površin. To je pomemben faktor, ki opredeljuje rezultate procesa obdelave z odrezavanjem. Pomemben prispevek pričujočega članka je tudi analiza funkcijskih parametrov in krivulj Abbott-Firestone za vrednotenje površin z vidika možnih interakcij komponent.

**Ključne besede: natančno rezkanje, kakovost površin, krivulja Abbott-Firestone, ANOVA, oslojena orodja**



*Naslov avtorja za dopisovanje: Tehniška univerza v Lublinu, Fakulteta za strojništvo, Poljska, j.korpysa@pollub.pl

Strojniški vestnik - Journal of Mechanical Engineering 69(2023)11-12, SI 55

Prejeto v recenzijo: 2023-06-08
Prejeto popravljeno: 2023-08-16
Odobreno za objavo: 2023-09-19

# Regulacijski algoritem z aktivnim odpravljanjem motenj za gnano verigo polirnega robota

Kaifeng Dong[1] – Jun Li[1] – Mengyao Lv[1] – Xin Li[1] – Wei Gu[2] – Gang Cheng[1,2,*]

[1] Kitajska rudarska in tehniška univerza, Šola za mehatroniko, Kitajska
[2] Shangdong Zhongheng Optoelectronic Technology Co., Kitajska

V članku je predstavljen predlog regulacijske strategije na podlagi izboljšanega algoritma z aktivnim odpravljanjem motenj (ADRC) za odpravo težav zaradi pomanjkljive zmogljivosti preprečevanja motenj, nizke regulacijske točnosti in slabe odpornosti proti interferencam pri vodenju gibanja robota za poliranje optičnih zrcal z obstoječimi regulacijskimi algoritmi.

Predstavljen je regulator ADRC za pogon sinhronskega motorja s trajnimi magneti (PMSM) v vsaki gnani verigi. Najprej je bila funkcija *fal* v izvirnem algoritmu ADRC izboljšana s funkcijo ***a wfal***. Na podlagi servosistema robota za poliranje optičnih zrcal sta bila zasnovana regulator ADRC prvega reda za tokovno zanko in regulator ADRC drugega reda za hitrostno-položajno zanko.

Regulacijski algoritem ADRC je bil končno uvožen v krmilnike gibanja za preizkus gibanja treh gnanih verig in vrha polirnega robota. Krivulje odgovora regulacijskih algoritmov PID in ADRC pri spreminjajočih se obremenitvah so bile simulirane z orodjem Simulink.

Zgrajena je bila tudi eksperimentalna platforma za določitev napake sledenja premika treh gnanih verig robota za poliranje optičnih zrcal. Napake sledenja središča premične platforme polirnega robota trajektoriji pri regulaciji ADRC in PID so bile določene s kinematičnimi izračuni. Rezultati razkrivajo, da so fluktuacije krivulje odgovora hitrosti pod obremenitvijo pri regulaciji ADRC majhne ter da se krivulja hitro ujame. Krivulja se dobro ujema s ciljno trajektorijo, določeno s simulacijami. Za krivuljo odgovora hitrosti pri PID-regulaciji ni značilen le prenihaj, temveč tudi večje fluktuacije pod obremenitvijo, ki pri simulacijah niso izginile. Napaka sledenja središča premične platforme trajektoriji v smereh X in Y pri regulaciji ADRC je precej manjša kot pri PID-regulaciji, s tem pa izpolnjuje zahteve za obdelavo velikih optičnih zrcal.

Algoritem ADRC tako zagotavlja boljšo odpornost proti motnjam in visoko točnost sledenja trajektoriji, kakor tudi hiter odgovor sistema. Model servosistema v pričujočem članku obravnava samo eno pogonsko verigo polirnega robota ter ne upošteva interakcij med premiki treh gnanih verig. Upoštevane so bile tudi idealizirane predpostavke za PMSM.

V prihodnje raziskave bo smiselno vključiti eksperimentalno in teoretično raziskavo vpliva PMSM ob upoštevanju treh gnanih verig polirnega robota. Novost pri študiji je uporaba izboljšanega regulacijskega algoritma ADRC za paralelni mehanizem robota za poliranje velikih optičnih zrcal ter eksperimentalno sledenje trajektoriji gibanja središča premične platforme robota.

Dokazano je bilo, da predlagani regulacijski algoritem ADRC izpolnjuje zahteve za obdelavo površine optičnih zrcal.

**Ključne besede: ADRC, sledenje trajektoriji, paralelni mehanizem, gnana veriga, PMSM, polirni robot, PID**

*Naslov avtorja za dopisovanje: Kitajska rudarska in tehniška univerza, Šola za mehatroniko, Kitajska, chg@cumt.edu.cn

# Izr. prof. dr. Igor Janežič

Hladni jesenski veter, ki si je utiral pot po deževni slovenski krajíni in s seboj ponesel zadnjo sapo klenega moža, zavednega Slovenca, ki je vse svoje življenje posvetil soustvarjanju napredka družbe in nesebičnemu razdajanju generacijam študentom in mladim strokovnjakom v gospodarstvu.

Izr. prof. dr. Igor Janežič se je rodil 19. julija 1934 v Kamniku. Po končani osnovni šoli, ki jo je obiskoval v Kamniku, se je vpisal na Tehniško srednjo šolo strojne smeri v Ljubljani in jo v letu 1953 zaključil. Sledila je dvoletna zaposlitev v podjetju TITAN Kamnik, kjer je delal v oddelku konstrukcij. Jeseni leta 1955 se je vpisal na univerzitetni študij na Fakulteti za strojništvo (FS), Univerze v Ljubljani (UL), ki ga je zaključil v letu 1961. Med študijem je bil strokovno angažiran in je sleherne počitnice izkoristil za praktično izpopolnjevanje v podjetjih Metalna Maribor, TAM Maribor in EMO Celje. Bil je štipendist podjetja FAFRAM Smederevo, kjer se je po zaključku študija tudi zaposlil do leta 1963 in medtem odslužil tudi vojaški rok.

Leta 1963 se je začela njegovo delovanje na FS UL, kjer je dobil priložnost kot asistent pri zaslužnem profesorju dr. Jožetu Hlebanji. Vodil je vaje pri predmetih Tehniško risanje in Strojni elementi. Leta 1970 je bil na podlagi uspešnega pedagoškega in strokovnega dela izvoljen v naziv predavatelj pri predmetu Strojni elementi. Pod mentorstvom prof. dr. Jožeta Hlebanje je leta 1970 zagovarjal magistrsko disertacijo z naslovom: Raziskava nosilnosti prilagodnih vijakov v debelostenih zvezah. Doktorski študij je prav tako pod mentorstvom prof. Hlebanje uspešno zaključil tri leta kasneje, leta 1973, z zagovorom doktorske disertacije z naslovom: Nosilnost dinamično obremenjenih vijačenih pririobnic.

Leta 1971 je se je strokovno izpopolnjeval na Tehniški univerzi (TU) Dresden v Nemčiji, leta 1981 pa tudi na TU Eindhoven na Nizozemskem. Raziskovalno delo prof. dr. Janežiča je bilo ves čas prepleteno z izzivi, ki so prihajali iz gospodarstva; le-to se je v tem času intenzivno razvijalo prav po zaslugi generacije strokovnjakov, kakršen je bil prof. dr. Janežič, ki je s svojimi izvirnimi konstrukcijskimi rešitvami na svoj način doprinašal k prenosu znanja neposredno v industrijsko prakso. O tem priča dolg seznam velikih podjetij, s katerimi je sodeloval: Iskra Kranj, Železarna Jesenice, Železarna Štore, Železarna Ravne, IKOM Šmarje pri Jelšah, Gorenje Velenje in ne nazadnje njemu domači: TITAN Kamnik.

Študenti so ga cenili prav po tem, da jih je seznanjal z aktualnimi razvojnimi trendi na področju konstruiranja in dimenzioniranja najrazličnejših strojev in naprav ter izdelkov; navidez dolgočasno konstruiranje je po njem postalo dinamično, vznemirljivo popotovanje skozi svet ustvarjanja in kreativnosti novih konstrukcijskih rešitev, ki so bile ljudem v pomoč, gospodarstvu so omogočale stalen razvoj, družbi pa blagostanje. Ne samo to, izr. prof. dr. Igor Janežič je bil v očeh generacij študentov cenjen kot uglajen gospod, vrhunska avtoriteta, izvrsten predavatelj, predvsem pa kot odprt in venomer iskren človek; profesor z veliko začetnico. Predaval je študentom na Fakulteti za strojništvo, na Biotehniški fakulteti in na Fakulteti za elektrotehniko in sicer pri predmetih Strojni elementi, Uvod v strojništvo, Mehanski sistemi, Mehanizmi in Finomehanika, Konstruiranje strojev, Mehanika in Mehanizmi. Bil je mentor štirim magistrom znanosti, 61 diplomiranim inženirjem strojništva in kar 115 inženirjem strojništva. Štirje njegovi diplomati so prejeli Prešernove nagrade za vrhunske študentske raziskovalne dosežke.

Bil je član pomembnih strokovnih združenj v ožji in širši domovini bivše države, pa tudi v mednarodnem prostoru. Med letoma 1977 in 1981 je bil član izvršnega odbora Zveze inženirjev in tehnikov strojništva in elektrotehnike Jugoslavije (SMEITJ). Med leti 1980 in 1985 je bil član uredniškega odbora revije Mašinstvo in član Jugoslovanskega društva za teorijo mehanizmov in strojev (JuToMM), v mednarodnem prostoru pa je bil član Združenja za stroje in mehanizme (IFTOMM) in član Združenja nemških inženirjev (VDI). Med leti 1982 in 1986 je bil član Strokovnega sveta Programsko interesne skupnosti za metalurgijo in strojništvo SRS. Je prejemnik Svečane listine Fakultete za strojništvo, Univerze v Ljubljani in Odlikovanja z redom dela.

Prof.dr. Igor Janežič je opravljal tudi odgovorne vodstvene funkcije na FS in UL; v dveh mandatnih obdobjih med leti 1983 in 1989 ter 1993 in 1995 je bil prodekan za pedagoško delo. V letu 1991 je prevzel vodenje Katedre za konstruiranje in delovne stroje hkrati pa je bil izvoljen v Svet UL. Sodeloval je pri ustanoviti oddelka Fakultete

za strojništvo v Novi Gorici, kjer je bil tudi njen vodja. Pedagoško, strokovno in znanstveno je bil aktiven vse do svoje upokojitve konec leta 2000.

Prof. dr. Igor Janežič je pustil globok pečat tako na matični Fakulteti za strojništvo, kot tudi na celotni Univerzi v Ljubljani ter predvsem v gospodarstvu. Toda, zdi se mi, da je na tem mestu vendarle potrebno ugotoviti predvsem, da prof.dr. Igor Janežič tako mene, kakor tudi slehernega od številnih generacij študentov ni pustil ravnodušnega – profesor, ki mu je bilo mar. Zaradi tega ga bomo v trajnem spominu ohranili tako njegovi sodelavci, s katerimi je soustvarjal odmevne zgodbe o uspehih, kot tudi študentje, ki jim je nesebično razdajal svoje obsežno strokovno znanje, na katerem temelji naša prihodnost.

Prof. dr. Mihael Sekavčnik, dekan

# Guide for Authors

All manuscripts must be in English. Pages should be numbered sequentially. The manuscript should be composed in accordance with the Article Template given above. The suggested length of contributions is 10 to 20 pages. Longer contributions will only be accepted if authors provide justification in a cover letter. For full instructions see the Information for Authors section on the journal's website: http://en.sv-jme.eu .

**SUBMISSION:**

Submission to SV-JME is made with the implicit understanding that neither the manuscript nor the essence of its content has been published previously either in whole or in part and that it is not being considered for publication elsewhere. All the listed authors should have agreed on the content and the corresponding (submitting) author is responsible for having ensured that this agreement has been reached. The acceptance of an article is based entirely on its scientific merit, as judged by peer review. Scientific articles comprising simulations only will not be accepted for publication; simulations must be accompanied by experimental results carried out to confirm or deny the accuracy of the simulation. Every manuscript submitted to the SV-JME undergoes a peer-review process.

The authors are kindly invited to submit the paper through our web site: http://ojs.sv-jme.eu. The Author is able to track the submission through the editorial process - as well as participate in the copyediting and proofreading of submissions accepted for publication - by logging in, and using the username and password provided.

**SUBMISSION CONTENT:**

The typical submission material consists of:

- A **manuscript** (A PDF file, with title, all authors with affiliations, abstract, keywords, highlights, inserted figures and tables and references),
- Supplementary files:
  - a **manuscript** in a WORD file format
  - a **cover letter** (please see instructions for composing the cover letter)
  - a ZIP file containing **figures** in high resolution in one of the graphical formats (please see instructions for preparing the figure files)
  - possible **appendicies** (optional), cover materials, video materials, etc.

Incomplete or improperly prepared submissions will be rejected with explanatory comments provided. In this case we will kindly ask the authors to carefully read the Information for Authors and to resubmit their manuscripts taking into consideration our comments.

**COVER LETTER INSTRUCTIONS:**

Please add a **cover letter** stating the following information about the submitted paper:

1. Paper **title**, list of **authors** and their **affiliations**. **One** corresponding author should be provided.
2. **Type of paper**: original scientific paper (1.01), review scientific paper (1.02) or short scientific paper (1.03).
3. A **declaration** that neither the manuscript nor the essence of its content has been published in whole or in part previously and that it is not being considered for publication elsewhere.
4. State the **value of the paper** or its practical, theoretical and scientific implications. What is new in the paper with respect to the state-of-the-art in the published papers? Do not repeat the content of your abstract for this purpose.
5. We kindly ask you to suggest at least two **reviewers** for your paper and give us their names, their full affiliation and contact information, and their scientific research interest. The suggested reviewers should have at least two relevant references (with an impact factor) to the scientific field concerned; they should not be from the same country as the authors and should have no close connection with the authors.
6. Please confirm that authors are willing/able to pay the Open Access **publication fee** as indicated in the Guide for Authors under Publication Fee, available at https://www.sv-jme.eu/guide-for-authors-online/.

**FORMAT OF THE MANUSCRIPT:**

The manuscript should be composed in accordance with the Article Template. The manuscript should be written in the following format:

- A **Title** that adequately describes the content of the manuscript.
- A list of **Authors** and their **affiliations**.
- An **Abstract** that should not exceed 250 words. The Abstract should state the principal objectives and the scope of the investigation, as well as the methodology employed. It should summarize the results and state the principal conclusions.
- 4 to 6 significant **key words** should follow the abstract to aid indexing.
- 4 to 6 **highlights;** a short collection of bullet points that convey the core findings and provide readers with a quick textual overview of the article. These four to six bullet points should describe the essence of the research (e.g. results or conclusions) and highlight what is distinctive about it.
- An **Introduction** that should provide a review of recent literature and sufficient background information to allow the results of the article to be understood and evaluated.
- A **Methods** section detailing the theoretical or experimental methods used.
- An **Experimental section** that should provide details of the experimental set-up and the methods used to obtain the results.
- A **Results** section that should clearly and concisely present the data, using figures and tables where appropriate.
- A **Discussion** section that should describe the relationships and generalizations shown by the results and discuss the significance of the results, making comparisons with previously published work. (It may be appropriate to combine the Results and Discussion sections into a single section to improve clarity.)
- A **Conclusions** section that should present one or more conclusions drawn from the results and subsequent discussion and should not duplicate the Abstract.
- **Acknowledgement** (optional) of collaboration or preparation assistance may be included. Please note the source of funding for the research.
- **Nomenclature** (optional). Papers with many symbols should have a nomenclature that defines all symbols with units, inserted above the references. If one is used, it must contain all the symbols used in the manuscript and the definitions should not be repeated in the text. In all cases, identify the symbols used if they are not widely recognized in the profession. Define acronyms in the text, not in the nomenclature.
- **References** must be cited consecutively in the text using square brackets [1] and collected together in a reference list at the end of the manuscript.
- **Appendix(-icies)** if any.

**SPECIAL NOTES**

**Units**: The SI system of units for nomenclature, symbols and abbreviations should be followed closely. Symbols for physical quantities in the text should be written in italics (e.g. *v*, *T*, *n*, etc.). Symbols for units that consist of letters should be in plain text (e.g. $ms^{-1}$, K, min, mm, etc.). Please also see: http://physics.nist.gov/cuu/pdf/sp811.pdf .

**Abbreviations** should be spelt out in full on first appearance followed by the abbreviation in parentheses, e.g. variable time geometry (VTG). The meaning of symbols and units belonging to symbols should be explained in each case or cited in a **nomenclature** section at the end of the manuscript before the References.

**Figures** (figures, graphs, illustrations digital images, photographs) must be cited in consecutive numerical order in the text and referred to in both the text and the captions as Fig. 1, Fig. 2, etc. Figures should be prepared without borders and on white grounding and should be sent separately in their original formats. If a figure is composed of several parts, please mark each part with a), b), c), etc. and provide an explanation for each part in Figure caption. The caption should be self-explanatory. Letters and numbers should be readable (Arial or Times New Roman, min 6 pt with equal sizes and fonts in all figures). Graphics (submitted as supplementary files) may be exported in resolution good enough for printing (min. 300 dpi) in any common format, e.g. TIFF, BMP or JPG, PDF and should be named Fig1.jpg, Fig2.tif, etc. However, graphs and line drawings should be prepared as vector images, e.g. CDR, AI. Multi-curve graphs should have individual curves marked with a symbol or otherwise provide distinguishing differences using, for example, different thicknesses or dashing.

**Tables** should carry separate titles and must be numbered in consecutive numerical order in the text and referred to in both the text and the captions as Table 1, Table 2, etc. In addition to the physical quantities, such as *t* (in italics), the units [s] (normal text) should be added in square brackets. Tables should not duplicate data found elsewhere in the manuscript. Tables should be prepared using a table editor and not inserted as a graphic.

**REFERENCES:**

A reference list must be included using the following information as a guide. Only cited text references are to be included. Each reference is to be referred to in the text by a number enclosed in a square bracket (i.e. [3] or [2] to [4] for more references; do not combine more than 3 references, explain each). No reference to the author is necessary.

References must be numbered and ordered according to where they are first mentioned in the paper, not alphabetically. All references must be complete and accurate. Please add DOI code when available. Examples follow.

**Journal Papers:**

Surname 1, Initials, Surname 2, Initials (year). Title. *Journal*, volume, number, pages, DOI code.

[1] Hackenschmidt, R., Alber-Laukant, B., Rieg, F. (2010). Simulating nonlinear materials under centrifugal forces by using intelligent cross-linked simulations. *Strojniški vestnik - Journal of Mechanical Engineering*, vol. 57, no. 7-8, p. 531-538, DOI:10.5545/sv-jme.2011.013.

Journal titles should not be abbreviated. Note that journal title is set in italics.

**Books:**

Surname 1, Initials, Surname 2, Initials (year). Title. Publisher, place of publication.

[2] Groover, M.P. (2007). *Fundamentals of Modern Manufacturing*. John Wiley & Sons, Hoboken.

Note that the title of the book is italicized.

**Chapters in Books:**

Surname 1, Initials, Surname 2, Initials (year). Chapter title. Editor(s) of book, book title. Publisher, place of publication, pages.

[3] Carbone, G., Ceccarelli, M. (2005). Legged robotic systems. Kordić, V., Lazinica, A., Merdan, M. (Eds.), Cutting Edge Robotics. Pro literatur Verlag, Mammendorf, p. 553-576.

**Proceedings Papers:**

Surname 1, Initials, Surname 2, Initials (year). Paper title. Proceedings title, pages.

[4] Štefanić, N., Martinčević-Mikić, S., Tošanović, N. (2009). Applied lean system in process industry. *MOTSP Conference Proceedings*, p. 422-427.

**Standards:**

Standard-Code (year). Title. Organisation. Place.

[5] ISO/DIS 16000-6.2:2002. *Indoor Air – Part 6: Determination of Volatile Organic Compounds in Indoor and Chamber Air by Active Sampling on TENAX TA Sorbent, Thermal Desorption and Gas Chromatography using MSD/FID.* International Organization for Standardization. Geneva.

**WWW pages:**

Surname, Initials or Company name. Title, from http://address, date of access.

[6] Rockwell Automation. Arena, from *http://www.arenasimulation.com,* accessed on 2009-09-07.

**EXTENDED ABSTRACT:**

When the paper is accepted for publishing, the authors will be requested to send an **extended abstract** (approx. one A4 page or 3500 to 4000 characters or approx. 600 words). The instruction for composing the extended abstract are published on-line: http://www.sv-jme.eu/information-for-authors/ .

**COPYRIGHT:**

Authors submitting a manuscript do so on the understanding that the work has not been published before, is not being considered for publication elsewhere and has been read and approved by all authors. The submission of the manuscript by the authors means that the authors automatically agree to publish the paper uder CC-BY 4.0 Int. or CC-BY-NC 4.0 Int. when the manuscript is accepted for publication. All accepted manuscripts must be accompanied by a Copyright Agreement, which should be sent to the editor. The work should be original work by the authors and not be published elsewhere in any language without the written consent of the publisher. The proof will be sent to the author showing the final layout of the article. Proof correction must be minimal and executed quickly. Thus it is essential that manuscripts are accurate when submitted. Authors can track the status of their accepted articles on https://en.sv-jme.eu/.

**PUBLICATION FEE:**

Authors will be asked to pay a publication fee for each article prior to the article appearing in the journal. However, this fee only needs to be paid after the article has been accepted for publishing. The fee is 380 EUR (for articles with maximum of 6 pages), 470 EUR (for articles with maximum of 10 pages), plus 50 EUR for each additional page. The additional cost for a color page is 90.00 EUR (only for a journal hard copy; optional upon author's request). These fees do not include tax.

Strojniški vestnik -Journal of Mechanical Engineering
Aškerčeva 6, 1000 Ljubljana, Slovenia, e-mail: info@sv-jme.eu

9 770039 248001
ISSN 0039-2480

http://www.sv-jme.eu

# Contents

## Papers